2-8-2021 2:00 PM

Investigating the Corrosion Behaviour of Ni-based alloys in Industrially Relevant Environments

Jeffrey D. Henderson, *The University of Western Ontario*

Supervisor: Noël, James J., *The University of Western Ontario*
Joint Supervisor: Shoesmith, David W., *The University of Western Ontario*
A thesis submitted in partial fulfillment of the requirements for the Doctor of Philosophy degree in Chemistry

Recommended Citation

Henderson, Jeffrey D., "Investigating the Corrosion Behaviour of Ni-based alloys in Industrially Relevant Environments" (2021). *Electronic Thesis and Dissertation Repository*. 7615.
https://ir.lib.uwo.ca/etd/7615

Abstract

Typical engineering materials may experience high corrosion rates when exposed to aggressive service conditions. Such conditions include high concentrations of aggressive anions and oxidants, high solution acidity, and/or high temperatures. Alloys with high corrosion resistance may be selected to avoid material failure caused by corrosion, for example, Ni-Cr-Mo alloys. These alloys exhibit excellent corrosion resistance due to the formation of a passive oxide film, primarily containing Cr and Mo. However, film breakdown can result in localized corrosion, *e.g.*, crevice corrosion. Localized corrosion processes can penetrate deep into the bulk alloy, threatening its integrity. While the oxide film and localized corrosion processes have been extensively studied, many mechanistic features remain unresolved.

Here, the corrosion behaviour of commercially available Ni-Cr-Mo alloys has been studied using electrochemical, spectroscopic, and microscopy techniques. Electrochemical measurements (Chapter 3) showed that increases in Cr content improve passive film properties, while increases in Mo content improve film stability in acidic solutions. Atomic emission spectroelectrochemistry (AESEC) measurements (Chapters 4 and 5) revealed a dynamic role for Mo deposition during film breakdown. Transpassive dissolution occurring in neutral solutions led to the deposition of Mo-rich species, while repassivation resulted in their release to solution. Surface activation followed by repassivation in acidic solution was found to cause a similar process. The mechanism of crevice corrosion (Chapter 6) was investigated using a galvanostatic technique combined with weight loss measurements. Internal cathodic reactions were found to be an important feature, intensifying damage by as much as 76 %, depending on the Mo content of the alloy. The effect of fluoride (Chapter 7) on the corrosion behaviour of Ni- and Fe-based alloys was investigated. Film stability was found to decrease in the presence of trace quantities, especially as the applied potential was increased.

The findings reported throughout this thesis suggest a delicate balance between Cr and Mo is required for optimal corrosion performance, however, an optimal alloy composition has yet to be determined. The results presented in this thesis provide new mechanistic information necessary for understanding the corrosion of these industrially important alloys.

Keywords

Ni-Cr-Mo, Hastelloy, chromium, molybdenum, passive film, crevice corrosion, cathodic reaction, alloy composition, electrochemistry, surface analysis, AESEC

Summary for Lay Audience

Both scientists and engineers continue to investigate the effect of alloy composition on corrosion performance. Knowledge of this relationship is essential for the accurate selection of materials used in the nuclear, aerospace, petrochemical, chemical processing, and other industries. While stainless steels are among the most commonly used alloys, during exposure to aggressive conditions they can fail due to elevated corrosion rates and localized corrosion processes. Such conditions include strong acids, strong oxidants, aggressive anions, and/or high temperatures. Under these conditions, highly corrosion resistant materials should be employed, for example, Ni-based alloys containing additions of Cr and Mo, sometimes referred to as Superalloys. The corrosion resistance exhibited by these alloys is the result of a protective oxide layer formed at the outermost surface of the alloy, which acts as a barrier to continued corrosion. Since countless variations of Ni-Cr-Mo alloys exist commercially, accurate material selection necessitates a thorough understanding of the relationship between composition and corrosion behaviour. The results presented in this thesis provide new mechanistic details necessary to understand and predict the corrosion of these industrially important alloys.

Co-Authorship Statement

This thesis includes both published, Chapters 3-6, and submitted data, Chapter 7. For all chapters, I (Jeffrey D. Henderson) have acted as the primary investigator and author, with the following contributions from co-authors:

Chapter 3: This manuscript was co-authored by Ms. Baian Almusned, Dr. Mojtaba Momeni, Ms. Samantha Anderson, Dr. Vahid Dehnavi, Dr. Dmitrij Zagidulin, Dr. David Shoesmith, and Dr. James Noël (*J. Electrochem. Soc.* **2020**, 167 (13), 131512). B.A. and S.A. assisted with electrochemical measurements. M.M., V.D., D.S., and J.N. assisted in the interpretation of data. D.Z. designed the software used to quantify breakdown behavior. J.D.H. prepared the first draft of the manuscript. All co-authors assisted in editing the original manuscript.

Chapter 4: This manuscript was co-authored by Dr. Xuejie Li, Dr. David Shoesmith, Dr. James Noël, and Dr. Kevin Ogle (*Corros. Sci.* **2019**, 147, 32-40). J.D.H. and X.L. conducted all experimental work. X.L., D.S., J.N., and K.O. assisted in the interpretation of data. J.D.H. prepared the first draft of the manuscript. All co-authors assisted in editing the original manuscript.

Chapter 5: This manuscript was co-authored by Dr. Xuejie Li, Dr. Fraser Filice, Dr. Dmitrij Zagidulin, Dr. Mark Biesinger, Mr. Brad Kobe, Dr. David Shoesmith, Dr. Kevin Ogle, and Dr. James Noël (*J. Electrochem. Soc.* **Accepted**, DOI: 10.1149/1945-7111/abe47a). J.D.H. and X.L. conducted all experimental work. F.F. and D.Z. assisted with glove box apparatus. M.B. and B.K. assisted with XPS data. X.L., D.W., K.O., and J.N. assisted in the interpretation of data. J.D.H. prepared the first draft of the manuscript. All co-authors assisted in editing the original manuscript.

Chapter 6: This manuscript was co-authored by Dr. Nafiseh Ebrahimi, Dr. Vahid Dehnavi, Dr. Mengnan Guo, Dr. David Shoesmith, and Dr. James Noël (*Electrochim. Acta*. **2018**, 283, 1600-1608). J.D.H. conducted all experimental work with N.E. and M.G. providing minor assistance. N.E., V.D., D.S., and J.N assisted in the interpretation of data. J.D.H. prepared the first draft of the manuscript. All co-authors assisted in editing the original manuscript.

Chapter 7: This manuscript was co-authored by Dr. Sridhar Ramamurthy, Dr. Fraser Filice, Dr. Mark Biesinger, Dr. David Shoesmith, Dr. G. Bryce McGarvey, and Dr. James Noël (**2021**, *Submitted*). J.D.H. conducted all experimental work with F.F. providing minor assistance. S.R., D.S., G.B.M. and J.N. assisted in the interpretation of data. J.D.H. prepared the first draft of the manuscript. All co-authors assisted in editing the original manuscript.

Acknowledgments

First, I would like to thank my supervisors, Dr. Dave Shoesmith and Dr. Jamie Noël, for providing the resources and guidance necessary to complete my Ph.D. studies. While at times I am sure I drove you both crazy, you pushed me to learn, motivated me when I felt discouraged, and gave me the freedom to explore my project. Most importantly, you did so with patience, a sense of humor, and a smile. I couldn't have asked for a better team.

I would also like to thank the entire Shoesmith/Noël research groups. While there are too many to name individually, I want to thank a few individuals for their specific role during my graduate studies: Dr. Dmitrij Zagidulin, thank you for giving me a hard time when needed (and not needed). You kept my research moving forward and pushed me to learn. Dr. Vahid Dehnavi, Dr. Jian Chen, and Dr. Mojtaba Momeni, thank you for the many conversations we shared, for your research advice, and for (gently) pointing out my mistakes. Lastly, I want to acknowledge the undergraduate research students whom I had the pleasure of supervising: Alyssa Coelho, Samantha Anderson, Baian Almusned, and Adam Morgan.

I would also like to thank the people outside of our research groups whom I was fortunate to work alongside. Again, there are too many to name, but I want to single out a few individuals: Dr. Mark Biesinger, Mr. Brad Kobe, and Dr. Sridhar Ramamurthy at Surface Science Western, for always having an open door, a willingness to go through data, and for their guidance and encouragement during my time at Surface Science Western. Dr. Bryce McGarvey for his help and guidance in carrying out the fluoride-based experiments. Mr. Ivan Barker for his help and guidance in conducting analyses at the Zircon and Accessory Phase Laboratory. Mr. Brian Dalrymple and Mr. Frank Van Sas from the Physics and Astronomy Machine Shop and Mr. Clayton Cook and Mr. Dan Sweiger from University Machine Services for their help in bringing our research ideas to life.

I also want to acknowledge everyone I met and worked with during my time at the École Nationale Supérieure de Chimie de Paris (Chimie ParisTech). Much of my success in Paris, I owe to my supervisors, Dr. Kevin Ogle and Dr. Philippe Marcus. Through these collaborations, I was fortunate to work alongside members of their research teams, all of whom made me feel welcome, were patient with my poor French, and were great mentors. While there are too many people to name individually, I would like to acknowledge Mr. Xuejie (Jackie) Li for his support during my time in Paris.

Lastly, I would like to acknowledge the support of my family. To parents, Mary-Ellen and Dan Henderson, I couldn't have done this without your unconditional love and support. While the research topics were foreign to you, you always showed interest and supported my progress and accomplishments. Last, but not least, I want to thank my girlfriend, Courtney Fast, for putting up with me at my best and my worst. I couldn't have done this without your endless encouragement, love, support, and humour. I should apologize though, for all the weekends worked in my first three years, anyone else would have thought I was crazy…

This thesis is dedicated to my parents,

Mary-Ellen and Dan Henderson

Table of Contents

List of Tables

List of Figures

List of Appendices

List of Symbols and Acronyms

Symbols

A	Surface area
a	Activity
C	Capacitance
$\mathrm{C}_{3\sigma}$	Detection limit
C_{DL}	Double-layer capacitance
C_{f}	Film capacitance
C_{M}	Instantaneous concentration of metal M
d	Lattice spacing
E	Potential
$\mathrm{E}_{\mathrm{APP}}$	Applied potential
E_{B}	Breakdown potential
$\mathrm{E}_{\mathrm{CORR}}$	Corrosion potential
E_{e}	Equilibrium potential (non-standard conditions)
$\mathrm{E}_{\mathrm{e}}{}^{\circ}$	Equilibrium potential (standard conditions)
$\mathrm{E}_{\mathrm{i=0}}$	Potential of zero current
$\mathrm{E}_{\mathrm{PASS}}$	Passivation potential
E_{R}	Repassivation potential
E_{T}	Transpassive potential
F	Faraday constant
f	Flow rate
I	Current
i	Current density
i_{A} (i_{anodic})	Anodic current density
i_{C} (i_{cathodic})	Cathodic current density
$\mathrm{i}_{\mathrm{CORR}}$	Corrosion current density
$\mathrm{i}_{\mathrm{CRIT}}$	Critical current density
i_{e}	Electrical current density
$\mathrm{i}_{\mathrm{e}}^{*}$	Convoluted electrical current density

i_M	Elemental current density
i_{net}	Net current density
i_o	Exchange current density
i_{PASS}	Passive current density
i_Σ	Sum elemental current density
j	Imaginary number ($j^2 = -1$)
K_{eq}	Equilibrium constant
K_{sp}	Solubility product
L	Inductance
m	Molar mass
m_{avg}	Molar mass (weighted average)
n	Number of electrons
n_{avg}	Number of electrons (weighted average)
n_B	Integer (Bragg’s Law)
p	Exponent (CPE)
Q_A	Total applied charge
Q_W	Charge equivalent to the weight loss
R	Resistance
R_{CT}	Charge transfer resistance
R_f	Film resistance
R_{int}	Interfacial resistance
R_L	Resistance associated with inductive element
R_P	Polarization Resistance
R_S	Solution resistance
V_M^{x-}	Metal vacancy
V_O^{2+}	Oxygen vacancy
W	Weight loss
X_M	Mass fraction of metal M
Y_o	Constant (CPE)
Z	Impedance
Z'	Impedance (real)

Z''	Impedance (imaginary)
$\lvert Z \rvert$	Impedance modulus
α	Transfer coefficient
β	Tafel slope
ΔG	Gibbs free energy change (non-standard conditions)
ΔG°	Gibbs free energy change (standard conditions)
η	Overpotential
θ	Phase shift
θ_B	Angle of incidence (Bragg’s Law)
Θ_M	Accumulation or excess dissolution of metal M
κ	Sensitivity factor
λ	wavelength of the incident beam
ν_M	Instantaneous dissolution rates
ν'_M	Normalized instantaneous dissolution rate
ΣR	Sum Resistance
φ_{spec}	Work function
ω	Angular frequency

Acronyms

AESEC	Atomic emission spectroelectrochemistry
APF	Atomic percent factor
ASTM	American Society for Testing and Materials
at.%	Atomic percent
B.E.	Binding energy
BSE	Backscattered electrons
B-V	Butler-Volmer
CCS	Critical crevice solution
CCT	Critical crevice temperature
CE	Counter electrode
CPE	Constant phase element
CPT	Critical pitting temperature

CSL	Coincidence site lattice
DFT	Density functional theory
DI	Deionized
EBSD	Electron backscatter diffraction
EDS	Energy-dispersive X-ray spectroscopy
EIS	Electrochemical impedance spectroscopy
FCC	Face-centred cubic
GD-OES	Glow discharge optical emission spectroscopy
HER	Hydrogen evolution reaction
HFM	High-field model
ICP	Inductively coupled plasma
ICP-AES	Inductively coupled plasma atomic emission spectroscopy
ICP-MS	Inductively coupled plasma mass spectrometry
IR	Ohmic potential drop
K.E.	Kinetic energy
LPR	Linear polarization resistance
MCBM	Mass charge balance model
ORR	Oxygen reduction reaction
PD-GS-PD	Potentiodynamic-galvanostatic-potentiodynamic
PDM	Point defect model
PDP	Potentiodynamic polarization
PREN	Pitting resistance equivalent number
PSP	Potentiostatic polarization
PTFE	Polytetrafluoroethylene
RE	Reference electrode
SCE	Saturated calomel electrode
SE	Secondary electron
SEM	Scanning electron microscopy
SHE	Standard hydrogen electrode
SVIM	Solute-vacancy interaction model
TEM	Transmission electron microscopy

ToF-SIMS	Time-of-flight secondary ion mass spectrometry
WE	Working electrode
W-T	Wagner-Traud
wt.%	Weight percent
XPS	X-ray photoelectron spectroscopy

Chapter 1

1 Introduction

1.1 Project motivation

As reported by the National Association of Corrosion Engineers, the cost of corrosion accounts for approximately 3.4% of the global GDP (US$2.55 trillion) [1]. Concerns associated with corrosion processes, including the cost, but also public and environmental health, are often mitigated by employing corrosion-resistant materials in place of conventional steels when service conditions are aggressive. Nickel (Ni) alloys, containing various amounts of chromium (Cr) and molybdenum (Mo), represent a collection of materials commonly used in place of conventional steels, due to their excellent resistance to highly corrosive environments. The ability of these alloys to resist corrosion is attributed to the formation of a passive oxide layer, primarily containing Cr and Mo. Despite the layer's ability to maintain low corrosion rates, breaches may result in localized corrosion, either as pits (on the exposed surface) or crevices (within occluded regions). These processes threaten material integrity, since they can penetrate deep into the bulk alloy, are often undetected during routine inspections, and can lead to material failure. Depending on the application, failure by such processes can have health, safety, and economic implications. Despite efforts to understand the corrosion behaviour of Ni-Cr-Mo alloys, many features remain unresolved, serving as the motivation for the work presented here.

Optimizing the composition of these alloy necessitates a thorough mechanistic understanding of the individual alloying elements. While intact, the passive film enforces low uniform corrosion rates, allowing for accurate lifetime predictions. However, breakdown processes can lead to high rates of dissolution and volatile corrosion rates. The work presented herein investigates the corrosion behaviour of commercially available Ni-Cr-Mo alloys.

To elucidate the effect of composition on corrosion performance, four commercially available alloys were selected based on their varying Cr and Mo contents. The concentration of the major alloying elements, *i.e.*, Ni, Cr, Mo, W, and Fe, present in these alloys is shown in Figure 1.1. A combination of electrochemical, spectroelectrochemical, and surface measurements have been used to investigate their behaviour under active, passive, and transpassive conditions. While electrochemical methods are sensitive and provide an overall measure of the electrochemical/corrosion behaviour, spectroelectrochemical techniques provide *in situ* analytical capabilities, allowing us to determine the fate of individual alloying elements. Additional investigations explore the mechanism of localized corrosion, specifically the role of cathodic reactions during crevice corrosion. Lastly, the effect of fluoride and chloride is discussed in the context of natural and accelerated corrosion conditions.

Data presented throughout this thesis, provide insight into the behaviour of various commercial alloys, as well as information regarding the action of individual alloying elements. As a result, scientists and engineers may continue to work toward optimizing material compositions and improving material selection criteria.

1.2 Ni-Cr-Mo alloys

The use of Ni-based alloys in most applications is prohibited by their high cost. Generally, they are employed only when the corrosion resistance of conventional materials (*e.g.,* stainless steels) is unsatisfactory or when safety is of paramount importance. The nuclear, aerospace, agricultural, pulp and paper, pharmaceutical, petrochemical, and chemical processing industries represent areas where Ni-based alloys are employed. To optimize the performance of these alloys, the composition and manufacturing processes are tailored toward the intended service environment. As a result, many Ni-based alloys exist commercially, with those containing Cr and Mo common due to their excellent corrosion resistance in aggressive environments.

1.2.1 Nickel

By itself, Ni is considered corrosion-resistant in both alkaline and non-oxidizing acidic solutions [2]. The mechanical properties of Ni, *e.g.*, ductility and toughness, make fabrication by conventional methods possible [3, 4]. When used as an alloy matrix, Ni has a high solubility for alloying elements. Cr and Mo can be added up to approximately 35 and 20 wt.%, respectively, while maintaining a single-phase structure [4], and in the as-received condition, corrosion resistant Ni-based alloys consist of a face-centred cubic (FCC) structure.

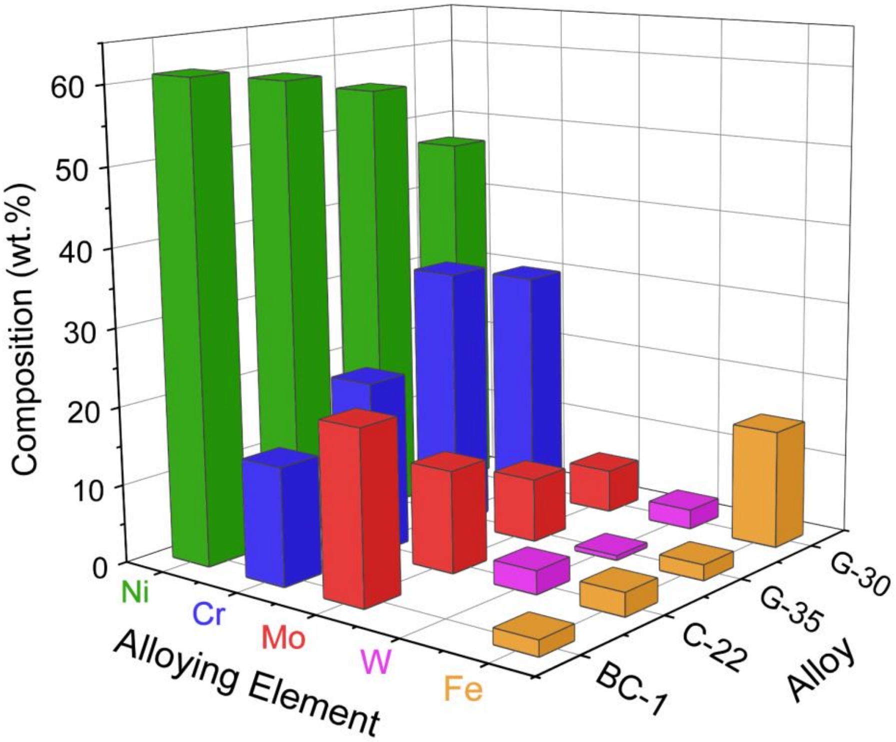

Figure 1.1 - Concentration (wt.%) of major alloying elements in Hastelloy BC-1, C-22, G-35, and G-30, according to the nominal compositions reported by Haynes International.

1.2.2 Chromium

For both Ni- and Fe-based alloys, additions of Cr are known to improve corrosion resistance in oxidizing environments [3]. This is attributed to the formation of a Cr-rich surface oxide which acts as a barrier between the metallic substrate and the oxidizing environment. As described by Marcus [5] and Taylor (*et al.*) [6], the low Cr-Cr bond strength and favourable O adsorption energy promote the formation of this protective oxide. Critical Cr contents to achieve a protective surface oxide have been reported to be in the range of 11-14 wt.% [7, 8].

1.2.3 Molybdenum

The addition of Mo is known to improve corrosion resistance in non-oxidizing and acidic environments [3, 4]. When added to Cr-containing alloys, the stability of the Cr-rich surface oxide is improved, especially in acidic chloride solutions. In particular, the ability of Mo additions to suppress metal dissolution is essential for the minimization of localized film damage.

1.2.4 Other alloying elements

While Cr and Mo are generally added in relatively large quantities, commercial Ni-Cr-Mo alloys commonly include other alloying elements in smaller quantities. A comprehensive summary of all alloying elements found in Ni-based alloys, along with their benefits to both corrosion and mechanical properties can be found elsewhere [3, 4]. As indicated in Figure 1.1, both W and Fe are found in the examined alloys and are discussed throughout this thesis. Additions of W benefit corrosion performance similar to additions of Mo. However, the large atomic mass of W necessitates twice as much, by weight, to achieve the same benefit as alloyed Mo. In addition to increases in weight, the high cost of W compared to Mo makes Mo additions the preferred option. On the other hand, the addition of Fe to Ni-based alloys is not to improve corrosion performance, but to reduce the costs of production.

1.3 Introduction to aqueous corrosion

Thermodynamic calculations predict the spontaneity of a given reaction based on the relative energies of the products and reactants. The pathway along which a spontaneous reaction proceeds, however, is not determined by thermodynamics but is governed by kinetics.

1.3.1 Thermodynamics of aqueous corrosion

In general, a redox process involves the coupling of two half-reactions, one an oxidation and the other a reduction reaction. In an aqueous corrosion system, the oxidation reaction, Reaction 1.1, representing a material degradation process, is coupled to a reduction reaction, Reaction 1.2. The two reactions must couple together to maintain charge balance.

Assuming the number of electrons transferred is equal for Reactions 1.1 and 1.2, the combined corrosion reaction can be expressed as shown in Reaction 1.3.

$$\mathrm{M} \rightarrow \mathrm{M}^{\mathrm{n}+} + \mathrm{n}\ \mathrm{e}^{-} \tag{1.1}$$

$$\mathrm{Ox} + \mathrm{n}\ \mathrm{e}^{-} \rightarrow \mathrm{Red} \tag{1.2}$$

$$\mathrm{M} + \mathrm{Ox} \rightarrow \mathrm{M}^{\mathrm{n}+} + \mathrm{Red} \tag{1.3}$$

For the combined reaction to proceed spontaneously, the potential difference (ΔE) between the reduction half-reaction and the oxidation half-reaction must be positive. As stated in Equation 1.4, where both $(\mathrm{E_e}°)_{\mathrm{Ox/Red}}$ and $(\mathrm{E_e}°)_{\mathrm{M/M^{n+}}}$ are expressed as standard reduction potentials, if ΔE is positive (*i.e.*, $(\mathrm{E_e}°)_{\mathrm{Ox/Red}} > (\mathrm{E_e}°)_{\mathrm{M/M^{n+}}}$) then the reaction will proceed spontaneously as written in Reaction 1.3. Standard values (°) are those measured under standard conditions, *i.e.*, standard temperature (298 K) and concentrations for all participating ions (1 M) and gases (1 atm). The potential of a reaction can be related to the change in Gibbs' Free Energy, Equation 1.5, where F is the Faraday constant (96,485 C $\mathrm{mol^{-1}}$), and n is the number of electrons transferred. Thermodynamics states that a given reaction will proceed only if the change in Gibbs free energy (ΔG) is less than zero. Therefore, the Gibbs free energy difference is negative only when ΔE is positive.

$$\Delta \mathrm{E}° = (\mathrm{E_e}°)_{\mathrm{Ox/Red}} - (\mathrm{E_e}°)_{\mathrm{M/M^{n+}}} \tag{1.4}$$

$$\Delta \mathrm{G}° = -\mathrm{nF}\Delta \mathrm{E}° \tag{1.5}$$

Under non-standard conditions, the change in Gibbs free energy can be obtained using Equation 1.6, where R is the universal gas constant (8.314 J $\mathrm{mol^{-1}\ K^{-1}}$), T is the absolute temperature (K), and $\mathrm{K_{eq}}$ is the equilibrium constant for the reaction.

$$\Delta \mathrm{G} = \Delta \mathrm{G}° + \mathrm{RT}\ln\left(\mathrm{K_{eq}}\right) \tag{1.6}$$

Substituting Equation 1.5 into Equation 1.6 yields a means of determining non-standard equilibrium potentials (E_e). The resulting expression, known as the Nernst equation, is given in Equation 1.7.

$$\Delta E_e = \Delta E_e{}^\circ - \frac{RT}{nF}\ln\left(K_{eq}\right) \tag{1.7}$$

For a given system, by calculating Nernst equations for all possible half-reactions, in addition to considering solubility equilibria, an E-pH (Pourbaix) diagram can be constructed [2, 9]. These diagrams identify the most stable state under a given condition, which is then used to say whether a material will be immune (*i.e.*, stable in a metallic state), passive (*i.e.*, forms a solid corrosion product), or active (*i.e.*, forms a soluble corrosion

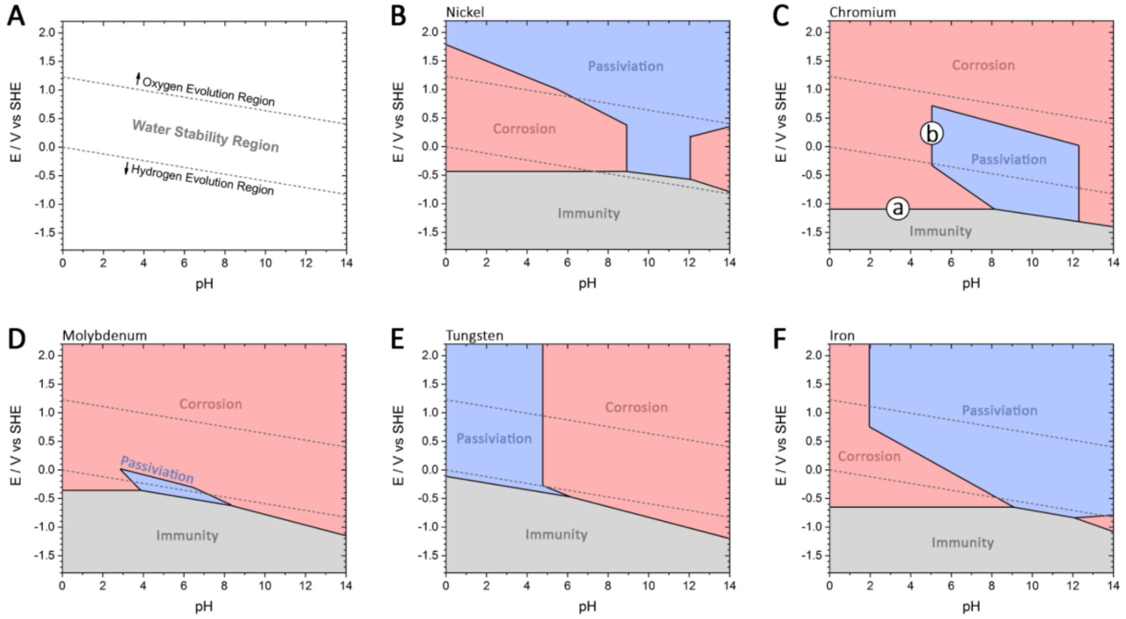

Figure 1.2 - Simplified Pourbaix (or E-pH) diagrams for the (A) H_2O, (B) Ni, (C) Cr, (D) Mo, (E) W, and (F) Fe, at 25°C. The concentration of dissolved metal cations used for calculations was 1 x 10^{-6} M. Regions of immunity, corrosion, and passivation are indicated based on the stability of metallic, soluble, and insoluble species, respectively. The original equilibrium data may be found in the '*Atlas of electrochemical equilibria in aqueous solution*' [2].

product). Simplified E-pH diagrams for H_2O and Ni, Cr, Mo, W, and Fe in H_2O are shown in Figure 1.2 (adapted from the '*Atlas of Electrochemical Equilibria in Aqueous Solution*' [2]).

The simplest E-pH diagram is that for H_2O. Shown in Figure 1.2(A), the diagram consists of two boundaries that are dependent on both E and pH. The lower and upper lines represent the $\mathrm{E_e}$ for the hydrogen evolution (HER) and oxygen reduction (ORR) reactions, respectively.

$$2\ \mathrm{H_2O} + 2\ \mathrm{e^-} \rightleftharpoons \mathrm{H_2} + 2\ \mathrm{OH^-} \tag{1.8}$$

For the HER, Reaction 1.8, assuming a partial pressure of H_2 of unity and a temperature of 298 K, the Nernst equation can be written according to Equation 1.9 and simplified to Equation 1.10.

$$(\mathrm{E_e})_{\mathrm{H^+/H_2}} = 0 - \frac{0.059}{2}\log\left(\frac{1}{(a_{\mathrm{H^+}})^2}\right) \tag{1.9}$$

$$(\mathrm{E_e})_{\mathrm{H^+/H_2}} = -0.059(\mathrm{pH}) \tag{1.10}$$

A similar procedure yields the Nernst equation for the ORR. The region between the two lines, Figure 1.2(A), indicates the water stability region which is particularly important in corrosion science due to the importance of the ORR and the HER as cathodic reactions. For this reason, the water stability region is overlaid on all E-pH diagrams, Figure 1.2(B-F).

Simplified E-pH diagrams defining regions of corrosion, immunity, and passivation for Ni, Cr, Mo, W, and Fe are shown in Figure 1.2(B-F). While boundaries for electrochemical reactions involving both E and pH are diagonal, some boundaries are either vertical (potential-independent acid-base reactions) or horizontal (pH-independent redox reactions). For example, the horizontal boundary indicated as (a) in Figure 1.2(C) corresponds to the $\mathrm{E_e}$ of Reaction 1.11. As described by the corresponding Nernst equation,

Equation 1.12, $(\mathrm{E_e})_{\mathrm{Cr^{2+}/Cr}}$ depends only on the concentration of $\mathrm{Cr^{2+}}$ in solution and for a fixed concentration of $\mathrm{Cr^{2+}}$ yields a horizontal boundary.

$$\mathrm{Cr^{2+}} + 2\ \mathrm{e^-} \rightleftharpoons \mathrm{Cr} \tag{1.11}$$

$$(\mathrm{E_e})_{\mathrm{Cr^{2+}/Cr}} = -0.913 - \frac{0.059}{2}\log\left(\frac{1}{a_{\mathrm{Cr^{2+}}}}\right) \tag{1.12}$$

A vertical boundary, (b) in Figure 1.2(C), corresponds to the acid-base solubility equilibrium for Reaction 1.13, which does not involve electron transfer and, as a result, is independent of potential. The reaction is described by the solubility product ($\mathrm{K_{sp}}$), Equation 1.14.

$$2\ \mathrm{Cr^{3+}} + 3\ \mathrm{H_2O} \rightleftharpoons \mathrm{Cr_2O_3} + 6\ \mathrm{H^+} \tag{1.13}$$

$$\mathrm{K_{sp}} = \frac{(a_{\mathrm{H^+}})^6}{(a_{\mathrm{Cr^{3+}}})^2} \tag{1.14}$$

While E-pH diagrams summarize the thermodynamically stable species at equilibrium, they yield no kinetic information, leading to several limitations. Firstly, the thermodynamically stable species predicted by E-pH diagrams may not be observed experimentally, due to kinetic considerations. Moreover, regions of passivation are generally assumed for conditions where solid corrosion products are predicted. However, whether these solids cause passivation will be governed by the physical properties of the solid on the surface (*e.g.*, porosity, adhesion, etc.). To fully understand the corrosion process, thermodynamic information must be coupled with kinetic information. Secondly, the validity of E-pH diagrams is limited to the equilibrium reactions considered in their construction. In the case where solution chemistry is complex and not completely understood, the omission of important reactions will result in an inaccurate diagram. This is a particularly important limitation for the discussion of alloys, since E-pH diagrams typically consider only one metallic system. As a result, the complex chemistry of mixed oxides is not captured by traditional E-pH diagrams. However, it is worth mentioning that some researchers have successfully considered mixed metal oxides for compositionally complex alloys [6, 10].

1.3.2 Kinetics of aqueous corrosion

While thermodynamic calculations help predict which reactions may occur, the extent and rate of corrosion is determined by the reaction kinetics. For corrosion processes, the rate can be obtained from mass loss measurements, analyzing solution composition, monitoring the production of gases, or by electrochemical measurements. While all these methods provide kinetic information, electrochemical measurements benefit from high sensitivity and generate mechanistic information. Here, a brief discussion of electrochemical kinetics is given in the context of corrosion [9, 11, 12].

Kinetic information is obtained electrochemically by measuring the flow of electrons, *i.e.*, the current (I). Since measured current increases with surface area, values are typically surface area normalized, *i.e.*, current densities (i). Consider the non-specific reversible redox reaction given in Reaction 1.15. At $\mathrm{E_e}$, no net reaction occurs, however, the forward (anodic, $\mathrm{i_A}$) and reverse (cathodic, $\mathrm{i_C}$) reactions occur at equal rates, resulting in a net current of zero. The magnitude of this reversible process is known as the exchange current density ($\mathrm{i_o}$) and is effectively an electrochemical rate constant for the dynamic equilibrium, Equation 1.16.

$$\mathrm{Red} \rightleftharpoons \mathrm{Ox} + \mathrm{n\,e^-} \tag{1.15}$$

$$\mathrm{i_o = i_A = |i_C|} \tag{1.16}$$

When the reaction is polarized away from $\mathrm{E_e}$ by an applied potential ($\mathrm{E_{APP}}$), *i.e.*, an overpotential ($\eta = \mathrm{E_{APP} - E_e}$) is applied, the relationship between i and η is exponential and described by the Butler-Volmer (B-V) equation, Equation 1.17,

$$\mathrm{i_{net} = i_A + i_C = i_o}\left[\exp\left[\frac{\alpha_\mathrm{A}\,\mathrm{n\,F}}{\mathrm{R\,T}}\eta\right] - \exp\left[-\frac{\alpha_\mathrm{C}\,\mathrm{n\,F}}{\mathrm{R\,T}}\eta\right]\right] \tag{1.17}$$

where α is a transfer coefficient ($\alpha_A + \alpha_C = 1$) [11, 13]. For Reaction 1.15, a graphical representation of Equation 1.17 is shown in Figure 1.3. The partial current contributions of the anodic and cathodic reactions are indicated as dashed lines, while the sum current (or net current) is indicated as a solid line. If a positive η is applied, the anodic and cathodic reactions are accelerated and decelerated, respectively. When the η is sufficiently high, as is the case for η_A in Figure 1.3, the cathodic reaction current will approach zero, with the net current becoming equal to that for the anodic reaction. In this case, Equation 1.17 can be simplified to Equation 1.18. A similar simplification can be adopted for a sufficiently negative η_C.

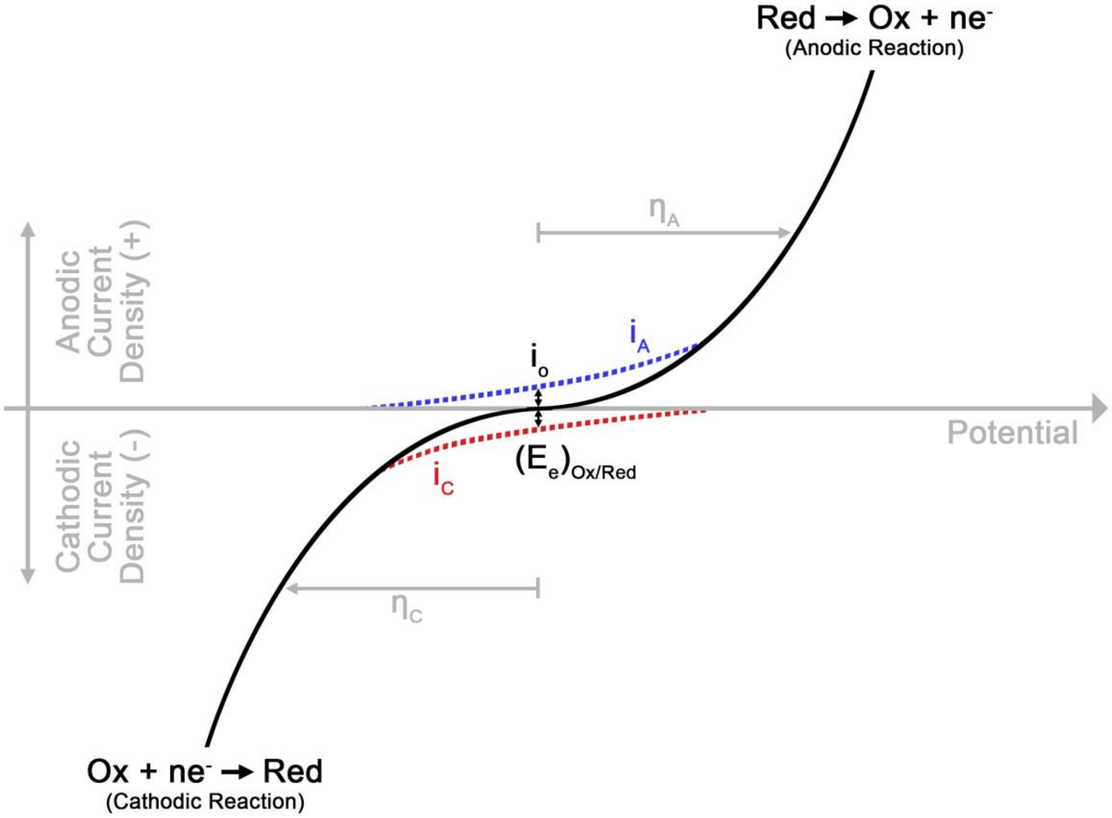

Figure 1.3 - Current-Potential (or Butler-Volmer) relationship for the non-specific reaction given in Equation 1.15. The contributions of the anodic and cathodic reactions are shown as blue and red dotted lines, respectively. The sum, or measured current, is represented as a solid black line.

$$i_{net} = i_A = i_o \left[\exp \left[\frac{\alpha\, n\, F}{R\, T} \eta \right] \right] \tag{1.18}$$

In a corrosion system, the anodic and cathodic reactions of at least two half-reactions must be coupled. For Reactions 1.19 and 1.20, the B-V relationships are represented by the blue and red lines in Figure 1.4. When coupled, the two half-reactions are polarized away from their equilibrium potentials, resulting in an irreversible system. In the absence of an applied potential, the potential will sit at a unique value at which the anodic and cathodic currents densities are equal, *i.e.*, $i_A = |i_C|$, referred to as the corrosion potential (E_{CORR}). The rate of the corrosion reaction at E_{CORR} is described by the corrosion current density (i_{CORR}), Equation 1.21. E_{CORR} has no thermodynamic significance, its value is determined by the intersection of the anodic and cathodic half-reaction currents; *i.e.*, it is determined by the kinetics of the two half-reactions.

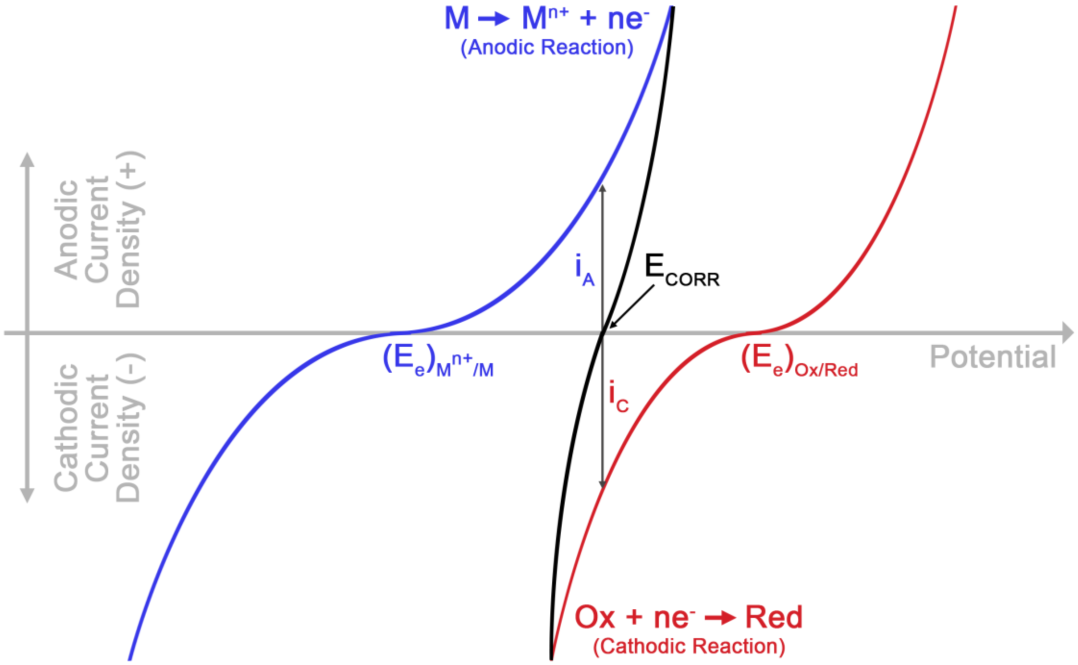

Figure 1.4 - Current-Potential relationship of two half reactions coupled in a corrosion process. The resulting relationship, shown in black, describes the corrosion process.

$$\mathrm{M} \rightleftharpoons \mathrm{M}^{n+} + n\,e^- \tag{1.19}$$

$$\mathrm{Ox} + n\,e^- \rightleftharpoons \mathrm{Red} \tag{1.20}$$

$$i_{\mathrm{CORR}} = i_A = |i_C| \tag{1.21}$$

The i-E relationship of the coupled half-reactions shares similarities with the B-V equation and is described by the Wagner-Traud (W-T) equation, Equation 1.22,

$$i_{\mathrm{net}} = i_{\mathrm{CORR}}\left[\exp\left[\frac{\alpha_A\, n\, F}{R\,T}\eta\right] - \exp\left[-\frac{\alpha_C\, n\, F}{R\,T}\eta\right]\right] \tag{1.22}$$

where α are the transfer coefficients of the anodic and cathodic half-reactions, n is the number of electrons involved in the balanced corrosion reaction, and η is the overpotential relative to E_{CORR} (*i.e.*, $\eta = E_{\mathrm{APP}} - E_{\mathrm{CORR}}$) [11, 13]. The i-E relationship given by the W-T equation is shown by the black curve in Figure 1.4.

Providing the E_{CORR} is sufficiently distance from both E_e, both reactions can be considered to be in their Tafel regions and the i-E relationship can be described by a semi-log plot, *i.e.*, log(i)-E, referred to as an Evans diagram, Figure 1.5. Here, the sign of the cathodic reaction is neglected, allowing the two half-reactions to be plotted in the same quadrant. However, the measured current is still the sum of the cathodic (–) and anodic (+) reactions, and the value of E_{CORR} depends on the intersection of the two reactions. While i_{CORR} cannot be experimentally measured using an ammeter, measurements of E_{CORR} are easily made against a known reference electrode. Using the Evans diagram, changes in E_{CORR} are rationalized according to changes in the kinetics of either half-reaction. For instance, a decrease in E_{CORR} may be explained by either the acceleration of the anodic reaction (*i.e.*, an increase in the slope) or a deceleration of the cathodic reaction.

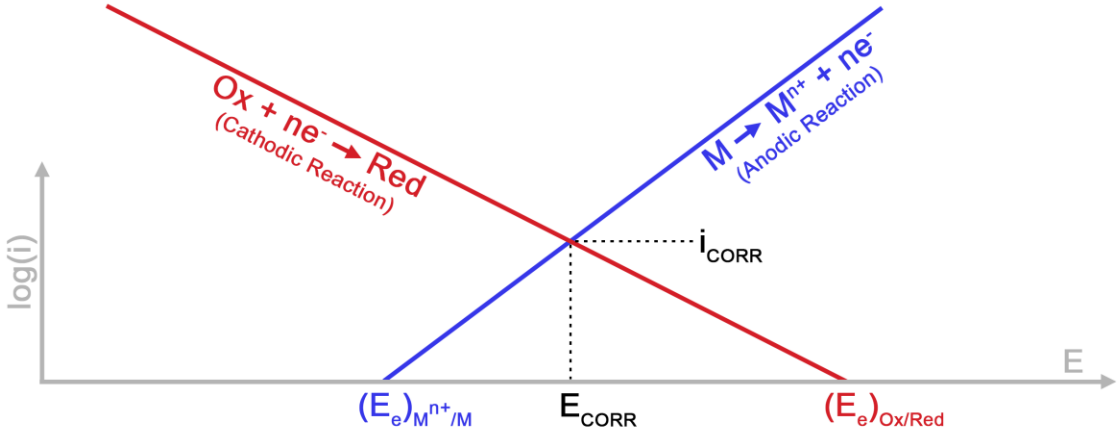

Figure 1.5 - Evans diagram (log(i)-E) for two half reactions coupled in a corrosion process. For simplicity, the nonlinear portion of each half reaction, *i.e.*, near the respective equilibrium potentials, is omitted.

In practice, deviations from the i-E relationship described by the B-V (and W-T) equation are commonly observed. The B-V relationship is only valid when the rate of the electrochemical reaction is controlled by the charge transfer process. If the reaction becomes controlled by the transport of species to, or from the surface, the reaction becomes transport limited. This results in the establishment of a limiting current related to the rate of mass transport [12]. Similarly, reaction kinetics will be influenced by the formation of corrosion products or oxide films formed on the electrode surface. For example, a passive film, *i.e.*, an oxide film formed on the electrode surface, can act as a barrier for the interaction of the underlying metal with solution. When present, a passive film results in a deviation from B-V type kinetics, with the current becoming independent of the E_{APP}.

1.4 Passivity

Formation of a thin surface oxide, commonly referred to as a passive film, is critical in maintaining low corrosion rates for many metals and alloys. The passive film forms due to the interaction of the bare metallic substrate with an oxidizing environment and is characterized by a compact, and chemically inert oxide. Once formed, the film acts as a barrier between the reactive metal and the oxidizing environment, therefore limiting the continued oxidation process [14, 15]. The electrochemical behaviour of a passive system is commonly studied using polarization techniques. As described by Wagner [16], “a metal may be called passive when the amount of metal consumed […] is significantly less under conditions corresponding to a higher affinity of the reaction”. In other words, increases in over-potential, *i.e.*, an increased affinity for oxidation, are expected to increase the anodic current (*i.e.*, reaction rate) based on the W-T equation, Equation 1.22, but for a passive system, the i-E relationship deviates from that described the W-T equation, with the current becoming independent of the applied potential.

Consider the generalized polarization curve presented in Figure 1.6. As the applied potential is increased above the E_{CORR}, the value of log(i) increases almost linearly, as described by the W-T equation. For a system capable of passivation, this region is referred to as the ‘active’ region. At some critical current density, i_{CRIT}, the reaction rate becomes independent of the applied potential and can no longer be described by the W-T equation. The potential at which this transition occurs is referred to as the passivation potential

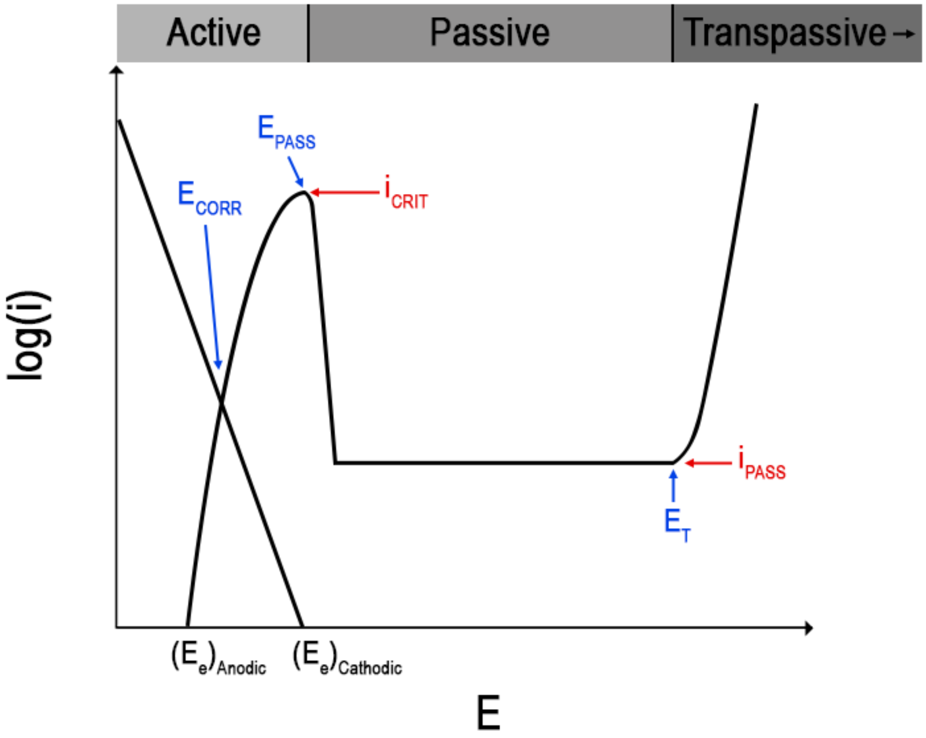

Figure 1.6 - Graphical representation of the polarization behaviour of an alloy exhibiting active-passive behaviour.

(E_{PASS}). Once formed, the passive film provides protection, limiting the rate of reaction (i_{PASS}) despite continued increases in applied potential. The range of potential in which the passive film is stable is referred to as the 'passive region'. When the applied potential exceeds a potential E_T, the reaction rate begins to increase in the transpassive region. This increase in current is commonly attributed to one, or both, of two processes: transpassive dissolution and O_2 evolution [13, 14, 17]**.** For Cr-containing alloys, the transpassive dissolution reaction involves the electrochemical conversion of the protective Cr(III) oxide into soluble Cr(VI) species [14]. This process is discussed in more detail in the section on passive film breakdown.

In the generalized polarization behaviour described above, three distinct regions are identified: the active, passive, and transpassive regions. In some cases, for example during the polarization of corrosion-resistant alloys exposed to non-aggressive environments, the active region may not be observed. Instead, as the applied potential is increased, values of log(i) approach the plateau, described by i_{PASS}. On a thermodynamic basis, this behaviour can be explained when the system transitions from a region of immunity directly into a region of passivity, however, this may also occur due to the presence of an oxide film formed before the polarization measurement.

1.4.1 Models and theories for passive film growth

Passive film formation occurs as a result of the potential difference between the metal and the oxidizing electrolyte (or atmosphere). For a bare metal, the potential drop occurs at the metal/electrolyte interface as shown in Figure 1.7(A). When a passive film is formed, a portion of the potential drop becomes distributed across the growing film, as shown in Figure 1.7(B). This results in the establishment of an electric field (*i.e.*, charge separation) which promotes the migration of charged species across the oxide. As a result of an interfacial potential drop and the development of an electric field, passive film growth occurs via complex processes involving both interfacial reactions and transport processes within the growing oxide. Several models have been proposed to explain the mechanism of oxide growth. While a summary of key models is provided here, a critical review of the different models can be found in the work of Seyeux *et al.* [18]].

Introduced by Cabrera and Mott [19], the High-Field Model (HFM) proposes that film growth is related to an electric field established across the thin oxide film. The electric field serves as a driving force for ionic migration of cations through the film where they can react with adsorbed oxygen atoms at the oxide/electrolyte interface. The thickening of the oxide causes a decrease in the electric field and eventually, steady-state thickness is obtained due to the inability of metal cations to move through the film. In its original form, the HFM considered metal cations as the only mobile ions in the film leading to a reaction at the oxide/air interface. Several years later, the HFM was expanded to consider the movement of anions across the film [20]. However, the HFM neglects any interfacial potential drop.

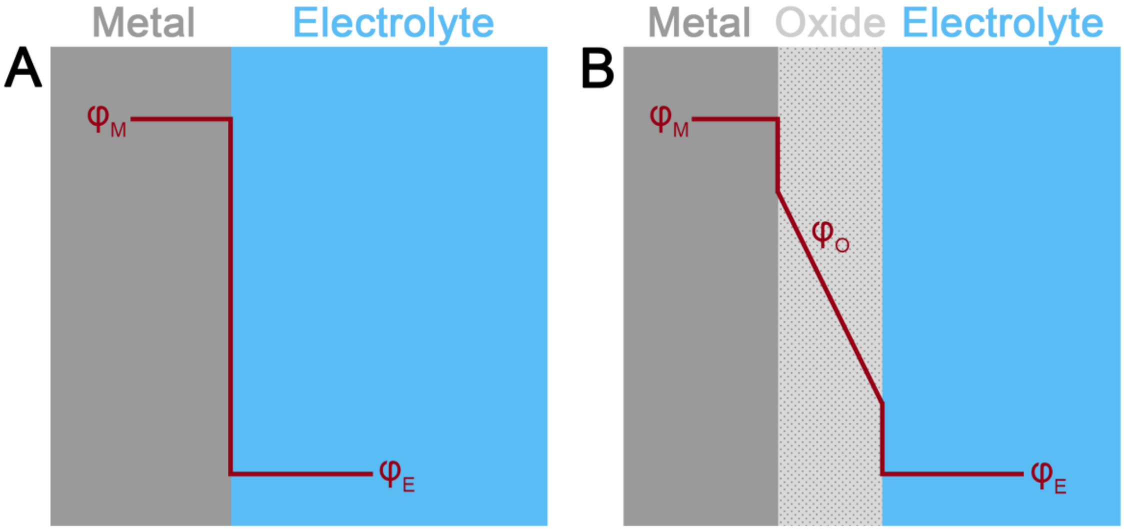

Figure 1.7 - Relative potential for (A) a bare metal and (B) a passive metal exposed in an electrolyte. The relative potential drop at the metal/electrolyte, metal/film, and film/electrolyte are shown in red.

Introduced by MacDonald *et al.* [21, 22], the Point Defect Model (PDM) extends the HFM by including processes of oxide film dissolution reactions and the mobility of both cations and anions through the oxide. A simplified schematic of the reactions considered in the PDM is shown in Figure 1.8. At the metal/oxide interface, metal cations are injected into the oxide either by the annihilation of an existing cation vacancy (V_M^{x-}), Reaction 1 in Figure 1.8, or by the formation of an anion vacancy (V_O^{2+}), Reaction 2 in Figure 1.8. At the oxide/electrolyte interface, metal cations are ejected from the oxide either by the creation of a cation vacancy, Reaction 3 in Figure 1.8, or by the chemical or electrochemical dissolution of the film, Reaction 4 in Figure 1.8. Lastly, oxygen atoms can be incorporated into the film by the reaction of adsorbed H_2O or O_2 with anion vacancies (V_O^{2+}), Reaction 5 in Figure 1.8. A key feature of the PDM is that the barrier layer oxide behaves like a defective semiconductor, containing both cation and anion vacancies which act as electronic dopants. These vacancies are mobile through the oxide allowing for their creation and annihilation at opposite interfaces. For example, cation vacancies are formed at the oxide/electrolyte and migrate to the metal/oxide interface where they can be annihilated. The same is true for anion vacancies which are formed at the metal/oxide interface and annihilated at the oxide/electrolyte interface. Reactions 1, 3, and 5, are considered conservative as they do not result in a change in film thickness, while reactions

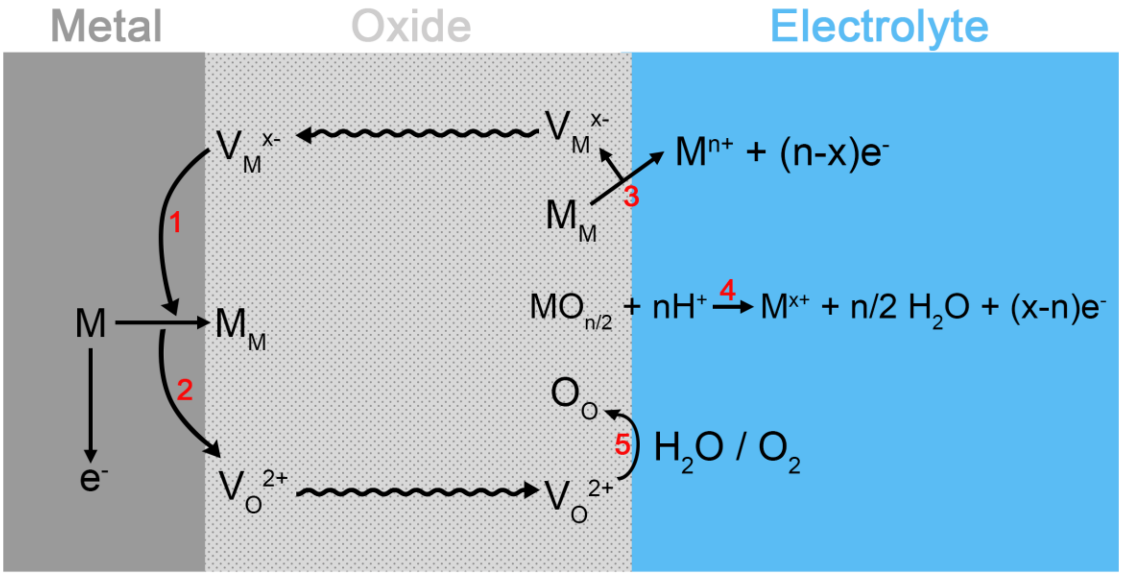

Figure 1.8 - Simplified schematic of the processes considered by the Point Defect Model. The injection of M into the oxide occurs by either (1) the annihilation of a cation vacancy (V_M^{x-}) or (2) the creation of anion vacancy (V_O^{2+}). At the oxide/electrolyte interface, M is released into solution by either (3) the creation of V_M^{x-} or by the (4) chemical/electrochemical dissolution of the oxide. Incorporation of O into the lattice occurs due to (5) the reaction of adsorbed H_2O/O_2 with V_O^{2+}.

2 and 4 are considered nonconservative since they cause changes in film thickness. As the film growth occurs, the electric field of the oxide is assumed to remain constant, maintained by a decreased potential drop at the metal/oxide interface. The system achieves a steady-state film thickness when $\varphi_{M/O} = \varphi_{O/F}$, *i.e.*, the rate of film growth equals the rate of destruction, Figure 1.7(B).

Recently, Momeni and Wren [23] proposed a Mass-Charge Balance Model (MCBM) which considers the mass and charge balance of three reactions: metal oxidation, oxide growth, and oxide dissolution. At all times, the rate of metal oxidation must be equal to the sum of the oxide growth and dissolution processes. Using classical rate equations, the MCBM predicts oxide growth and dissolution rates as a function of important parameters such as temperature, pH, and applied potential. While the MCBM does not discuss the mechanism of oxide growth, it has been successfully used to predict the time-dependent potentiostatic oxide growth and dissolution of pure Fe, Co-Cr, and Fe-Ni-Cr alloys.

While these models are used to predict the kinetics of oxide growth, they cannot explain many of the complex structural features observed in passive oxide films. For example, how dopants arrive in the oxide and how they affect behaviour. Recent observations suggest non-equilibrium solute capture occurs during early-stage oxidation of Ni-Cr-Mo alloys [24, 25], implying that approximations made for ideal, thermodynamically stable oxides (*e.g.,* Cr_2O_3, NiO, etc.), may not be valid. Here, when oxide formation occurs faster than the thermodynamic phases can reach equilibrium, solute atoms become trapped in the oxide above solubility limits. In the context of solute capture, the PDM was extended to a solute-vacancy interaction model (SVIM) which explained how minor alloying elements impact film breakdown [26].

1.4.2 Passive films formed on Ni-Cr-Mo alloys

1.4.2.1 Effect of alloying elements

Passive films formed on Ni-based alloys are known to offer excellent corrosion resistance under conditions involving high temperature, acidity, and oxidizing species. The properties of the passive film are largely influenced by the alloy composition. As a result, extensive efforts have been and continue to be invested in understanding the relationship between alloy composition, passive film properties, and corrosion performance.

Early work by Bouyssoux *et al.* examined the structure of the oxide film present on electrochemically passivated Cr electrodes using X-ray photoelectron spectroscopy (XPS) and Auger electron spectroscopy [27]. Their findings showed that the oxide was comprised of an inner Cr_2O_3 layer and an outer $Cr(OH)_3$ layer. While this study focused on pure Cr, their findings have translated directly to observations made on many Cr-containing alloys, where the inner and outer portions of the passive film are enriched in Cr oxide and hydroxide, respectively [28, 29]. The crystallographic structure of passive films formed on Cr and Cr-containing alloys has been described as disordered [30, 31], however, crystallization has been shown to occur with increasing time, temperature, and applied potential [17, 30, 32-34].

Based on polarization experiments, additions of Cr to Ni have been shown to suppress active dissolution and to decrease passive current densities [35, 36]. Lloyd *et al.* highlighted several benefits of increased Cr-content in commercial alloys, including open-circuit ennoblement, increased oxide thickness, and the suppression of defects in the oxide [37]. To achieve the maximum benefit cost-effectively, attempts have been made to identify the critical concentration of alloyed Cr required to establish passivity [7, 8, 15, 38]. Whitman and Chappell studied a series of Fe-Cr alloys exposed in a humidity chamber and found that a drastic decrease in corrosion rate occurred when the Cr content was equal to (or exceeded) 13 wt.% [39]. For Ni-Cr alloys, Hodge and Wilde found that more than 10 wt.% Cr was required to develop passivity in acidic solution [40]. Hayes *et al.* observed that increases beyond 11 wt.% Cr resulted in only minor improvements to the corrosion behaviour of Ni-Cr-Mo alloys in NaCl solutions in a range of pH between 3 and 11 [7]**.** Generally, critical Cr concentrations have been reported to be greater than 10-13 wt.%, with the differences accredited to the various experimental conditions employed. The basis for a critical concentration was suggested by Sieradzki and Newman, who claimed the formation of a three-dimensional Cr_2O_3 lattice across an alloy surface becomes possible only at a critical concentration [41]. This concept was revisited by McCafferty, who proposed that the formation of a continuous $–O^{II}–Cr^{III}–O^{II}–$ network required a Cr cation fraction of approximately 0.34 or greater in the oxide film [42-44]. Achieving this oxide composition has been shown to require ~12-14 and ~8-10 wt.% Cr in the Fe-Cr and Ni-Cr systems, respectively [42, 45, 46].

For Cr-containing alloys, the addition of Mo promotes the accumulation of oxidized Mo species in the outer portion of the Cr-rich passive film. For Fe-based alloys containing both Cr and Mo, Clayton and Lu [47] observed the enrichment of high valence Mo species at the film/electrolyte interface and proposed a bilayer model to describe the passive film with the inner and outer portions Cr- and Mo-rich, respectively. Using time-of-flight secondary ion mass spectrometry (ToF-SIMS) and XPS, Lloyd *et al.* found similar enrichment behaviour for a series of Ni-based alloys containing Cr and Mo [48]. In general, Mo-oxides enriched in the passive film have been described as a complex mixture of Mo(IV), Mo(V), and Mo(VI) species [48, 49]. Concerning corrosion, Mo-enrichment has been shown to result in the suppression of active dissolution [50-53], a reduction in passive current density [50, 54], and an increase in the resistance to localized corrosion [7, 47, 55]. While the benefits of Mo are known empirically, research continues to investigate the mechanism(s) by which corrosion resistance is improved. In general, observations can be separated into two categories: those that improve passive film stability, and those that benefit the repair of film damage.

Observations related to film stability often use the bilayer description proposed by Clayton and Lu, which suggests that the enrichment of high valence Mo species, *e.g.*, MoO_4^{2-}, provides cation-selective properties in the outer portion of the passive film [47]. This offers an explanation for why Mo additions cause increased passive film stability in Cl^- containing solutions. Additionally, Mo oxides are more stable than their related chloride complexes, making them an effective barrier in Cl^--containing solutions [6]. This bilayer model has been used to explain empirical observations under a range of experimental conditions [56, 57]. However, recent research has offered more detail on how Mo-enrichment increases film stability. Using *in situ* transmission electron microscopy (TEM), Yu *et al.* showed that the addition of Mo to Ni-Cr alloys decreased the probability of Kirkendall void formation at the oxide/metal interface [24], which is related to the process of film breakdown. Using density functional theory (DFT) calculations, the authors reasoned that high valence Mo species stabilized cation vacancies and decreased their mobility and, hence, ability to form voids [24, 58]. It has also been suggested that Mo additions stabilize the adsorption of oxygen on the alloy surface. In first principles model calculations by Samin and Taylor, small amounts of alloyed Mo were found to help stabilize the adsorption of oxygen, an important precursor to oxide formation [59].

The second category of observations is related to an improved ability to repair film damage, *i.e.,* stimulate repassivation. Since this is directly related to film breakdown processes, only a brief discussion is given here, with more mechanistic information provided with the discussion of passive film breakdown, Section 1.5. Researchers have attributed an improved repassivation behaviour to the deposition of Mo-rich corrosion products on damaged surface sites. In a study by Hashimoto *et al.,* hexavalent Mo species were found to enrich at the surface of Fe-Cr-Mo alloys following conditions of active dissolution. This deposition caused a decrease in current density relative to samples without Mo additions, suggesting the formation of a partially protective surface film [50]. In studies by Newman *et al.*, scratch and artificial pit methodologies were used to promote active dissolution. Their results demonstrated an improved repassivation behaviour for alloys containing Mo; however, they did not analyze the composition of the resulting films [60-62]. In addition to the suppression of active dissolution, the ability of Mo to control damage to the passive film has also been demonstrated for transpassive conditions. Using XPS and ToF-SIMS, Lloyd *et al.* studied the composition of the passive film on a number of Ni-based alloys following growth at constant applied potentials in 1 M NaCl + 0.1 M H_2SO_4 (85°C) [48]. When applied potentials were $\geq$ 500 mV (vs Ag/AgCl), where the Cr_2O_3 barrier layer is compromised by oxidative dissolution, Mo-enrichment was observed. Overall, observations have found that, when the Cr-rich barrier layer is compromised, either during active or transpassive dissolution, Mo-rich corrosion products become enriched on the surface to provide partial protection.

Additions of W exert an influence on passive film properties similar to that observed for Mo additions [48, 63]. In acidic chloride solutions, the addition of W was found to improve the stability of the film on alloy C-22 (13 wt.% Mo + 3 wt.% W) compared to the film on alloy C-2000 (16 wt.% Mo) [48]. In a separate study on alloy C-22, high valence W (and

Mo) species were found to concentrate in the outer regions of the passive film following transpassive dissolution [49].

Passive films formed on Ni-based alloys have also been shown to contain oxidized Ni species [37, 64, 65], with the relative amount depending on exposure conditions. The amount of oxidized Ni in the passive film increases as the solution pH is increased, as expected due to the increased stability of NiO and $Ni(OH)_2$ in alkaline solutions [2]. Ni oxides are generally found within the inner Cr-rich region [48, 66]**,** leading some researchers to suggest the existence of a mixed oxide (*e.g.*, $NiCr_2O_4$, etc.) [24, 67-69]. Recently, Yu *et al.* have demonstrated the presence of metastable non-stoichiometric oxides (*i.e.*, $Ni_{1-x}Cr_xO$ and $Ni_{2-x}Cr_xO$) during the early-stage of gas-phase oxidation of Ni-22Cr and Ni-22Cr-6Mo alloys [24].

1.4.2.2 Effect of solution pH

Solution pH is an important environmental factor influencing the behaviour of passive oxides, since solubilities are a function of pH [2, 70]. In acidic solution, the solubilities of Ni, Cr, and Fe, are generally enhanced. Gray and Orme reported that in hydrochloric acid, passive film breakdown can occur at a critical solution pH of ~0.5 (90°C) for alloy C-22 [71]. Using a combination of electrochemical impedance spectroscopy (EIS) and ellipsometry, the passive film was found to thin as the pH decreased [71-73] and was completely removed in a solution of 3 M HCl [72]. In the work of Zhang *et al.*, increasing the solution acidity, from pH 7 to 1, resulted in a similar thinning of the passive oxide formed on alloy C-2000 [74]. Considering the ratio of $Cr_2O_3^-/MoO_3^-$ in ToF-SIMS depth profiles, the authors proposed a decrease in Cr oxide and enrichment of Mo oxide contents as solution acidity increased.

Mishra *et al.* studied the passive film properties of several commercial Ni-based alloys in chloride-containing solutions buffered by bicarbonate (pH 8.3) [65, 75]. Using a combination of XPS and Auger electron spectroscopy, they found that the thickness of passive films formed during polarization in the transpassive domain doubled when compared to films formed in the passive domain. This was attributed to the enrichment of

$Ni(OH)_2$ in the film, which is insoluble at pH 8.3. In polarization studies, this enrichment resulted in a partially protective secondary passive region.

1.4.2.3 Effect of temperature

Temperature is another important environmental factor influencing the passive oxide. For a series of commercial Ni-based alloys exposed to acidic (pH 1) chloride solution, Lloyd *et al.* showed that increases in temperature caused increases in current density, and in some cases film breakdown, during potentiostatic polarization experiments [48, 76]. Gray *et al.* found that, with increasing temperature, the critical solution pH required for film breakdown increased, *e.g.*, pH 0.5 (60°C) and pH 0.75 (90°C) [73]. Using a combination of angle-resolved XPS and ToF-SIMS, Zhang *et al.* showed the enhancement of film-growth at elevated temperatures (90°C) [77]. Increases in temperature, from 25 to 90°C, resulted in an increased passive film thickness. As the temperature was increased to 90°C, the concentration of oxidized Ni species in the passive film increased at the expense of Cr and Mo oxides.

1.5 Passive film breakdown

In the passive state, Ni-based alloys exhibit low corrosion rates, typically ≤ 1 μm per year [78]. Any damage incurred by the passive film can cause corrosion rates to intensify. If the passive film is completely removed, while corrosion rates will be high, they will be approximately uniform across the surface. If passive film breakdown occurs locally, either as a pit (on the exposed surface) or a crevice (within an occluded region), high corrosion rates will occur at discrete sites. This represents a challenge for lifetime assessments since the high rates of localized corrosion are difficult to predict. The resulting damage can penetrate deep into a material and is difficult to detect visually. Ni-based alloys are generally considered immune to localized corrosion in the form of pitting [6, 48, 79]; however, crevice corrosion has been identified as a potential risk for these alloys [80].

1.5.1 Crevice corrosion

While crevice corrosion shares several mechanistic features with pitting corrosion [80], it is a distinct process that relies on the presence of a restrictive geometry [3]. In service, crevice geometries can form under gaskets, joints, washers, rivets, bolts, flanges, or even some surface deposits, and as a result, are virtually unavoidable during the design process. Several theories have been proposed to help explain the mechanism of crevice corrosion, including the critical crevice solution (CCS) [81, 82], IR drop [83, 84], and metastable pitting theories [85].

1.5.1.1 Critical crevice solution (CCS) theory

In a series of publications, Oldfield and Sutton developed a mathematical model, the critical crevice solution (CCS) theory, to predict the change in crevice chemistry [81, 82]. They proposed that crevice corrosion in aerated chloride solution occurred in four main stages: (i) oxygen depletion within the crevice, (ii) an increase in acidity and chloride content, (iii) passive film breakdown, and finally (iv) the propagation of damage. Initially, the depletion of oxygen led to the generation of a concentration cell, with the separated anodic and cathodic reactions inside and outside the crevice, respectively. In the crevice, protons are produced by metal cation hydrolysis, resulting in a decrease in solution pH due to the restricted mass transport, Figure 1.9. With an increasing concentration of cations (H^+, M^{n+}, $M(OH)^{n-1+}$, etc.) within the crevice, anions (Cl^-) are forced to migrate into the

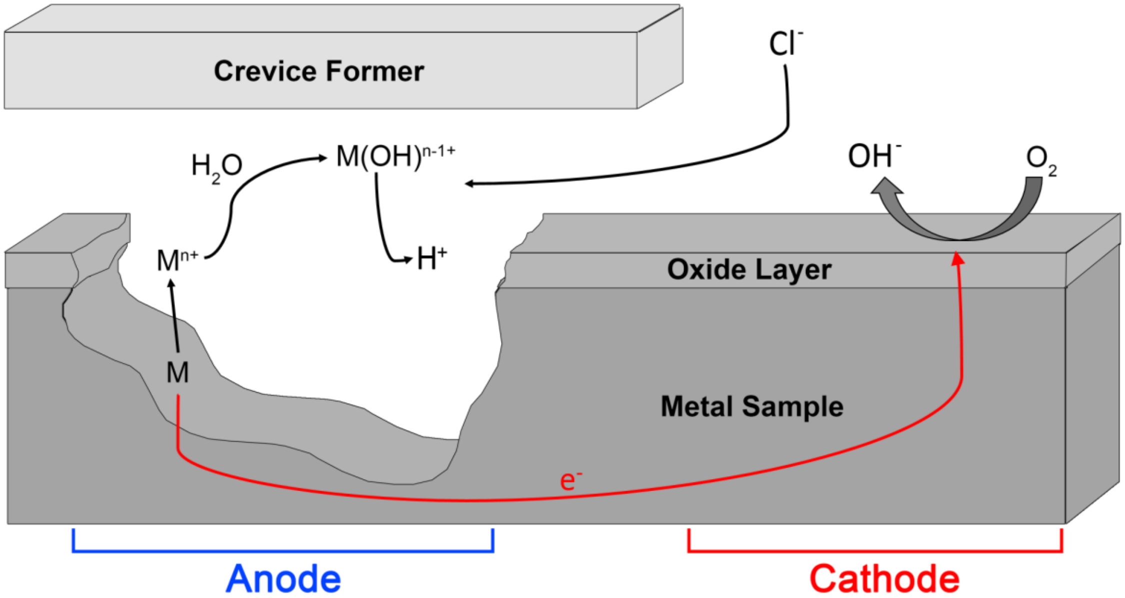

Figure 1.9 - Schematic representation showing the processes during the propagation of crevice corrosion, as described by critical crevice solution theory.

crevice to maintain charge neutrality. Together, the decreasing pH and increasing Cl^- concentration eventually establish a CCS, sufficiently aggressive to induce the breakdown of the passive oxide film. The final stage of this process is the propagation of crevice damage due to anodic metal dissolution concentrated within the crevice, supported mainly by O_2 reduction on the external surface. According to the CCS theory, the initial decrease in O_2 concentration and subsequent increase in H^+ and Cl^- concentrations causes both the initiation and propagation of crevice damage. In general, during the crevice corrosion of corrosion-resistant materials, critical crevice solutions have $pH < 0$ [86-89].

Nash and Kelly [90], analyzed solutions within a crevice during both the incubation and propagation stages for stainless steel using an *ex-situ* chromatographic analysis technique. Based on the concentration of dissolved metal cations and the related hydrolysis reactions, the solution pH was only considered low enough to disrupt the passive film during stable propagation. In a study by Sridhar and Dunn, the mechanism of crevice corrosion was studied using microelectrodes positioned directly in a crevice [91]. Their findings suggest that decreases in pH and increases in Cl^- concentration occur only after crevice corrosion initiates, implying that the critical crevice chemistry is a feature, but not necessarily the cause, of crevice corrosion. More recently, using fluorescent indicators sensitive to changes in both H^+ and Cl^- concentrations, Nishimoto *et al.* demonstrated that a gradual development of critical chemistry occurs during incubation, followed by an abrupt change in concentrations at the onset of activation [87]. These findings suggest that while solution chemistry is a feature of crevice corrosion, additional mechanistic features should be considered.

While restricted mass transport is a key feature in CCS theory, it does not address the existence of concentration gradients within the occluded region. For instance, since mass transport becomes increasingly restricted as a function of depth into a crevice, one would expect the most aggressive conditions to develop at the maximum depth into the crevice. In the work of Miller *et al.*, crevice damage was found to initiate in the deepest parts of the crevice and progress toward the mouth of the crevice [92]. Conversely Ebrahimi *et al.* showed that crevice damage occured at some critical depth near the opening (or mouth) of the crevice rather than at the deepest location [55]. Differences in propagation behaviour may be the result of different experimental methodologies. While Ebrahimi *et al.* used small applied currents (≤ 80 μA), Miller *et al.* used a constant applied potential which resulted in higher currents (mA). Additionally, CCS theory does not consider the effect of increased electrolyte resistance caused by the occluded geometry of a crevice.

1.5.1.2 IR drop theory

Pickering and Frankenthal proposed an IR drop theory in which crevice corrosion was explained by an ohmic potential drop (IR) within the occluded geometry of a crevice (or pit) [83, 84]. An IR drop between the outside and inside of the crevice occurs due to the combination of current (I) from metal dissolution and high electrolyte resistance (R) caused by the crevice geometry. As shown in Figure 1.10, at a critical depth inside the crevice, the IR drop becomes enough to disrupt the maintenance of the passive film and place the local potential in the active region of the polarization curve. This causes the initiation and accumulation of crevice damage. Changes to the magnitude of the IR drop may result, due to variations in crevice geometry caused by, for example, the introduction of solid corrosion products or gas bubbles. In some cases, the IR drop theory has been used to explain the commonly observed crevice damage morphology, which initiates at a critical depth into the crevice [86, 88, 93]. Data obtained for potentiostatically driven crevices suggests that the evolution of damage cannot be explained using only polarization data and involves the movement of a corrosion front within the crevice [92, 94]. Additionally, the IR drop theory does not account for the observed changes in solution chemistry. Without the development of aggressive crevice chemistry, the active to passive transition inherent in the IR drop theory is often absent from the polarization behaviour of corrosion-resistant materials. Lillard *et al.* suggested that the IR drop theory alone cannot explain the crevice corrosion process [89], and that the developing crevice chemistry must also be considered as it increases current densities and allows the critical IR drop to be achieved.

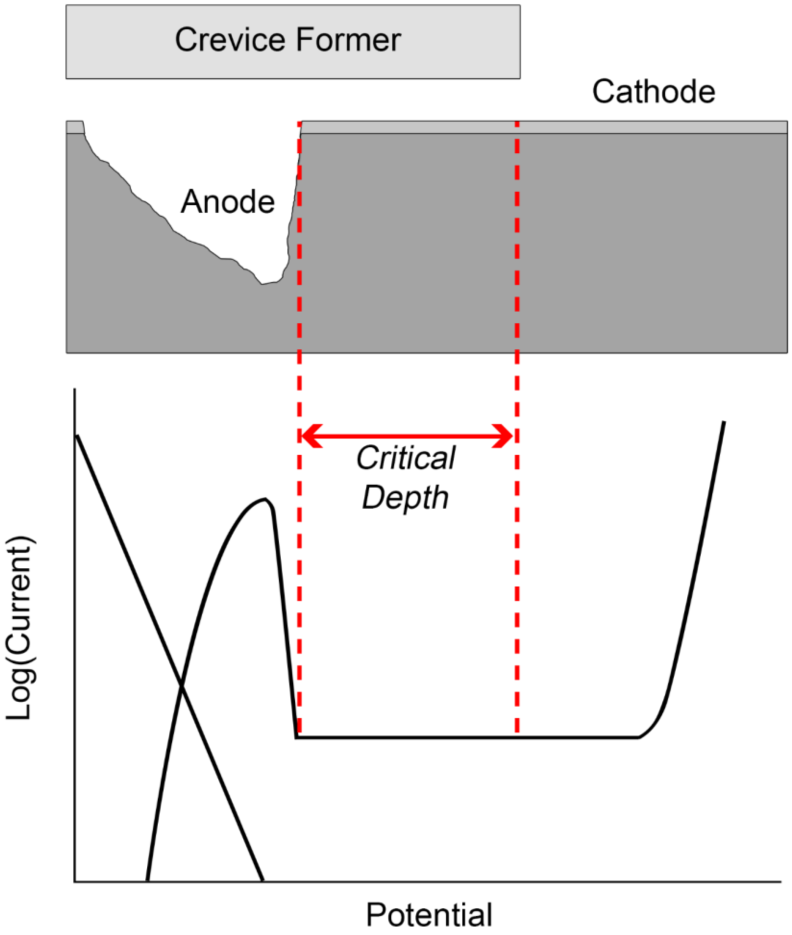

Figure 1.10 - Schematic representation of the IR drop theory. The high solution resistance within the occluded geometry causes the potential within the crevice to decrease relative to that in bulk solution. For an alloy exhibiting active-passive polarization behaviour, at a critical depth into the crevice, indicated by dashed lines, the resistance is sufficient to decrease the local potential into the active region.

1.5.1.3 Metastable pitting theory

Initially presented by Stockert and Boehni [85], the occluded geometry of a crevice was proposed to stabilize metastable pitting behaviour, eventually leading to the initiation and propagation of crevice corrosion. When pit initiation occurs on a surface exposed to bulk solution, propagation only occurs if the pit geometry can maintain an IR drop and/or critical chemistry. If the pit is metastable and the pit site returns to a passive state, the Cl^-, H^+, and M^{n+} ions generated within the pit will dissipate into the bulk solution. However, when pit initiation occurs at a high enough frequency and density within a crevice, the restrictive geometry can stabilize active behaviour, leading to the propagation of crevice corrosion. In other words, each metastable event contributes cumulatively to the chemistry required to initiate crevice corrosion. According to Laycock, *et al.* crevice corrosion occurs only after a critical amount of damage has occurred within a crevice [95]. Kehler and Scully demonstrated that during the crevice corrosion of Ni-based alloys C-22 and 625, the coalescence of metastable pits was an important feature of early-stage crevice corrosion [96]. Similar behaviour has been identified during the crevice corrosion of Ti alloys [97, 98].

1.5.2 Transpassive dissolution

In highly oxidizing environments passive film breakdown may also occur by the electrochemical conversion of the Cr(III)-rich oxide into more soluble Cr(VI) species, referred to as transpassive dissolution [11, 99]. The potential of a corroding system, *i.e.*, E_{CORR}, increases in the presence of strong oxidants, and if high enough, transpassive dissolution will occur. In polarization experiments, transpassive dissolution is observed as an exponential increase in measured current, as indicated in Figure 1.6. Transpassive dissolution is distinguished from other breakdown processes by the dependence of current on the applied potential. This concept will be discussed in more detail during the discussion of breakdown susceptibility.

$$\mathrm{Cr_2O_3} + 5\ \mathrm{H_2O} \rightleftharpoons 2\ \mathrm{CrO_4^{2-}} + 6\ \mathrm{e^-} + 10\ \mathrm{H^+} \tag{1.23}$$

The electrochemical reaction describing the transpassive dissolution of Cr_2O_3 is given in Reaction 1.23. Since the Cr-rich oxide is considered responsible for the barrier layer properties of the passive film [51, 100], its destruction exposes the underlying metal to solution. In the case of Ni-Cr-Mo alloys, during transpassive dissolution neither Ni nor Mo are expected to form protective oxides, according to thermodynamic calculations [2], especially at lower pH values. As a result, anodic polarization becomes a driving force for anodic dissolution, resulting in high rates of corrosion. The mechanism of transpassive dissolution is complex, with several claims involving the presence of intermediate Cr(IV) species [101] and the incorporation of Cr(VI) into the oxide before its dissolution [99].

1.5.3 The role of aggressive anions

Halide ions (*e.g.*, F^-, Cl^-, Br^-, I^-) are known to be particularly aggressive in destabilizing passive oxide films, with Cl^- being the most studied halide ion. While consensus exists on their aggressive nature, the action of individual anions is an area of considerable debate. While a complete discussion is beyond the scope of this thesis, a summary is provided, and a more thorough discussion can be found elsewhere [102]. During the passive film breakdown, aggressive anions are described by whether their action takes place at the metal/oxide or oxide/solution interface. These are referred to as penetration and adsorption mechanisms, respectively.

In penetration mechanisms, anions are transported through the passive oxide to the metal/oxide interface. Commonly, the high electric field and defect structure within the oxide is thought to facilitate this transport process. According to the PDM, the incorporation of halide ions into oxygen vacancies enhances the diffusion rate of cation vacancies [22, 103]. If these cation vacancies accumulate at the metal/oxide interface, voids can form within the oxide film, leading to breakdown. In this concept, localized breakdown is rationalized by heterogeneous features in the film containing high concentrations of defects [103]. In adsorption mechanisms, anions are adsorbed onto the oxide film, with Hoar and Jacob proposing that oxide breakdown occurs via complexation reactions which facilitate the transfer of cations into solution [104]. If the formation and transfer of metal-chloride complexes into solution exceeds the rate of film growth, the oxide film will begin to thin. As the passive film thins, the film resistance decreases, causing the interfacial potential drop to increase. As a result, thinning of the oxide is an autocatalytic step towards metal dissolution. Marcus *et al.* [34] proposed that these processes are influenced by the nanostructure of the oxide film. At defect sites, *e.g.*, oxide grain boundaries, the resistance of the oxide is less than at homogenous oxide film locations, making grain boundaries preferred sites for thinning and vacancy transport.

1.5.4 Measuring susceptibility

1.5.4.1 Pitting resistance equivalent number (PREN)

Understanding the susceptibility of an alloy to film breakdown processes is essential to guide material selection. The Pitting Resistance Equivalent Number (PREN), derived from empirical observations, is a method of qualitatively ranking the pitting resistance of alloys based on their composition. The higher the PREN value, the higher the resistance to film breakdown in the form of pitting or crevice corrosion [63, 80, 86, 105]. Initially developed for stainless steel [106], PREN calculations have been adapted for use with Ni-based alloys [63]. The equation used to calculate the PREN for Ni-based alloys is given in equation 1.24, where alloying element concentrations are in weight percent (wt.%).

$$\mathrm{PREN} = [\mathrm{Cr}] + 3.3\left[[\mathrm{Mo}] + 0.5\,[\mathrm{W}]\right] \tag{1.24}$$

While PREN values are useful in ranking the susceptibility of alloys, they do not provide any mechanistic information. As a result, information regarding how an alloying element operates during film formation, breakdown, or repassivation, is unelucidated. It is also important to consider that since the equation used to determine PREN is based on empirical observations, PREN rankings can only be considered valid for the studied environment (*e.g.*, solution composition, pH, temperature, etc.). Additionally, the PREN calculation considers only Cr, Mo, and W; however, it has been shown that other alloying elements influence resistance to film breakdown. As an example, Mishra *et al.* demonstrated that small amounts of alloyed Cu, ~1.6 wt.%, inhibit the initiation of crevice corrosion [107]. Similarly, alloying additions of Nb have been shown to benefit pitting resistance [108]. However, neither Cu nor Nb are commonly considered in PREN value calculations. Despite the obvious limitations, PREN has proven useful as a rapid and qualitative approach to ranking commercial alloys.

1.5.4.2 Critical temperatures

The relative susceptibility to film breakdown processes may also be compared using critical temperatures. These temperatures are defined as the minimum temperature for which film breakdown can occur and are reported for both pitting and crevice corrosion, and referred to as the Critical Pitting Temperature (CPT) or Critical Crevice Temperature (CCT), respectively. In general, an alloy is considered more resistant to film breakdown processes the higher the critical temperature. Values of CPT and CCT demonstrate similar trends; however, values of CCT are generally lower than the corresponding values of CPT [80, 109]. Using values of CCT or CPT to rank the susceptibility of alloys to film breakdown yields similar information to PREN values, but has the advantage of providing quantitative information. A comparison of CCT and PREN values is illustrated in Figure 1.11 for a collection of values reported in the literature [80, 105, 109].

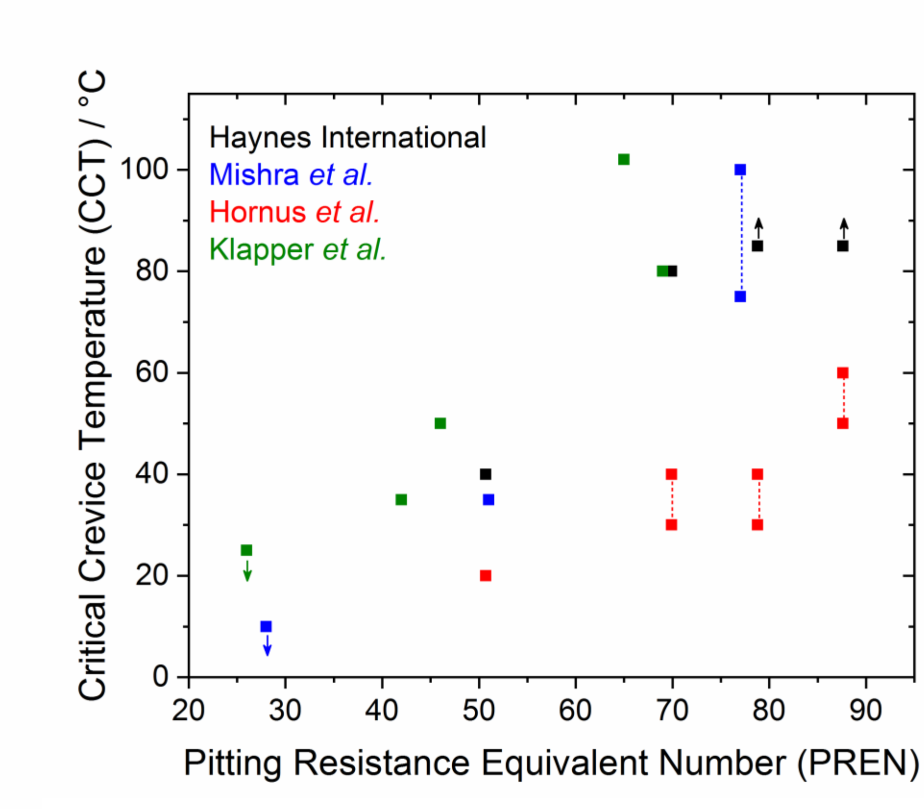

Figure 1.11 - Comparison of Critical Crevice Temperature with PREN values. PREN values were calculated according to Equation 1.24. Values reported as a range are indicated with dashed lines. Values reported as less than or greater than are indicated by arrows.

While critical temperature values have the advantage of quantifying a temperature threshold, like PREN, they yield no mechanistic information. The threshold information provided by CCT (and CPT) measurements is also specific to the conditions used during measurements. For example, the ASTM standard for the determination of CCT recommends the use of acidified ferric chloride ($FeCl_3$) solution [110], which will not necessarily represent service conditions.

1.5.4.3 Breakdown/repassivation potentials

Other parameters used to determine alloy susceptibility to film breakdown are critical potentials, referred to as breakdown (E_B) and repassivation (E_R) potentials. Breakdown of the passive film can occur at potentials ≥ E_B, while metastable pitting and propagation can continue only if the potential is ≥ E_R, which is lower than E_B [102]. A graphical representation of E_B and E_R in the context of a cyclic polarization measurement is presented in Figure 1.12. As the applied potential is scanned linearly in the positive direction, an abrupt increase in current is observed at E_B. This process may be distinguished from the

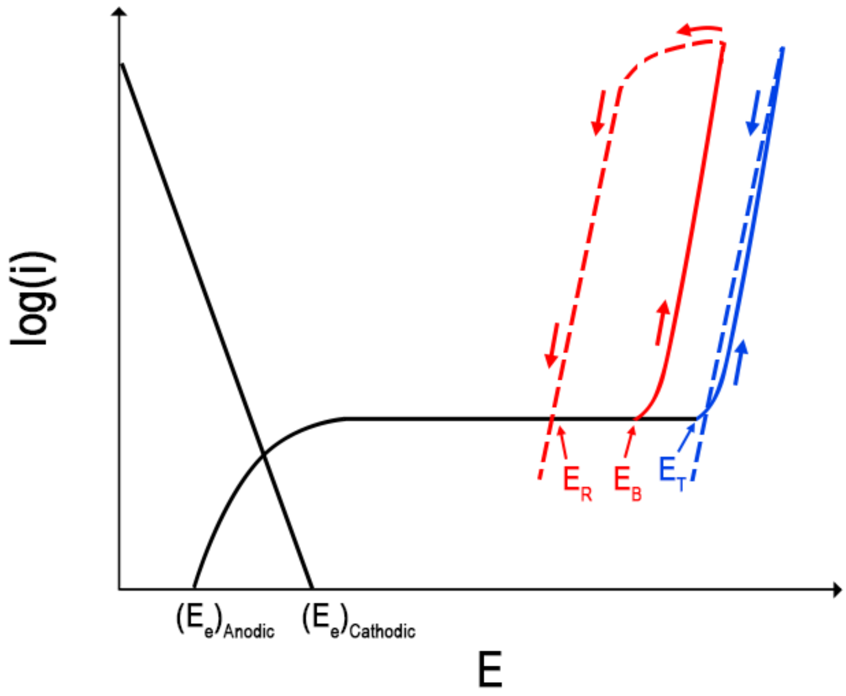

Figure 1.12 - Graphical representation of a cyclic polarization curve for an alloy which rapidly forms a passive film. At high applied potentials film breakdown leading to pitting or crevice corrosion is indicated by the red line and breakdown leading to transpassive dissolution by the blue line, with the values of E_B, E_R, and E_T indicated.

transpassive dissolution process, discussed above, by the behaviour on a reverse scan, as shown by the dashed lines in Figure 1.12. In the case of film breakdown resulting in either pitting or crevice corrosion, the reverse scan is independent of the applied potential and demonstrates hysteresis, indicated by the red dashed line in Figure 1.12. This is the result of the self-sustaining nature of localized corrosion, which causes the current to persist during the reverse scan. Repassivation is said to occur once the current on the reverse scan decreases to the passive current density on the forward scan. The potential at which this occurs is termed E_R. On the other hand, during transpassive dissolution, the reverse scan closely traces the i-E behaviour on the forward scan, indicated by the blue dashed line in Figure 1.12. In general, an alloy is considered more resistant to film breakdown processes the higher the values of E_B and E_R. Values of E_B and E_R are reported as pitting or crevice breakdown potentials, E_{PIT} and E_{CREV} respectively, depending on the experimental setup.

In particular, E_R has been described as an effective and conservative parameter to predict susceptibility to localized corrosion [93, 111-113]. Dunn *et al.* investigated the relationship between E_B, E_R, and E_{CORR}, for stainless steel 316L and alloy 825 using both artificial pit and crevice assemblies [111]. No evidence of localized corrosion was observed when E_{CORR} remained below E_R. Kehler *et al.* demonstrated a decrease of $E_{R,CREVICE}$ values with increasing temperature, and Cl^- concentration for both alloys 625 and C-22 [93], consistent with the findings of several other studies [112, 114]. Using a series of Ni-Cr-Mo alloys with increasing Mo-content, Hayes *et al.* demonstrated that E_R increased with increasing Mo content [7]. Given a dependence on Mo-content, it comes as no surprise that values of E_R correlate with calculated PREN values [86, 105]. While critical potentials provide a quantifiable threshold for different service conditions, they are unable to provide any mechanistic information. Additionally, experimental parameters such as scan rate and applied charge have been shown to affect measurements [111, 113].

1.5.5 The role of alloying elements during breakdown

While the methods described above are useful for ranking relative corrosion resistance as well as defining service thresholds, they do not provide any mechanistic information. Additions of Mo have been identified to have a critical role in resisting localized damage. While Cr is necessary for an alloy to form a protective passive film, in the event the passive film is compromised, alloyed Mo is beneficial in controlling the dissolution rate and promoting repassivation. Based on measurements of E_B and E_R for a series of commercial alloys, the effects of Cr, Mo, and W, on crevice corrosion were studied by Mishra and Shoesmith [63]. While increases in Cr content were found to improve passivity, alloying additions of Mo were identified as a key component in resisting initiation as well as promoting repassivation of crevice corrosion. With increased Mo-content, values of critical temperature and potential were found to increase.

The transport and distribution of alloying elements following the crevice corrosion of alloy C-22 were studied post mortem by Shan and Payer [88]. Compiling information obtained using XPS, Auger electron spectroscopy, and energy-dispersive X-ray spectroscopy (EDS), the distribution of elements within a corroded area was reconstructed, Figure 1.13. While dissolution was thought to occur in a congruent manner, the transport of individual alloying elements was different. These differences were attributed mainly to the pH gradient which developed. Cations or chloride complexes of Ni, Cr, Fe, and Co have a high solubility in the CCS and freely transport out of the occluded region, where they then encounter increased pH and precipitate. Mo (and W) were found to precipitate directly within the crevice due to their relatively low solubility and stability at low pH.

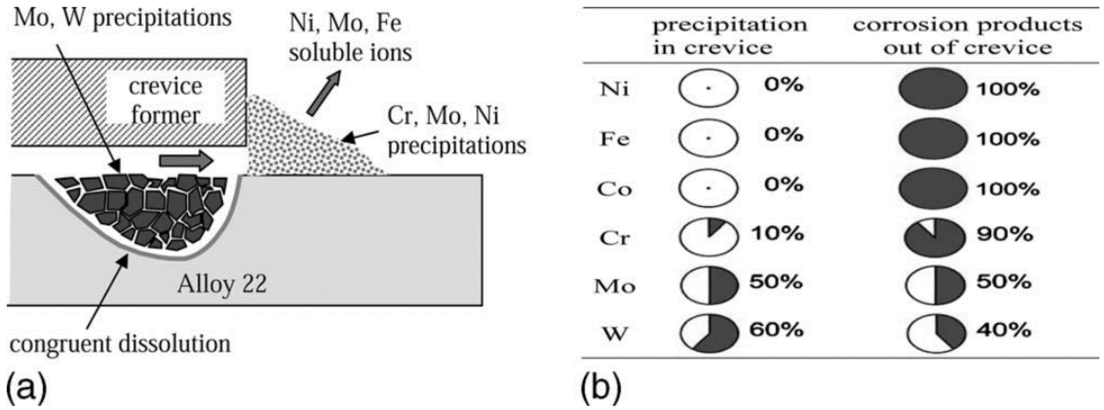

Figure 1.13 - (a) Graphical representation and (b) qualitative distribution of metal elements within a corroded crevice coupon. Originally published by Shan and Payer [88].

While the nature of these corrosion products has been discussed, the exact mechanism leading to their distribution remains to be determined. Lillard *et al.* proposed that during the initial stages of crevice corrosion, before the pH inside the crevice decreases, Mo oxidation leads to the production of MoO_4^{2-} [89], Reaction 1.25. However, as damage propagates and the pH decreases within the crevice, MoO_4^{2-} becomes unstable and is reduced to MoO_2, and eventually Mo^{3+}. In particular, it was proposed that MoO_4^{2-} inhibits dissolution through a competitive adsorption process with Cl^-. While competitive adsorption explains the benefit of alloyed-Mo in resisting the initiation of localized corrosion, it does not explain the observation of Mo-rich corrosion products in damage sites. The formation of polymeric molybdates has been suggested, according to reaction 1.26 [115]. Jakupi *et al.* found evidence of these polymeric species while studying the Mo(W)-rich corrosion products deposited within a corroded crevice region using Raman spectroscopy [116]. It has been proposed that the process of polymerization inhibits corrosion by consuming protons (H^+) within the occluded geometry [89, 91, 115]. However, the production of each MoO_4^{2-} species produces 8 H^+, equation 1.25, meaning that H^+ consumption during polymerization is insignificant.

$$\mathrm{Mo} + 4\ \mathrm{H_2O} \rightarrow \mathrm{MoO_4^{2-}} + 8\ \mathrm{H^+} \tag{1.25}$$

$$8\ \mathrm{MoO_4^{2-}} + 12\ \mathrm{H^+} \rightleftharpoons \mathrm{Mo_8O_{26}^{4-}} + 6\ \mathrm{H_2O} \tag{1.26}$$

The formation of Mo(W)-rich corrosion products within an active crevice has been shown to have a role in stifling active dissolution [55, 117, 118]. Using electron backscatter diffraction (EBSD), Jakupi *et al.* showed that during the early stages of corrosion on alloy C-22, damage was located at microstructural features such as triple points, along with accumulation of corrosion product [118]. In a separate study, Jakupi *et al.* used confocal laser scanning microscopy to investigate the morphology of crevice damage on alloy C-22 [117]. It was found that at low applied currents damage penetrated into the alloy, while at high applied currents damage was forced to spread laterally across the crevice region due to the accumulation of molybdate species at rapidly corroding sites.

In the study by Ebrahimi *et al.*, active crevice propagation was found to be self-sustaining [55]. Shown in Figure 1.14, the current transients and corresponding potential behaviour suggest that damage was driven by O_2 reduction external to the crevice, while damage could be sustained by H^+ reduction inside the crevice. Unfortunately, they were unable to quantify the role of H^+ reduction, but demonstrated that the deposition of polymeric molybdates within the crevice stifled propagation at localized breakdown sites.

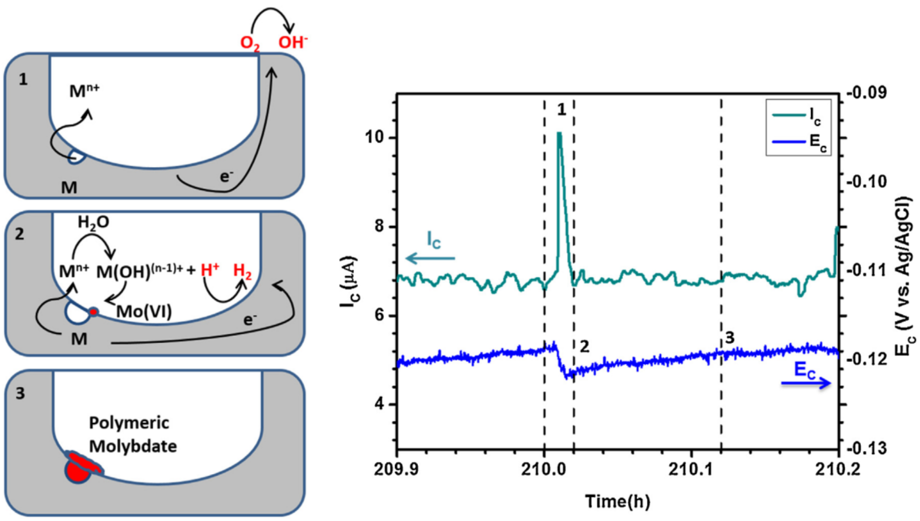

Figure 1.14 - Graphical representation (left) showing the (1) initiation, (2) propagation, and (3) stifling of active areas during crevice corrosion of alloy BC-1 exposed to 5 M NaCl solution at 120°C. The corresponding current and potential measurements are shown (right). Originally published by Ebrahimi *et al.* [55].

1.6 References

[1] G. Koch, N. Thompson, O. Moghissi, J. Payer, J. Varney, IMPACT (International measures of prevention, application, and economics of corrosion technologies) study, in: NACE, March, National Association of Corrosion Engineers, Houston, TX, 2016.

[2] M. Pourbaix, Atlas of electrochemical equilibria in aqueous solution, NACE, 1974.

[3] R.W. Revie, Uhlig's corrosion handbook, John Wiley & Sons, 2011.

[4] J.R. Davis, Nickel, cobalt, and their alloys, ASM international, 2000.

[5] P. Marcus, On some fundamental factors in the effect of alloying elements on passivation of alloys, *Corrosion Science*, 36 (1994) 2155-2158.

[6] C.D. Taylor, P. Lu, J. Saal, G.S. Frankel, J.R. Scully, Integrated computational materials engineering of corrosion resistant alloys, *npj Materials Degradation*, 2 (2018).

[7] J.R. Hayes, J.J. Gray, A.W. Szmodis, C.A. Orme, Influence of chromium and molybdenum on the corrosion of nickel-based alloys, *Corrosion*, 62 (2006) 491-500.

[8] R.W. Revie, Corrosion and corrosion control: an introduction to corrosion science and engineering, John Wiley & Sons, 2008.

[9] R.G. Kelly, J.R. Scully, D. Shoesmith, R.G. Buchheit, Electrochemical techniques in corrosion science and engineering, CRC Press, 2002.

[10] P. Lu, J.E. Saal, G.B. Olson, T. Li, O.J. Swanson, G.S. Frankel, A.Y. Gerard, K.F. Quiambao, J.R. Scully, Computational materials design of a corrosion resistant high entropy alloy for harsh environments, *Scripta Materialia*, 153 (2018) 19-22.

[11] D.W. Shoesmith, Corrosion: fundamentals, testing, and protection, in: S.D. Cramer, B.S. Covino (Eds.) ASM Handbook, ASM International, 2003, pp. 42-51.

[12] A.J. Bard, L.R. Faulkner, Electrochemical methods: fundamentals and applications, 2 ed., John Wiley & Sons Inc., 2001.

[13] E. McCafferty, Introduction to corrosion science, Springer Science & Business Media, 2010.

[14] J. Kruger, Corrosion: fundamentals, testing, and protection, in: S.D. Cramer, B.S. Covino (Eds.) ASM Handbook, ASM International, 2003, pp. 61-67.

[15] H.H. Uhlig, Passivity in metals and alloys, *Corrosion Science*, 19 (1979) 777-791.

[16] C. Wagner, Passivity and inhibition during the oxidation of metals at elevated temperatures, *Corrosion Science*, 5 (1965) 751-764.

[17] P. Marcus, Corrosion mechanisms in theory and practice, CRC press, 2011.

[18] A. Seyeux, V. Maurice, P. Marcus, Oxide film growth kinetics on metals and alloys, *Journal of The Electochemical Society*, 160 (2013) C189-C196.

[19] N. Cabrera, N.F. Mott, Theory of the oxidation of metals, *Reports on Progress in Physics*, 12 (1949) 163-184.

[20] F.P. Fehlner, N.F. Mott, Low-temperature oxidation, *Oxidation of Metals*, 2 (1970) 59-99.

[21] C.Y. Chao, L.F. Lin, D.D. Macdonald, A point defect model for anodic passive films (i. film growth kinetics), *Journal of The Electrochemical Society*, 128 (1981) 1187.

[22] D.D. Macdonald, The point defect model for the passive state, *Journal of The Electochemical Society*, 139 (1992) 3434-3449.

[23] M. Momeni, J.C. Wren, A mechanistic model for oxide growth and dissolution during corrosion of Cr-containing alloys, *Faraday Discussion*, 180 (2015) 113-135.

[24] X.-x. Yu, A. Gulec, C.M. Andolina, E.J. Zeitchick, K. Gusieva, J.C. Yang, J.R. Scully, J.H. Perepezko, L.D. Marks, In situ observations of early stage oxidation of Ni-Cr and Ni-Cr-Mo alloys, *Corrosion*, 74 (2018) 939-946.

[25] X.X. Yu, A. Gulec, Q. Sherman, K.L. Cwalina, J.R. Scully, J.H. Perepezko, P.W. Voorhees, L.D. Marks, Nonequilibrium solute capture in passivating oxide films, *Physical Review Letters*, 121 (2018) 145701.

[26] M. Urquidi, D.D. Macdonald, Solute-vacancy interaction model and the effect of minor alloying elements on the initiation of pitting corrosion, *Journal of The Electrochemical Society*, 132 (1985) 555.

[27] G. Bouyssoux, M. Romand, H.D. Polaschegg, J.T. Calow, XPS and AES studies of anodic passive films grown on chromium electrodes in sulphuric acid baths, *Journal of Electron Spectroscopy and Related Phenomena*, 11 (1977) 185-196.

[28] T. Jabs, X-Ray Photoelectron spectroscopic examinations of electrochemically formed passive layers on Ni-Cr alloys, *Journal of The Electrochemical Society*, 144 (1997) 1231.

[29] S.-P. Jeng, P.H. Holloway, C.D. Batich, Surface passivation of Ni/Cr alloy at room temperature, *Surface Science*, 227 (1990) 278-290.

[30] D. Zuili, V. Maurice, P. Marcus, In situ scanning tunneling microscopy study of the structure of the hydroxylated anodic oxide film formed on Cr(110) single-crystal surfaces, *The Journal of Physical Chemistry B*, 103 (1999) 7896-7905.

[31] A.R. Brooks, C.R. Clayton, K. Doss, Y.C. Lu, On the role of Cr in the passivity of stainless steel, *Journal of The Electrochemical Society*, 133 (1986) 2459.

[32] M.P. Ryan, R.C. Newman, G.E. Thompson, A scanning tunnelling microscopy study of structure and structural relaxation in passive oxide films on Fe-Cr alloys, *Philosophical Magazine B*, 70 (1994) 241-251.

[33] D.H. Hur, Y.S. Park, Effect of temperature on the pitting behavior and passive film characteristics of alloy 600 in chloride solution, *Corrosion*, 62 (2006) 745-750.

[34] P. Marcus, V. Maurice, H.H. Strehblow, Localized corrosion (pitting): a model of passivity breakdown including the role of the oxide layer nanostructure, *Corrosion Science*, 50 (2008) 2698-2704.

[35] J.R. Myers, F.H. Beck, M.G. Fontana, Anodic polarization behavior of nickel-chromium alloys in sulfuric acid solutions, *Corrosion*, 21 (1965) 277-287.

[36] A.P. Bond, H.H. Uhlig, Corrosion behavior and passivity of nickel-chromium and cobalt-chromium alloys, *Journal of The Electrochemical Society*, 107 (1960) 488.

[37] A.C. Lloyd, J.J. Noël, N.S. McIntyre, D.W. Shoesmith, The open-circuit ennoblement of alloy C-22 and other Ni-Cr-Mo alloys, *Journal of Metals*, 57 (2005) 31-35.

[38] S. Boudin, J.L. Vignes, G. Lorang, M. Da Cunha Belo, G. Blondiaux, S.M. Mikhailov, J.P. Jacobs, H.H. Brongersma, Analytical and electrochemical study of passive films formed on nickel-chromium alloys: influence of the chromium bulk concentration, *Surface and Interface Analysis*, 22 (1994) 462-466.

[39] W.G. Whitman, E.L. Chappell, Corrosion of steels in the atmosphere, *Industrial & Engineering Chemistry*, 18 (1926) 533-535.

[40] F.G. Hodge, B.E. Wilde, Effect of chloride ion on the anodic dissolution kinetics of chromium-nickel binary alloys in dilute sulfuric acid, *Corrosion*, 26 (1970) 246-250.

[41] K. Sieradzki, R.C. Newman, A percolation model for passivation in stainless steels, *Journal of The Electrochemical Society*, 133 (1986) 1979.

[42] E. McCafferty, Graph theory and the passivity of binary alloys, *Corrosion Science*, 42 (2000) 1993-2011.

[43] E. McCafferty, Relationship between graph theory and percolation approaches in the passivity of Fe–Cr binary alloys, *Journal of The Electrochemical Society*, 155 (2008) C501.

[44] E. McCafferty, Oxide networks, graph theory, and the passivity of Ni–Cr–Mo ternary alloys, *Corrosion Science*, 50 (2008) 3622-3628.

[45] L.J. Oblonsky, M.P. Ryan, H.S. Isaacs, In situ determination of the composition of surface films formed on Fe-Cr alloys, *Journal of The Electrochemical Society*, 145 (1998) 1922.

[46] K. Asami, K. Hashimoto, S. Shimodaira, An XPS study of the passivity of a series of iron-chromium alloys in sulphuric acid, *Corrosion Science*, 18 (1978) 151-160.

[47] C.R. Clayton, Y.C. Lu, A bipolar model of the passivity of stainless steel: the role of Mo Addition, *Journal of The Electochemical Society*, 133 (1986) 2465-2473.

[48] A.C. Lloyd, J.J. Noël, S. McIntyre, D.W. Shoesmith, Cr, Mo and W alloying additions in Ni and their effect on passivity, *Electrochimica Acta*, 49 (2004) 3015-3027.

[49] D. Zagidulin, X. Zhang, J. Zhou, J.J. Noël, D.W. Shoesmith, Characterization of surface composition on alloy 22 in neutral chloride solutions, *Surface and Interface Analysis*, 45 (2013) 1014-1019.

[50] K. Hashimoto, K. Asami, K. Teramoto, An X-ray photo-electron spectroscopic study on the role of molybdenum in increasing the corrosion resistance of ferritic stainless steels in HCl, *Corrosion Science*, 19 (1979) 3-14.

[51] A. Mishra, D.W. Shoesmith, P. Manning, Materials selection for use in concentrated hydrochloric acid, *Corrosion*, 73 (2017) 68-76.

[52] J.H. Gerretsen, J.H. De Wit, The role of molybdenum in the active-passive transition of iron-chromium alloys, *Electrochimica Acta*, 36 (1991) 1465-1467.

[53] M.B. Rockel, The effect of molybdenum on the corrosion behaviour of iron-chromium alloys, *Corrosion*, 29 (1973) 393-396.

[54] K. Hashimoto, K. Asami, A. Kawashima, H. Habazaki, E. Akiyama, The role of corrosion-resistant alloying elements in passivity, *Corrosion Science*, 49 (2007) 42-52.

[55] N. Ebrahimi, J.J. Noël, M.A. Rodriguez, D.W. Shoesmith, The self-sustaining propagation of crevice corrosion on the hybrid BC1 Ni–Cr–Mo alloy in hot saline solutions, *Corrosion Science*, 105 (2016) 58-67.

[56] W.P. Tian, H.W. Yang, S.D. Zhang, Synergistic effect of Mo, W, Mn and Cr on the passivation behavior of a Fe-based amorphous alloy coating, *Acta Metallurgica Sinica (English Letters)*, 31 (2018) 308-320.

[57] A. Tomio, M. Sagara, T. Doi, H. Amaya, N. Otsuka, T. Kudo, Role of alloyed molybdenum on corrosion resistance of austenitic Ni–Cr–Mo–Fe alloys in H_2S–Cl^- environments, *Corrosion Science*, 98 (2015) 391-398.

[58] K. Lutton Cwalina, C.R. Demarest, A.Y. Gerard, J.R. Scully, Revisiting the effects of molybdenum and tungsten alloying on corrosion behavior of nickel-chromium alloys in aqueous corrosion, *Current Opinions in Solid State & Materials Science*, 23 (2019).

[59] A.J. Samin, C.D. Taylor, First-principles investigation of surface properties and adsorption of oxygen on Ni-22Cr and the role of molybdenum, *Corrosion Science*, 134 (2018) 103-111.

[60] R. Newman, The dissolution and passivation kinetics of stainless alloys containing molybdenum (part ii), *Corrosion Science*, 25 (1985) 341-350.

[61] R. Newman, The dissolution and passivation kinetics of stainless alloys containing molybdenum (part i), *Corrosion Science*, 25 (1985) 331-339.

[62] R.C. Newman, E.M. Franz, Determination of the minimum surface enrichment of molybdenum required to inhibit active dissolution of an Fe-Cr-Ni-Mo alloy, *Journal of The Electrochemical Society*, 131 (1984) 223.

[63] A.K. Mishra, D.W. Shoesmith, Effect of alloying elements on crevice corrosion inhibition of nickel-chromium-molybdenum-tungsten alloys under aggressive conditions: an electrochemical study, *Corrosion Science*, 70 (2014) 721-730.

[64] N. Ebrahimi, M.C. Beiesinger, D.W. Shoesmith, J.J. Noël, The influence of chromium and molybdenum on the repassivation of nickel-chromium-molybdenum alloys in saline solutions, *Surface Interface Analysis*, 49 (2017) 1359-1365.

[65] A.K. Mishra, S. Ramamurthy, M. Biesinger, D.W. Shoesmith, The activation/depassivation of nickel–chromium–molybdenum alloys in bicarbonate solution: part i, *Electrochimica Acta*, 100 (2013) 118-124.

[66] X. Zhang, D. Zagidulin, D.W. Shoesmith, Characterization of film properties on the Ni Cr Mo alloy C-2000, *Electrochimica Acta*, 89 (2013) 814-822.

[67] K.F. Quiambao, S.J. McDonnell, D.K. Schreiber, A.Y. Gerard, K.M. Freedy, P. Lu, J.E. Saal, G.S. Frankel, J.R. Scully, Passivation of a corrosion resistant high entropy alloy in non-oxidizing sulfate solutions, *Acta Materialia*, 164 (2019) 362-376.

[68] X. Wu, S. Voyshnis, A. Seyeux, Y. Chumlyakov, P. Marcus, ToF-SIMS study of oxide films thermally grown on nickel-base alloys, *Corrosion Science,* 141 (2018) 175-181.

[69] A.Y. Musa, M. Behazin, J.C. Wren, Potentiostatic oxide growth kinetics on Ni-Cr and Co-Cr alloys: potential and pH dependences, *Electrochimica Acta*, 162 (2015) 185-197.

[70] C.F. Baes, R.E. Mesmer, The hydrolysis of cations, Wiley, New York, 1976.

[71] J.J. Gray, C.A. Orme, Electrochemical impedance spectroscopy study of the passive films of alloy 22 in low pH nitrate and chloride environments, *Electrochimica Acta*, 52 (2007) 2370-2375.

[72] J.J. Gray, B.S. El Dasher, C.A. Orme, Competitive effects of metal dissolution and passivation modulated by surface structure: an AFM and EBSD study of the corrosion of alloy 22, *Surface Science*, 600 (2006) 2488-2494.

[73] J.J. Gray, J.R. Hayes, G.E. Gdowski, B.E. Viani, C.A. Orme, Influence of solution pH, anion concentration, and temperature on the corrosion properties of alloy 22, *Journal of The Electrochemical Society*, 153 (2006) B61.

[74] X.S. Zhang, Kinetics of O_2 reduction on oxide-covered Ni-Cr-Mo alloys, in: Chemistry, University of Western Ontario, London, Ontario, 2012.

[75] A.K. Mishra, D.W. Shoesmith, The activation/depassivation of nickel–chromium–molybdenum alloys: an oxyanion or a pH effect - part ii, *Electrochimica Acta*, 102 (2013) 328-335.

[76] A.C. Lloyd, D.W. Shoesmith, N.S. McIntyre, J.J. Noël, Effects of temperature and potential on the passive corrosion properties of alloys C22 and C276, *Journal of The Electrochemical Society*, 150 (2003) B120.

[77] X. Zhang, D.W. Shoesmith, Influence of temperature on passive film properties on Ni–Cr–Mo alloy C-2000, *Corrosion Science*, 76 (2013) 424-431.

[78] R.B. Rebak, J.H. Payer, Passive corrosion behaviour of alloy 22, in, U.S. Department of Energy Office of Scientific and Technical Information, 2006.

[79] H.H. Huang, Effect of chemical composition on the corrosion behavior of Ni-Cr-Mo dental casting alloys, *Journal of Biomedical Materials Research*, 60 (2002) 458-465.

[80] H.S. Klapper, N.S. Zadorozne, R.B. Rebak, Localized corrosion characteristics of nickel alloys: a review, *Acta Metallurgica Sinica (English Letters)*, 30 (2017) 296-305.

[81] J.W. Oldfield, W.H. Sutton, Crevice corrosion of stainless steels i. a mathematical model, *British Corrosion Journal*, 13 (1978) 13-22.

[82] J.W. Oldfield, W.H. Sutton, Crevice corrosion of stainless steels ii. experimental studies, *British Corrosion Journal*, 13 (1978) 104-111.

[83] H.W. Pickering, R.P. Frankenthal, On the mechanism of localized corrosion of iron and stainless steel, *Journal of The Electochemical Society*, 119 (1972) 1297-1304.

[84] H.W. Pickering, The significance of the local electrode potential within pits, crevices and cracks, *Corrosion Science*, 29 (1989) 325-341.

[85] L. Stockert, H. Boehni, Susceptibility to crevice corrosion and metastable pitting of stainless steels, in: Materials Science Forum, Trans Tech Publ, 1989, pp. 313-328.

[86] N.S. Zadorozne, C.M. Giordano, M.A. Rodriguez, R.M. Carranza, R.B. Rebak, Crevice corrosion kinetics of nickel alloys bearing chromium and molybdenum, *Electrochimica Acta*, 76 (2012) 94-101.

[87] M. Nishimoto, J. Ogawa, I. Muto, Y. Sugawara, N. Hara, Simultaneous visualization of pH and Cl^- distributions inside the crevice of stainless steel, *Corrosion Science*, 106 (2016) 298-302.

[88] X. Shan, J.H. Payer, Characterization of the corrosion products of crevice corroded alloy 22, *Journal of The Electochemical Society*, 156 (2009) C313-C321.

[89] R.S. Lillard, M.P. Jurinski, J.R. Scully, Crevice corrosion of alloy 625 in chlorinated ASTM artificial ocean water, *Corrosion*, 50 (1994) 251-265.

[90] B.K. Nash, R.G. Kelly, Characterization of the crevice solution chemistry of 304 stainless steel, *Corrosion Science*, 35 (1993) 817-825.

[91] N. Sridhar, D.S. Dunn, Effect of applied potential on changes in solution chemistry inside crevices on type 304L stainless steel and alloy 825, *Corrosion*, 50 (1994) 857-872.

[92] D.M. Miller, R.S. Lillard, An investigation into the stages of alloy 625 crevice corrosion in an ocean water environment: initiation, propagation and repassivation in a remote crevice assembly, *Journal of The Electrochemical Society*, 166 (2019) C3431-C3442.

[93] B.A. Kehler, G.O. Ilevbare, J.R. Scully, Crevice corrosion stabilization and repassivation behavior of alloy 625 and alloy 22, *Corrosion*, 57 (2001) 1042-1065.

[94] R.S. Lillard, S. Mehrazi, D.M. Miller, Quantifying alloy 625 crevice corrosion using an image differencing technique: part i. initiation and propagation, *Journal of The Electrochemical Society*, 167 (2020) 021511.

[95] N.J. Laycock, J. Stewart, R.C. Newman, The initiation of crevice corrosion in stainless steels, *Corrosion Science*, 39 (1997) 1791-1809.

[96] B.A. Kehler, J.R. Scully, Role of metastable pitting in crevices on crevice corrosion stabilization in alloys 625 and 22, *Corrosion*, 61 (2005) 665-684.

[97] X. He, J.J. Noël, D.W. Shoesmith, Crevice corrosion damage function for grade-2 titanium of iron content 0.078wt% at 95°C, *Corrosion Science*, 47 (2005) 1177-1195.

[98] L. Yan, J.J. Noël, D.W. Shoesmith, Hydrogen absorption into grade-2 titanium during crevice corrosion, *Electrochimica Acta*, 56 (2011) 1810-1822.

[99] P. Schmuki, S. Virtanen, A.J. Davenport, C.M. Vitus, Transpassive dissolution of Cr and sputter-deposited Cr oxides studied by in situ X-ray near-edge spectroscopy, *Journal of The Electrochemical Society*, 143 (1996) 3997-4005.

[100] V. Maurice, P. Marcus, Progress in corrosion science at atomic and nanometric scales, *Progress in Materials Science*, 95 (2018) 132-171.

[101] M. Bojinov, G. Fabricius, T. Laitinen, T. Saario, Transpassivity mechanism of iron–chromium–molybdenum alloys studied by AC impedance, DC resistance and RRDE measurements, *Electrochimica Acta*, 44 (1999) 4331-4343.

[102] J. Soltis, Passivity breakdown, pit initiation and propagation of pits in metallic materials - review, *Corrosion Science*, 90 (2015) 5-22.

[103] L.F. Lin, C.Y. Chao, D.D. Macdonald, A point defect model for anodic passive film (ii. chemical breakdown and pit initiation), *Journal of The Electrochemical Society*, 128 (1981) 1194.

[104] T.P. Hoar, W.R. Jacob, Breakdown of passivity of stainless steel by halide ions, *Nature*, 216 (1967) 1299-1301.

[105] E.C. Hornus, M.A. Rodriguez, R.M. Carranza, C.M. Giordano, R.B. Rebak, Effect of environmental variables on crevice corrosion susceptibility of Ni-Cr-Mo alloys for nuclear repositories, *Procedia Materials Science*, 8 (2015) 11-20.

[106] M. Lindgren, E. Huttunen-Saarivirta, H. Peltola, J. Romu, T. Sarikka, H. Hänninen, P. Pohjanne, Crevice corrosion of stainless steels 904L, 2205, and 2507 in high-temperature sulfuric acid solution containing chlorides: influence of metal cations, *Corrosion*, 74 (2018) 225-240.

[107] A.K. Mishra, X. Zhang, D.W. Shoesmith, The role of copper on the crevice corrosion behavior of nickel-chromium-molybdenum alloys in aggressive solutions, *Corrosion*, 72 (2016) 356-367.

[108] S. Schmigalla, A. Heyn, Determination of critical pitting temperatures for Ni-Cr-Mo alloys using electrochemical noise measurements, *Materials and Corrosion*, 64 (2013) 700-707.

[109] A. Mishra, D. Richesin, R.B. Rebak, Localized corrosion study of Ni-Cr-Mo alloys for oil and gas applications, in: CORROSION 2015, NACE International, 2015, pp. 1-15.

[110] Standard test methods for pitting and crevice corrosion resistance of stainless steels and related alloys by use of ferric chloride solution, in: ASTM G48-11, American Society for Testing and Materials, 2015.

[111] D.S. Dunn, G.A. Cragnolino, N. Sridhar, An electrochemical approach to predicting long-term localized corrosion of corrosion-resistant high-level waste container materials, *Corrosion*, 56 (2000) 90-104.

[112] D.S. Dunn, Y.M. Pan, L. Yang, G.A. Cragnolino, Localized corrosion susceptibility of alloy 22 in Chloride Solutions: part 1—mill-annealed condition, *Corrosion*, 61 (2005) 1078-1085.

[113] G.S. Frankel, Corrosion: fundamentals, testing, and protection, in: S.D. Cramer, B.S. Covino (Eds.) ASM Handbook, ASM International, 2003, pp. 236-241.

[114] K.J. Evans, A. Yilmaz, S.D. Day, L.L. Wong, J.C. Estill, R.B. Rebak, Using electrochemical methods to determine alloy 22’s crevice corrosion repassivation potential, *Journal of Metals*, 57 (2005) 56-61.

[115] M.A. Cavanaugh, J.A. Kargol, J. Nickerson, N.F. Fiore, The anodic dissolution of a Ni-base superalloy, *Corrosion*, 39 (1983) 144-150.

[116] P. Jakupi, F. Wang, J.J. Noël, D.W. Shoesmith, Corrosion product analysis on crevice corroded alloy-22 specimens, *Corrosion Science*, 53 (2011) 1670-1679.

[117] P. Jakupi, J.J. Noël, D.W. Shoesmith, The evolution of crevice corrosion damage on the Ni–Cr–Mo–W alloy-22 determined by confocal laser scanning microscopy, *Corrosion Science*, 54 (2012) 260-269.

[118] P. Jakupi, J.J. Noël, D.W. Shoesmith, Intergranular corrosion resistance of sigma-3 grain boundaries in alloy 22, *Electrochemical and Solid-State Letters*, 13 (2010) C1-C3.

Chapter 2

2 Experimental

This chapter summarizes the general details and the principles of the experimental techniques employed in this thesis. Specific details on experimental parameters and procedures are included with each data chapter.

2.1 Experimental sample

2.1.1 Materials

Hastelloy materials were provided by Haynes International (Kokomo, IN, USA). Stainless-steel alloys were purchased from McMaster-Carr (Elmhurst, IL, USA). All materials were received as mill-annealed sheets of varying thickness. The composition of each alloy is provided in the experimental sections of the data chapters. Experimental samples were cut and machined to the desired dimensions.

2.1.2 Sample preparation

All samples were ground with wet SiC paper to remove surface damage caused by the machining process. Depending on the experiment, the extent of surface preparation varied. For electrochemical measurements, P1200 SiC paper was used as a final grinding step. Samples subjected to surface analysis were finally prepared using a 1 μm diamond suspension. Following all surface preparations, samples were sonicated in a 1:1 mixture of EtOH and deionized (DI) water (18.2 MΩ cm) and dried in a stream of Ar-gas.

2.2 Electrochemical experiments

2.2.1 Electrochemical cells

Depending on the intended test conditions, one of four electrochemical cells was employed. Two of the four cells, the glass and the polytetrafluoroethylene (PTFE) cell, are shown in detail below. The third cell was designed specifically for coupling electrochemical and spectroscopic measurements and is discussed in Section 2.3. The fourth cell, used for crevice corrosion experiments performed at high temperatures, is discussed in Section 2.4.

2.2.1.1 Three-compartment glass cell

A schematic of the three-compartment glass cell used to conduct electrochemical measurements is shown in Figure 2.1. A water jacket, which encased the main compartment, was connected to an isothermal water circulator to control solution temperature. The working electrode (WE) was situated in a central compartment, with a platinum counter electrode (CE) and a saturated calomel reference electrode (RE) housed in separate compartments. The three compartments were separated by porous glass frits to minimize solution transfer. A Luggin capillary was used to connect the RE compartment to the main cell body to minimize the ohmic potential drop (IR) through solution. External electrical interference was minimized by placing the entire electrochemical cell in a grounded Faraday cage.

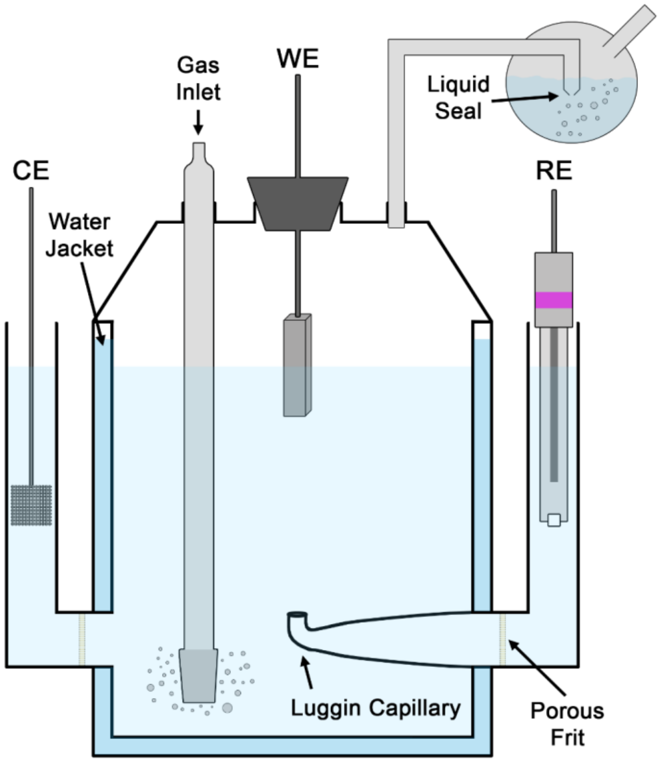

Figure 2.1 - Schematic of the three-compartment glass cell used to conduct electrochemical measurements. Components referenced in-text are also indicated.

When stated, the concentration of dissolved O_2 was removed by purging the electrolyte and pressurizing the cell with Ar-gas. The Ar-gas was introduced to the cell using a glass tube terminating in a porous glass plug. Positive pressure was maintained in the cell by the fitted ground glass joints and a water-filled bubbler. Parafilm wax was used to seal any additional joints. Before the start of deaerated experiments, the cell was purged by a high flow of Ar-gas for approximately 1 hour. When the experiment was to begin, the flow rate was reduced.

2.2.1.2 PTFE cell

Experiments involving fluoride (F^-) were conducted in a custom-built PTFE cell to avoid the reaction between F^- and glass (SiO_2). A schematic of the PTFE cell, positioned within a custom heating reservoir, is shown in Figure 2.2(A). Two lids were constructed for use with the cell, depending on experimental needs. The first lid was designed with three inlets for electrode connections, depicted in Figure 2.2(B). A second lid was designed with eight inlets for electrode connections, allowing the use of up to six WEs, depicted in Figure 2.2(C). In all cases, a saturated Ag/AgCl electrode and a platinum coil were employed as the RE and CE, respectively. Both lids contain a gas inlet and outlet for solution sparging.

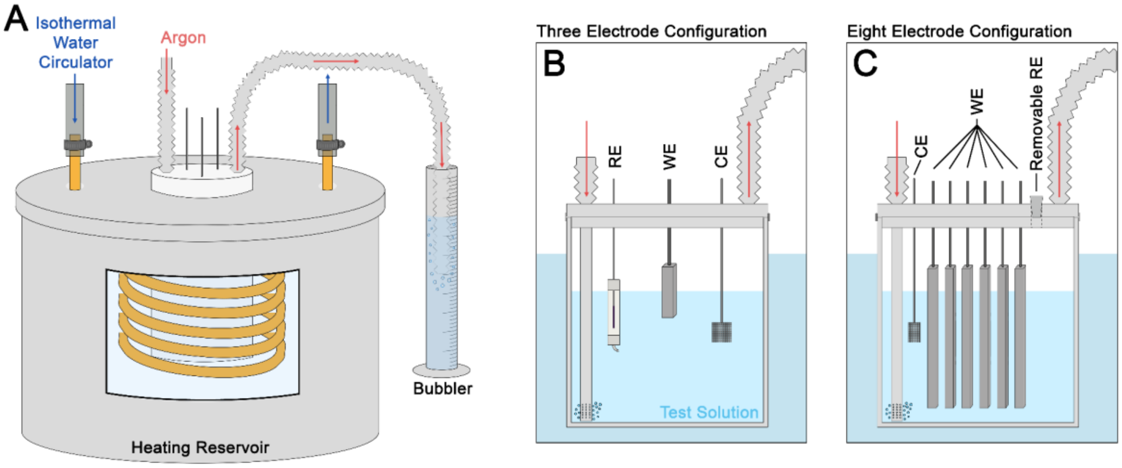

Figure 2.2 - Schematic of the (A) fully assembled PTFE electrochemical cell placed within the heating reservoir. Insets show the cross section of the electrochemical cell in the (B) three electrode and (C) eight electrode configuration.

All connections were secured using PTFE tape to prevent unwanted leaks. The assembled cell was secured with a clamp to prevent any movement of the lid or fittings during experimentation.

The temperature of the PTFE cell was regulated using a custom-built isothermal heating reservoir filled with water, shown in Figure 2.2(A). Reservoir temperatures were maintained using an isothermal water circulator, similar to the glass cell setup, but with the heated water circulated through a long copper coil. To maintain the water level within the heating reservoir, a float mechanism was installed to replenish any water lost due to evaporation. The large volume of water within the heating reservoir minimized any change in temperature caused by this replenishment process.

2.2.2 Electrochemical techniques

A variety of electrochemical techniques were used in this thesis and their basic principles are described below. All measurement described in this thesis were found to be reproducible as demonstrated by repeated experiments.

2.2.2.1 Corrosion potential (E_{CORR}) measurements

One of the simplest electrochemical parameters to measure is the potential of a freely corroding sample with respect to a RE, known as the corrosion potential (E_{CORR}). As discussed in Chapter 1, E_{CORR} is the unique potential at which the anodic and cathodic reaction rates are equal in terms of electron count. Consequently, the value of E_{CORR} is dictated by the kinetics of the two half-reactions and must not be confused with an equilibrium potential [1, 2]. While dictated by kinetics, E_{CORR} does not provide quantifiable kinetic information. Instead, E_{CORR} indicates the relative activity and stability of the corroding sample. Mechanistic information is obtained by rationalizing increases or decreases in E_{CORR} as due to changes in the kinetics of the anodic/cathodic reactions. For example, during exposure to non-aggressive environments, Ni-Cr-Mo alloys typically exhibit increases in E_{CORR} with time. This is attributed to passive film growth and a decreased rate of metal dissolution.

2.2.2.2 Linear polarization resistance (LPR) measurements

Linear polarization resistance (LPR) measurements, often coupled to E_{CORR} measurements, provide *in situ* rate information on the corroding system [1]. The sum of the two exponential I-E relationships described by the Wagner-Traud (W-T) equation (Equation 1.22) can be linearized within a small potential perturbation, typically ± 10 mV vs E_{CORR}, Figure 2.3 [3, 4]. The slope of this linear region yields a resistance value, Equation 2.1, referred to as a polarization resistance (R_P).

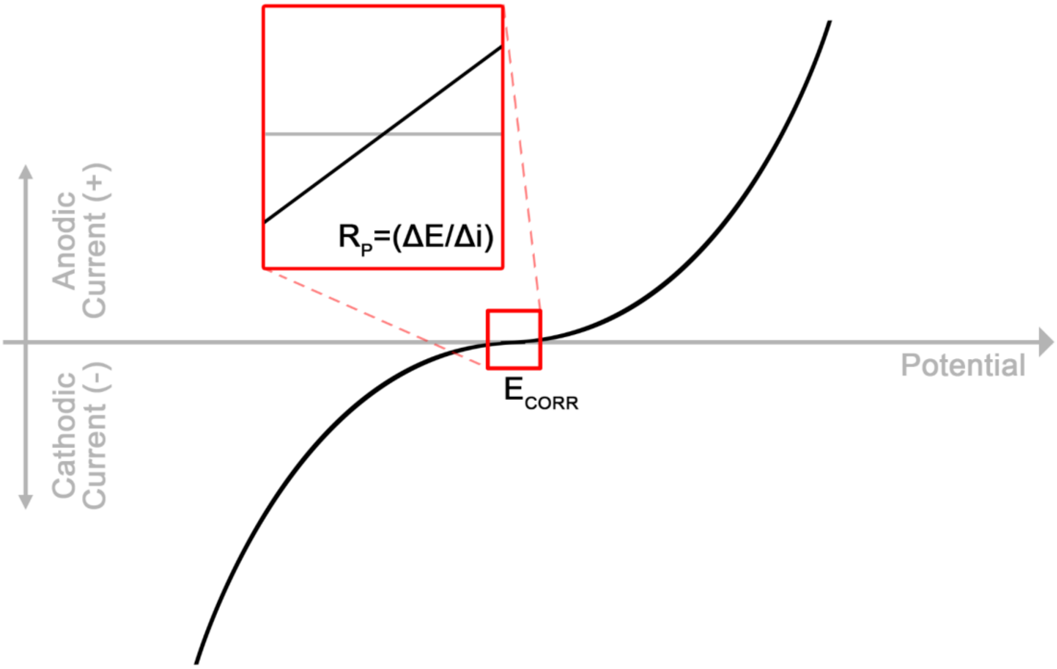

Figure 2.3 - Graphical representation of the generalized i-E relationship for a reaction described by W-T (B-V) kinetics. Indicated in the red inset is the linear region considered in linear polarization resistance measurements.

$$R_P = \left(\frac{\Delta E}{\Delta i}\right)_{\eta \to 0} \tag{2.1}$$

Stern and Geary [3] introduced a method of using Tafel slopes (β) to convert values of R_P to values of i_{CORR}. The authors derived a relationship between R_P, i_{CORR}, and the Tafel slopes (β) of the anodic and cathodic reactions, Equation 2.2.

$$R_P = \frac{\beta_A \beta_C}{2.3(\beta_A + \beta_C)} \left(\frac{1}{i_{CORR}} \right) \tag{2.2}$$

$$R_P \propto {i_{CORR}}^{-1} \tag{2.3}$$

However, this calculation can be used only if β_A and β_C are known. In the case of passive alloys, values of β_A cannot be experimentally obtained. Instead, the proportionality between R_P and i_{CORR}, Equation 2.3, can be used to quantify changes in the corrosion rate over time. Since only small overpotentials are used, R_P measurements are considered non-destructive, allowing measurements to be made as a function of time [1]. To avoid deviations from linear behaviour, scan rates are generally maintained at approximately 10 mV min^{-1}, as described in ASTM G59 and G61 [5, 6].

2.2.2.3 Potentiodynamic polarization measurements

In potentiodynamic polarization (PDP) measurements, an applied potential is scanned linearly while the current response is recorded. As opposed to LPR measurements, PDP measurements investigate a large range of applied potential, commonly extending beyond 1 V. As a result, these tests are considered destructive. The data are plotted as log(i) vs E and referred to as a polarization curve. Polarization curves provide information on the behaviour of a given system as a function of potential and can identify regions of active, passive, and transpassive behaviour. Additional information regarding film breakdown behaviour can be obtained using cyclic measurements. This is especially useful for studying features of localized corrosion.

2.2.2.4 Potentiostatic polarization measurements

In potentiostatic polarization (PSP) measurements, a constant applied potential is maintained while the current response is recorded as a function of time. Selecting an applied potential greater or less than E_{CORR} allows the anodic or cathodic reactions to be investigated, respectively. For a passive system, selecting an applied potential within the passive region allows the study of the film growth process. Generally, when an active-passive material is held at a potential within the passive region, current densities decrease as a function time due to the growth of, and elimination of defects in, the surface oxide. Moreover, the stability of the protective film is analyzed by considering any momentary increase in current density.

A similar measurement, referred to as galvanostatic polarization, uses a constant applied current while recording the potential response as a function of time, as further discussed in Section 2.4.

2.2.2.5 Electrochemical impedance spectroscopy (EIS)

Electrochemical impedance spectroscopy (EIS) is a technique used to determine interfacial and material parameters (*e.g.*, capacitance, resistance, charge mobility, film thickness, etc.) [1, 7]. Like other spectroscopies, a method of excitation is applied to the system under study, and the response caused by this excitation is measured as a function of frequency. In EIS, the excitation source is a small-amplitude potential perturbation in the form of a sine wave. The response of the system is the current which is also in the form of a sine wave, but with a different amplitude and possibility a phase shift (θ) compared to the input signal. A schematic of the excitation (input) and response (output) is shown in Figure 2.4.

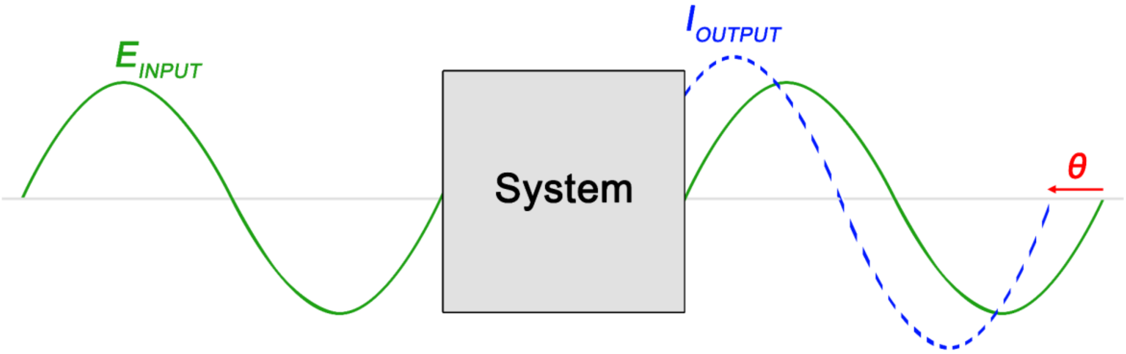

Figure 2.4 - Schematic showing the sinusoidal input potential (E_{INPUT}) and the corresponding output current (I_{OUTPUT}) signal in electrochemical impedance spectroscopy. While the frequency remains unchanged both the amplitude and phase of I_{OUTPUT} can differ from those of E_{INPUT}.

The input potential is expressed as a function of time, Equation 2.4, where ω is the angular frequency of the sine wave and |ΔE| is the amplitude of the potential [1, 7].

$$\mathrm{E}(t) = |\Delta \mathrm{E}| \sin(\omega \mathrm{t}) \tag{2.4}$$

The output current can also be expressed as a function of time, Equation 2.5, where $|\Delta \mathrm{I}|$ is the amplitude of the current response, and θ is the phase shift with reference to the input signal [1, 7].

$$\mathrm{I}(t) = |\Delta \mathrm{I}| \sin(\omega \mathrm{t} + \theta) \tag{2.5}$$

The impedance (Z) is the transfer function which relates the input potential to the current response. The Z, *i.e.*, the restriction of current flow under conditions of changing (AC) potential, is analogous to Ohm's law, which describes the restriction of current for a constant (DC) potential. The value of $\mathrm{Z}(\omega)$ can be expressed according to Equation 2.6:

$$\mathrm{Z}(\omega) = \frac{\mathrm{E}(\mathrm{t})}{\mathrm{I}(\mathrm{t})} = \frac{|\Delta \mathrm{E}| \sin(\omega \mathrm{t})}{|\Delta \mathrm{I}| \sin(\omega \mathrm{t} + \theta)} \tag{2.6}$$

Values of $\mathrm{Z}(\omega)$ can also be expressed as a complex-valued vector comprised of both in-phase (Z') and out-of-phase (Z'') components, Equation 2.7. An example of an impedance vector plotted on the Cartesian coordinate system is shown in Figure 2.5 [1].

$$\mathrm{Z}(\omega) = \mathrm{Z}'(\omega) + \mathrm{j}\, \mathrm{Z}''(\omega) \tag{2.7}$$

The magnitude of the impedance (|Z|) is given by:

$$|Z| = \sqrt{(Z')^2 + (Z'')^2} \tag{2.8}$$

And the phase angle (θ) by:

$$\theta = \tan^{-1}\left(\frac{\mathrm{Z}''}{\mathrm{Z}'}\right) \tag{2.9}$$

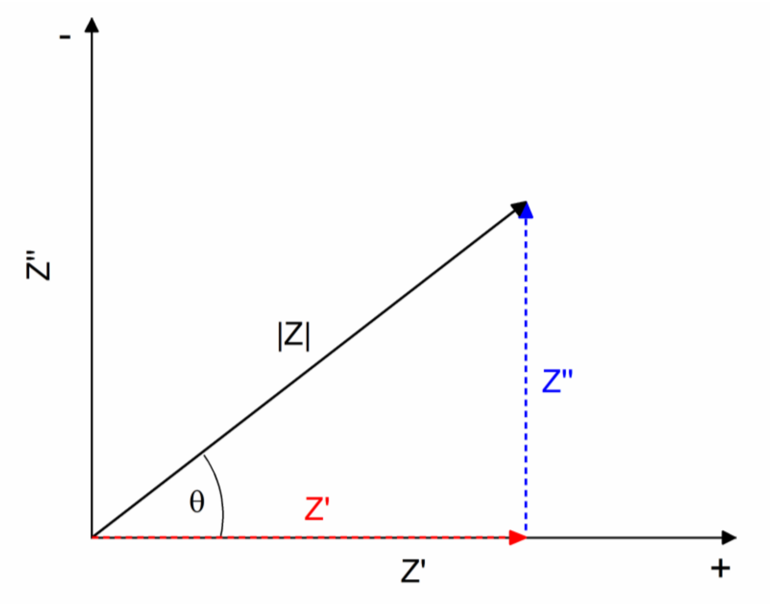

Figure 2.5 - An impedance vector with the real (Z') and imaginary components (Z'') shown. The magnitude of the impedance (|Z|) and the relationship to the phase shift (θ) are indicated.

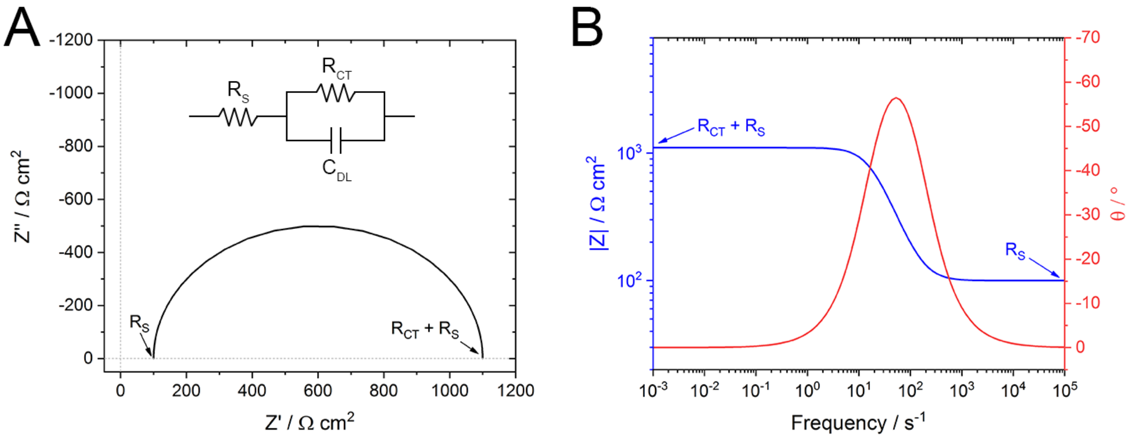

Figure 2.6 - Simulated impedance response of an equivalent circuit consisting of three circuit elements, shown as inset in panel (A). Values used for the circuit elements are as follows: R_S = 100 Ω cm^2, R_{CT} = 1000 Ω cm^2, and C_{DL} = 1 x 10^{-5} F cm^2. The response is represented in both (A) Nyquist and (B) Bode formats.

Spectra are collected by investigating the response of a system at discrete input frequencies, typically between 10^{-3} and 10^{5} s^{-1}. The resulting data are commonly represented in either a Nyquist (Z' vs Z'') or a Bode (log|Z| and θ vs log(frequency)) format. For a simulated impedance response, discussed in more detail below, the Nyquist and Bode plots are shown in Figure 2.6(A) and (B), respectively.

Equivalent electrical circuits are used to extract quantitative information from the frequency-dependent impedance response of a system [1, 7]. This is done by constructing an equivalent circuit with frequency-dependent impedance behaviour similar to that recorded as the experimental data. For a simple electrode interface, three circuit elements are required: (1) two resistors, one for solution resistance (R_S) and the other for charge transfer resistance (R_{CT}) at the interface, and (2) a capacitor for the double layer capacitance (C_{DL}) at the interface. The elements are arranged such that the parallel interfacial processes (R_{CT} and C_{DL}) are in series with the R_S. This circuit is shown in the inset of Figure 2.6(A).

The transfer functions ($Z(\omega)$) for a resistor, capacitor, constant phase element, and inductor, are shown in Table 2.1, where R is a resistance, C is a capacitance, Y_o is the constant and p is the exponent for the constant phase element (CPE), and L is an inductance.

Table 2.1 - Transfer functions for common circuit elements [1,7].

Circuit Element	**Impedance**
Resistor (R)	$Z(\omega) = R$
Capacitor (C)	$Z(\omega) = \frac{1}{(j\ \omega\ C)}$
Constant Phase Element (CPE)	$Z(\omega) = \frac{1}{Y_o\ (j\ \omega)^p}$
Inductor (L)	$Z(\omega) = j\ \omega\ L$

The $Z(\omega)$ of an equivalent circuit can be described by the sum of the individual transfer functions, with elements in series adding ($Z_{total} = Z_1 + Z_2$), and elements in parallel adding as reciprocals ($1/Z_{total} = 1/Z_1 + 1/Z_2$) [1]. For the equivalent circuit representing a simple electrode interface, Figure 2.6(A) (inset), the $\mathrm{Z}(\omega)$ is given in Equation 2.10. As the ω approaches infinity, the resistance tends to R_S, and, as the ω approaches zero, $\mathrm{Z}(\omega)$ tends to the sum of R_S and R_{CT}. This allows the R_{CT} and R_S to be separated [1].

$$\mathrm{Z}(\omega) = \left(\mathrm{R_s} + \frac{\mathrm{R_{CT}}}{1 + \omega^2\,\mathrm{C_{DL}^2}\,\mathrm{R_{CT}^2}}\right) - \mathrm{j}\left(\frac{\omega\,\mathrm{C_{DL}^2}\,\mathrm{R_{CT}^2}}{1 + \omega^2\,\mathrm{C_{DL}^2}\,\mathrm{R_{CT}^2}}\right) \tag{2.10}$$

In practice, replicating the frequency-dependent impedance response of a system can require the use of additional circuit elements in more complex electrical equivalent circuits than the simple electrode interface described above. While including additional circuit elements, *i.e.*, additional variables, can be expected to improve the quality of a fit, discretion should be used to consider only elements that match experimental observations and describe real physical processes. Some examples of behaviour which may impact the equivalent circuit include the presence of a passive film, the diffusion of species, or electrochemical reactions involving adsorbed intermediates.

For a passive film, an additional resistor and capacitor (parallel) are needed, in series with the solution and interfacial processes. These additional elements describe the resistance and capacitance of the oxide film. However, the response of experimental interfaces may not be properly described using only resistors and capacitors, and instead require the use of other circuit elements. In particular, the use of ideal capacitors cannot represent the local variations in properties across an electrode surface which results in a lateral distribution of time-constants. In an equivalent circuit, non-ideal capacitance is accounted for using a constant phase element (CPE) in place of an ideal capacitor [1, 7]. The $\mathrm{Z}(\omega)$ of a CPE is given in Table 2.1, where the exponent p varies between 0 and 1. When exponent $\mathrm{p} = 1$, the CPE behaves like an ideal capacitor: however, when $\mathrm{p} = 0$, the CPE behaves like an ideal resistor. Methods have been proposed to convert values of $\mathrm{Y_o}$ into a capacitance [8] and are generally considered appropriate to use when $\mathrm{p} > 0.85$. In the situation where the electrochemical current is partially controlled by diffusion processes, a Warburg circuit element may be used. This is a special case of the CPE in which $\mathrm{p} = 0.5$. Experimentally, this results in a low-frequency phenomenon in which a 45° phase angle is observed in the Nyquist plot.

An additional circuit element, the inductor (L), is often required in situations where dissolution proceeds via an adsorbed intermediate. Inductive behaviour represents the special case where the rate of formation and consumption of the adsorbed intermediate are dependent on one another [9, 10]. In other words, the overall rates of formation/consumption reactions are dependent on the concentration of the adsorbate (or surface coverage), in addition to the rate constant being dependent on the applied potential. As a result, the relaxation of an adsorbed intermediate causes the measured current to lead the applied potential perturbation. This behaviour causes positive values of Z" and θ in the Nyquist and Bode plots, respectively. Unfortunately, the concept of a true electrical inductor, which implies the storage of energy in the form of a magnetic field, cannot be related to a physical process in an electrochemical system. As a result, the significance of the inductor circuit element remains an area of ongoing discussion [9, 11].

2.3 Atomic emission spectroelectrochemistry (AESEC)

Electrochemical measurements are sensitive and unparalleled in their ability to measure reaction kinetics. However, when used alone they are limited in their ability to elucidate the chemical details of complex redox processes. The combined dissolution and oxide film formation processes occurring on compositionally complex alloys represent one such situation, where several redox reactions occur at the same time. Furthermore, the dissolution processes are often accompanied by selective dissolution and surface enrichment processes, which together govern dealloying and film formation. To elucidate such mechanisms, *ex situ* surface analyses have been employed to identify changes at the alloy surface which can then be related to the electrochemical measurements. While such experiments have led to significant scientific contributions, they cannot measure changes accurately as a function of time and in some cases, suffer from the possibility of modifications resulting from exposure to air after the experiment.

Coupling electrochemical techniques with spectroscopic methods, referred to as spectroelectrochemistry, allows complex redox chemistry to be investigated *in situ* (or *operando*). While many spectroelectrochemistry techniques exist, the use of an electrochemical flow cell coupled to inductively coupled plasma atomic emission spectroscopy (ICP-AES) is a particularly attractive technique in corrosion research. The technique, referred to as ‘atomic emission spectroelectrochemistry’ (AESEC), was initially employed for the study of 304 stainless steel [12]. Since its introduction, AESEC has been successfully employed in several studies [13-15]. A variation of the AESEC technique has also been used in which an inductively coupled plasma mass spectrometer (ICP-MS) is used in place of the ICP-AES instrument [16]. While the use of a mass spectrometery has benefits over ICP-AES, *i.e.*, cost of operation, isotopic information, multi-element analysis (etc.), difficulties can arise in concentrated saline solutions [17].

2.3.1 Principles

Information related to electrochemical measurements has been omitted from this section, since it has been discussed above. Instead, a brief introduction to the ICP-AES technique is given. The principle of atomic emission spectroscopy, sometimes referred to as optical emission spectroscopy, involves the detection of narrow bands of light, ~0.001 nm, emitted during the relaxation of excited atoms [18]. When exposed to a source of energy, in this case high temperature, collisions result in excitation or ionization of individual atoms. These excited atoms quickly return to their more stable ground states by releasing photons. Since elements contain a unique set of discrete energy levels, elements can be easily identified based on their emission spectrum. Quantification can be achieved by comparing the emission intensity measured for the analyte to the emission intensities measured for a series of calibration standards. Limits of detection are typically on the order of ppb ($\mu g\ L^{-1}$) for most modern spectrometers [19, 20].

Detection limits benefit from the use of an ICP torch, the current industry standard for emission spectroscopy. Both the high temperatures and the stability afforded by the ICP lead to several advantages over other excitation methods, *e.g.*, flame or furnaces. Briefly, the plasma provides enough energy to atomize, excite, and even ionize refractory complexes (*e.g.*, carbides and oxides), leading to increased sensitivity. This is directly related to the Boltzmann distribution, Equation 2.11, where N^*/N_0 is the relative population of the different states, g^* and g_0 is the degeneracy of excited and ground states, k is the Boltzmann constant (1.381×10^{-23} J K^{-1}), ΔE is the energy separation of the two states, and T is temperature (K) [18]. As temperature increases, the proportion of atoms in the excited state also increases, and therefore the subsequent photo-relaxation process is more intense. While there are many advantages to the use of an ICP torch, the extremely high flow rates of Ar-gas (5-20 L min^{-1}) make their operation relatively expensive.

$$\frac{N^*}{N_0} = \frac{g^*}{g_0} e^{-\Delta E/kT} \qquad (2.11)$$

2.3.2 Instrumentation

The AESEC setup may be separated into three components; the electrochemical flow cell, the ICP-AES instrument, and the data acquisition interface. A schematic of the first two components is shown in Figure 2.7. In addition to the summary included here, a detailed discussion of the AESEC setup can be found in previous publications [12, 21]. The first component of the AESEC instrument is the custom-built electrochemical flow cell, shown on the left side of Figure 2.7. This cell consists of two compartments, separated by an ionically conductive membrane. In the first compartment, the WE is installed by the application of pressure against an O-ring. The electrolyte is then introduced through the bottom of the flow cell, passing the surface of the WE, and exiting through the top of the cell toward the ICP-AES, the second component of the instrument. The flow of electrolyte is maintained using calibrated peristaltic pumps. The temperature is controlled by heating both the electrolyte and the WE directly. Incoming electrolyte is drawn directly from a reservoir housed within an isothermal bath. Additionally, a hollowed brass disk, connected to an isothermal water circulator, is held in contact behind the WE. The second compartment of the electrochemical cell houses the RE and CE, a saturated Ag/AgCl (0.197 V vs SHE) and a Pt electrode, respectively.

Downstream of the electrochemical flow cell is the ICP-AES, the second component of the AESEC instrument, shown on the right side of Figure 2.7. Electrolyte exiting the flow cell is introduced into the ICP using a nebulizer. The high temperatures afforded by the Ar-plasma, typically 6,000-10,000 K, result in a high efficiency for atomization and ionization of all species exiting the flow cell. The ICP-AES instrument, an Ultima 2C spectrometer (Horiba Jobin-Yvon), is used for the detection of species released from the WE in

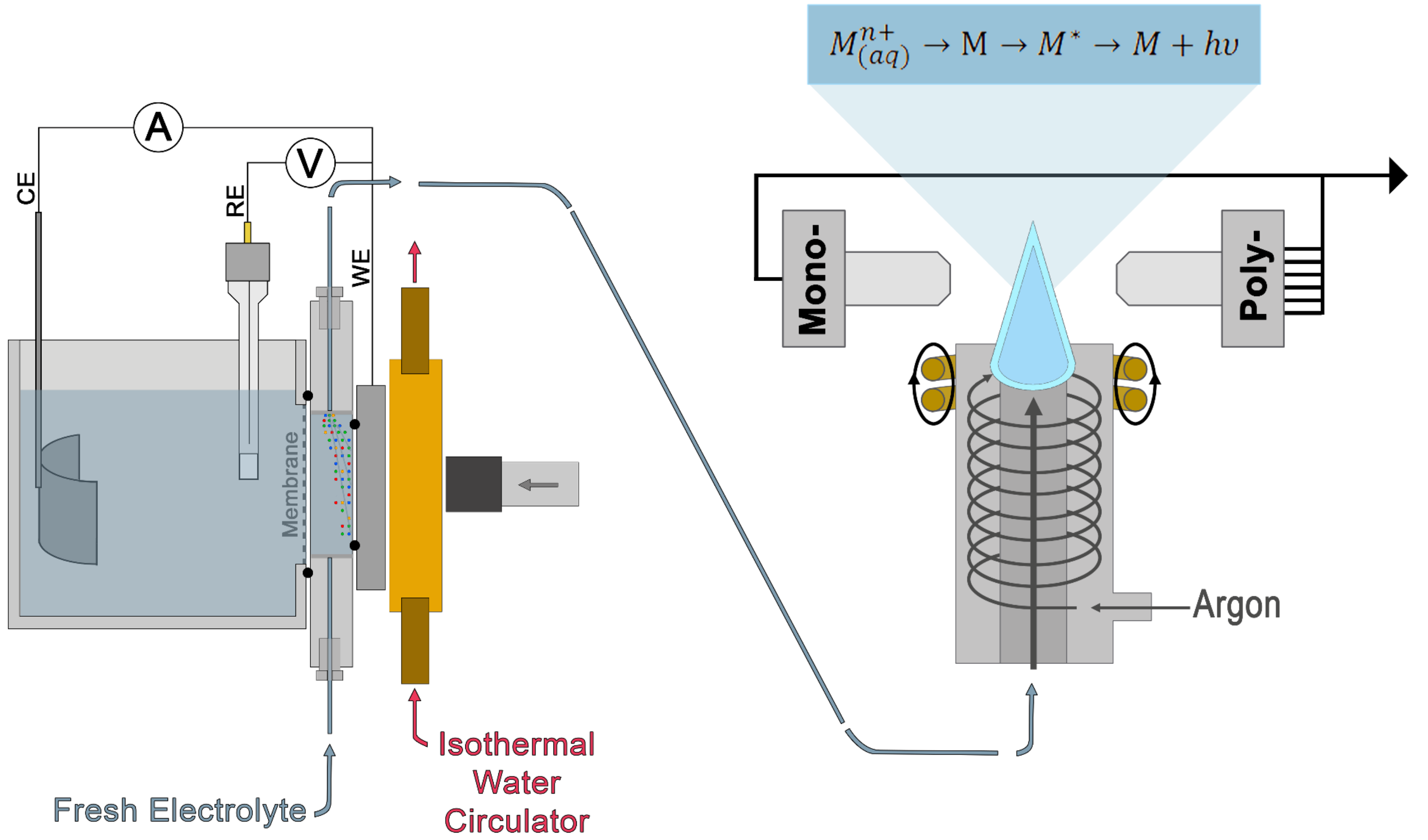

Figure 2.7 - Schematic of the AESEC setup, including the electrochemical flow cell (left) and the inductively coupled plasma atomic emission spectrometer (right).

real-time. Together, independent mono- and polychromators are used to measure multiple emission lines simultaneously. While the monochromator offers higher spectral resolution, the polychromator provides the ability to monitor multiple lines simultaneously.

The third and final component of the AESEC instrument is the data collection system and user interface, not shown. The software, Quantum™ (Horiba Jobin-Yvon), allows for simultaneous recording of up to 12 photomultiplier tubes. Integrated over one second, signals are sent directly to the software to be logged. In addition to the output signals from the spectrometer, the potentiostat, a Gamry Reference 600, is interfaced with the data collection software. The ability to record both spectroscopic information as well as the electrochemical potential/current data on the same time scale allows true simultaneous measurements.

2.3.3 Data treatment

Procedures used during the treatment of AESEC data have been reported previously [12, 21]. Following each experiment, detection limits ($\mathrm{C}_{3\sigma}$) were calculated for each emission line according to Equation 2.12, where σ_B is the standard deviation of the background signal and κ is the sensitivity factor determined from standard calibration procedure.

$$\mathrm{C}_{3\sigma} = 3\,\frac{\sigma_\mathrm{B}}{\kappa} \tag{2.12}$$

Instantaneous emission intensities for each line were converted into instantaneous concentrations (C_M) using a standard calibration procedure. Values of C_M were then converted into instantaneous dissolution rates (ν_M) according to Equation 2.13, where f is the flow rate of electrolyte and A is the exposed surface area of the WE:

$$\nu_\mathrm{M} = \mathrm{f}\,\frac{\mathrm{C}_\mathrm{M}}{\mathrm{A}} \tag{2.13}$$

Features of congruent/incongruent dissolution were distinguished by comparing the concentration of metal ion in the electrolyte to the composition of the bulk material, *i.e.*, using normalized dissolution rates (v'_{M}). Values of v'_{M} were calculated against the bulk alloying element, Ni, according to Equation 2.14,

$$v'_{\mathrm{M}} = \left({}^{X_{\mathrm{Ni}}}\!/_{X_{\mathrm{M}}}\right) v_{\mathrm{M}} \tag{2.14}$$

where X_{Ni} and X_{M} represent the mass fractions of Ni and metal M, respectively. Congruent dissolution occurs when $v'_{\mathrm{M}} = \nu_{\mathrm{Ni}}$, *i.e.*, the two constituents dissolve at rates relative to their bulk composition. When $v'_{\mathrm{M}} > \nu_{\mathrm{Ni}}$, a selective dissolution process occurs, in which metal M dissolves at a rate faster than expected from its bulk composition. In contrast, when $v'_{\mathrm{M}} < \nu_{\mathrm{Ni}}$, metal M is accumulating on the surface. Selective dissolution and/or accumulation of metal M can be quantified by mass balance, Θ_{M}, as shown in Equation 2.15:

$$\Theta_{\mathrm{M}} = \int_0^t \left(\left({}^{X_{\mathrm{M}}}\!/_{X_{\mathrm{Ni}}}\right) v_{\mathrm{Ni}} - v_{\mathrm{M}}\right) dt \tag{2.15}$$

Instantaneous dissolution rates (ν_{M}) were also converted to corresponding elemental currents (i_{M}) according to Faraday’s law, Equation 2.16:

$$i_{\mathrm{M}} = \frac{\upsilon_{\mathrm{M}}\, F\, n}{m} \tag{2.16}$$

where F is Faraday’s constant, m is the molar mass of metal M, and n is the number of electrons transferred in the oxidation reaction of metal M. The summation of all elemental currents (i_{Σ}) may then be compared to currents (i_e) recorded by the potentiostat during electrochemical measurements. Before the comparison of i_{Σ} and i_e can be made, a convolution process must be used to treat the electrical current. This procedure, detailed in previous publications [12], corrects for the residence time and diffusion processes in the AESEC setup.

2.4 Crevice corrosion experiments

2.4.1 Crevice assembly

The WE assembly used in crevice corrosion experiments is shown in Figure 2.8. From 3.18 mm (1/8”) thick plate stock, 15 mm wide strips were cut and formed into V-shaped WEs. A single crevice was formed between the flat portion of the V-shaped WE and the PTFE crevice former. The creviced region was tightened using threaded hardware machined from the same material as the WE. Udel® bushings were used to avoid unwanted electrical contact between the hardware and the WE. A Udel® block was used to provide a rigid structure on which pressure was applied to the crevice region. Crevice thickness was kept consistent between repeat experiments by using a PTFE spacer of the same thickness as the crevice former. Similar electrode assemblies have been used in previous experiments [22-27].

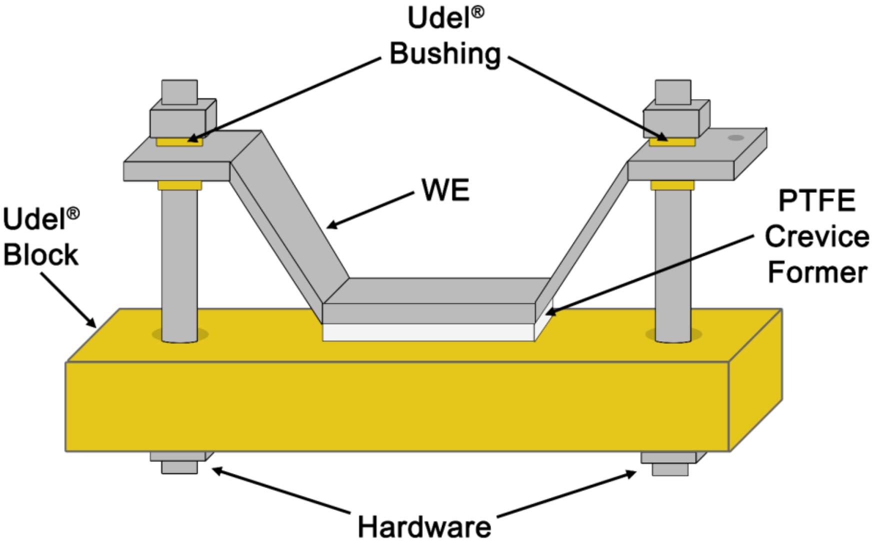

Figure 2.8 - Schematic of the V-shaped crevice electrode.

Before each experiment, the flat surface of the WE was ground using wet SiC papers, sonicated in a mixture of equal parts EtOH and DI water, rinsed with DI water, and dried under a stream of Ar-gas. Since mass loss calculations were important to crevice experiments, detailed below, the prepared WEs were stored in a vacuum desiccator for 24 h before each experiment, allowing for accurate initial weight measurements.

Immediately before the experimental setup, all miscellaneous pieces of the crevice assembly, including the Udel® bushings and block, the PTFE crevice former, and the hardware, were sonicated, rinsed, and dried using Ar-gas. Both the PTFE crevice former and the flat surface of the WE were immersed in the experimental solution before assembling the crevice electrode, ensuring the presence of electrolyte within the crevice.

2.4.2 Electrochemical cell

Crevice experiments were carried out in a Hastelloy pressure vessel (Parr Instrument Co., Model 4621) outfitted as an electrochemical cell, Figure 2.9. Electrical connections were made through four pressure-tight electrode inlets. All connections, as well as the vessel interior, were lined with PTFE to avoid unwanted electrical contacts. A three-electrode configuration was used in which the single crevice assembly, detailed above, served as the WE. The RE was a homemade Ag/AgCl (0.197 V vs SHE) electrode. The CE was constructed of the same material as the WE. During placement of the WE in the cell, solution levels were maintained only slightly above the creviced region, ensuring a single crevice and minimizing exposure of the WE external to the crevice. Once assembled, the vessel was pressurized (414 kPa) with ultra-high purity N_2-gas. The vessel was then placed within a heating mantle (Parr Instrument Co., Model 4913) and the temperature elevated to and maintained at 120 ± 2 °C. Once the temperature stabilized, the desired experiment was carried out.

After each experiment, the vessel was removed from the heating mantle and allowed to cool before being disassembled. Unless otherwise stated, corrosion products formed on the WE were removed. This was done through manual swabbing and sonication in a (1:1) mixture of EtOH and DI water. Once cleaned, the sample was then rinsed with DI water, dried in Ar-gas, and stored in a vacuum desiccator. After a minimum of 24 h, the corroded electrode was weighed to obtain an accurate weight loss.

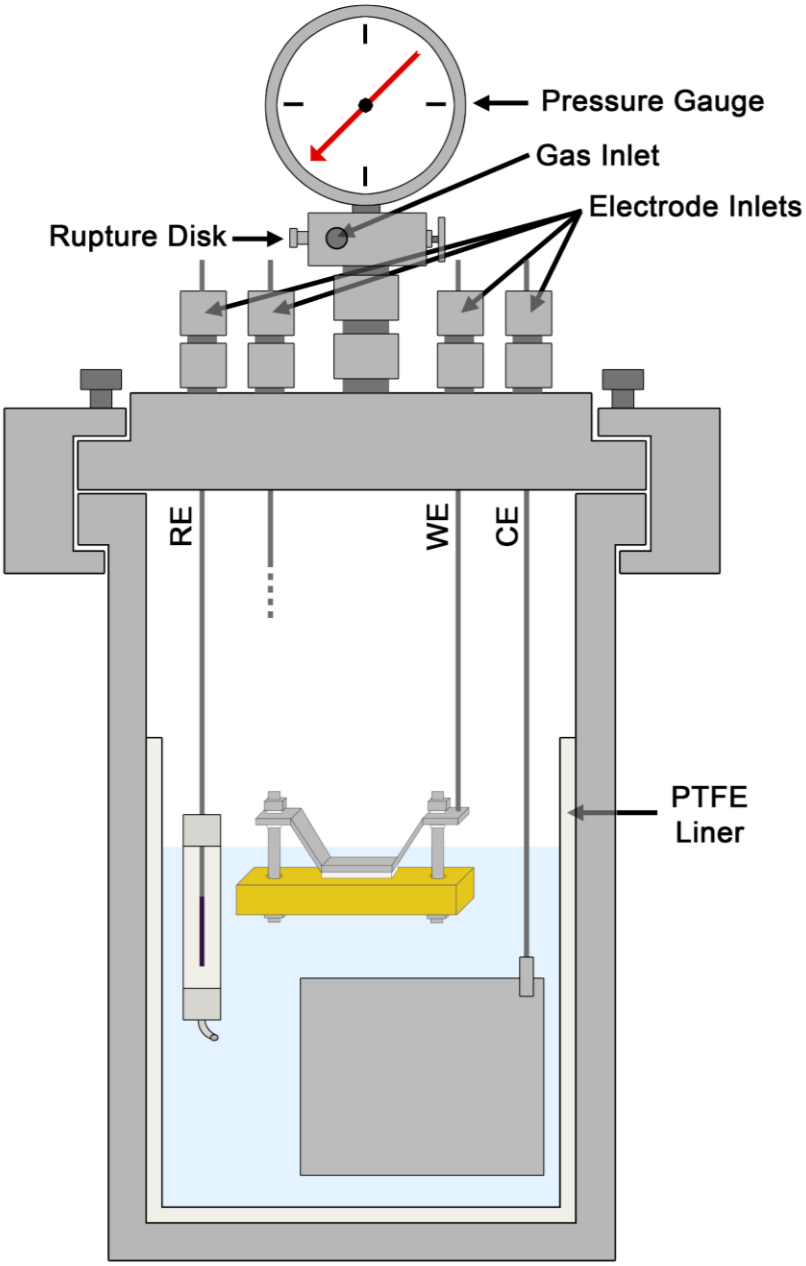

Figure 2.9 - Schematic of the Hastelloy pressure vessel outfitted as a three- electrode electrochemical cell.

2.4.3 Galvanostatic polarization

In galvanostatic polarization measurements, a constant current is applied between the WE and CE, while the change in potential between the WE and RE is monitored as a function of time. The galvanostatic approach provides control over both the corrosion rate and total applied charge ($\mathrm{Q_A}$), with $\mathrm{Q_A}$ being a direct measurement of the extent of damage. For crevice corrosion experiments, galvanostatic polarization measurements were used to guarantee initiation while avoiding the application of constant, high applied potentials. Additionally, galvanostatic polarization measurements provided control over $\mathrm{Q_A}$, which can then be compared to values of $\mathrm{Q_W}$, the equivalent charge determined from weight loss measurements. Values of $\mathrm{Q_W}$ were obtained by applying Faraday's law, Equation 2.17, where W is the weight loss, F is Faraday's constant, $\mathrm{n_{avg}}$ is the weighted average oxidation number of metal cations, and $\mathrm{m_{avg}}$ is the weighted average molar mass, calculated based on the alloy composition.

$$\mathrm{Q_W} = \mathrm{W\,F}\left(\frac{\mathrm{n_{avg}}}{\mathrm{m_{avg}}}\right) \tag{2.17}$$

2.5 Surface analytical techniques

2.5.1 Electron imaging and spectroscopy

The scanning electron microscope (SEM) uses a high energy electron beam, typically accelerated at voltages ≤ 30 keV, to 'illuminate' a sample surface. The electron beam is collimated and positioned using a series of complex electromagnetic lenses. Two-dimensional images are obtained by scanning the electron beam across the surface while monitoring the various signals produced through the interaction of incident (or primary) electrons with a sample. The interaction between primary electrons and a sample results in the emission of different signals, including backscattered electrons (BSE), secondary electrons (SE), Auger electrons, and characteristic X-rays [28, 29]. An illustration of the interaction volume of the primary electron beam, as well as the approximate depths of the measured signals within a sample surface, is shown in

Figure 2.10. While approximate dimensions are provided in Figure 2.10, the interaction volume varies widely with the acceleration voltage of the primary electron beam as well as with the sample itself [28]. The signals produced by the interaction of the primary electron beam with the sample, yield different yet complementary information.

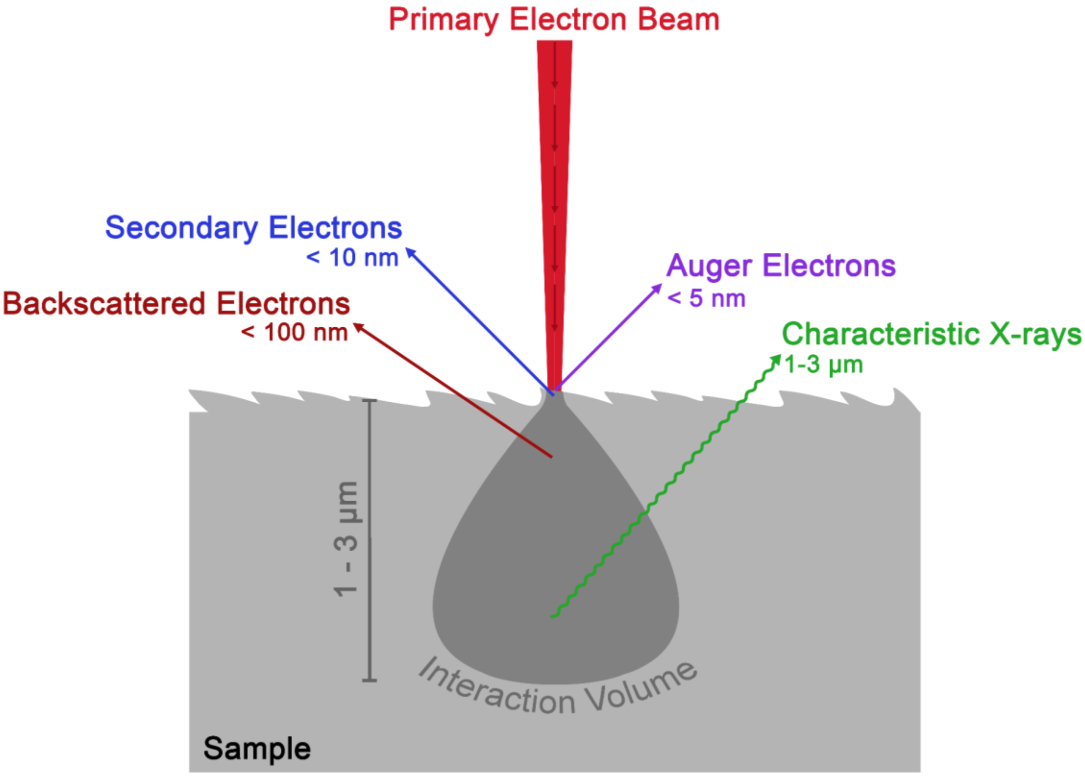

Figure 2.10 - A representation of the interaction volume produced from penetration of the primary electron beam into the sample. The signals produced by these interactions and their relative depths are shown.

2.5.1.1 Backscattered electrons (BSE)

Produced by the elastic scattering of primary electrons from within the sample, BSEs exit the sample with only slightly less kinetic energy than the incident primary beam. As a result of their relatively high kinetic energy, BSEs escape from deep within the interaction volume [30]. For this reason, the spatial resolution of the BSE signal is lower than other signals which are emitted from closer to the surface, *e.g.*, secondary electrons. While spatial resolution is not ideal, BSEs have the benefit of showing differences in elemental composition. Since the probability of a high-angle elastic scattering event increases with increasing atomic number, compositional information is obtained in the form of image contrast [30]. Increased counts (or bright pixels) are observed in areas rich in heavy elements compared to areas composed of lighter elements. Crystallographic information may also be obtained from BSE, as discussed below.

2.5.1.2 Secondary electrons (SE)

Atomically bound electrons from within the sample may be ejected in the event of an inelastic collision with the incoming primary electrons. An inelastic collision results in the transfer of energy to the bound electron, followed by its ejection as a SE. Typically, SEs are low in energy (≤ 50 eV) and can only escape from the outer portion of the interaction volume, shown in Figure 2.10. As a result, SEs are commonly used to image since they provide high spatial resolution as well as topographic information [29].

2.5.1.3 Energy-dispersive X-ray spectroscopy (EDS) and Auger electron spectroscopy

In the event a core-shell vacancy is created by the ejection of a SE, an outer shell electron will fall into the core vacancy to minimize energy. During this relaxation process, the difference in energy between electron shells is released as an X-ray photon. The relaxation process may also occur by the ejection of an outer shell electron, known as an Auger electron [29, 30]. Since the energy of the ejected photon or electron involves discrete energy levels, they can be used to determine the atom of origin, with the intensities giving concentration information. Since X-rays penetrate further than electrons [31], characteristics X-rays are detected from great depths in the interaction volume (Figure 2.10).

2.5.1.4 Electron backscatter diffraction (EBSD)

Electron backscatter diffraction (EBSD) is used to obtain crystallographic information on polycrystalline materials [32]. This includes information related to grain orientation, grain boundary properties, surface strain, and phase identification. Since the EBSD technique utilizes an electron microscope, outfitted with a specialized detector, the high spatial resolution afforded by the collimated primary electron beam is translated to EBSD data. A schematic showing the general experimental setup is shown in Figure 2.11. Interaction of primary electrons with atomic crystallographic planes causes the diffraction of the electrons. Enhanced electron intensity is observed for diffracted electrons which satisfy Bragg's law, Equation 2.18, where n_B is an integer, θ_B is the angle of incidence of the electron on the diffracting plane, and d is the spacing of the diffracting plane. The resulting band of enhanced electron intensity, known as a Kikuchi band, is captured by a phosphor screen detector. Patterns collected by the phosphor screen are generally composed of many Kikuchi bands, each corresponding to the diffraction of different crystallographic planes. Complex indexing software is then used to determine the orientation of the diffracting crystal.

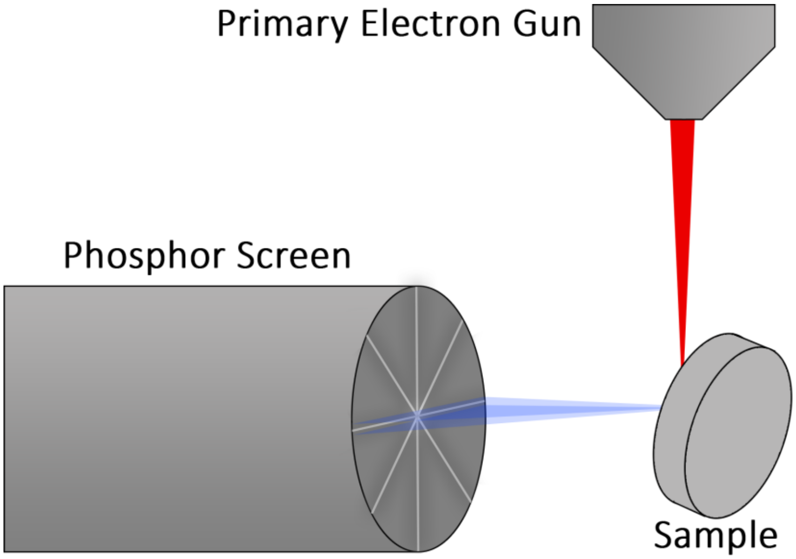

Figure 2.11 - Schematic showing the production of Kikuchi bands due to the diffraction of a primary electron beam.

$$n_B\lambda = 2d\sin\theta_B \tag{2.18}$$

2.5.2 X-ray photoelectron spectroscopy

X-ray photoelectron spectroscopy (XPS) is commonly used to study the surface composition and electronic configuration of a sample [33, 34]. Compared to other surface sensitive techniques, XPS has the advantage of providing both the elemental composition as well as oxidation state information. The principle of XPS is based on the analysis of photoelectrons produced from a sample exposed to a monochromatic X-ray source, typically the Al Kα (1486.8 eV). This process, known as the photoelectric effect, is shown in Figure 2.12. The high surface sensitivity of XPS is a consequence of the relatively low kinetic energy (K.E.) of escaping photoelectrons, which permits their escape from only shallow depths, typically 5-10 nm below the surface [34].

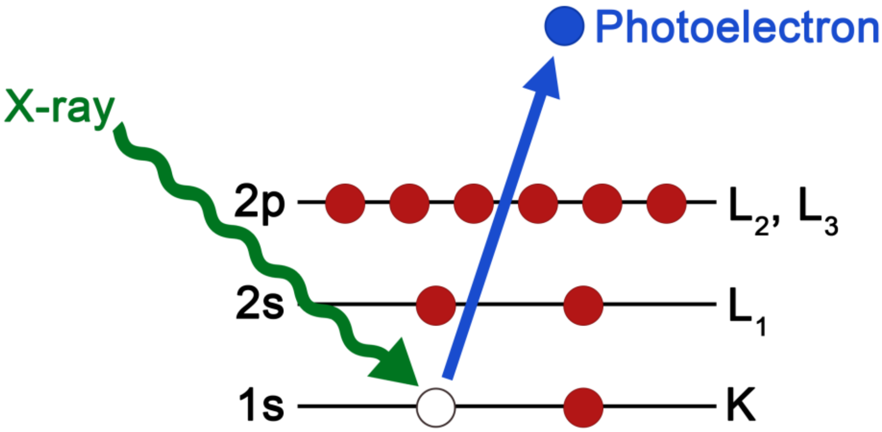

Figure 2.12 - Production of a photoelectron via the interaction of an incident X-ray with an originally atomically bound core shell electron. The K.E. of the ejected photoelectron is measured by the spectrometer.

When an X-ray photon penetrates the surface of a sample, it can interact with an atomically bound electron in the sample. If the photon energy (hν) is high enough to overcome the forces holding the electron to the nucleus, known as the binding energy (B.E.), the electron will be ejected from the atom. This ejected electron exits with a kinetic energy (K.E.) characteristic of the atom from which it came as well as the oxidation state of the atom. Since the energy of the incident X-ray is known (hν) and the K.E. of the escaping photoelectron is measured by the spectrometer, the B.E. can be determined using the relationship

$$\mathrm{B.E.} = \mathrm{hv} - \mathrm{K.E.} - \varphi_{\mathrm{spec}} \tag{2.19}$$

where φ_{spec} is the work function of the spectrometer, which describes the energy lost by the photoelectron as it is detected by the spectrometer, typically on the order of a few eV [33].

A typical XPS spectrum is represented as the photoelectron intensity (or count) plotted as a function of the photoelectron B.E. (or K.E.). While the photoelectron B.E. provides information on the atom of origin, signal intensities are related to the atomic concentrations within the area analyzed. Two types of spectra are commonly obtained; survey and high-resolution spectra. In survey spectra, a large energy window is scanned, allowing the identification and quantification of elements present in the surface layer. While survey spectra generally require only a few minutes of acquisition time, they do not provide the energy resolution to resolve chemical state information. By utilizing a decreased pass energy, high-resolution spectra provide the energy resolution required to separate chemical state information. High-resolution spectra have the disadvantage of drastically increased acquisition times. As a result, these spectra are collected only for narrow energy windows that encompass the photoelectron signal of interest (*e.g.*, the energy range corresponding to photoelectrons emitted from certain atomic orbitals: C 1s, O 1s, Ni 2p, Cr 2p, Mo 3d, etc.).

Quantification and deconvolution of experimental spectra was done using CasaXPS software (v.2.3.19). All spectra were charge-corrected according to the aliphatic (C-C) signal observed in the high-resolution C 1s spectrum (284.8 eV). During all quantifications, a Shirley background subtraction was used. Aware of the growing issue of incorrectly interpreted XPS data in the literature [35], only fitting parameters obtained for high-quality standard samples were considered in the deconvolution of high-resolution spectra. An approach was adopted in which the spectral envelopes produced by high-quality standard spectra were replicated using a series of constrained peak shapes.

2.6 References

[1] R.G. Kelly, J.R. Scully, D. Shoesmith, R.G. Buchheit, Electrochemical techniques in corrosion science and engineering, CRC Press, 2002.

[2] A. Groysman, Corrosion for everybody, Springer Science & Business Media, 2009.

[3] M. Stern, A.L. Geary, Electrochemical polarization I. A theoretical analysis of the shape of polarization curves, *Journal of The Electrochemical Society*, 104 (1957) 56-63.

[4] M. Stern, R.M. Roth, Anodic behavior of iron in acid solutions, *Journal of The Electrochemical Society*, 104 (1957) 390.

[5] ASTM(G59-97), Standard test method for conducting potentiodynamic polarization resistance measurements, in: American Society for Testing and Materials, 2014.

[6] ASTM(G61-68), Standard test method for conducting cyclic potentiodynamic polarization measurements for localized corrosion susceptibility of iron-, nickel-, or cobalt-based alloys, in: American Society for Testing and Materials, 2018.

[7] M.E. Orazem, B. Tribollet, Electrochemical impedance spectroscopy, 2nd ed., Wiley, 2017.

[8] G.J. Brug, A.L.G. van den Eeden, M. Sluyters-Rehbach, J.H. Sluyters, The analysis of electrode impedances complicated by the presence of a constant phase element, *Journal of Electroanalytical Chemistry and Interfacial Electrochemistry*, 176 (1984) 275-295.

[9] D.A. Harrington, P. van den Driessche, Mechanism and equivalent circuits in electrochemical impedance spectroscopy, *Electrochimica Acta*, 56 (2011) 8005-8013.

[10] P. Córdoba-Torres, M. Keddam, R.P. Nogueira, On the intrinsic electrochemical nature of the inductance in EIS, *Electrochimica Acta*, 54 (2008) 518-523.

[11] D. Klotz, Negative capacitance or inductive loop? – A general assessment of a common low frequency impedance feature, *Electrochemistry Communications*, 98 (2019) 58-62.

[12] K. Ogle, S. Weber, Anodic dissolution of 304 stainless steel using atomic emission spectroelectrochemistry, *Journal of The Electrochemical Society*, 147 (2000) 1770.

[13] J. Han, K. Ogle, Dealloying of $MgZn_2$ intermetallic in slightly alkaline chloride electrolyte and its significance in corrosion resistance, *Journal of The Electrochemical Society*, 164 (2017) C952-C961.

[14] X. Li, K. Ogle, The passivation of Ni-Cr-Mo alloys: time resolved enrichment and dissolution of Cr and Mo during passive-active cycles, *Journal of The Electrochemical Society*, 166 (2019) C3179-C3185.

[15] X. Li, P. Zhou, K. Ogle, S. Proch, M. Paliwal, A. Jansson, J. Westlinder, Transient stainless-steel dissolution and its consequences on ex situ bipolar plate testing procedures, *International Journal of Hydrogen Energy*, 45 (2020) 984-995.

[16] K. Lutton, K. Gusieva, N. Ott, N. Birbilis, J.R. Scully, Understanding multi-element alloy passivation in acidic solutions using operando methods, *Electrochemistry Communications*, 80 (2017) 44-47.

[17] A.A. Ammann, Inductively coupled plasma mass spectrometry (ICP MS): a versatile tool, *Journal of Mass Spectrometry*, 42 (2007) 419-427.

[18] D.C. Harris, Quantitative chemical analysis, 8th ed., W. H. Freeman and Company, New York, 2010.

[19] D.A. Skoog, F.J. Holler, S.R. Crouch, Principles of instrumental analysis, 6th ed. ed., Thomson Brooks/Cole, 2007.

[20] C.B. Boss, K.J. Fredeen, Concepts, Instrumentation and techniques in inductively coupled plasma optical emission spectrometry, 3rd ed., PerkinElmer, 2004.

[21] K. Ogle, Atomic Emission Spectroelectrochemistry: Real-time rate measurements of dissolution, corrosion, and passivation, *Corrosion*, 75 (2019) 1398-1419.

[22] N. Ebrahimi, P. Jakupi, J.J. Noël, D.W. Shoesmith, The role of alloying elements on the crevice corrosion behavior of Ni-Cr-Mo alloys, *Corrosion*, 71 (2015) 1441-1451.

[23] P. Jakupi, J.J. Noël, D.W. Shoesmith, Crevice corrosion initiation and propagation on alloy-22 under galvanically-coupled and galvanostatic conditions, *Corrosion Science*, 53 (2011) 3122-3130.

[24] P. Jakupi, J.J. Noël, D.W. Shoesmith, The evolution of crevice corrosion damage on the Ni–Cr–Mo–W alloy-22 determined by confocal laser scanning microscopy, *Corrosion Science*, 54 (2012) 260-269.

[25] P. Jakupi, D. Zagidulin, J.J. Noël, D.W. Shoesmith, Crevice corrosion of Ni-Cr-Mo alloys, *ECS Transactions*, 3 (2007) 259-271.

[26] N. Ebrahimi, J.J. Noël, M.A. Rodriguez, D.W. Shoesmith, The self-sustaining propagation of crevice corrosion on the hybrid BC1 Ni–Cr–Mo alloy in hot saline solutions, *Corrosion Science*, 105 (2016) 58-67.

[27] A.K. Mishra, D.W. Shoesmith, Effect of alloying elements on crevice corrosion inhibition of nickel-chromium-molybdenum-tungsten alloys under aggressive conditions: an electrochemical study, *Corrosion Science*, 70 (2014) 721-730.

[28] W. Zhou, Z.L. Wang, Scanning microscopy for nanotechnology: techniques and applications, Springer science & business media, 2007.

[29] K.D. Vernon-Parry, Scanning electron microscopy: an introduction, *III-Vs Review*, 13 (2000) 40-44.

[30] R.F. Egerton, Physical principles of electron microscopy, Springer, 2005.

[31] D.P. Woodruff, Modern techniques of surface science, Cambridge university press, 2016.

[32] A.J. Schwartz, M. Kumar, B.L. Adams, D.P. Field, Electron backscatter diffraction in materials science, Springer, 2009.

[33] J.F. Moulder, W.F. Stickle, P.E. Sobol, K.D. Bomben, Handbook of X-ray photoelectron spectroscopy, Perkin-Elmer Corporation, Eden Prairie, Minnesota, United States of America, 1992.

[34] P. Van der Heide, X-ray photoelectron spectroscopy: an introduction to principles and practices, John Wiley & Sons, 2011.

[35] M.R. Linford, V.S. Smentkowski, J.T. Grant, C.R. Brundle, P.M.A. Sherwood, M.C. Biesinger, J. Terry, K. Artyushkova, A. Herrera-Gomez, S. Tougaard, W. Skinner, J.J. Pireaux, C.F. McConville, C.D. Easton, T.R. Gengenbach, G.H. Major, P. Dietrich, A. Thissen, M. Engelhard, C.J. Powell, K.J. Gaskell, D.R. Baer, Proliferation of faulty materials data analysis in the literature, *Microscopy and Microanalysis*, 26 (2020) 1-2.

Chapter 3

3 Investigating the influence of Cr and Mo additions to commercial Ni-based alloys exposed to neutral and acidic chloride solutions

(Henderson (*et al.*), *J. Electrochem. Soc.*, **2020**, 167 (13), 131512.)

Abstract:

The corrosion behaviour of four commercially available Ni-based alloys is presented for both natural and potential-controlled corrosion in chloride solutions. Electrochemical evidence suggests a balance of Cr and Mo is essential to maintaining passive film stability in chloride solutions, especially those in which acidic conditions may develop. In near-neutral solutions, increased Cr content results in lower corrosion rates and improved passive properties; however, an increase in Cr content above 15 wt.% provided only minor additional benefits. In acidic solutions, Mo content is essential to corrosion resistance and imparts two major benefits: increased film stability and rapid repassivation of breakdown events. Since localized corrosion and the critical chemistry which accompanies these processes are of concern in many chloride-containing applications, a delicate balance of Cr and Mo must be considered; although optimal concentrations have yet to be determined.

3.1 Introduction

Corrosion-resistant alloys, such as those based on a Ni-matrix, rely on additions of Cr and Mo, among other alloying elements (*e.g.*, W, Cu, etc.), to promote the formation of an oxide film. Serving as a physical barrier, the oxide functions by slowing the dissolution of the underlying reactive substrate [1]. With applications of these alloys in the nuclear, aerospace, chemical, and petrochemical processing industries, a thorough understanding of the passive film, in relation to alloy composition, is essential for both proper material selection and accurate lifetime assessments. In neutral solutions (pH ~7), oxides formed on

Cr-containing alloys have been shown to be dominated by a Cr(III)-rich barrier layer and as a result, exhibit excellent corrosion resistance [2, 3]. However, in acidic environments, the increased solubility of Cr(III) species can lead to the destruction of this passive layer [4, 5]. Additions of Mo have been shown to increase the resistance to corrosion in acidic solutions. Empirical relationships such as the pitting resistance equivalent number (PREN) [6] and the atomic percent factor (APF) [7, 8] have been successfully used to describe the benefits Cr and Mo; but are limited in the mechanistic information they provide. While the relationship between alloyed Cr and Mo has been extensively studied [9-11], ongoing research [3, 12-16] continues to provide new information.

High chloride solutions are of principal interest, due to their industrial relevance and their importance in the mechanism of crevice corrosion [17]. Crevice corrosion has been regarded as a potentially dangerous process for Ni-Cr-Mo alloys, due to its difficult detection, unpredictability, and self-sustaining nature. While Ni-Cr-Mo alloys are considered immune to pitting in near-neutral chloride environments, the presence of an occluded geometry can lead to local acidification which may eventually challenge the integrity of the passive film. According to some studies, the pH inside an active crevice on Ni-Cr-Mo alloys can be as low as zero [10, 18]. Once activated, metal dissolution inside the crevice couples to O_2 reduction on surfaces outside the crevice, and with H^+ reduction inside the crevice [19]. Previously [20], we have shown that the contribution of H^+ reduction can almost double the extent of corrosion damage, but decreases as the Mo content of the alloy increases. Due to the potential severity of crevice corrosion, it is essential to understand the relationship between alloyed Cr and Mo and the corrosion reaction in conditions anticipated both inside and outside a crevice; *i.e.*, in acidic and near-neutral chloride solutions, respectively. Through an improved understanding, alloy compositions, as well as lifetime assessments, may be optimized.

The corrosion behaviour of four commercially available Ni-based alloys, Hastelloy BC-1, C-22, G-35, and G-30, has been investigated in 3 M NaCl and 1 M HCl + 2 M NaCl solutions at 75 °C. While acidity is of primary interest, the importance of cathodic reactions (O_2 and H^+ reduction) was also investigated by changing the O_2 concentration. Furthermore, both the open-circuit and polarization behaviours were investigated. Here, discussion is limited to electrochemical studies, including corrosion potential (E_{CORR}) monitoring, linear polarization resistance (LPR), electrochemical impedance spectroscopy (EIS), and both dynamic and static polarization measurements. A complementary study of film composition is underway.

3.2 Experimental

3.2.1 Sample preparation

Materials were provided by Haynes International (Kokomo, IN, USA) in the mill-annealed sheet form. Nominal compositions, as reported by the manufacturer, are summarized in Table 3.1, while the measured compositions, determined by inductively coupled plasma atomic emission spectroscopy (ICP-AES) (Cambridge Materials Testing Limited, Cambridge, ON), are summarized in Table 3.2. Unless otherwise stated, discussions will refer to the nominal composition provided by the manufacturer.

Table 3.1 - Nominal compositions of the examined alloys (wt.%) as reported by Haynes International. Maximum allowable concentrations are indicated by ‘M’. The balance of the composition is nickel in each of these alloys.

Alloy	Ni	Cr	Mo	Fe	W	Cu	Nb	Co	Mn	V	Al	Si	C
G-35	Bal.	33.2	8.1	2^M	0.6	0.3^M	--	1^M	0.5^M	--	0.4^M	0.6^M	0.05^M
G-30	Bal.	30	5.5	15	2.5	2	0.8	5	1.5	--	--	0.8^M	0.03^M
C-22	Bal.	22	13	3	3	0.5^M	--	2.5^M	0.5^M	0.35^M	--	0.08^M	0.01^M
BC-1	Bal.	15	22	2^M	--	--	--	--	0.25	--	0.5^M	0.08^M	0.01^M

Experimental coupons were fabricated with the dimensions 0.6 x 0.6 x 6 cm^3. Avoiding the use of epoxy and the subsequent opportunity for crevice corrosion to occur, these ‘stick’ electrodes were partially submerged directly in the experimental solutions. Observations of minimal waterline corrosion were made only in naturally aerated acidic solutions and were considered insignificant compared to corrosion damage present elsewhere on the coupon. Prior to all measurements, coupons were ground to a final surface preparation of P1200 using wet SiC paper with water as lubricant. Coupons were then sonicated in EtOH (95%), rinsed in deionized (DI) water (18.2 MΩ cm), and dried in a stream of ultra-high purity Ar gas (Praxair, Mississauga, ON). Applying this procedure ensured that the surfaces demonstrated reproducible electrochemical behaviour.

Table 3.2 - Actual compositions of the examined alloys (wt.%) as determined by ICP-AES. Chemical analysis was performed in accordance with ASTM E1019-18, E1097-12, and E1479-16.

Alloy	**Ni**	**Cr**	**Mo**	**Fe**	**W**	**Cu**	**Mn**	**Al**	**Si**	**C**
G-35	56.3	33.4	7.98	0.54	0.07	0.02	0.45	0.24	< 0.01	< 0.010
G-30	42.1	29.0	4.97	14.75	2.77	1.70	1.13	0.15	0.24	0.016
C-22	57.6	20.7	12.97	3.74	2.80	0.06	0.27	0.28	< 0.01	0.012
BC-1	60.9	14.4	22.1	0.85	0.01	0.03	0.25	0.18	< 0.01	0.011

Solutions were prepared using reagent grade NaCl and concentrated HCl (Caledon Laboratory Chemicals, Georgetown, ON). The chloride concentration in all solutions was kept constant by substituting NaCl for HCl in equimolar quantities, with the studied concentrations being 3 M NaCl and 1 M HCl + 2 M NaCl. Where indicated, dissolved O_2 was removed by an initial high rate of sparging with ultra-high purity Ar followed by continuous sparging for the duration of the experiment.

3.2.2 Electrochemical methods

Experiments were conducted in a three-compartment glass electrochemical cell. A water jacket, which encased the main compartment, was connected to an isothermal water circulator. The circulator was used to maintain a solution temperature of 75 ± 1 °C. The counter electrode (CE), a platinum flag, and the reference electrode (RE), a saturated calomel electrode (SCE), were housed in their own compartments, isolated from the main compartment by porous glass frits. Prior to each experiment, the RE was calibrated against a ‘master’ electrode, used only for calibration purposes. Following each experiment, the surface area of the ‘stick’ working electrode (WE) was measured to allow for the conversion of the measured current into current density.

Electrochemical measurements were made using either a Model 1287 potentiostat or 2100 Analytical Modulab (Solartron Analytical, Hampshire, UK). Corrosion behaviour was studied by monitoring the corrosion potential (E_{CORR}) for a period of 6 h, with linear polarization resistance (LPR) measurements made every 30 min. LPR measurements involved polarizing the WE ± 10 mV (vs. E_{CORR}) at a scan rate of 10 mV min^{-1}. Polarization resistance (R_P) values were then calculated from the slopes of the linear current density (i) vs potential (E) plots (*i.e.*, $R_P = \Delta E/\Delta i$). In separate experiments, electrochemical impedance spectroscopy (EIS) measurements were performed at the end of a 6 h E_{CORR} measurement. Spectra were acquired at E_{CORR} by the application of a sinusoidal perturbation (± 10 mV) at 11 points per decade in the frequency range from 10^5 to 10^{-3} Hz. A second spectrum was recorded using a frequency scan in the reverse direction to ensure that the system under investigation was stable during the EIS measurement.

In the study of polarization behaviour, both dynamic- and static-polarization techniques were used. Dynamic experiments were initiated at −0.050 V (vs. E_{CORR}) and scanned in the positive direction at 10 mV min^{-1} until either the potential reached 1.1 V (vs. SCE) or the absolute current reached 10 mA. In static experiments, a fixed potential of 0 V (vs. SCE), was applied and the resulting current response monitored as a function of time.

3.3 Results

3.3.1 Corrosion potential (E_{CORR}) and polarization (R_p) measurements

During immersion in near-neutral chloride solution, all alloys exhibited behaviour consistent with the formation of a passive film. A summary of E_{CORR} and R_P measurements made in aerated 3 M NaCl is given in Figure 3.1(A). Overall, both E_{CORR} and R_P were found to increase toward steady-state values. For all alloys, R_P values were found to be on the order of 10^6 Ω cm^2, consistent with the passive behaviour expected for these alloys in nonaggressive solutions [2, 21], and with the rapid formation of a Cr-rich oxide barrier layer [22, 23]. Values of R_P increased only slightly with the Cr content of the alloy: BC-1 (15 wt.% Cr) < C-22 (22 wt.% Cr) < G-30 (30 wt.% Cr) < G-35 (33.2 wt.% Cr). The benefit of increasing the Cr content > 15 wt.% was minor.

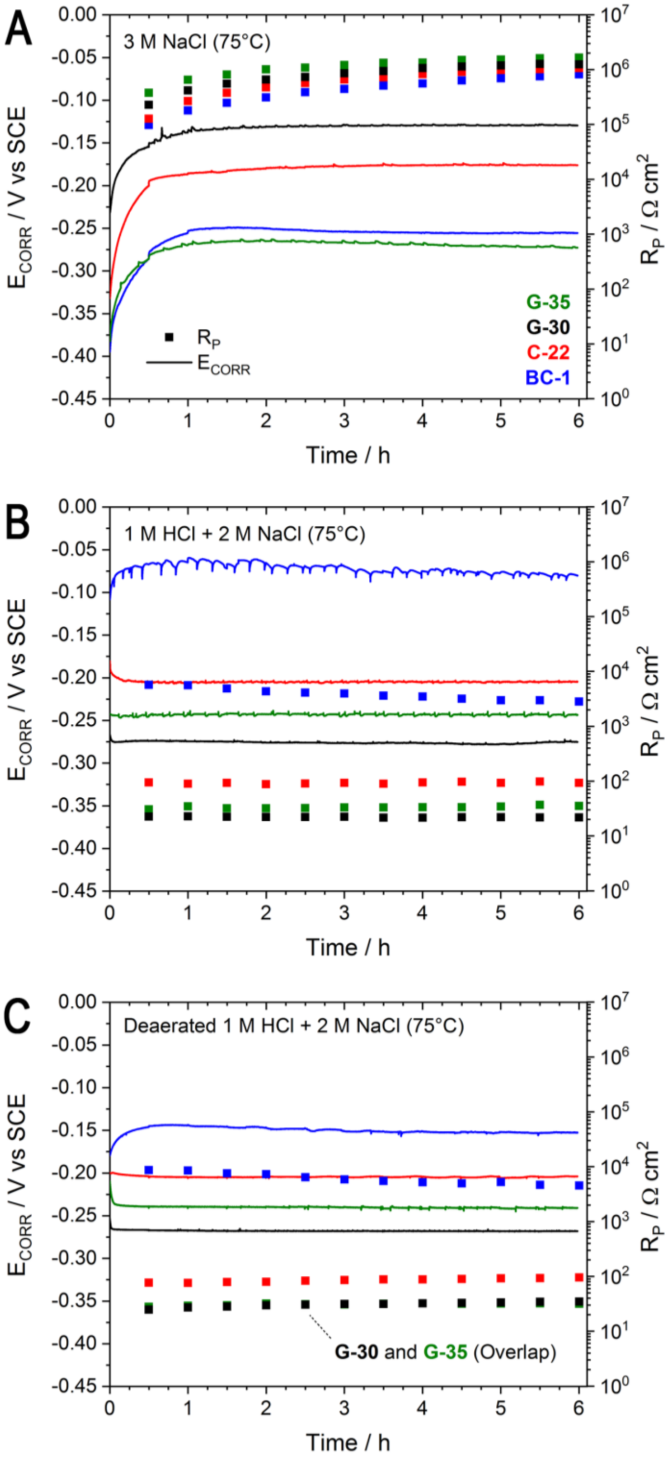

Figure 3.1 - Corrosion potential (E_{CORR}) and polarization resistance (R_P) measurements on alloys BC-1, C-22, G-35, and G-30 exposed to (A) aerated 3 M NaCl, (B) aerated 1 M HCl + 2 M NaCl, and (C) deaerated 1 M HCl + 2 M NaCl (75°C).

Unlike R_P values, E_{CORR} exhibited no clear dependence on the Cr content of individual alloys. Previously, Lloyd *et al.* showed that an increased Cr content led to open-circuit ennoblement [22]. In the present work, this was found to be true only for BC-1, C-22 and G-30, whose E_{CORR} increased with Cr content: BC-1 (15 wt.% Cr) < C-22 (22 wt.% Cr) < G-30 (30 wt.% Cr). However, the highest-Cr-containing alloy, G-35 (33.2 wt.%), had the lowest E_{CORR} at the end of the 6-h immersion period. Based on the empirically determined alloy compositions, Table 3.2, the E_{CORR} increased with Fe content in the order G-35 (0.54 wt.% Fe) ≈ BC-1 (0.85 wt.% Fe) < C-22 (3.74 wt.% Fe) < G-30 (14.75 wt.% Fe). This could be due to the presence of Fe_2O_3 or a Fe-containing spinel [5, 24]. Since E_{CORR} is dependent on the kinetics of the anodic and cathodic half-reactions, this trend could indicate either increased anodic or decreased cathodic reaction kinetics.

A decrease in solution pH resulted in large changes to both E_{CORR} and R_P, compared to the values measured in near-neutral solution. The E_{CORR} and R_P values recorded in aerated 1 M HCl + 2 M NaCl solution are shown in Figure 3.1(B). Alloys C-22, G-30, and G-35, displayed comparable behaviour. Rather than increasing toward a steady-state, E_{CORR} rapidly stabilized and remained constant for the remainder of the experiment. It is worth mentioning that E_{CORR} values stabilized significantly faster in acidic solution than in the near-neutral chloride solution. This suggests that the rate of reaction in acidic solution is faster than that in near-neutral solution. Similarly, R_P quickly stabilized at low values, on the order of 10 Ω cm^2. In this solution, R_P values were approximately five orders of magnitude lower than those measured in the near-neutral solution, indicating the establishment of active conditions. In acidic solution, the high solubility of Cr(III) would be expected to challenge the Cr(III) barrier layer [25]. Evidence for active conditions is presented below in the discussion of the dynamic polarization measurements.

Measurements on alloy BC-1 suggested the surface remained partially protected in acidic solution, Figure 3.1(B). Values of E_{CORR} rapidly increased to a maximum, which then decreased slightly with time. The maximum value was ~0.2 V higher than that measured in near-neutral solution. The negative-going transients observed in E_{CORR} suggest localized events occurring on the surface. Each potential transient indicates a momentary acceleration of the anodic reaction, consistent with metastable pitting behaviour through a protective layer [19, 20]. Unfortunately, the temporary influence of metastable events could not be captured by periodic R_P measurements. Values of R_P were on the order of 10^3 Ω cm^2. While lower than those measured in near-neutral solution, they were approximately three orders of magnitude greater than values measured on alloys C-22, G-30, and G-35, exposed to the same solution. Together, these potential transients and the R_P values suggest that BC-1 maintains, at least to some extent, a partially protective passive film in an aerated 1 M HCl + 2 M NaCl solution. This combination of an increase in E_{CORR} and higher R_P values for BC-1 than on C-22, G-30, and G-35 alloys, suggests the anodic reaction is suppressed by the presence of a surface film. Given the high Mo content of BC-1, it is likely that this film is Mo-rich. It has been suggested that alloying with Mo stabilizes the Cr-rich oxide film in acidic solutions [9, 26-28]. For Cr/Mo containing alloys, this is often attributed to the formation of a Mo-rich oxide layer over an inner Cr-rich barrier layer [3, 29-33]. These results confirm a role for Mo in protecting an alloy from degenerating to active corrosion, providing the Mo content is > 13 wt.%. For Mo < 13 wt.%, any Cr(III) barrier layer is dissolved and active corrosion can be achieved.

In addition to changes in behaviour caused by decreases in pH, changes caused by the removal of dissolved O_2 were also studied. The E_{CORR} and R_P values recorded in Ar-sparged 1 M HCl + 2 M NaCl are shown in Figure 3.1(C). For C-22, G-35, and G-30, the removal of O_2 produced E_{CORR} and R_P values comparable to those recorded in the naturally aerated acidic solution. This suggests that O_2 plays a minor role as the oxidant in comparison to H^+ at E_{CORR} when the alloy is active. In both aerated and deaerated solutions, E_{CORR} values for these alloys were near or below the equilibrium potential for H^+ reduction, −0.244 V (vs. SCE) at pH 0 and 75°C. In addition, the formation of bubbles was observed for alloys C-22 and G-35 and most copiously for alloy G-30.

By contrast, the removal of dissolved O_2 caused noticeable changes in the behaviour of BC-1. The general trends in E_{CORR} were similar for both the aerated and the Ar-sparged solution conditions, *i.e.,* a rapid increase followed by a gradual decline over the 6-h period. However, values measured in the Ar-sparged solution were found to be ~0.1 V lower than those measured in naturally aerated solution. Additionally, the negative-going potential transients observed in the naturally aerated solution were absent in the Ar-sparged solution, confirming the role of O_2 in their generation. Previously, Ebrahimi *et al.* demonstrated that, while H^+ reduction was enough to maintain localized events on alloy BC-1, O_2 was an important oxidant during their initiation [19]. R_P values measured in Ar-sparged solution were only slightly higher than those measured in aerated solution.

3.3.2 Electrochemical impedance

Representative impedance spectra collected in aerated 3 M NaCl solution are shown in Figure 3.2. In Nyquist plots, not shown, depressed semi-circles with diameters on the order of 10^6 Ω cm^2 were found for all alloys. This is consistent with the R_P values discussed above. The corresponding Bode plots are shown in Figure 3.2(A) and (B). The low frequency impedance modulus, |Z|, suggests that an increase in Cr-content provides only a minor benefit for Cr concentrations > 15 wt.%. The phase angle plot shows two time-constants for all four alloys, one at high (~10^3 Hz) and the other at low (~10^{-1} Hz) frequency. The electrical equivalent circuit used to fit the spectra is shown in the inset of Figure 3.2(B). The impedance response of similar systems has been investigated and appropriate equivalent circuits discussed [2, 34-37]. Ebrahimi *et al.* attributed the high and low frequency time-constants to interfacial charge transfer and film processes, respectively [35]. More specifically, the high and low frequency time-constants were said to involve the charge transfer process at the film/solution interface and the dielectric processes occurring within a thin defective film, respectively. More complex circuits involving additional time-constants [2] have been proposed, including the need for diffusional (Warburg) elements to improve the fit of the equivalent circuit [34, 38]. However, the inclusion of a Warburg element was not found to significantly improve the fit to the spectra in Figure 3.2 and was therefore avoided.

In all cases, a constant phase element (CPE) was used in place of a capacitor to account for the non-ideal capacitive response of the surface [39, 40]. For the low frequency time-constant, attributed to the response of the film, the CPE exponent was > 0.85 for all alloys. On the other hand, CPE exponents corresponding to the interfacial process (~10^3 Hz) were

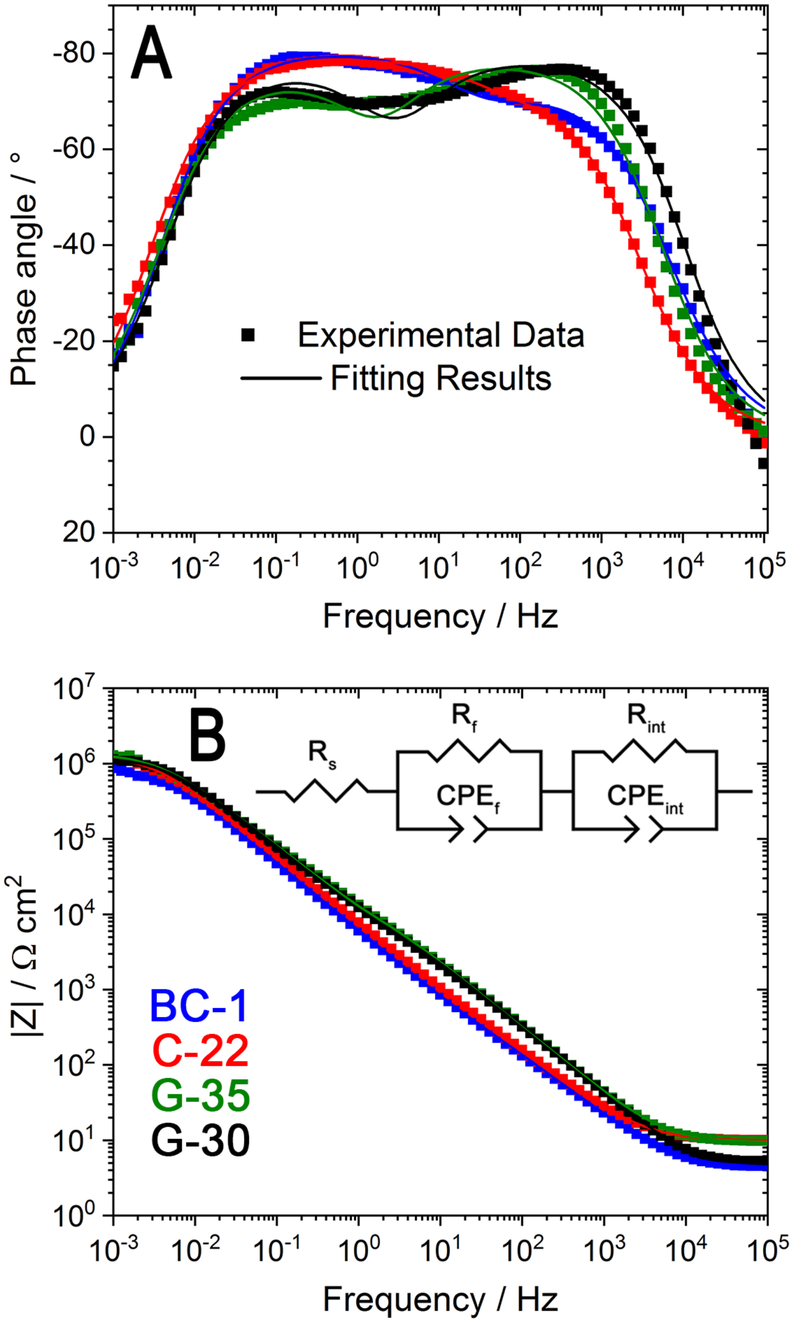

Figure 3.2 - EIS recorded on alloys BC-1, C-22, G-35, and G-30 after 6-h exposure to aerated 3 M NaCl (75°C). Points indicate experimental data while solid curves represent the result of equivalent circuit fitting.

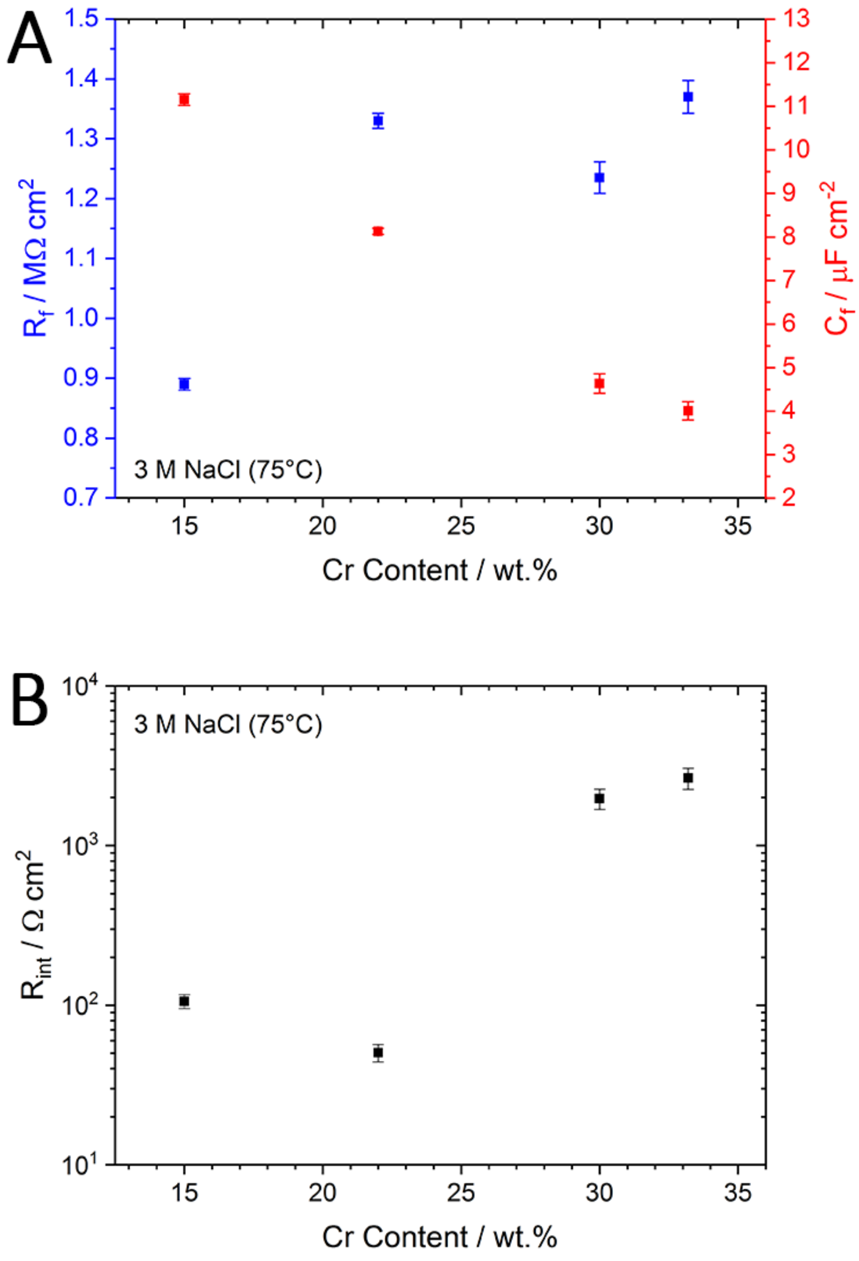

Figure 3.3 - Dependence of (A) film resistance (R_f), film capacitance (C_f), and (B) interfacial resistance (R_{int}) on alloy Cr content after 6-h exposure to 3 M NaCl solution (75°C). Values of capacitance were obtained from CPE_f according to the procedure proposed by Brug *et al*. [38]. The error bars indicate the goodness of fit obtained from linear least squares fitting.

lower, suggesting the contribution of a diffusive impedance. Using the method developed by Brug *et al.* [41], the CPE_f values were converted into equivalent capacitances (C_f) and plotted together with the resistance values (R_f). The results are plotted as a function of Cr content in Figure 3.3(A). In general, values of R_f increased with increasing Cr-content, except on G-30, for which R_f was lower than expected. This probably indicates an effect of the higher Fe content in G-30 on the passive film. Opposite to the trend in R_f, values of C_f were found to decrease with increasing Cr-content. The low values of C_f are in the range expected for a thin passive oxide. The increase in R_f, accompanied by a decrease in C_f, is consistent with an improvement in passive film properties due to its thickening and/or the elimination of point defects, with the latter reflected in a decrease in the dielectric constant of the film [34, 38]. Overall, the impedance data presented here suggest that increasing Cr content to > 15 wt.% results in only minor improvements in passivity. However, as is clear by inspection of Figure 3.2(A) and (B), significant differences in the alloy/oxide interfacial properties are observed. The resistance to charge transfer at the metal/oxide interface (R_{int}) for the two high Mo(W)/low Cr alloys, BC-1 and C-22, are considerably lower (by more than a factor of 10) than those for the high Cr/low Mo(W) alloys, Figure 3.3(B), with the low CPE exponents suggesting either a possible diffusive contribution or local film inhomogeneities. These results indicate a degradation of the inner barrier layer as the Mo(W)/Cr ratio is increased.

Representative impedance spectra collected in aerated 1 M HCl + 2 M NaCl are shown in Figure 3.4. For alloy BC-1, two time-constants were observed, similar to the spectrum recorded in near-neutral 3 M NaCl, however, the absolute impedance was over two orders of magnitude lower. For the other alloys, the low frequency value of |Z| decreased to very low values, Figure 3.4(B). In addition, a low frequency inductive response, reflected in the temporary positive value of the phase angle, Figure 3.4(A), is observed. Such an inductive response may occur at sufficiently low frequencies for the BC-1 alloy but could not be detected in our experiments, since valid impedance data could only be recorded for frequencies $\geq 10^{-2}$ Hz. At lower frequencies, the film breakdown events observed in E_{CORR} measurements, Figure 3.1(B), led to erratic data. As a result, the impedance spectra violated the stability criterion required for valid data. Consequently, the circuit containing two RC

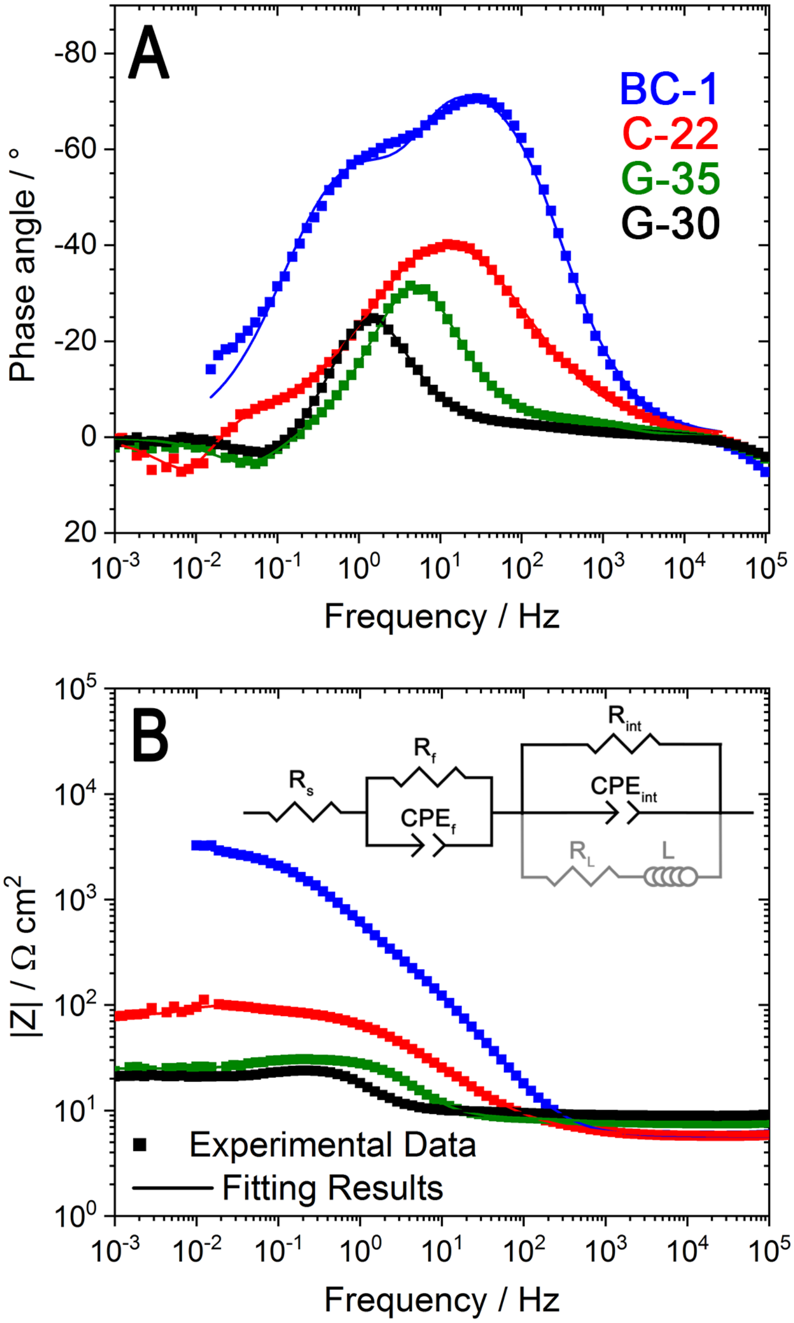

Figure 3.4 - EIS recorded on alloys BC-1, C-22, G-35, and G-30 after 6-h exposure to aerated 1 M HCl + 2 M NaCl (75°C). Points indicate experimental data while solid curves represent the result of equivalent circuit fitting.

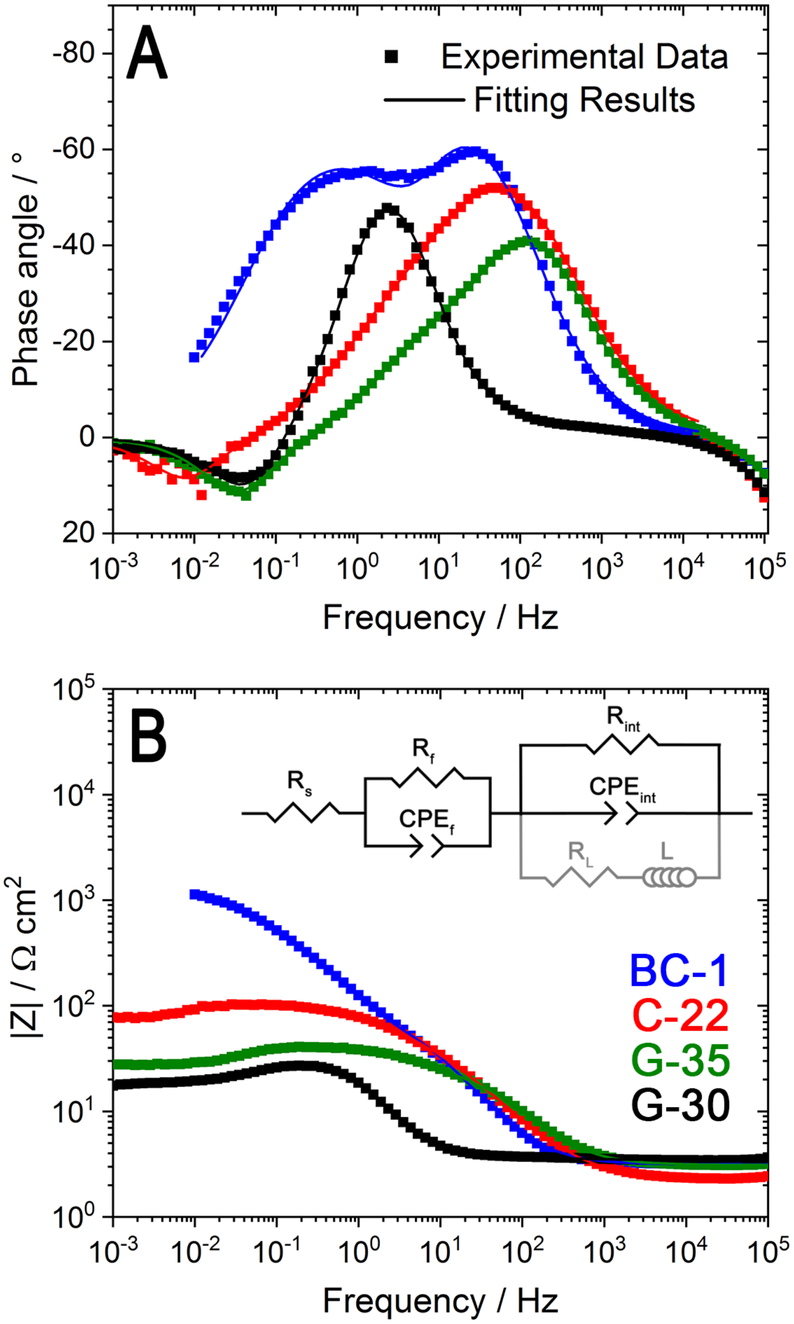

Figure 3.5 - EIS recorded on alloys BC-1, C-22, G-35, and G-30 after 6-h exposure to deaerated 1 M HCl + 2 M NaCl (75°C). Points indicate experimental data while solid curves represent the result of equivalent circuit fitting.

time-constants, Figure 3.4(B) (inset), was used to fit the spectra for BC-1, while the three time-constant circuit incorporating the inductor (L) and resistor (R_L), was used to fit the spectra recorded for the other three alloys. Low frequency inductive effects are commonly attributed to the influence of surface adsorbed cation states, discussed in more detail below.

Representative impedance spectra collected in deaerated 1 M HCl + 2 M NaCl are shown in Figure 3.5. Values of |Z| were comparable with those observed in the aerated case and exhibited a similar overall increase as the Mo(W) content increased. As observed for aerated conditions, the spectrum obtained for BC-1 was fitted using the two time-constant circuit (inset to Figure 3.5(B)). For the alloys undergoing active corrosion, the three time-constant circuit including L and R_L was required. Small changes in R_f, R_{int} and R_L were observed with no clear dependence on the Mo(W) content.

The overall influence of Mo and aeration on the resistive properties of the surface films is shown in Figure 3.6, which plots the total interfacial resistance ($\sum R = R_f + R_{int} + R_L$) as a function of Mo content for both aerated and deaerated conditions, with the influence of aeration detectable only at the highest Mo content. Values of $\sum R$ shown in Figure 3.6 are comparable to R_P values discussed with Figure 3.1(B) and (C). Since the CPE exponents were in many cases < 0.8, the conversion of the respective CPE parameters to capacitances was dubious. Of particular interest is the value for BC-1, since the impedance spectra show the presence of a substantial film while exposed to acidic solutions. Since the CPE exponent was > 0.8 for aerated conditions the CPE was converted to an equivalent capacitance, yielding a value of 120 μF cm^2, which is considerably higher than observed for neutral conditions, 11 μF cm^2. Coupled with the relatively high value of R_f, this indicates the presence of a highly defective surface film. Similarly, high values of capacitance are observed under transpassive conditions [34] when the destruction of the Cr(III) barrier layer at high potentials leads to the formation of a partially protective Mo-dominated layer.

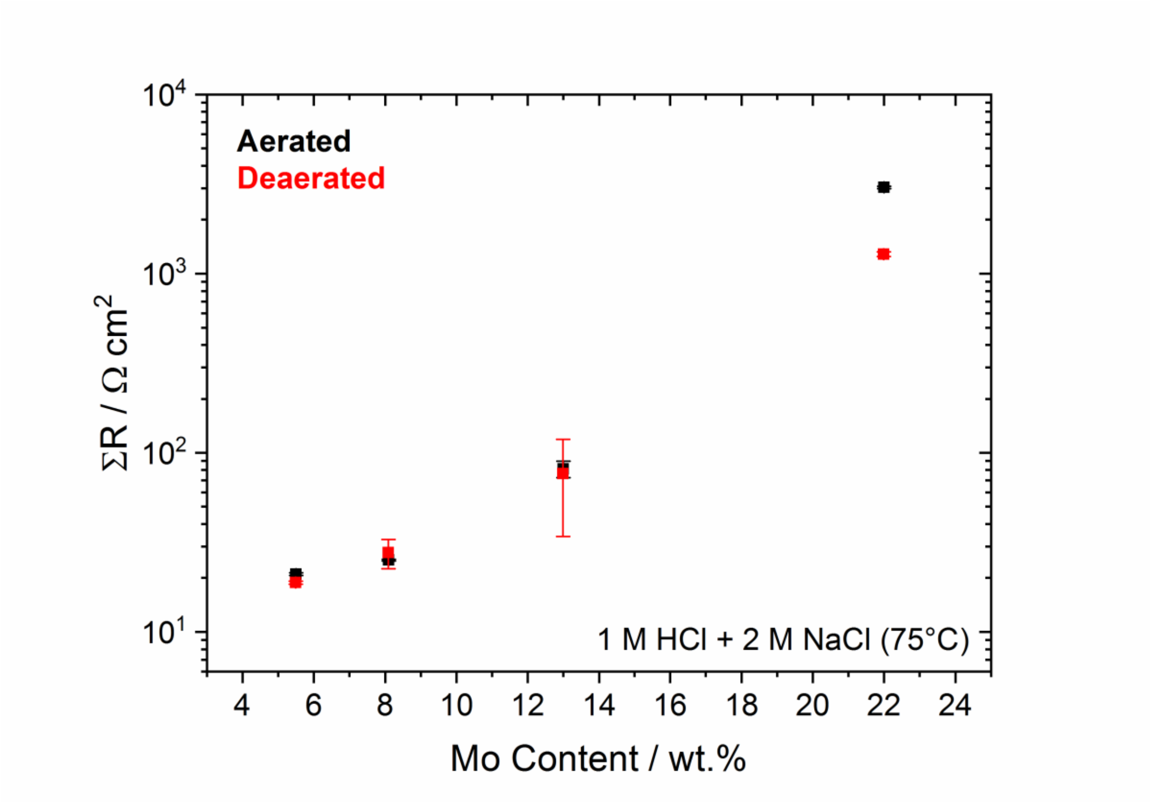

Figure 3.6 - Relationship between Mo content and the total resistance (ΣR) calculated from equivalent circuit fitting of impedance spectra obtained in aerated and deaerated 1 M HCl + 2 M NaCl solution (75°C). The error bars indicate the goodness of fit obtained from linear least squares fitting.

3.3.3 Dynamic and static polarization

Figure 3.7(A) shows linear polarization curves recorded in a neutral 3 M NaCl solution. For potentials positive of E_{CORR}, all the alloys exhibited a passive region, extending up to ~0.2 V (vs SCE). For the three high-Cr alloys, the current densities in the passive region were effectively the same, while that for alloy BC-1 was noticeably higher, as expected, given its lower Cr content. For higher potentials, the film thickness has been shown to increase [32], however, the onset of Cr(III) oxidation to Cr(VI) results in damage to the barrier layer [34, 42]. Online measurements have shown that the transpassive dissolution of Ni-based alloys proceeds with elevated dissolution rates of Ni and Cr with the surface

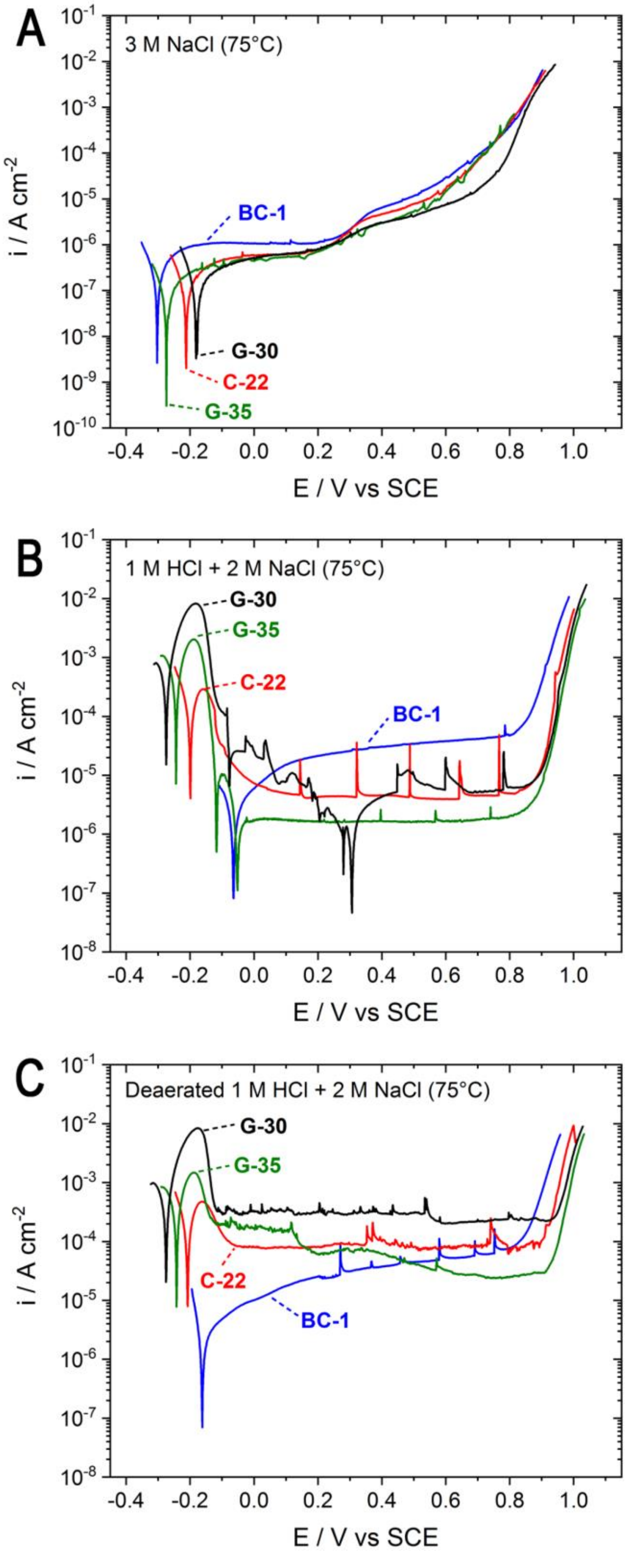

Figure 3.7 - Polarization behaviour of alloys BC-1, C-22, G-35, and G-30 in (A) aerated 3 M NaCl, (B) aerated 1 M HCl + 2 M NaCl (B), and (C) deaerated 1 M HCl + 2 M NaCl (75°C).

enrichment of Mo [13]. This process leads to increased currents which are slightly higher for the alloys with lower Cr contents. For all alloys, a secondary passive region was observed between ~0.4 V and 0.6 V. This was consistent with previous observations and attributed to surface enrichment with $Ni(OH)_2$ [43, 44]. For alloy G-30, this secondary passive region was extended to ~0.7 V (vs SCE), a feature attributed to the formation of insoluble Fe(III) oxide.

In aerated 1 M HCl + 2 M NaCl solution, Figure 3.7(B), an active-to-passive transition was observed for all alloys except BC-1. The peak currents related to active dissolution were found to decrease with increasing Mo content as expected from published literature [26, 45]. The observation of active behaviour for all alloys, except BC-1, was consistent with the E_{CORR}/R_P and EIS measurements, which indicated active behaviour for G-35, G-30 and C-22. For potentials more positive than the active-to-passive transition, where film formation occurred, the behaviour was complicated by a switch from anodic to cathodic current for alloys G-30 and G-35. For both alloys, the measured current eventually returned to anodic values as the applied potential was increased. Additionally, all alloys exhibited current transients, again with the exception of BC-1.

Polarization curves conducted in deaerated 1 M HCl + 2 M NaCl solutions, Figure 3.7(C), generally displayed higher currents through the passive region and yielded only anodic current values (~−0.1 V to 0.8 V (vs SCE)), indicating that the net currents (i_{net}) in this potential region under aerated conditions were the sum of an anodic passive current (i_{anodic}) and a cathodic current ($i_{cathodic}$) for O_2 reduction. Consequently, the polarization curves acquired in deaerated solution allowed for i_{anodic} to be easily compared between alloys. For potentials immediately positive of the active-to-passive transition (*i.e.*, up to ~0.1 V (vs SCE)), the current was independent of potential for the three high Cr alloys and decreased as the Mo(W) content increased. At potentials ≥ 0.1 V (vs SCE) the currents for the three alloys showed no consistent trend with composition, remained independent of potential for C-22 and G-30, and decreased with potential for G-35. The passive current for G-30, the high Fe containing alloy, was considerably higher than that of the other two alloys, indicating that the advantage of Fe in suppressing the current at high potentials in neutral solution was lost in acidic solutions, in which Fe^{3+} is much more soluble [25]. For alloy

BC-1, the current behaviour in this potential region (−0.1 V to 0.8 V) was significantly different to that of the other three alloys. While one to two orders of magnitude lower at the low end of this potential range, it increased steadily with potential to values approaching, and in the case of G-35 exceeding, the currents observed on alloys with lower Mo(W) contents.

The contributions from the cathodic current in the passive region were determined by subtracting the currents recorded in deaerated solution (i_{anodic}) from those measured in aerated solution ($i_{net} = i_{anodic} + i_{cathodic}$). The results are plotted against the applied potential for all four alloys in Figure 3.8. Overall, no clear dependence of the current on the Mo(W)/Cr ratio was observed. For the alloy BC-1, with the highest Mo(W)/Cr ratio, the

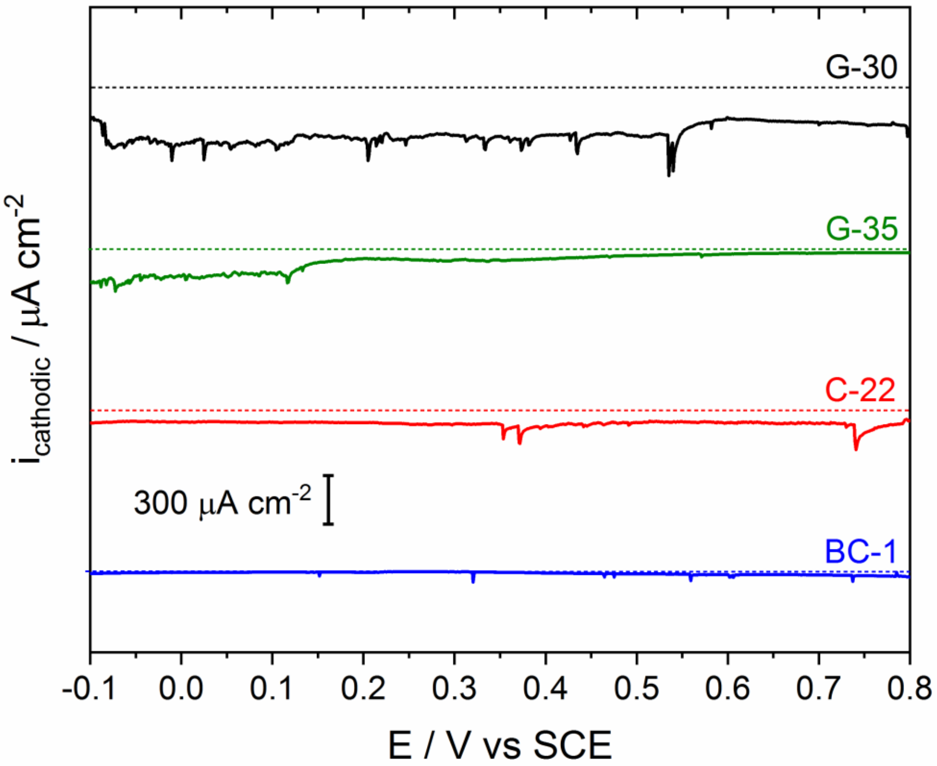

Figure 3.8 - Cathodic current densities related to O_2 reduction throughout the region of film formation in 1 M HCl + 2 M NaCl (75°C). Values obtained from the difference in current densities measured in naturally aerated and deaerated solutions; $i_{aerated} - i_{deaerated} = (i_{anodic} + i_{cathodic}) - i_{anodic}$. Dashed lines indicate the offset locations of i = 0.

O_2 reduction current was effectively zero over the full potential range. For C-22 and G-35 relatively small values of $i_{cathodic}$ were observed, with the value for G-35 decreasing with increased potential while that for C-22 remained potential-independent. By far the largest cathodic current was observed for G-30, which differs in composition from G-35 only in the Fe content. While transport processes were anticipated to limit the rate of O_2 reduction, especially at potentials far below the equilibrium potential, the large differences in cathodic currents for the alloys suggested presently unresolved chemical factors must also be involved.

In both aerated and deaerated acidic solutions, films formed at higher potentials were found to be susceptible to localized breakdown events. These instabilities were investigated in more detail under potentiostatic conditions. Figure 3.9(A) shows the currents recorded at an applied potential of 0 V (vs SCE) in deaerated 1 M HCl + 2 M NaCl. This potential was well above the active regions for those alloys which exhibited active behaviour but below potentials at which more unpredictable behaviour was observed, Figure 3.7(C). Figure 3.9(B) shows magnifications of individual transients for each alloy, which all exhibited the standard shape involving a rapid initiation followed by an exponential recovery. It is clear that the severity of breakdown and the time for recovery varies with the Mo(W) content of the alloy. However, the charge associated with individual transients was difficult to measure due to the long current tails for individual transients, in particular those recorded for the low Mo alloys, for which decay to the background passive current density was slow and incomplete.

The differences between the different alloys were characterized by determining the frequency of breakdown events and the maximum amplitude of individual events, Figure 3.9(C) and (D), respectively. The plotted values are based on 3-4 repeated experiments. This means the large error bars reflect an inability to totally capture the distributions of stochastic events. The frequency of breakdown events decreased markedly with increased alloy Mo(W) content, while the maximum current amplitude was low for all alloys except the high-Fe G-30 alloy. Interestingly, for this last alloy, the high frequency of high amplitude events led to a slow, but continuous, increase in the background passive current, indicating an inability of G-30 to completely repassivate.

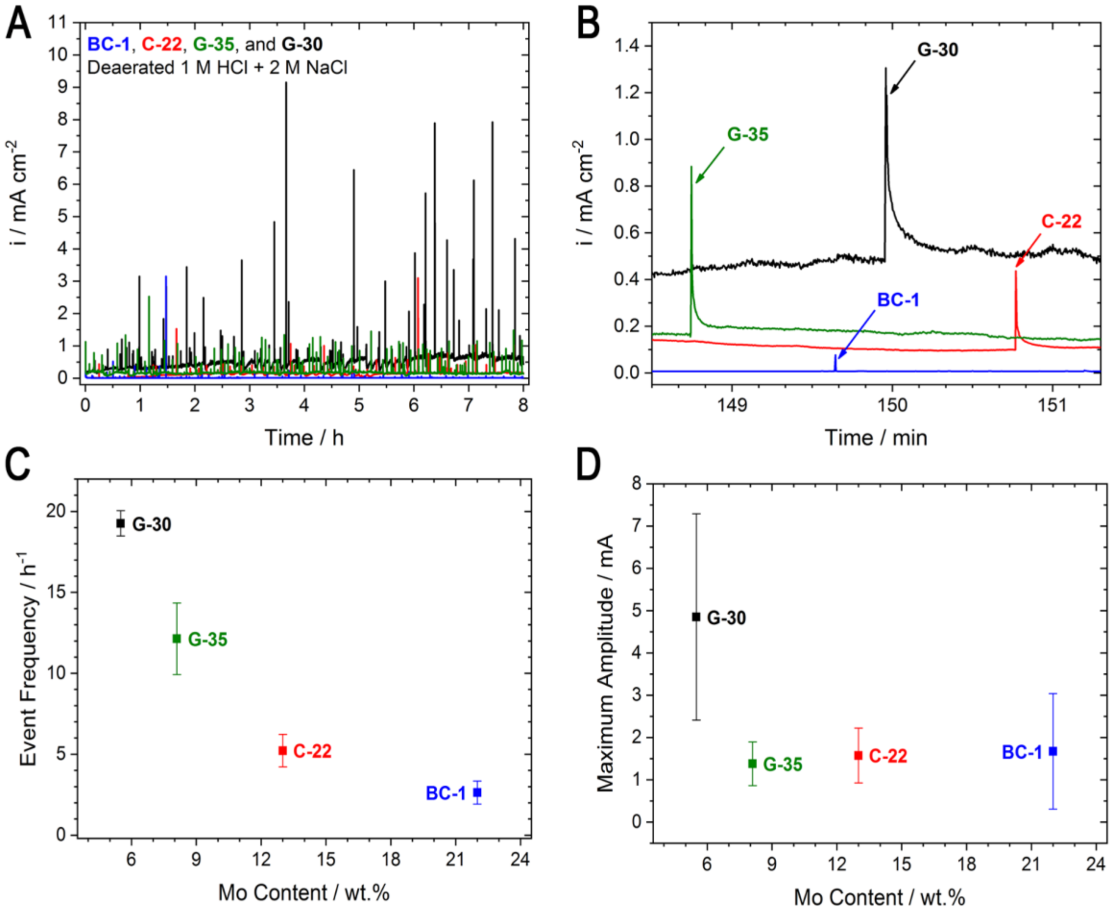

Figure 3.9 - Current-time response of potentiostatic experiments at 0 V (vs. SCE) on alloys BC-1, C-22, G-35, and G-30 in deaerated 1 M HCl + 2 M NaCl (75°C). Data collected over an 8-h period are shown in (A), while (B) shows a magnified region for better comparison of current transients. Quantification of the average event frequency and maximum amplitude is given in (C) and (D), respectively.

3.4 Discussion

3.4.1 Passive films formed under neutral conditions

In many studies, passive films grown at E_{CORR} have been characterized during or after exposure to acidic solution, where the release of the alloy matrix element, in this case Ni^{2+}, accelerates the enrichment of Cr and Mo within the oxide [22, 46]. These films are commonly characterized by the enrichment of Cr at the alloy/oxide interface, while Mo segregates to the oxide/solution interface. However, a similar segregation process has also been demonstrated in air-formed oxide films [33], indicating that it is a universal feature, irrespective of the oxidizing exposure environment. Consequently, such a process would be expected in our experiments in neutral solution.

The results in Figure 3.3(A) indicate that the film resistance, R_f, while slightly lower for the Fe-containing G-30, is only marginally influenced by changes in Cr content ≥ 22 wt.%. A lower R_f was observed for alloy BC-1, containing the lowest Cr-content. At only ~15 wt.%, the Cr content may be close to the minimum required to form the $–Cr^{III}–O^{II}–Cr^{III}–$ network necessary to establish a coherent Cr_2O_3 barrier layer. According to percolation theory, a critical cation fraction is required in the oxide to achieve a passive state in Fe- and Ni-based alloys containing Cr [47, 48].

Interestingly, a lower interfacial resistance, R_{int}, Figure 3.3(B), was observed for both BC-1 and C-22. As indicated in Figure 3.3(A), this was accompanied by a higher film capacitance, C_f, relative to the values measured for the two high-Cr alloys, G-30 and G-35. This combination of effects suggests that the inner layers present on BC-1 and C-22 are more defective than those on the other two alloys. Given the high Cr content of alloy C-22, it seems unlikely that the slightly inferior properties are attributable to a compositional inability to form a coherent $–Cr^{III}–O^{II}–Cr^{III}–$ network. A possibility is that the inner oxide found on BC-1 and C-22 has a higher Mo(W) content than that of the two high Cr alloys, caused by a more restricted segregation process in neutral solution where Ni^{2+} dissolution is limited. This would be consistent with recent studies that were interpreted based on the solute vacancy interaction model [49] and recent experiments indicating the likelihood that

Mo is present in the form of individual cations, due to non-equilibrium solute capture in rapidly grown Ni(II)/Cr(III) oxides [16].

It is possible that these lower values of R_{int} reflect a slower approach to a final steady-state passive film structure for these alloys. That this may be the case is suggested by the difference in relative values of R_P between the four alloys which are less divergent after 6 h of exposure than after shorter exposure times. For all four alloys, R_P values increase slightly over the full exposure period, suggesting a slow improvement in film properties, either due to thickening or to the elimination of point defects.

3.4.2 Passive films formed under acidic conditions

The behaviour observed at E_{CORR} (Figure 3.1) and under applied potential polarization (Figure 3.7) confirms that, under acidic conditions, alloys G-35, G-30, and C-22 are active, while BC-1 maintains a weakly passive film, exhibiting passive current densities $> 10^{-5}$ A cm^{-2}. In EIS experiments, the inductive response observed at low frequency, Figure 3.4, is similar to behaviour commonly found on active metal surfaces, generally attributed to coupled electrochemical reactions involving adsorbed intermediates [1, 39]. Inductive responses have been reported during the dissolution of Fe-based alloys in acid media [11, 50-53] as well as for Ni [54, 55], Cr [56, 57], and Mo [58, 59] systems. Since all of these elements are found in the studied alloys, inductive responses are to be expected. It is likely that the oxidation of each of these metal cations involves adsorbed states, some possibly involving the co-adsorption of anions as well.

Both Jakupi *et al.* [60] and Ebrahimi *et al.* [4] showed that Mo was retained at active sites under the active corrosion conditions prevailing inside a propagating crevice, while Ni and Cr were not. More recently, Li and Ogle confirmed [46] that similar behaviour, involving only the retention of Mo, was observed under active conditions not involving a crevice geometry. Jakupi *et al.* [60] investigated the nature of Mo deposits formed inside an actively corroded crevice using Raman spectroscopy. While they found it difficult to be specific, due to the complexity of the Mo polymerization process, this study indicated the presence of MoO_2, Mo_4O_{11} and ill-defined polymeric species such as $Mo_{36}O_{112}^{8-}$. When W was present, no spectral differences were observed, although W would be expected to exert a similar response to Mo. Bojinov *et al.* [58] proposed a complex anodic reaction sequence for Mo involving multiple adsorbed species with an initial step in which Mo(III) was reversibly converted to Mo(IV).

The change in behaviour from active, involving inductive responses in the EIS, to passive, involving a capacitive response, as the Mo(W) content of the alloy increased could then possibly be explained by a shift from reversible adsorbed states at low Mo contents to the MoO_2 and polymeric species at higher contents. The observation of an active-passive transition for G-30, G-35 and C-22 confirms the occurrence of active behaviour, with the absence of such a transition for BC-1 expected in the presence of a corrosion-resistant Mo oxide/molybdate layer. At low potentials in the passive region (as defined by the polarization curves in the absence of O_2, Figure 3.7(C)) the lower passive current in higher-Mo(W) alloys demonstrates that the Mo(W) content is crucial in sustaining passivity and in suppressing the events which initiate localized film breakdown [14, 20-26, 29, 61-63].

The ability of Mo to enhance the passivity of Fe-based alloys has been explained in terms of a bipolar model [29] with an outer layer Mo-oxide protecting an inner Cr(III) barrier layer. It was proposed that the outer layer contained anionic Mo species (*e.g.,* MoO_4^{2-}), giving the oxide/solution interface a certain cation selective nature to repel aggressive anions, such as Cl^-, which would induce film breakdown. As noted by Lutton Cwalia *et al.* [12] this segregation process facilitates the formation of a continuous Cr_2O_3 layer and suppresses cation vacancy motion. Thus, while this model offers an explanation for a decrease in the number of attempted breakdown events as the Mo(W) content increases, it does not necessarily explain the suppression of the current amplitude when transients do occur. As shown in Figure 3.9, as the Mo(W) content decreases, transients become more frequent and severe compared to those on high-Mo alloys. It is well-established that Mo-rich corrosion products deposit in areas of active corrosion and suppress active behavior [4, 10, 19]. Recent studies by Li and Ogle [46] show that when the potential applied to C-22 is in an active region (in 2 M H_2SO_4), Ni, Cr, and Fe are released to solution, but not Mo. This indicates that a breakdown event in a passive oxide would retain Mo(W) at the breakdown site at a rate dictated by the Mo(W) content of the alloy. This is consistent with the observations of Maurice *et al.* [14] who observed the accumulation of Mo at nanoscale defects in the passive film formed on an Fe-based single crystal containing Cr, Ni, and Mo additions.

3.4.3 The role of the oxygen reduction reaction

While H^+ reduction is the dominant cathodic reaction observed in polarization curves recorded in aerated acidic solution, O_2 reduction also occurs throughout the passive region, Figure 3.8. Previously, Zhang *et al.* [38] explored the kinetics of the O_2 reduction (in neutral 5 M NaCl at 70°C) in relation to oxide film properties on alloy C-22. They found that higher rates of O_2 reduction occurred on films which had been damaged and subsequently repaired. They attributed the increased rate to either enriched Mo-species, which could catalyze the reaction, or a more defective oxide film structure. It was later shown that Mo enrichment during film breakdown is a dynamic process, meaning that Mo-species quickly accumulate, then are subsequently removed during film repair [13]. As a result, the observations made by Zhang *et al.*, as well as those in this study, indicate that it is the presence of oxide defects that leads to increased cathodic activity. Since O_2 reduction currents show little dependence on potential, Figure 3.8, and were proportional to the passive current densities (Figure 3.7(C)), it appears that the rate of O_2 reduction was dependent on the physical properties of the passive film (possibly defect structure and composition) with a possible influence of transport for alloy G-30.

3.5 Conclusion

The relationship between Cr and Mo alloying additions was investigated during the corrosion of commercially available Ni-based alloys in both neutral and acidic chloride solutions. In neutral solution, corrosion rates were found to be dependent on the Cr content at both E_{CORR} and other applied potentials. All alloys appeared to be immune to localized corrosion in neutral chloride solutions in these experiments, likely a result of the sufficiently high Mo content (≥ 5.5 wt.% Mo). In contrast to those made in the neutral solution, electrochemical measurements made in acidic chloride solution suggest that Mo becomes increasingly important to the alloy's corrosion performance and provides two distinct benefits.

Firstly, alloyed Mo was found to increase the stability of the passive film during exposure to acidic solution. During corrosion at E_{CORR}, the alloy with the highest Mo content, BC-1 (22 wt.% Mo), was found to retain a partially protective oxide film even in 1 M HCl + 2 M NaCl solution. This resulted in polarization resistance values that were approximately two orders of magnitude higher than those recorded for the alloys with lower Mo contents; C-22, G-35, and G-30. Furthermore, the impedance spectra collected on low-Mo alloys demonstrated low-frequency inductive features, consistent with a dissolution mechanism involving adsorbed intermediates. During potentiodynamic experiments, increased Mo content was found to suppress features of active dissolution and, unexpectedly, alloys G-35 and G-30 displayed a transition from net anodic to net cathodic current at applied potentials higher than the active-passive transition. The removal of O_2, the anticipated cathodic reagent, allowed us to show that, while Cr appears to dictate the properties of this film in aerated solutions, in fact it is Mo that stabilizes the film. Secondly, a higher Mo content was found to benefit the repassivation behaviour of alloys exposed to acidic chloride solution. Localized events on oxides grown at fixed potentials occur with a higher frequency and severity on low-Mo alloys.

Here, a summary of the relationship between Cr/Mo additions in commercially relevant alloys has been given. Findings suggest that a balance should be maintained between additions of Cr and Mo, although the optimal composition remains unknown. Indeed, the transient and pH-dependent nature of the Mo oxide response to corrosive conditions suggest that the optimal Cr/Mo(W) ratio may differ by exposure environment. Since localized corrosion is of concern in most applications that expose the alloy to chloride, the Mo content should be strongly considered during alloy selection for its ability to both stabilize the oxide film and repair localized breakdown sites.

3.6 References

[1] P. Marcus, Corrosion mechanisms in theory and practice, CRC Press, Boca Raton, FL, 2011.

[2] N. Priyantha, P. Jayaweera, D.D. Macdonald, A. Sun, An electrochemical impedance study of alloy 22 in NaCl brine at elevated temperature. i. corrosion behavior, *Journal of Electroanalytical Chemistry*, 572 (2004) 409-419.

[3] N. Dong, C. Zhang, H. Li, B. Zhang, P. Han, A combined experimental and first-principle study on the oxidation mechanism of super austenitic stainless steel S32654 at 900 °C, *Scientific Reports*, 7 (2018) 1-10.

[4] N. Ebrahimi, P. Jakupi, J.J. Noël, D.W. Shoesmith, The role of alloying elements on the crevice corrosion behavior of Ni-Cr-Mo alloys, *Corrosion*, 71 (2015) 1441-1451.

[5] M. Pourbaix, Atlas of electrochemical equilibria in aqueous solution, NACE, 1974. Houston, TX, 2nd English ed.,

[6] A.K. Mishra, D.W. Shoesmith, Effect of alloying elements on crevice corrosion inhibition of nickel-chromium-molybdenum-tungsten alloys under aggressive conditions: an electrochemical study, *Corrosion Science*, 70 (2014) 721-730.

[7] N. Sridhar, J.B.C. Wu, P.E. Manning, Corrosion resistant Ni-Cr-Mo alloys, *JOM*, 37 (1985) 51-53.

[8] R.B. Rebak, J.H. Payer, Passive corrosion behaviour of alloy 22, in, U.S. Department of Energy Office of Scientific and Technical Information (2006), UCRL-CONF-218309

[9] M.B. Rockel, The effect of molybdenum on the corrosion behaviour of iron-chromium alloys, *Corrosion*, 29 (1973) 393-396.

[10] X. Shan, J.H. Payer, Characterization of the corrosion products of crevice corroded alloy 22, *Journal of The Electrochemical Society*, 156 (2009) C313-C321.

[11] M. Bojinov, I. Betova, R. Raicheff, Influence of molybdenum on the transpassivity of a Fe + 12%Cr alloy in H_2SO_4 solutions, *Journal of Electroanalytical Chemistry*, 430 (1997) 169-178.

[12] K. Lutton Cwalina, C.R. Demarest, A.Y. Gerard, J.R. Scully, Revisiting the effects of molybdenum and tungsten alloying on corrosion behavior of nickel-chromium alloys in aqueous corrosion, *Current Opinions in Solid State & Materials Science*, 23 (2019) 129-141.

[13] J.D. Henderson, X. Li, D.W. Shoesmith, J.J. Noël, K. Ogle, Molybdenum surface enrichment and release during transpassive dissolution of Ni-based alloys, *Corrosion Science*, 147 (2019) 32-40.

[14] V. Maurice, H. Peng, L.H. Klein, A. Seyeux, S. Zanna, P. Marcus, Effects of molybdenum on the composition and nanoscale morphology of passivated austenitic stainless steel surfaces, *Faraday Discussions*, 180 (2015) 151-170.

[15] C.D. Taylor, P. Lu, J. Saal, G.S. Frankel, J.R. Scully, Integrated computational materials engineering of corrosion resistant alloys, *Npj Materials Degradation*, 2 (2018).

[16] X.X. Yu, A. Gulec, C.M. Andolina, E.J. Zeitchick, K. Gusieva, J.C. Yang, J.R. Scully, J.H. Perepezko, L.D. Marks, In situ observations of early stage oxidation of Ni-Cr and Ni-Cr-Mo alloys, *Corrosion*, 74 (2018) 939-946.

[17] J.W. Oldfield, W.H. Sutton, Crevice corrosion of stainless steels ii. experimental studies, *British Corrosion Journal*, 13 (1978) 104-111.

[18] M. Nishimoto, J. Ogawa, I. Muto, Y. Sugawara, N. Hara, Simultaneous visualization of pH and Cl^- distributions inside the crevice of stainless steel, *Corrosion Science*, 106 (2016) 298-302.

[19] N. Ebrahimi, J.J. Noël, M.A. Rodriguez, D.W. Shoesmith, The self-sustaining propagation of crevice corrosion on the hybrid BC1 Ni–Cr–Mo alloy in hot saline solutions, *Corrosion Science*, 105 (2016) 58-67.

[20] J.D. Henderson, N. Ebrahimi, V. Dehnavi, M. Guo, D.W. Shoesmith, J.J. Noël, The role of internal cathodic support during the crevice corrosion of Ni-Cr-Mo alloys, *Electrochimica Acta*, 283 (2018) 1600-1608.

[21] H. Huang, Surface characterization of passive film on NiCr-based dental casting alloys, *Biomaterials*, 24 (2003) 1575-1582.

[22] A.C. Lloyd, J.J. Noël, N.S. McIntyre, D.W. Shoesmith, The open-circuit ennoblement of alloy C-22 and other Ni-Cr-Mo alloys, *Journal of Metals*, 57 (2005) 31-35.

[23] A.C. Lloyd, J.J. Noël, S. McIntyre, D.W. Shoesmith, Cr, Mo and W alloying additions in Ni and their effect on passivity, *Electrochimica Acta*, 49 (2004) 3015-3027.

[24] Y. Dou, S. Han, L. Wang, X. Wang, Z. Cui, Characterization of the passive properties of 254SMO stainless steel in simulated desulfurized flue gas condensates by electrochemical analysis, XPS and ToF-SIMS, *Corrosion Science*, (2019) 108405.

[25] C.F. Baes, R.E. Mesmer, The hydrolysis of cations, Wiley, New York, 1976.

[26] A. Mishra, D.W. Shoesmith, P. Manning, Materials selection for use in concentrated hydrochloric acid, *Corrosion*, 73 (2017) 68-76.

[27] R. Newman, The dissolution and passivation kinetics of stainless alloys containing molybdenum (part ii), *Corrosion Science*, 25 (1985) 341-350.

[28] R. Newman, The dissolution and passivation kinetics of stainless alloys containing molybdenum (part i), *Corrosion Science*, 25 (1985) 331-339.

[29] C.R. Clayton, Y.C. Lu, A bipolar model of the passivity of stainless steel: the role of Mo addition, *Journal of The Electrochemical Society*, 133 (1986) 2465-2473.

[30] E. Gardin, S. Zanna, A. Seyeux, A. Allion-Maurer, P. Marcus, Comparative study of the surface oxide films on lean duplex and corresponding single phase stainless steels by XPS and ToF-SIMS, *Corrosion Science*, 143 (2018) 403-413.

[31] X. Zhang, D.W. Shoesmith, Influence of temperature on passive film properties on Ni–Cr–Mo Alloy C-2000, *Corrosion Science*, 76 (2013) 424-431.

[32] X. Zhang, D. Zagidulin, D.W. Shoesmith, Characterization of film properties on the Ni Cr Mo Alloy C-2000, *Electrochimica Acta*, 89 (2013) 814-822.

[33] J.D. Henderson, A. Seyeux, S. Zanna, M.C. Biesinger, D.W. Shoesmith, J.J. Noël, P. Marcus, Investigating the transport mechanisms governing the oxidation of Hastelloy BC-1 by in situ ToF-SIMS, *Corrosion Science*, 159 (2019) 108138.

[34] P. Jakupi, D. Zagidulin, J.J. Noël, D.W. Shoesmith, The impedance properties of the oxide film on the Ni-Cr-Mo alloy-22 in neutral concentrated sodium chloride solution, *Electrochimica Acta*, 56 (2011) 6251-6259.

[35] N. Ebrahimi, M.C. Biesinger, D.W. Shoesmith, J.J. Noël, The influence of chromium and molybdenum on the repassivation of nickel-chromium-molybdenum alloys in saline solutions, *Surface Interface Analysis*, 49 (2017) 1359-1365.

[36] K. Lutton, K. Gusieva, N. Ott, N. Birbilis, J.R. Scully, Understanding multi-element alloy passivation in acidic solutions using operando methods, *Electrochemistry Communications*, 80 (2017) 44-47.

[37] J.J. Gray, C.A. Orme, Electrochemical impedance spectroscopy study of the passive films of alloy 22 in low pH nitrate and chloride environments, *Electrochimica Acta*, 52 (2007) 2370-2375.

[38] X. Zhang, Z. Qin, D. Zagidulin, J.J. Noël, D.W. Shoesmith, Effect of oxide film properties on the kinetics of O_2 reduction on alloy C-22, *Journal of The Electrochemical Society*, 164 (2017) C911-C917.

[39] M.E. Orazem, B. Tribollet, Electrochemical impedance spectroscopy, Wiley, New York, 2017.

[40] B. Hirschorn, M.E. Orazem, B. Tribollet, V. Vivier, I. Frateur, M. Musiani, Determination of effective capacitance and film thickness from constant-phase-element parameters, *Electrochimica Acta*, 55 (2010) 6218-6227.

[41] G.J. Brug, A.L.G. van den Eeden, M. Sluyters-Rehbach, J.H. Sluyters, The analysis of electrode impedances complicated by the presence of a constant phase element, *Journal of Electroanalytical Chemistry and Interfacial Electrochemistry*, 176 (1984) 275-295.

[42] M. Bojinov, G. Fabricius, T. Laitinen, T. Saario, G. Sundholm, Conduction mechanism of the anodic film on chromium in acidic sulphate solutions, *Electrochimica Acta*, 44 (1998) 247-261.

[43] A.K. Mishra, D.W. Shoesmith, The activation/depassivation of nickel-chromium-molybdenum alloys: an oxyanion or a pH effect - part ii, *Electrochimica Acta*, 102 (2013) 328-335.

[44] A.K. Mishra, S. Ramamurthy, M. Biesinger, D.W. Shoesmith, The activation/depassivation of nickel-chromium-molybdenum alloys in bicarbonate solution - part i, *Electrochimica Acta*, 100 (2013) 118-124.

[45] E. McCafferty, Introduction to corrosion science, Springer, New York, 2010.

[46] X. Li, K. Ogle, The Passivation of Ni-Cr-Mo Alloys: Time resolved enrichment and dissolution of Cr and Mo during passive-active cycles, *Journal of The Electrochemical Society*, 166 (2019) C3179-C3185.

[47] E. McCafferty, Relationship between graph theory and percolation approaches in the passivity of Fe–Cr binary alloys, *Journal of The Electrochemical Society*, 155 (2008) C501.

[48] E. McCafferty, Oxide networks, graph theory, and the passivity of Ni–Cr–Mo ternary alloys, *Corrosion Science*, 50 (2008) 3622-3628.

[49] M. Urquidi, D.D. Macdonald, Solute-vacancy interaction model and the effect of minor alloying elements on the initiation of pitting corrosion, *Journal of The Electrochemical Society*, 132 (1985) 555-558.

[50] D.C. Silverman, Corrosion prediction in complex environments using electrochemical impedance spectroscopy, *Electrochimica Acta*, 38 (1993) 2075-2078.

[51] A. Pardo, M.C. Merino, A.E. Coy, F. Viejo, R. Arrabal, E. Matykina, Effect of Mo and Mn additions on the corrosion behaviour of AISI 304 and 316 stainless steels in H_2SO_4, *Corrosion Science*, 50 (2008) 780-794.

[52] G. Bellanger, J.J. Rameau, Effect of slightly acid pH with or without chloride in radioactive water on the corrosion of maraging steel, *Journal of Nuclear Materials*, 228 (1996) 24-37.

[53] S. Naharajan, N. Rajendran, Crevice corrosion behaviour of superaustenitic stainless steels: dynamic electrochemical impedance spectroscopy and atomic force microscopy studies, *Corrosion Science*, 51 (2009) 217-224.

[54] G. Cordeiro, O.R. Mattos, Anodic dissolution of nickel in concentrated sulfuric acidic solutions, *Journal of Applied Electrochemistry*, 26 (1996) 1083-1092.

[55] M.R. Barbosa, J.A. Bastos, J.J. Garcia-Jareno, F. Vicente, Chloride role in the surface of nickel electrode, *Electrochimica Acta*, 44 (1998) 957-965.

[56] J.A.L. Dobbelaar, J.H.W. de Wit, Impedance measurements and analysis of the corrosion of chromium, *Journal of The Electrochemical Society*, 137 (1990) 2038-2046.

[57] A.I. Karayan, E. Maya-Visuet, H. Castaneda, Transpassivity characterization of the alloy UNS N08367 in a chloride-containing solution, *Journal of Solid State Electrochemistry*, 18 (2014) 3191-3202.

[58] M. Bojinov, I. Betova, R. Raicheff, A model for the transpassivity of molybdenum in acidic sulphate solutions based on ac impedance measurements, *Electrochimica Acta*, 41 (1996) 1173-1179.

[59] R.D. Armstrong, M.F. Bell, A.A. Metcalfe, The anodic dissolution of molybdenum in alkaline solutions - electrochemical measurements, *Journal of Electroanalytical Chemistry*, 84 (1977) 61-72.

[60] P. Jakupi, F. Wang, J.J. Noël, D.W. Shoesmith, Corrosion product analysis on crevice corroded alloy-22 specimens, *Corrosion Science*, 53 (2011) 1670-1679.

[61] G. Frankel, G. Thornton, S. Street, T. Rayment, D. Williams, A. Cook, A. Davenport, S. Gibbon, D. Engelberg, C. Ornek, A. Mol, P. Marcus, D. Shoesmith, C. Wren, K. Yliniemi, G. Williams, S. Lyon, R. Lindsay, T. Hughes, J. Lutzenkirchen, S.T. Cheng, J. Scully, S.F. Lee, R. Newman, C. Taylor, R. Springell, J. Mauzeroll, S. Virtanen, S. Heurtault, J. Sullivan, Localised corrosion: general discussion, *Faraday Discussions*, 180 (2015) 381-414.

[62] J.R. Scully, Corrosion chemistry closing comments: opportunities in corrosion science facilitated by operando experimental characterization combined with multi-scale computational modelling, *Faraday Discussions*, 180 (2015) 577-593.

[63] D.D. Macdonald, Some personal adventures in passivity—A review of the point defect model for film growth, *Russian Journal of Electrochemistry*, 48 (2012) 235-258.

Chapter 4

4 Molybdenum surface enrichment and release during transpassive dissolution of Ni-based alloys

(Henderson (*et al.*), *Corros. Sci.*, **2019**, 147, 32-40.)

Abstract:

The role of alloyed Mo during transpassive dissolution of four commercially available Ni-based alloys in neutral chloride solution was investigated by atomic emission spectroelectrochemistry. Time-resolved dissolution rates of Ni, Cr, Mo, and Fe were obtained as a function of applied potential. Mo enrichment occurred at the transpassive potentials and redissolved when the potential returned to the passive domain. These results suggest a mechanism of Mo enrichment and release that could play a significant role in repassivation in initially neutral electrolytes such as occurs during crevice corrosion. It is proposed that Mo precipitation and redissolution are driven by local pH changes.

4.1 Introduction

Ni-based alloys are frequently used to replace conventional steels when service conditions become aggressive and high corrosion rates ensue. Applications include, but are not limited to, the nuclear, petrochemical, and chemical processing industries. These alloys, which differ mainly in composition, are continuously being modified to improve corrosion and/or mechanical properties [1,2]. However, successfully tailoring composition to a given application requires the thorough understanding of how individual alloying elements affect behavior. Chromium is, of course, the most significant constituent as concerns corrosion resistance, and its role in passivity has been thoroughly documented [3,4]. The significance of the other alloying elements, such as Fe and Mo, on corrosion resistance is less well understood. These elements may be of critical importance in the transpassive potential domain, where the electrochemical conversion of the Cr(III) oxide into soluble Cr(VI) species occurs [3,5,6], making the Cr(III) based passive film less stable. This may be problematic for some industrial applications in which the Ni alloy is exposed to electrolytes containing large amounts of oxidizing impurities, resulting in high corrosion potentials [7,8].

Molybdenum, in particular, remains an interesting alloying component, as it is well known to enhance corrosion resistance. For example, in the empirically defined PREN (pitting resistance equivalent number) for both Ni-based alloys and stainless steels, the %Mo counts 3.3x the %Cr [2,6,9]. Nevertheless, the exact mechanisms by which Mo increases the corrosion resistance remain elusive. Benefits of Mo addition include the suppression of active dissolution and increased resistance to localized corrosion [3,10]. Among the proposed mechanisms, two concepts are frequently discussed. First, Mo has been suggested to concentrate at defect sites of the oxide film, acting as a reinforcement or filler at defect locations in the oxide [11,12]. Second, Mo oxides, found in the outer portion of Cr-dominated oxide films, are believed to provide a cation-selective nature to the oxide film, preventing the ingress of aggressive Cl^- ions [13,14].

The mechanism of passivation for Fe-Cr and Ni-Cr alloys involves a selective dissolution of Fe and Ni, leaving behind a Cr(III) oxide film [15-17]. For austenitic stainless steel, it has been suggested that when the passive film is breached, Mo oxides form a temporary protective film which slows down active dissolution sufficiently to allow the Cr(III) passive film to reform [18]. This is important in the mechanism of pitting and crevice corrosion in that the local electrolyte conditions may not favor the spontaneous formation of a Cr(III) oxide film and this temporary protection could be a determining factor in the corrosion resistance.

This temporary protection hypothesis suggests that the release mechanism of Mo could therefore play a critical role in the corrosion resistance of Cr-Mo alloys of Ni or Fe. At present, studies of the effect of Mo have been limited to conventional electrochemistry and *ex situ* surface analysis. While these studies demonstrated a tendency of Mo to concentrate at the oxide/solution interface, no kinetic information concerning its release and its build-up on the surface have been presented, to our knowledge [19-21].

In this work, atomic emission spectroelectrochemistry (AESEC) was used to give, for the first time, a quantitative observation of Mo retention and release during the transpassive dissolution of commercial Ni-Cr-Mo alloys. These findings demonstrate that Mo is enriched at the surface during the onset of transpassive dissolution. During repassivation, the surface-enriched Mo was selectively removed. Notably, the degree of Mo enrichment and subsequent dissolution at the surface were found to increase with increasing Fe content of the alloy. This was attributed to the rapid hydrolysis of Fe(III) compared to Ni(II), leading to an increased local acidification, which is known to promote the deposition of Mo-species.

4.2 Experimental

4.2.1 Materials

Alloys used in this study were provided by Haynes International (Kokomo, IN, USA) in the form of mill-annealed sheets. Coupons were cut to dimensions of 25 × 10 mm^2 to fit in the requirements of the flow cell. Coupon thickness varied between 5 and 10 mm, based on the thickness of the original sheet. The nominal composition of each alloy, as reported by Haynes International, is provided in Table 4.1.

Table 4.1 - Nominal compositions (wt.%) as reported by Haynes International. M indicates the maximum concentration of an individual alloying element, while, Bal. indicates the alloying element making up the balance due to fluctuations in composition.

Alloy	**Ni**	**Cr**	**Mo**	**Fe**	**W**	**Cu**	**Nb**	**Co**	**Mn**	**V**	**Al**	**Si**	**C**
BC-1	Bal.	15	22	2^M	--	--	--	--	0.25	--	0.5^M	0.08^M	0.01^M
C-22	Bal.	22	13	3	3	0.5^M	--	2.5^M	0.5^M	0.35^M	--	0.08^M	0.01^M
G-35	Bal.	33.2	8.1	2^M	0.6	0.3^M	--	1^M	0.5^M	--	0.4^M	0.6^M	0.05^M
G-30	Bal.	30	5.5	15	2.5	2	0.8	5	1.5	--	--	0.8^M	0.03^M

Since the analysis of AESEC data relies heavily on the use of accurate compositions, *i.e.*, for normalization purposes, the precise composition of each alloy was determined by glow discharge optical emission spectroscopy (GD-OES) and is given in Table 4.2. For discussion purposes both compositions (Table 4.1, Table 4.2) are included here.

Table 4.2 - Alloy composition (wt.%) as obtained by GD-OES compositional analysis.

Alloy	**Ni**	**Cr**	**Mo**	**Fe**	**W**	**Cu**	**Nb**	**Co**	**Mn**	**V**	**Al**	**Si**	**C**
BC-1	59.7	16.5	22.3	0.76	0.01	0.007	0.03	0.17	0.27	0.02	0.19	<0.01	<0.01
C-22	52.7	25.1	13.8	3.79	3.09	0.04	0.03	0.65	0.25	0.20	0.20	0.02	0.01
G-35	52.7	36.5	8.5	0.78	0.04	0.01	0.05	0.38	0.45	0.04	0.23	0.22	0.05
G-30	38.03	31.4	5.5	15.9	2.8	1.8	0.81	2.1	1.21	0.06	0.16	0.24	0.014

Prior to each measurement, coupons were ground using wet SiC paper, with the final surface preparation using P1200 grit. Coupons were then rinsed with deionized (DI) water (18.2 MΩ cm), followed by EtOH, and dried in a stream of N_2 gas. Careful surface preparation produced reproducible surface conditions and ensured a proper seal between the coupon and flow cell.

Solutions were prepared using reagent grade NaCl (Carl Roth GmbH) and DI water. Standard solutions, used to quantify inductively coupled plasma atomic emission spectrometer (ICP-AES) data, were prepared using aliquots of metal standards (SCP Science) in the experimental electrolyte (1 M NaCl). Calibration was performed immediately following each experiment.

4.2.2 Electrochemical measurements

Electrochemical measurements were made using either a Gamry Reference 600 (for AESEC) or a Biologic VSP potentiostat (conventional electrochemistry). All electrochemical measurements were carried out in a custom-built PTFE flow cell designed for use with the AESEC setup. The flow cell, briefly summarized below, has been extensively detailed elsewhere [22,23]. The working electrode (WE) was affixed to the flow cell with an exposed surface area of 1 cm^2 by the application of a fixed pneumatic pressure against an O-ring. A second compartment, isolated from the flow cell compartment by a porous membrane, housed the reference (RE) and counter electrodes (CE). A saturated Ag/AgCl electrode (0.197 V vs SHE) served as the RE against which all potentials were measured. A platinum flag was used as the CE. All electrochemical experiments described herein were repeated at least twice.

The temperature was maintained at approximately 75 °C by placing the experimental electrolyte in an isothermal circulating bath. During the experimental procedure, electrolyte introduced to the flow cell was drawn directly from the reservoir housed within the isothermal bath. Additionally, a hollowed Cu heating disk, connected to the circulating component of the isothermal bath, was fixed behind the WE. Together, this maintained the temperature of the WE and electrolyte at approximately 75 °C during all measurements. The flow rate was controlled using the built-in peristaltic pump of the ICP-AES instrument. Prior to each experiment the flow rate was calibrated to be approximately 2.75 mL min^{-1}.

Cyclic polarization experiments were initiated 0.100 V vs Ag/AgCl below the corrosion potential and scanned positively at a scan rate of 0.5 mV s^{-1}, until a potential of 1 V vs Ag/AgCl was reached. The scan was then reversed, and the potential scanned negatively until it reached the initial $E_{i=0}$. Separate potentiostatic experiments were conducted using three potential steps. Initially, samples were held in the passive region 0.300 V vs Ag/AgCl for 5 min. Subsequently, samples were brought into the transpassive domain 1.00 V vs Ag/AgCl for a period of 1, 2, or 4 min, indicated for each experiment. Finally, the return to the initial applied potential 0.300 V vs Ag/AgCl caused the sample to repassivate.

4.2.3 AESEC measurements and data treatment

Details regarding the data acquisition and treatment have been described by Ogle *et al.* [22]. Briefly, the downstream positioning of the ICP-AES instrument, an Ultima 2C spectrometer (Horiba Jobin-Yvon, France), allows for the detection of cations released from the WE in real-time. A Burgener PEEK Mira Mist® Nebulizer (Horiba Jobin-Yvon, France) was used to introduce electrolyte leaving the flow cell into the ICP. The resultant aerosol enters a 40.68 MHz inductively coupled Ar plasma, operating at 1.2 kW. Independent monochromator and polychromator optics were used to monitor emission lines from the ICP torch. The monochromator was used for a single element with high spectral resolution, in this case Mo, while the polychromator was used to simultaneously detect other elements of interest. Emission lines used for the elements of interest and their respective limits of detection are summarized in Table 4.3. The detection limit ($C_{3\sigma}$) was calculated according to Equation 4.1, where σ_B is the standard deviation of the background signal and κ the sensitivity factor determined from the calibration standards.

$$C_{3\sigma} = 3\frac{\sigma_B}{\kappa} \tag{4.1}$$

Table 4.3 - Experimental emission lines and limits of detection.

Element	Wavelength /nm	Detection Limit, $C_{3\sigma}$ /ppb	Equivalent, i_M /µA
Ni	231.60	22.8	1.9
Cr	267.72	10.0	0.93
Mo	202.03	4.61	0.23
Fe	259.94	9.40	0.81

Upon completion of AESEC experiments, instantaneous emission intensities for each metal were converted into instantaneous concentrations (C_M) by standard calibration. C_M values were then converted into instantaneous dissolution rates (ν_M) according to Equation 4.2, where f is the flow rate and A the surface area:

$$\nu_M = f\frac{C_M}{A} \tag{4.2}$$

Congruent and incongruent dissolution behaviour were distinguished by comparing the composition of the electrolyte to that of the bulk material. This was done by normalizing individual dissolution rates against that of the bulk alloying element, Ni, according to Equation 4.3.

$$\nu'_M = \left({}^{X_{Ni}}/_{X_M}\right)\nu_M \tag{4.3}$$

where X_M is the mass fraction of element M as determined by GD-OES (Table 4.2). Perfect congruent dissolution occurs when $\nu'_M = \nu_{Ni}$, *i.e.*, the two are dissolving at equal rates relative to the bulk composition. If $\nu'_M > \nu_{Ni}$, it implies the selective dissolution of alloying element M as compared to the bulk alloy composition. In contrast, $\nu'_M < \nu_{Ni}$ implies that excess M is concentrating at the surface. The quantity of excess M, Θ_M, at time, t, may be determined by mass balance as:

$$\Theta_{M} = \int_{0}^{t} \left(\left({}^{X_{M}}/_{X_{Ni}} \right) \nu_{Ni} - \nu_{M} \right) dt \qquad (4.4)$$

The elemental current density or metal M, i_M, was determined by conversion of the corresponding instantaneous dissolution rate (ν_M) according to Equation 4.5:

$$i_M = \frac{\nu_M\, F\, n}{m} \qquad (4.5)$$

where F is Faraday’s constant, m the molar mass of metal M and n the number of electrons transferred in the oxidation reaction of metal M. The later assumes that the oxidation state of the dissolved M is known or may be surmised from equilibrium calculations. This is a formal definition only, as dissolution may occur via non-faradaic processes such as the dissolution of oxide films.

4.3 Results

4.3.1 Cyclic polarization

The polarization behavior of BC-1, C-22, and G-35, is shown in Figure 4.1(A) and that of G-30, in Figure 4.1(B). All four alloys exhibited passive behavior, with the alloys of higher Cr content having higher potentials of zero current, $E_{i=0}$, and lower passive current densities, i_{pass}, consistent with previous studies [5]. Table 4.4 summarizes the values of $E_{i=0}$ and i_{pass} for the different alloys. The anodic branch of the polarization curves may be divided into three potential domains: (1) a passive domain from $E_{i=0}$ to approximately 0.300 V vs Ag/AgCl, (2) a second passive domain starting near 0.300 V vs Ag/AgCl, indicated by an increase in the anodic current followed by a current plateau; and (3) the transpassive domain, indicated by a steady increase in the current, beginning at

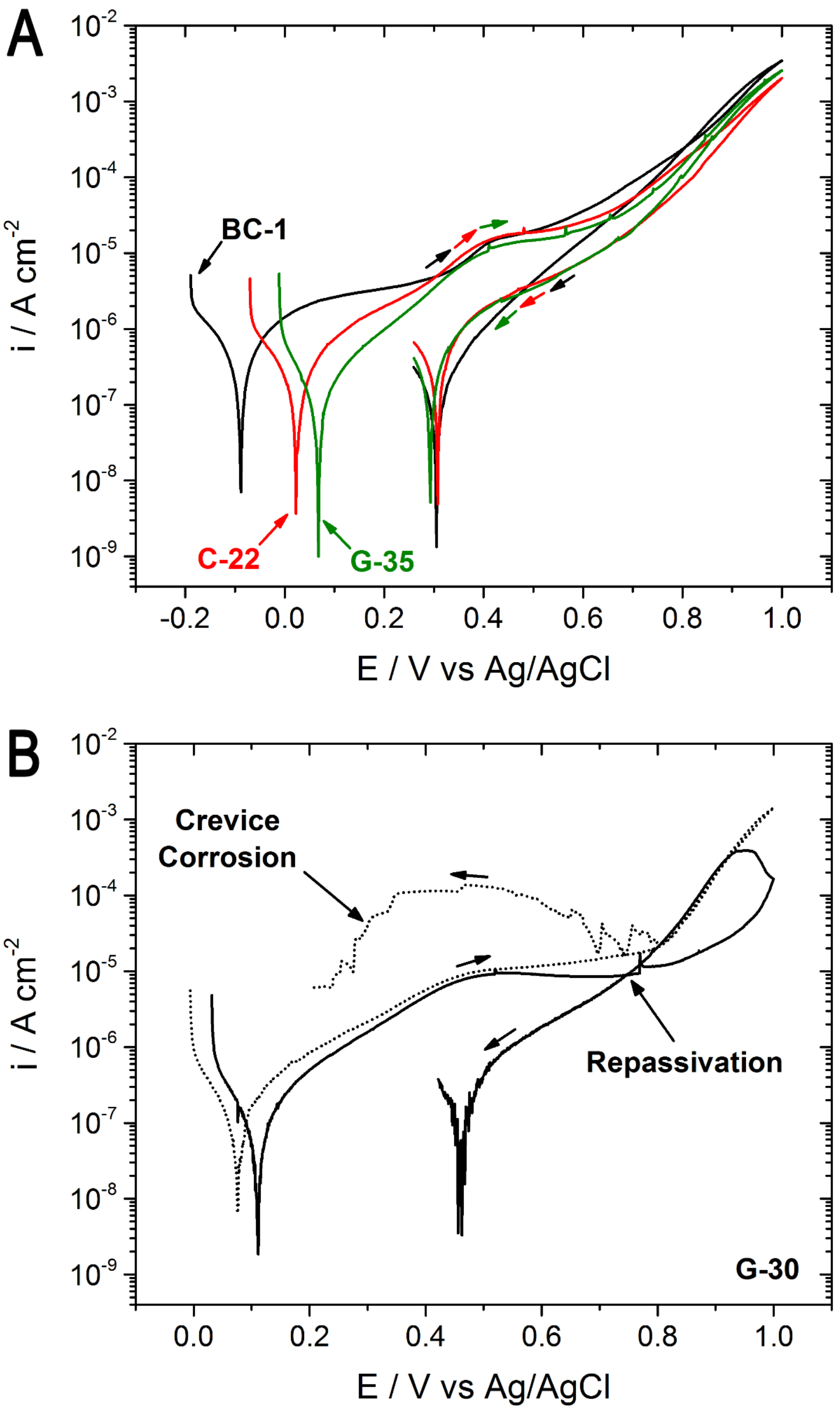

Figure 4.1 - (A) Cyclic polarization behaviour of alloy (A) BC-1, C-22, G-35, and (B) G-30 in 1 M NaCl at 75 °C.

approximately 0.600 V for alloys BC-1, C -22, and G-35, and at 0.800 V vs Ag/AgCl for alloy G-30. The extended passive region of G-30 is believed to be the result of Fe(III) oxide stability at high potentials [24].

Return scans showed a ready repassivation for alloys BC-1, C-22, and G-35, without significant hysteresis. This was indicated by the current density retracing the forward scan until ultimately achieving values lower than those recorded during the forward scan. In all cases, $E_{i=0}$ was shifted positive relative to its value on the forward scan. Interestingly, all three alloys exhibited approximately the same $E_{i=0}$ values on the reverse scan. The decreased current densities observed on the reverse scan have been attributed to the repair of the Cr(III) barrier layer [25].

Table 4.4 - Approximate potential of zero current on the forward scan, $E_{i=0}$, and passive current density, i_{pass}, estimated at 0.200 V vs Ag/AgCl. Values are averaged over repeat experiments.

Alloy	**$E_{i=0}$ / V**	**i_{pass} / A cm^{-2}**
BC-1	−0.090	3.4×10^{-6}
C-22	0.019	1.9×10^{-6}
G-35	0.066	9.7×10^{-7}
G-30	0.076	8.6×10^{-6}

The reverse scan on alloy G-30 (Figure 4.1(B)) showed an interesting irreproducibility: It was frequently found to have hysteresis or a complete loss of I-E relationship, as shown by the solid and dotted curves, respectively. Both behaviors suggest the onset of localized corrosion processes, with one eventually repassivating (solid line) and the other becoming self-sustaining (dotted line). The process occurring during the self-sustaining localized process was confirmed to be crevice corrosion by optical observations of damage along the impression of the O-ring. Since crevice corrosion itself is not the focus of the present work, only AESEC data in which active crevice corrosion was not observed are discussed.

Within the passive region, no metal cations were detected by ICP-AES. This was attributed to the low corrosion rates afforded by the Cr-rich oxide film present in this region. Only at transpassive potentials (*i.e.*, the breakdown of the secondary passive region) were cations detected, approximately 0.600 V for alloys BC-1, C-22, and G-35, and 0.800 V vs Ag/AgCl for alloy G-30. Polarization in the transpassive domain led to an exponential increase in dissolution rates as a function of potential. The resultant AESEC data for cyclic polarization experiments is shown in Figure 4.2. All alloys demonstrate patterns of incongruent dissolution, indicated by $\nu'_{M} \neq \nu_{Ni}$. Comparison of normalized rates reveals the decreased dissolution rate of Cr, Mo, and Fe, relative to Ni, suggesting the enrichment of these elements at the electrode surface. In other words, Ni was selectively removed from the oxide during transpassive dissolution while other alloying elements were enriched, at least to some extent.

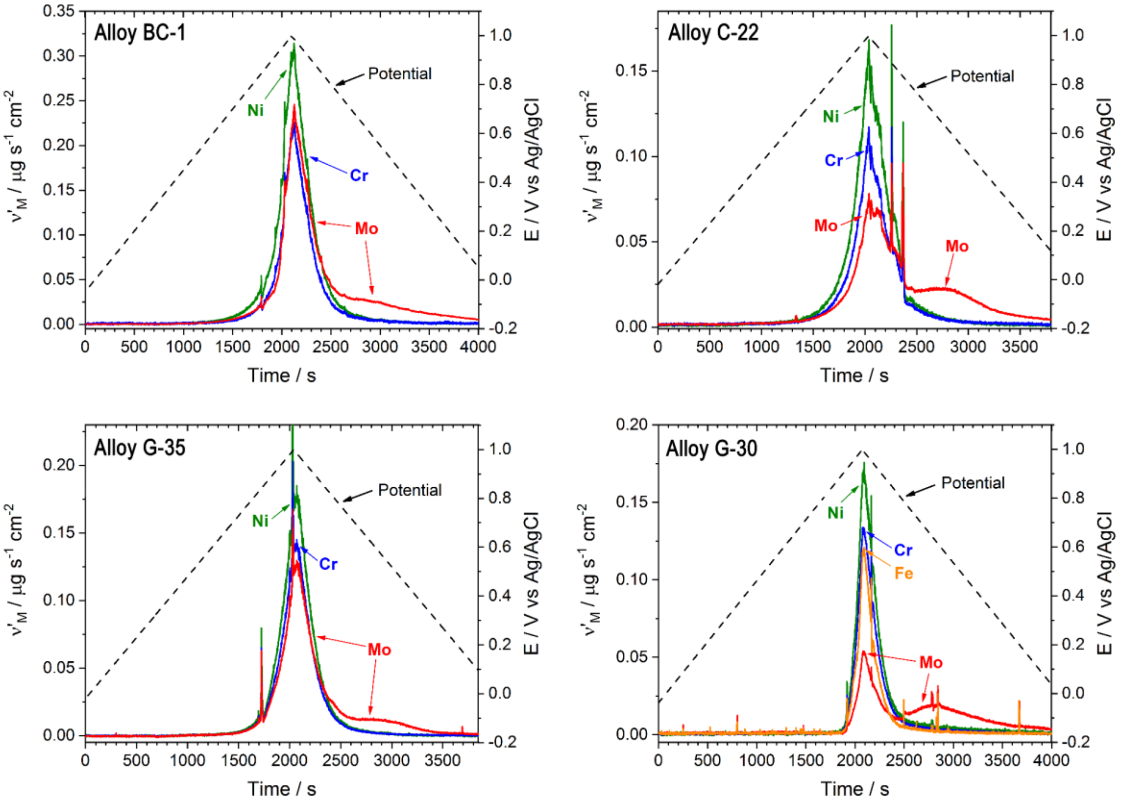

Figure 4.2 - Normalized dissolution rates of alloys BC-1, C-22, G-35, and G-30, during cyclic polarization experiments in 1 M NaCl at 75 °C. All dissolution rates are normalized against the bulk material, Ni, Equation 4.3.

Of particular interest in Figure 4.2, and the focus of this article, is the unusual behavior of Mo during the reverse scan. Interestingly, repassivation resulted in ν'_{Mo} becoming larger than ν_{Ni}, suggesting the selective dissolution of Mo. While repassivation resulted in receding values of ν_{Ni}, ν'_{Cr}, and ν'_{Fe}, the elevated rates of Mo dissolution persisted for some time following repassivation. While Mo appears to be initially retained at the surface during transpassive dissolution, it is subsequently released during repassivation. This feature is particularly pronounced for alloy G-30, and a thorough discussion of normalized data is conducted below for potentiostatic experiments.

4.3.2 Potentiostatic polarization

To better quantify the kinetics and mechanism of Mo retention and dissolution, a four-step potentiostatic experiment was performed: (1) the WE was held in the passive region (0.300 V vs Ag/AgCl) for 300 s to obtain a steady-state passive film; (2) the potential was then stepped to the transpassive domain (1.00 V vs Ag/AgCl) for 120 s; (3) the WE was returned to the passive region, and (4) finally released to open-circuit. The resulting data, expressed as normalized dissolution rates and elemental currents, are presented in Figure 4.3, Figure 4.4, respectively.

In the analysis of the normalized dissolution data, the observations are similar to those made during cyclic experiments. Notably, potentiostatic experiments avoided complications arising from localized processes apparent in potentiodynamic experiments. While samples were held in the passive region, step 1, no metal cations were detected by ICP-AES. Following the application of the transpassive potential, step 2, all alloys demonstrated a surge of metal dissolution. The relative intensities of the normalized dissolution rates were similar to those found during cyclic experiments. In all cases, Ni was found to be the dominant cation released from the WE, while Cr, Mo, and Fe were apparently retained, to some extent, at the surface. Of the alloying elements monitored, Mo showed the greatest tendency for surface enrichment. During repassivation all alloys exhibited the selective dissolution of Mo species as shown in Figure 4.3, interpreted as a subsequent release of surface enriched Mo. The extent of Mo retention and release was greatest for alloy G-30 and quite significant for C-22. Interestingly, this process did not correlate directly with the Mo content of the alloy.

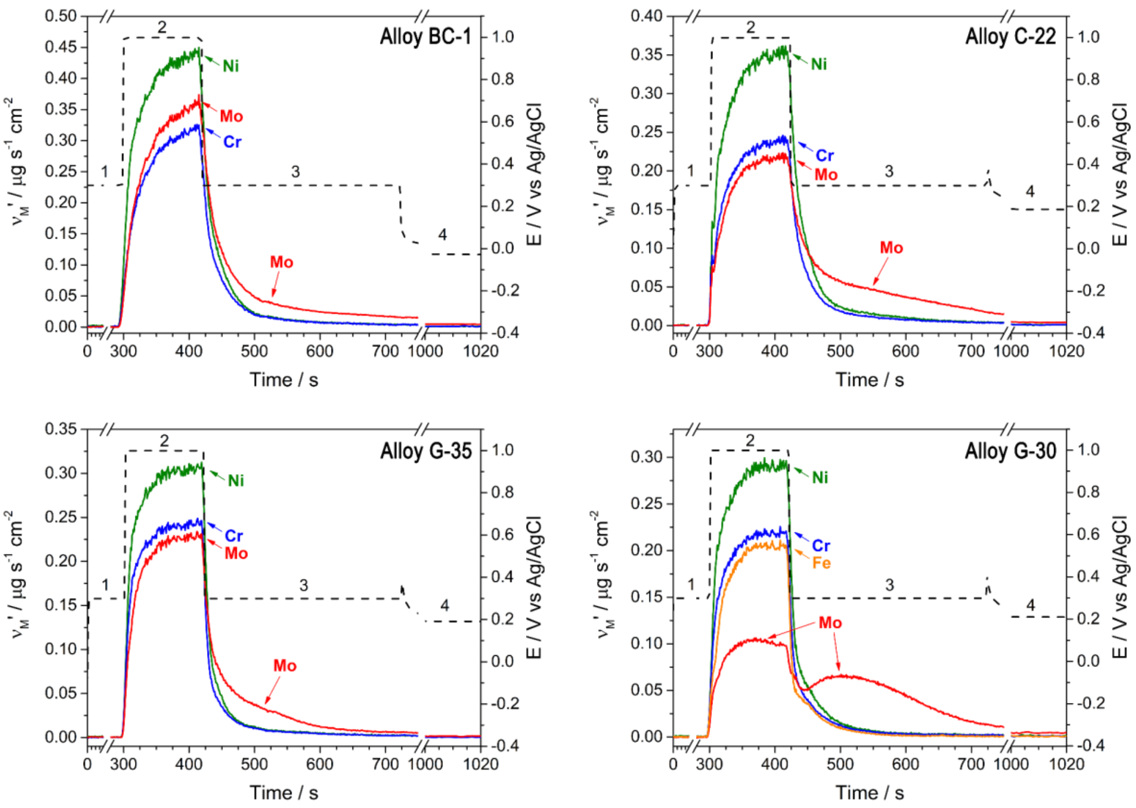

Figure 4.3 - Normalized dissolution rates of alloys BC-1, C-22, G-35, and G-30, during potentiostatic polarization experiments in 1 M NaCl at 75 °C. All dissolution rates are normalized against the bulk material, Ni, Equation 4.3.

Additionally, the stoichiometry of dissolution was monitored with ICP-AES during potentiostatic experiments. To directly compare the elemental current densities, i_M, to the electrical current density, i_e, a convolution procedure was carried out. Details of this convolution have been published previously [22]. Briefly, convolution involves correcting the instantaneous electrical current density, i_e, for the distribution of residence times in the flow cell. In this way, the elemental current densities, i_M, may be compared directly with the convoluted electrical current density, i_e^*. As shown in Figure 4.4, significant currents were detected only after the application of the transpassive potential. The convoluted electrical current density recorded by the potentiostat, i_e^*, the current contributed by individual alloying elements, i_M, and the sum current from all elemental currents, i_Σ, are compared in Figure 4.4. Values of i_M were calculated according to the following oxidation states: Ni(II), Cr(VI), Mo(VI), and Fe(III). Oxidation state information was based on both thermodynamics as well as findings in the literature [20,24]. Since dissolution prior to the transpassive domain was negligible, oxidation states were selected based on the environment for transpassive dissolution.

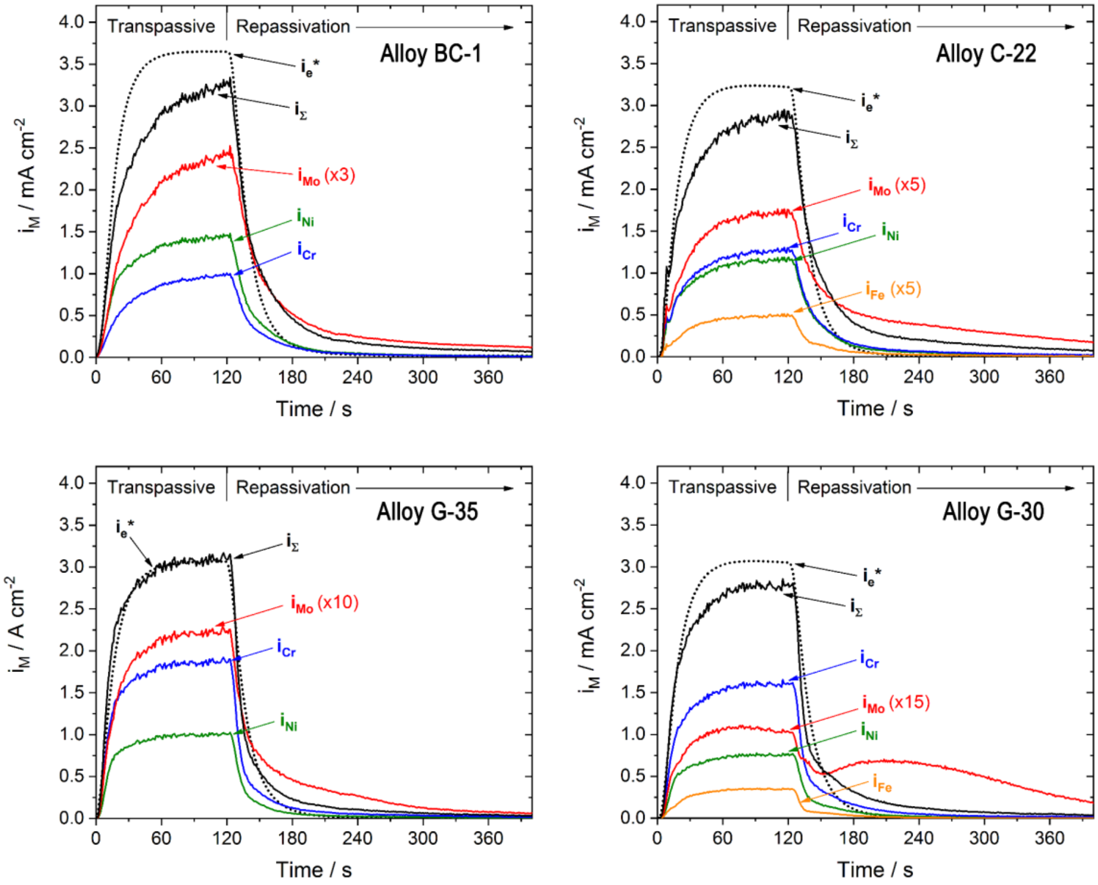

Figure 4.4 - Instantaneous elemental, i_M, sum, i_Σ, and convoluted electrochemical current, i_e*, for potentiostatic polarization experiments in 1 M NaCl at 75 °C.

Using the dissolution rates and elemental currents obtained during potentiostatic experiments, information on alloy composition and faradaic yield was extracted. A summary of this information is detailed in Table 4.5. Using elemental dissolution rates, the total dissolved metal was used to determine a relative alloy composition for comparison to the compositions provided by Haynes International and GD-OES analysis, Table 4.1 and 4.2 respectively. Since in the ICP-AES data, only Ni, Cr, Mo, and Fe were quantified, the compositions provided by Haynes International and by GD-OES analysis were reweighted for a valid comparison. As shown in Table 4.5, the reweighted compositions are in agreement with only minor discrepancies. Since AESEC data shows dissolution occurs incongruently, the alloy composition determined by ICP-AES is expected to be affected by surface enrichment processes. For example, the surface enrichment of Cr species, highlighted in AESEC data above, leads to a consistently lower Cr content in ICP-AES analysis. Important for the upcoming discussion section is the low amount of Fe detected for alloys BC-1 and G-35 by both GD-OES and ICP-AES. As reported by Haynes, these alloys are expected to contain a maximum concentration of 2% Fe, however, based on both GD-OES and ICP-AES data presented here, the Fe content is in fact much lower, approximately 0.6%.

Table 4.5 - Reweighted alloy compositions, considering Ni, Cr, Mo, and Fe, and faradaic yields determined for potentiostatic experiments shown in Figure 4.3 and Figure 4.4.

Alloy	Source	Ni /%	Cr /%	Mo /%	Fe /%	Faradaic Yield /%
BC-1	Haynes Int.	62.6	15.2	22.2	--	92.2
	GD-OES	60.1	16.7	22.4	0.7	
	ICP-AES	64.6	12.7	22.6	0.5	
C-22	Haynes Int.	59.6	23.4	13.8	3.2	98.4
	GD-OES	55.2	26.3	14.5	3.9	
	ICP-AES	62.7	20.3	13.7	3.3	
G-35	Haynes Int.	58.4	33.4	8.2	--	95.8
	GD-OES	53.2	37.1	8.6	0.8	
	ICP-AES	59.1	32.5	8.4	0.6	
G-30	Haynes Int.	46.0	32.1	5.9	16.0	105.6
	GD-OES	41.9	34.6	6.0	17.5	
	ICP-AES	49.9	31.2	5.2	13.8	

In addition to comparing the re-weighted alloy compositions, faradaic yields were determined by the direct comparison of i_e^* and i_Σ from Figure 4.4. The values obtained for alloys BC-1, C-22, G-35, and G-30 are shown in Table 4.5. The average faradaic yield, 98.0%, implies that the metallic dissolution measured by ICP-AES is in good agreement with the instantaneous current densities recorded by the potentiostat. However, minor discrepancies in faradaic yields may be the result of additional anodic processes undetected by the ICP-AES, *e.g.*, O_2 evolution or oxide formation.

4.3.3 Mo enrichment

As detailed in the discussion of Figure 4.3, the high degree of Mo-enrichment observed for alloy G-30, made this alloy ideal for the further study of enrichment/dissolution phenomenon. Additional experiments were conducted as a function of time spent in the transpassive domain, shown in Figure 4.5. Generally, as time spent in the transpassive domain increased, so did the signal corresponding to Mo dissolution during repassivation.

Direct comparison of the enrichment and dissolution of Mo is possible by considering the excess Mo, Θ_{Mo}, during steps 2 and 3, enrichment and dissolution, respectively. The calculation of excess Mo was made according to Equation 4.4. In step 2, the degree of enrichment is visualized as the difference between the integrals of Ni and Mo dissolution rates. In step 3, the dissolution of surface-enriched Mo is the difference between Mo and Ni dissolution rates. For clarity, the regions considered as enrichment and dissolution are graphically depicted in Figure 4.6(A).

Values corresponding to enrichment and dissolution are compared in Figure 4.6(B) as a function of time polarized in the transpassive region. The amount of Mo-enrichment was found to be proportional to the time spent in the transpassive region. The dissolution process followed a similar relationship; however, it was consistently lower than the degree of enrichment. Comparison of the two values of Θ_{Mo} yields a percent difference of between 40.2 and 56.8%. Discrepancy between these values suggests that the surface-enriched Mo species are not completely removed during repassivation. This implies that previous studies, which demonstrated enrichment of Mo in the oxide following transpassive polarization, have likely underestimated the extent of Mo-enrichment during transpassive dissolution. In such experiments, immediately following the application of a transpassive potential, the relaxation of the WE to a passive potential and subsequent repassivation can be expected to initiate the release of Mo species. This process is anticipated to occur rapidly prior to the removal of the WE from solution.

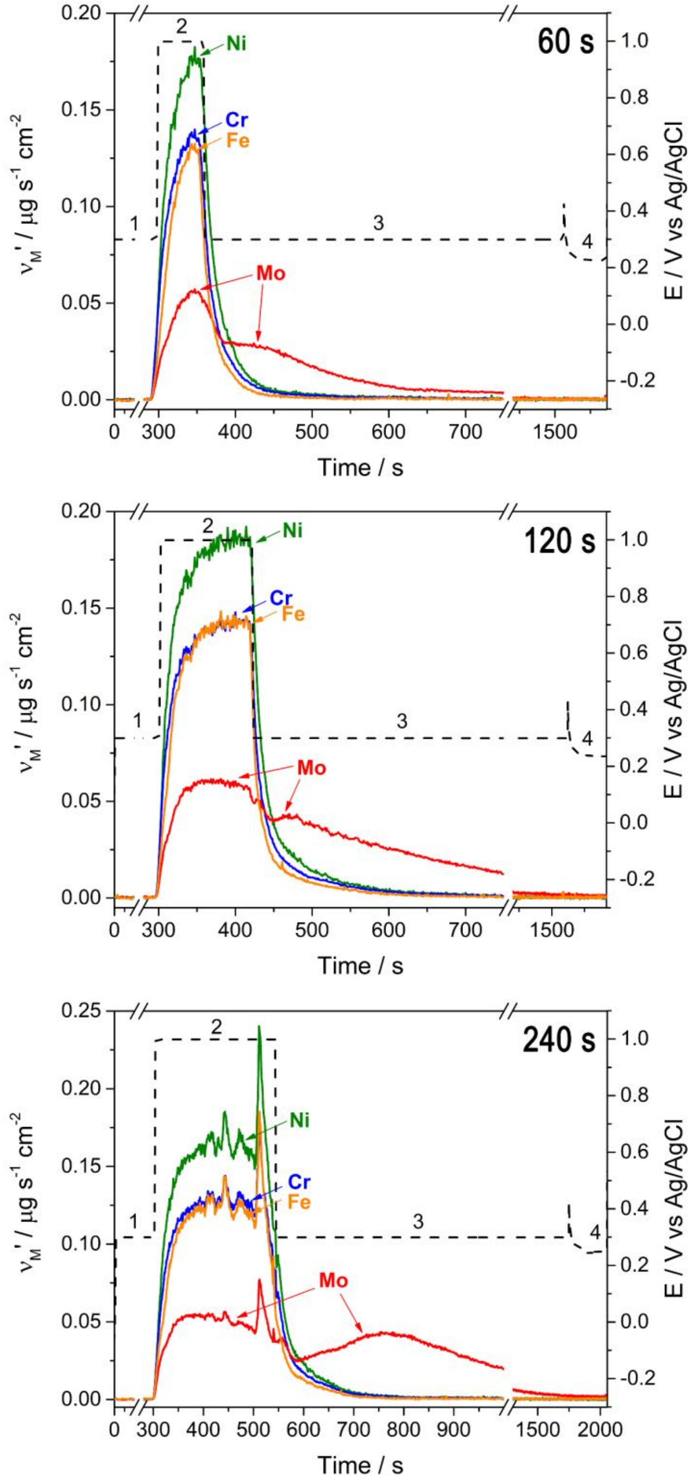

Figure 4.5 - Normalized dissolution rates of alloy G-30 in 1 M NaCl at 75 °C with varied times polarized in the transpassive region, identified as step 2. All dissolution rates are normalized against the bulk material, Ni, Equation 4.3.

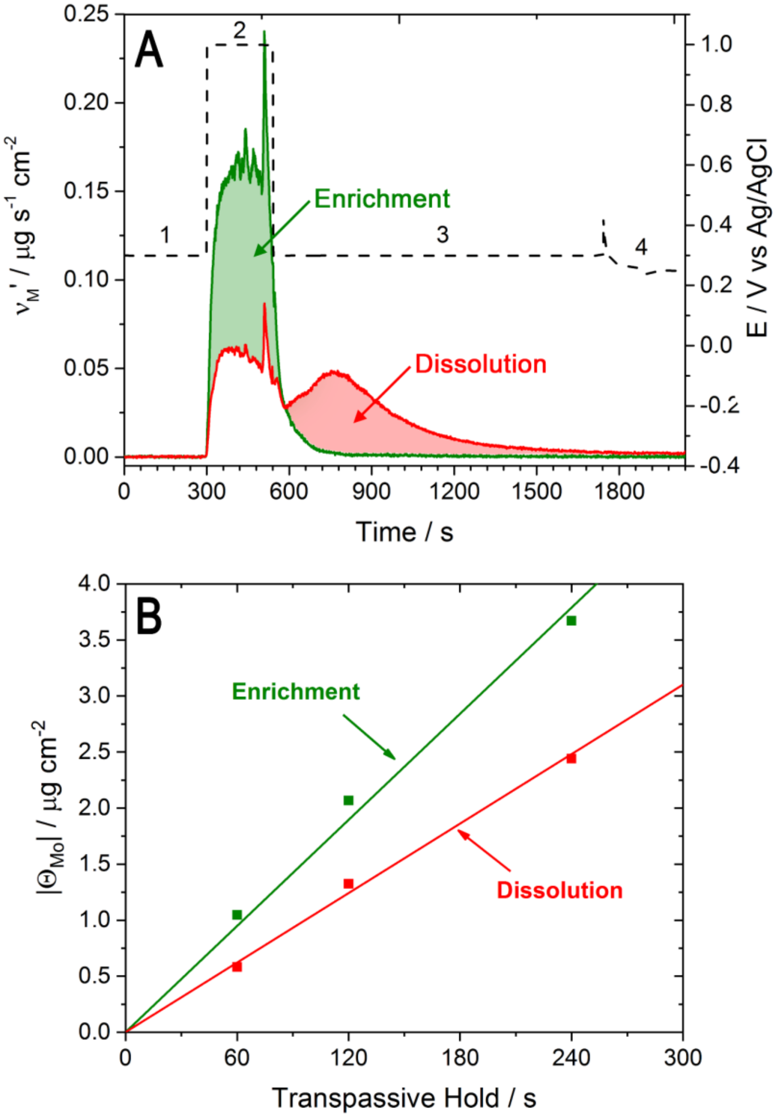

Figure 4.6 - Comparison of the enrichment and dissolution of Mo species during transpassive dissolution and repassivation of alloy G-30, respectively. (A) graphical depiction of areas considered as enrichment / dissolution of molybdenum species. (B) Comparison of enrichment and dissolution as a function of time polarized in the transpassive region.

4.4 Discussion

These results represent the first real-time quantitative measurement of the Mo enrichment during transpassive dissolution and its release during the return to the passive state. Obviously, this observation would lend support to the temporary protection hypothesis described in the introduction. When an oxide is compromised, either due to transpassive dissolution or modification in solution chemistry (*i.e.*, pit or crevice), Mo oxides should precipitate on the surface. As the exposed material repassivates, these Mo-rich oxides would dissolve.

It is reasonable to suppose that the enrichment/release mechanism is triggered by changes in the local pH. It is well known that Mo oxides precipitate at low pH, as shown in the equilibrium calculations of Figure 4.7, and a significant decrease in pH may be associated with the high rate of metal dissolution anticipated during transpassive dissolution. Highlighted in Figure 4.7 are the experimentally determined pH values for the initial solution (~7.4) and the solution expelled during transpassive dissolution. Since *in situ* pH measurements were not available in the current flow cell design, downstream collection of transpassive solution was subject to diffusion processes and therefore, experimentally measured values (~3-4) are expected to over-estimate the true pH at the corroding surface. The idea that this process is pH dependent is supported by the fact that the largest Mo retention was associated with the alloy with the highest Fe-content. In particular, Fe(III) cations are expected to undergo a more extensive hydrolysis as compared to Ni(II) [24,26], resulting in a lower pH. The role of Fe content on this behaviour is further supported by the fact that C-22, containing 3% Fe, has larger amounts of retained Mo, compared to BC-1 and G-35, which contain at most ~0.6% Fe, based on both GD-OES and ICP-AES analysis. Nevertheless, the data presented here are only suggestive as to the role of Fe.

In summary of the AESEC results, a graphical illustration of the enrichment/release process is presented in Figure 4.8. While the potential is in the passive region, a passive oxide, known to be rich in Cr(III) [3], covers the surface and limits the dissolution of the underlying substrate. However, as the system is brought into the transpassive domain, the electrochemical conversion of Cr(III) to Cr(VI) results in the destruction of this protective oxide. As a result, cations begin to be released from the metallic substrate into solution. The ensuing hydrolysis reactions lead to a drop in local pH and the deposition of Mo-rich corrosion products, which are insoluble under acidic conditions (Figure 4.7). When the system is returned to the passive region, the reestablishment of the protective oxide, again, limits dissolution and allows the previously developed pH gradient at the surface to dissipate. The return to the initial pH (~7) results in the increased solubility of the Mo-rich products and therefore their release from the surface.

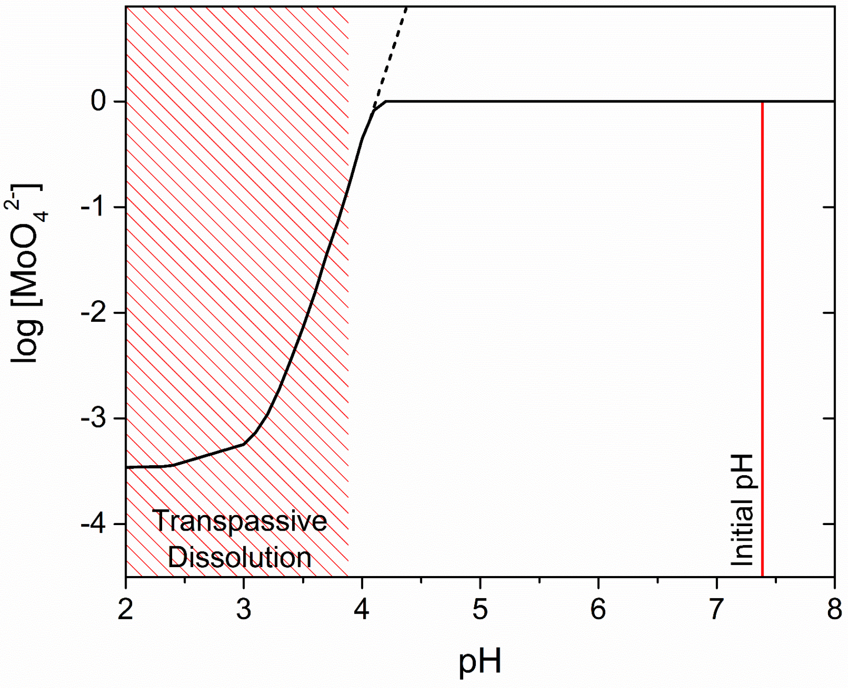

Figure 4.7 - Solubility of Mo(VI), MoO$_4^{2-}$, as a function of pH. Calculation done for a [MoO$_4^{2-}$] of 1 mol L^{-1}, however, the dotted line indicates how solubility is anticipated to change as concentration increases. Data reproduced from Hydra-Medusa software.

This enrichment may play an important role in the repassivation of the material. While the work presented here measures only the degree of enrichment/release and does not attempt to assess its effect on passivity, it is the first account of this dynamic process. Other investigations have shown that under transpassive conditions Mo concentrates in the outer portion of the oxide film [19,20,27]. However, as in the cyclic polarization experiments, repassivation resulted in a release of at least a portion of the surface-enriched Mo. The *ex situ* methodology employed in previous investigations has prevented the observation of this dynamic process.

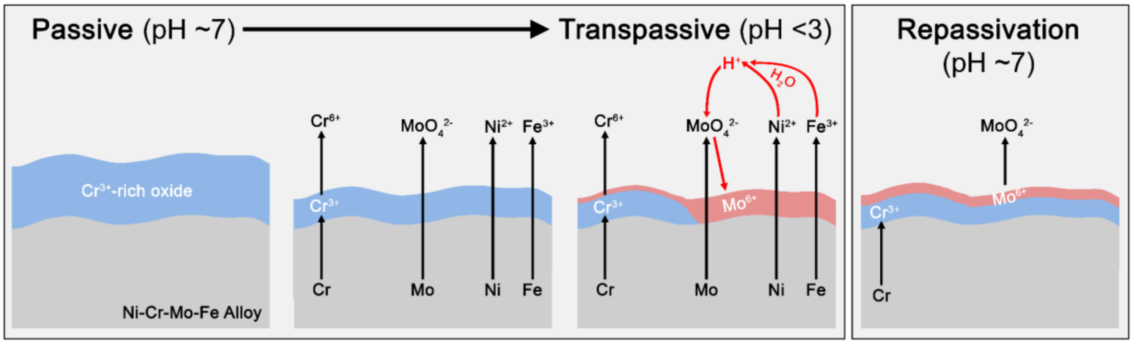

Figure 4.8 - Graphical representation of the surface enrichment during the onset of transpassive dissolution and subsequent release of Mo species during the repassivation of Ni-based alloys.

The process of Mo deposition at low pH has been extensively studied in the context of crevice corrosion [28-34]. Shan and Payer demonstrated that Mo-rich corrosion products deposit as solid species within the acidified crevice, while species of Ni, Cr, and Fe are transported outside of the acidified environment before depositing [28]. The Mo-rich corrosion products found to deposit within the crevice were later characterized by Jakupi *et al*. by energy dispersive X-ray spectroscopy (EDS) and Raman spectroscopy [31]. While thermodynamics would suggest the formation of MoO_3, their findings suggest the formation of polymeric molybdates, including $Mo_7O_{24}^{6-}$ and $Mo_8O_{26}^{4-}$, under the acidic conditions present during crevice corrosion.

The occasional observation of crevice corrosion on the G-30 alloy is interesting, and the ability to observe this may represent another line of research for the future. Unfortunately, we were not able to identify the reasons why crevice corrosion was observed in some circumstances and not in others. Previous work has demonstrated that, compared to C-22 and BC-1, alloy G-30 is particularly susceptible to crevice corrosion in hot concentrated chloride solutions [33]. In general, the initiation of crevice corrosion is random and depends on many variables including solution chemistry, crevice geometry, and the ensuing damage morphology. An extensive discussion on the factors involved during the crevice corrosion of Ni-Cr-Mo alloys can be found in a recent review by Carranza and Rodríguez [35].

4.5 Conclusions

For the first time, the dynamic behaviour of Mo during the transpassive dissolution of Ni-Cr-Mo alloys has been explored using the *operando* measurement afforded by AESEC. Alloying additions of Cr, Mo, and Fe appear to be retained on the alloy surface, compared to Ni, during transpassive dissolution. Immediately following repassivation, the Mo species enriched during transpassive dissolution were released from the surface, while the enriched Cr and Fe were not. As the time spent in the transpassive region increased, so did the enrichment in Mo surface species.

The dual phenomena of transpassive Mo-enrichment and dissolution were found to be particularly pronounced on the high Fe-containing alloy, Hastelloy G-30. This was attributed to the increased local acidification due to the release of rapidly hydrolyzed Fe(III). Decreased pH has been extensively linked to the deposition of Mo-rich corrosion product, especially in the context of crevice corrosion.

4.6 References

[1] D.C. Agarwal, J. Klower, Nickel base alloys: Corrosion challenges in the new millennium, in: CORROSION 2001, NACE, 2001.

[2] H.S. Klapper, N.S. Zadorozne, R.B. Rebak, Localized corrosion characteristics of nickel alloys: a review, *Acta Metallurgica Sinica (English Letters)*, 30 (2017) 296-305.

[3] A. Mishra, D.W. Shoesmith, P. Manning, Materials selection for use in concentrated hydrochloric acid, *Corrosion*, 73 (2017) 68-76.

[4] K. Lutton, K. Gusieva, N. Ott, N. Birbilis, J.R. Scully, Understanding multi-element alloy passivation in acidic solutions using operando methods, *Electrochemistry Communications*, 80 (2017) 44-47.

[5] J.R. Hayes, J.J. Gray, A.W. Szmodis, C.A. Orme, Influence of chromium and molybdenum on the corrosion of nickel-based alloys, *Corrosion Science*, 62 (2006) 491-500.

[6] N.S. Zadorozne, C.M. Giordano, M.A. Rodriguez, R.M. Carranza, R.B. Rebak, Crevice corrosion kinetics of nickel alloys bearing chromium and molybdenum, *Electrochimica Acta*, 76 (2012) 94-101.

[7] B. Laurent, N. Gruet, B. Gwinner, F. Miserque, K. Rousseau, K. Ogle, The kinetics of transpassive dissolution chemistry of stainless steels in nitric acid: The impact of Si, *Electrochimica Acta*, 258 (2017) 653-661.

[8] P. Fauvet, Corrosion issues in nuclear fuel reprocessing plants, in: D. Féron (Ed.) Nuclear corrosion science and engineering, Woodhead Publishing, Cambridge, 2012, pp. 679-728.

[9] M. Lindgren, E. Huttunen-Saarivirta, H. Peltola, J. Romu, T. Sarikka, H. Hänninen, P. Pohjanne, Crevice corrosion of stainless steels 904L, 2205, and 2507 in high-temperature sulfuric acid solution containing chlorides: influence of metal cations, *Corrosion*, 74 (2018) 225-240.

[10] K. Hashimoto, K. Asami, A. Kawashima, H. Habazaki, E. Akiyama, The role of corrosion-resistant alloying elements in passivity, *Corrosion Science*, 49 (2007) 42-52.

[11] R. Newman, The dissolution and passivation kinetics of stainless alloys containing molybdenum (part i), *Corrosion Science*, 25 (1985) 331-339.

[12] V. Maurice, H. Peng, L.H. Klein, A. Seyeux, S. Zanna, P. Marcus, Effects of molybdenum on the composition and nanoscale morphology of passivated austenitic stainless steel surfaces, *Faraday Discussions*, 180 (2015) 151-170.

[13] C.R. Clayton, Y.C. Lu, A bipolar model of the passivity of stainless steel: the role of Mo addition, *Journal of The Electrochemical Society*, 133 (1986) 2465-2473.

[14] A. Tomio, M. Sagara, T. Doi, H. Amaya, N. Otsuka, T. Kudo, Role of alloyed molybdenum on corrosion resistance of austenitic Ni–Cr–Mo–Fe alloys in H_2S–Cl– environments, *Corrosion Science*, 98 (2015) 391-398.

[15] A. Machet, A. Galtayries, S. Zanna, L. Klein, V. Maurice, P. Jolivet, M. Foucault, P. Combrade, P. Scott, P. Marcus, XPS and STM study of the growth and structure of passive films in high temperature water on a nickel-base alloy, *Electrochimica Acta*, 49 (2004) 3957-3964.

[16] K. Ogle, M. Mokaddem, P. Volovitch, Atomic emission spectroelectrochemistry applied to dealloying phenomena ii. selective dissolution of iron and chromium during active-passive cycles of an austenitic stainless steel, *Electrochimica Acta*, 55 (2010) 913-921.

[17] C.-O.A. Olsson, D. Landolt, Passive films on stainless steels - chemistry, structure and growth, *Electrochimica Acta*, 48 (2003) 1093-1104.

[18] K. Hashimoto, K. Asami, K. Teramoto, An X-ray photo-electron spectroscopic study on the role of molybdenum in increasing the corrosion resistance of ferritic stainless steel in HCl, *Corrosion Science*, 19 (1979) 3-14.

[19] X. Zhang, D.W. Shoesmith, Influence of temperature on passive film properties on Ni–Cr–Mo alloy C-2000, *Corrosion Science*, 76 (2013) 424-431.

[20] X. Zhang, D. Zagidulin, D.W. Shoesmith, Characterization of film properties on the Ni Cr Mo alloy C-2000, *Electrochimica Acta*, 89 (2013) 814-822.

[21] A.C. Lloyd, J.J. Noël, S. McIntyre, D.W. Shoesmith, Cr, Mo and W alloying additions in Ni and their effect on passivity, *Electrochimica Acta*, 49 (2004) 3015-3027.

[22] K. Ogle, S. Weber, Anodic dissolution of 304 stainless steel using atomic emission spectroelectrochemistry, *Journal of The Electrochemical Society*, 147 (2000) 1770-1780.

[23] V. Shkirskiy, P. Maciel, J. Deconinck, K. Ogle, On the time resolution of the atomic emission spectroelectrochemistry method, *Journal of The Electrochemical Society*, 163 (2016) C37-C44.

[24] M. Pourbaix, Atlas of electrochemical equilibria in aqueous solutions, NACE, 1974. Houston, TX, 2nd English ed.,

[25] N. Ebrahimi, M.C. Biesinger, D.W. Shoesmith, J.J. Noël, The influence of chromium and molybdenum on the repassivation of nickel-chromium-molybdenum alloys in saline solutions, *Surface and Interface Analysis*, 49 (2017) 1359-1365.

[26] C.F. Baes, Jr., R.E. Mesmer, The hydrolysis of cations, Wiley, New York, 1976.

[27] B. Yang, J. Li, X. Gong, Y. Nie, Y. Li, Effects of Cu addition on the corrosion behavior of NiCoCrMo alloys in neutral chloride solution, *RSC Advances*, 7 (2017) 40779-40790.

[28] X. Shan, J.H. Payer, Characterization of the corrosion products of crevice corroded alloy 22, *Journal of The Electrochemical Society*, 156 (2009) C313-C321.

[29] N. Ebrahimi, J.J. Noël, M.A. Rodriguez, D.W. Shoesmith, The self-sustaining propagation of crevice corrosion on the hybrid BC1 Ni–Cr–Mo alloy in hot saline solutions, *Corrosion Science*, 105 (2016) 58-67.

[30] A.K. Mishra, D.W. Shoesmith, Effect of alloying elements on crevice corrosion inhibition of nickel-chromium-molybdenum-tungsten alloys under aggressive conditions: an electrochemical study, *Corrosion Science*, 70 (2014) 721-730.

[31] P. Jakupi, F. Wang, J.J. Noël, D.W. Shoesmith, Corrosion product analysis on crevice corroded alloy-22 specimens, *Corrosion Science*, 53 (2011) 1670-1679.

[32] N. Ebrahimi, P. Jakupi, J.J. Noël, D.W. Shoesmith, The role of alloying elements on the crevice corrosion behavior of Ni-Cr-Mo alloys, *Corrosion*, 71 (2015) 1441-1451.

[33] J.D. Henderson, N. Ebrahimi, V. Dehnavi, M. Guo, D.W. Shoesmith, J.J. Noël, The role of internal cathodic support during the crevice corrosion of Ni-Cr-Mo alloys, *Electrochimica Acta*, 283 (2018) 1600-1608.

[34] R.S. Lillard, M.P. Jurinski, J.R. Scully, Crevice corrosion of alloy 625 in chlorinated ASTM artificial ocean water, *Corrosion Science*, 50 (1994) 251-265.

[35] R.M. Carranza, M.A. Rodriguez, Crevice corrosion of nickel-based alloys considered as engineering barriers of geological repositories, *Materials Degradation*, 1 (2017) 9.

Chapter 5

5 Investigating the role of Mo and Cr during the activation and passivation of Ni-based alloys in acidic chloride solution

(Henderson (*et al.*), *J. Electrochem. Soc.*, **Accepted**, DOI: 10.1149/1945-7111/abe47a)

Abstract:

The elemental dissolution behaviour of commercially available Ni-based alloys was investigated in the context of surface activation, spontaneous passivation, and electrochemically-assisted passivation in hydrochloric acid solution using atomic emission spectroelectrochemistry (AESEC). Following surface activation, the spontaneous passivation of each alloy was found to proceed by the accumulation of mainly Mo-rich, but also Cr-rich oxides. An alloy's ability to recover from surface activation was found to improve with increased Mo content. For the alloy with the lowest Mo content considered here, approximately 8 wt.% Mo, spontaneous passivation was unsuccessful and active dissolution was observed. For alloys with higher Mo contents, greater than 13 wt.% Mo, spontaneous passivation occurred quickly, and dissolution rates stabilized at values comparable to those found for the native oxide, *i.e.*, before perturbation by an applied potential. Mo(IV) oxides were found to be the species accumulating during spontaneous passivation using *ex situ* X-ray photoelectron spectroscopy (XPS). During electrochemically-assisted passivation, *i.e.*, applying a potential within the passive region, a portion of the previously accumulated Mo was removed while Cr oxides accumulated at the surface. However, based on the dissolution rates observed after electrochemically-assisted passivation, Cr-content did not dictate the barrier layer properties.

5.1 Introduction

Ni-based alloys containing various alloying elements, including both Cr and Mo, have become important industrial materials due to their corrosion resistance in aggressive environments. Serving as the alloy matrix, Ni can accommodate high concentrations of alloying elements while maintaining a single-phase (FCC) structure [1]. Alloying additions of Cr promote the formation of a Cr-rich barrier oxide, which is primarily responsible for protecting the underlying metallic substrate [2, 3]. Alloying additions of Mo into Cr-containing alloys have been shown to result in the accumulation of oxidized Mo species on the outside of the Cr-rich oxide [4]. By itself, the Cr-rich oxide provides excellent protection in oxidizing environments; however, the presence of Mo species becomes increasingly important at low pH and high chloride concentration [5, 6]. These conditions are commonly associated with localized corrosion processes, including both pitting and crevice corrosion [7-9]. Resistance to localized corrosion is influenced by the Mo content, which increases both film stability and repassivation behaviour [4, 5, 10].

Alloying additions Cr and Mo are recognized to act synergistically in improving corrosion resistance, but many mechanistic features remain unclear. The current understanding of how Mo additions impact the corrosion behaviour of Cr containing alloys has been summarized by Lutton Cwalina *et al.* [11]. First-principles calculations by Samin *et al.* demonstrated that additions of Mo enhance the adsorption of oxygen on the surface of Ni-Cr alloys [12]. Using *in situ* transmission electron microscopy, Yu *et al.* showed that during early-stage gas-phase oxidation, Mo additions decrease the formation of voids in the oxide layer formed on Ni-Cr alloys [13]. Using scanning tunneling microscopy, Maurice *et al.* observed nanoscale surface defects in passivated Fe-Cr alloys [14]. When Mo was added to the alloy, defects were found to generate a nanostructured ‘plug’, which appeared to act as a healing phenomenon for the defects. Based on the observations in these studies, the influence of Mo can be generally summarized in terms of two main outcomes: increased oxide stability and improved ability to repair oxide film damage.

Currently, limited information has been published regarding the *in situ* (or *operando*) dissolution behaviour of Ni-based alloys. This hinders efforts to optimize alloy composition, which requires a thorough understanding of how composition affects corrosion performance in a range of exposure conditions. Atomic emission spectroelectrochemistry (AESEC), and other similar techniques, have proven valuable in studying the *in situ* dissolution behaviour of corroding systems, including both active and passive systems [15-17]. In our previous study, the AESEC technique was used to reveal a previously unreported dynamic behaviour of alloyed Mo during the transpassive film breakdown on Ni-Cr-Mo alloys in 1 M NaCl [18]. Here, the dissolution behaviour of three commercial Ni-based alloys was investigated during surface activation, spontaneous passivation, and electrochemically-assisted passivation in 1 M HCl. Results obtained by AESEC were then compared to *ex situ* surface analyses performed by X-ray photoelectron spectroscopy (XPS).

5.2 Experimental

5.2.1 Materials

Materials used in this study were provided by Haynes International in the form of mill-annealed sheets. To conform to the dimensions of the electrochemical flow cell used for AESEC measurements, samples were machined to 25 mm x 10 mm. The thickness of individual samples varied depending on the thickness of the original as-received sheet. Nominal alloy compositions, as reported by Haynes International, have been summarized in Table 5.1. Alloy compositions are included in Table 5.2, determined according to ASTM E1019-18, ASTM E1097-12, and ASTM E1479-16 procedures. These more accurate compositions were used in the quantification of AESEC measurements and will be referenced throughout the text.

Table 5.1 - As reported by Haynes International, the nominal composition of Hastelloy samples are summarized. Values are given in wt.% where M indicates the maximum concentration of an individual alloying element, while, Bal. indicates the alloying element making up the balance due to fluctuations in composition.

Alloy	**Ni**	**Cr**	**Mo**	**Fe**	**W**	**Cu**	**Co**	**Mn**	**V**	**Al**	**Si**	**C**
BC-1	Bal.	15	22	2^M	--	--	--	0.25	--	0.5^M	0.08^M	0.01^M
C-22	Bal.	22	13	3	3	0.5^M	2.5^M	0.5^M	0.35^M	--	0.08^M	0.01^M
G-35	Bal.	33.2	8.1	2^M	0.6	0.3^M	1^M	0.5^M	--	0.4^M	0.6^M	0.05^M

Before experiments, sample surfaces were prepared using wet silicon carbide (SiC) paper. Samples to be used in electrochemical measurements were ground using P600, P800, P1000, and P1200 grit SiC paper. Samples intended for surface analyses were further ground using P2500 and P4000 SiC paper, followed by polishing with a 1-μm diamond suspension. After surface preparation, samples were rinsed with deionized (DI) water (18.2 MΩ cm), followed by EtOH, and then dried in a stream of high purity N_2 or Ar gas.

Table 5.2 - Summary of the empirically determined compositions for alloy BC-1, C-22, and G-35. Values are given in wt.%. Analysis carried out by Cambridge Materials Testing Limited according to ASTM E1019-18, ASTM E1097-12, and ASTM E1479-16.

Alloy	**Ni**	**Cr**	**Mo**	**Fe**	**W**	**Cu**	**Co**	**Mn**	**V**	**Al**	**Si**	**C**
BC-1	60.9	14.4	22.10	0.85	0.01	0.03	--	0.25	--	0.18	<0.01	0.011
C-22	57.6	20.7	12.97	3.74	2.80	0.06	--	0.27	--	0.28	<0.01	0.012
G-35	56.3	33.4	7.98	0.54	0.07	0.02	--	0.45	--	0.24	<0.01	<0.010

Experimental solutions were prepared with reagent grade HCl and DI water. Quantification of inductively coupled plasma atomic emission spectroscopy (ICP-AES) data involved the use of standard solutions. These standards were prepared using aliquots of metal standards (SCP Science) directly in the experimental electrolyte (1 M HCl).

5.2.2 Electrochemical methods

Electrochemical experiments were carried out using either a Reference 600 (Gamry Instruments, Warminster, PA, USA) or a Solartron Analytical model 1287 (Solartron Analytical, Hampshire, UK) potentiostat. Experiments were conducted in a custom-built PTFE flow cell designed for AESEC measurements. A brief description of this flow cell is provided below, with an extensive description having been published elsewhere [16, 19, 20]. The exposed area of the working electrode (WE) was limited to 1 cm^2. The flow rate in the WE compartment was maintained at ~2.75 mL min^{-1} using a peristaltic pump. The counter (CE) and reference electrodes (RE) were housed in a second compartment, separated from the flow cell by an ionically conductive membrane. A saturated Ag/AgCl electrode (0.197 V vs. SHE) and a Pt flag served as the RE and CE, respectively. All electrochemical measurements were repeated at least once.

The temperature during electrochemical measurements was maintained at 75 °C by pre-heating the electrolyte and directly heating the WE affixed to the flow cell. Electrolyte temperatures were maintained by placing the solution reservoir in either an isothermal bath or on a hot plate. The WE temperature was maintained by placing a heating element directly on the back of the metal sample, in contact with the surface opposite to the flow cell. Here, the heating element was either a hollowed Cu heating disk connected to an isothermal bath or an electric heating assembly containing thermistors connected to a digital temperature controller, allowing for closed-loop temperature regulation. Together, these controls maintained experimental temperatures of 75 ± 1 °C during all experiments. All experiments were performed in naturally aerated solutions, apart from those conducted within a glove box for surface analysis, discussed below.

Both dynamic- and static-polarization experiments were conducted using the described experimental setup. Dynamic polarization experiments were initiated at –0.4 V (vs. Ag/AgCl) and scanned positively at a scan rate of 0.5 mV s^{-1}, until a final potential of 1.0 V (vs. Ag/AgCl). Static polarization experiments involved several potential steps. Initially, samples were exposed to the solution at open-circuit as temperatures stabilized, then they were subjected to an applied potential of –0.8 V (vs. Ag/AgCl) for 60 s, followed by a 300 s period at open circuit to facilitate relaxation. Samples were then subjected to an applied potential of 0.6 V (vs. Ag/AgCl) for 60 s before again being released to open circuit (300 s) to facilitate relaxation. These two steps, cathodic and anodic polarization followed by an open circuit potential (OCP) measurement, were repeated three to four times each. Potentials used for cathodic and anodic polarization (–0.8 V and 0.6 V, respectively) were selected based on polarization behaviour observed during dynamic measurements, as well as procedures used in previous publications [21].

5.2.3 AESEC measurements and data treatment

The AESEC setup has been described in detail previously [16, 20]. Briefly, situated downstream of the electrochemical flow cell is an ICP-AES instrument (Ultima 2C spectrometer, Horiba Jobin-Yvon, France). Species released during electrochemical experiments were carried from the WE surface by the flow of fresh electrolyte and injected into the plasma of the spectrometer. The emission intensity at wavelengths specific to each element was measured and used to quantify the instantaneous elemental dissolution rates of the alloy components.

Solution exiting the flow cell was introduced to the ICP using a Burgener PEEK Mira Mist® Nebulizer (Horiba Jobin-Yvon, France). Species exposed to the plasma operating at 1 kW and 40.68 MHz, undergo atomization and excitation, with the subsequent relaxation processes generating emission lines characteristic of the atom of origin. Independent mono- and polychromator optics allow the simultaneous monitoring of several emission lines. Since Mo was the alloying element present in the lowest concentrations, it was detected using the monochromator to provide increased spectral resolution. For experiments involving low dissolution rates, emission intensities exhibited poor signal-to-noise ratios. When necessary, data were treated with a boxcar average (n = 5) as used and discussed previously [22]. Unless otherwise stated, data were not subjected to averaging.

Table 5.3 - Experimental emission lines and limits of detection.

Element	**Wavelength** / nm	**Detection Limit, $C_{3\sigma}$** / ppb (wt.)
Ni	231.60	10.8 ± 0.3
Cr	367.72	4.8 ± 0.2
Mo	202.03	1.4 ± 0.1

For the elements studied, emission lines and their detection limits are summarized in Table 5.3. Experimental detection limits ($C_{3\sigma}$) were calculated using Equation 5.1, where σ_B is the standard deviation of the background signal and κ is the sensitivity factor determined from the calibration standards.

$$C_{3\sigma} = 3\,\frac{\sigma_B}{\kappa} \tag{5.1}$$

Standard calibration was used to convert time-varying emission line intensities into instantaneous concentrations ($\mathrm{C_M}$). Values of $\mathrm{C_M}$ were then converted into instantaneous dissolution rates (ν_M) according to Equation 5.2, where f is the flow rate and A the surface area of the WE.

$$\nu_\mathrm{M} = \mathrm{f}\frac{\mathrm{C_M}}{\mathrm{A}} \tag{5.2}$$

Congruent and incongruent dissolution behaviours were distinguished by comparing metal ion ratios in the electrolyte to those in the bulk material. This was done by normalizing individual dissolution rates against the bulk alloying element, Ni, according to Equation 5.3, where $\mathrm{X_M}$ is the mass fraction of alloying element M. Values used for mass fractions were determined from the empirical data in Table 5.2 to ensure accuracy.

$$\nu'_\mathrm{M} = \left({}^{\mathrm{X_{Ni}}}\!/_{\mathrm{X_M}}\right)\nu_\mathrm{M} \tag{5.3}$$

Features of increased, decreased, and congruent dissolution were identified relative to the bulk composition by considering normalized dissolution rates. For instance, congruent dissolution was observed when ν'_M was approximately equal to ν_Ni, *i.e.*, alloying element M was dissolving at a rate proportional to its bulk alloy composition. When ν'_M exceeded values of ν_Ni, alloying element M was being selectively removed from the alloy matrix in comparison to Ni; *i.e.*, the dissolution rate of M was higher than expected based on its bulk alloy composition. On the other hand, when ν'_M was less than ν_Ni, alloying element M was accumulating on the surface of the alloy; *i.e.*, its dissolution rate was less than expected based on its bulk alloy composition. The quantity of excess M, Θ_M, at time, t, was calculated using Equation 5.4.

$$\Theta_\mathrm{M} = \int_0^\mathrm{t}\left((\mathrm{X_M}/\mathrm{X_{Ni}})\nu_\mathrm{Ni} - \nu_\mathrm{M}\right)\mathrm{dt} \tag{5.4}$$

Instantaneous dissolution rates were also converted into elemental current densities ($\mathrm{i_M}$), that represent the ion fluxes in electrical units, according to Equation 5.5, where F is Faraday's constant, m is the molar mass of metal M and, n is the number of electrons transferred in the oxidation reaction of metal M.

$$\mathrm{i_M} = \frac{\nu_\mathrm{M}\,\mathrm{F}\,\mathrm{n}}{\mathrm{m}} \tag{5.5}$$

To directly compare the elemental current densities, $\mathrm{i_M}$, to the electrical current density, $\mathrm{i_e}$, a convolution procedure was carried out to correct for the residency time in the flow cell and through the intermediate capillaries. Details of this convolution have been published previously [16]. Comparison of the sum of all elemental currents (i_Σ) with the convoluted electrochemical current density ($\mathrm{i_e^*}$) provides the opportunity to separate anodic current contributions leading to dissolution, oxide growth, gas evolution, etc..

5.2.4 XPS measurements

Samples prepared for surface analysis underwent the identical electrochemical treatment used when making ICP-AES measurements but inside a N_2-purged glove box with the atmospheric O_2 content maintained at ~50 ppm to minimize further oxidation following the electrochemical experiment. Solutions used for electrochemical treatments within the glove box required deaeration to help control the atmospheric O_2 concentration. This was done by sparging the solution with Ar gas before its introduction to the glove box. Upon the completion of electrochemical treatments, samples were transferred and stored in an Ar-purged glove box with an O_2 content maintained at < 0.1 ppm to avoid oxidation during the period between preparation and XPS analysis. When required, samples were then introduced into the XPS instrument using a custom-built Ar-filled glove box connected directly to the spectrometer.

XPS measurements were carried out using a Kratos AXIS Supra spectrometer. All spectra were collected using a monochromatic Al Kα X-ray source (photon energy = 1486.6 eV) operating at 12 mA and 15 kV (180 W). During analysis, the pressure inside the analysis chamber was maintained at $\leq 10^{-8}$ Torr. Calibration of the instrument work function was done using the binding energy (B.E.) of a standard metallic Au sample ($4f_{7/2}$ at 83.95 eV). In all spectra, photoelectrons were collected at a take-off angle of 90° from a 700 x 400 µm area. Survey spectra were recorded in a B.E. window from 0 to 1200 eV using a pass energy of 160 eV and a step size of 1 eV. High-resolution spectra of the C 1s, O 1s, Ni 2p, Cr 2p, Mo 3d, and S 2p lines were collected using a pass energy of 20 eV and a step size of 0.1 eV. All spectra were charge-corrected against the aliphatic (C-C) adventitious carbon signal set to 284.8 eV. All signal processing and deconvolution was performed with CasaXPS software (ver. 2.3.19) using a Shirley background subtraction. Deconvolution of high-resolution spectra was done using previously detailed fitting parameters and constraints collected from high-quality standard reference samples (Ni [23, 24], Cr [23, 25], Mo [26]).

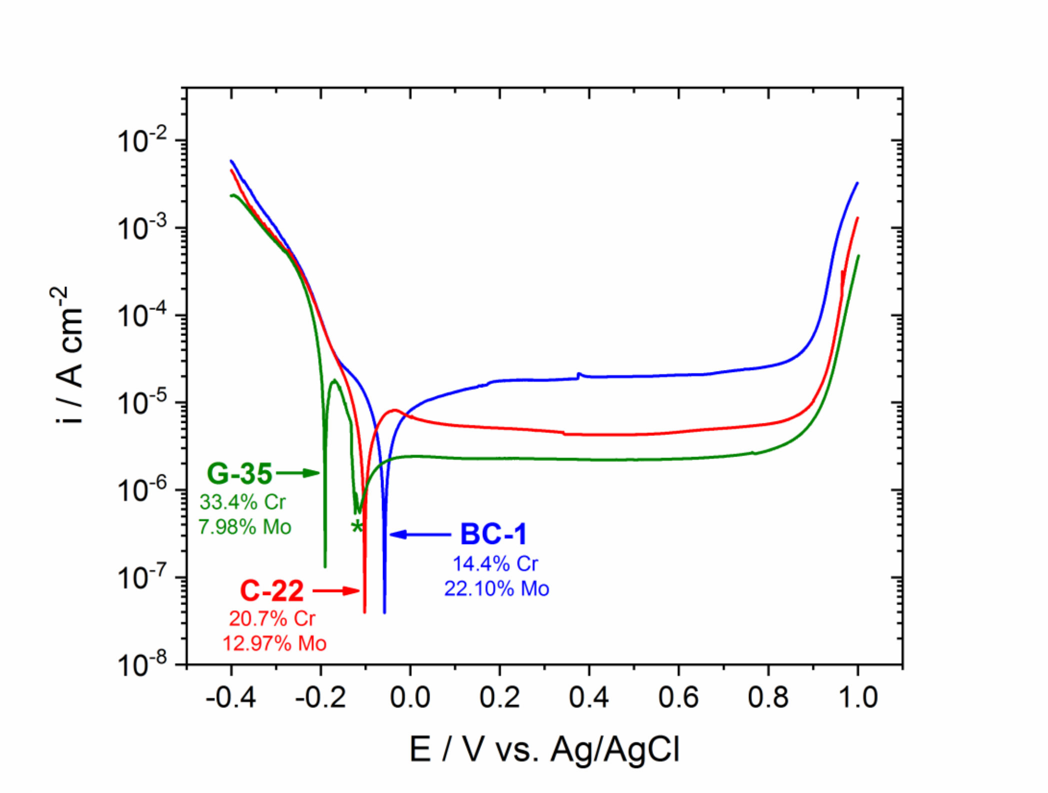

Figure 5.1 - Polarization behaviour of alloys BC-1, C-22, and G-35 in 1 M HCl at 75°C. For alloy G-35, the region of net cathodic current at applied potentials positive of the active-to-passive transition (–0.125 V to –0.113 V) is indicated (*). Alloy compositions (wt.%) shown here were taken from Table 5.2.

5.3 Results and discussion

5.3.1 Potentiodynamic polarization behaviour

Current densities recorded during potentiodynamic scans on the three alloys in aerated 1 M HCl (75°C) are presented in Figure 5.1. Current densities associated with active dissolution were influenced by changes in Mo content, as shown previously [5, 6], with alloy G-35 (7.98 wt.% Mo) displaying the most pronounced active-to-passive transition and alloy BC-1 (22.10 wt.% Mo) showing no such transition. The values of zero-current potential ($E_{i=0}$) were also found to exhibit a positive shift as the Mo content was increased.

At more positive applied potentials all three alloys exhibited a potential-independent current density, indicating passivity until ~0.85 V. At applied potentials ≥ 0.85 V, the transpassive conversion of Cr(III) into soluble Cr(VI) species is observed [27-29]. As expected, alloys with larger Cr contents exhibited lower passive current densities, Figure 5.1. At applied potentials positive of the active-to-passive transition for alloy G-35, the measured current density switched from net anodic to net cathodic between ~–0.13 and –0.11 V, as previously observed for this alloy and shown to be due to the reduction of O_2 dissolved in the solution [30].

The electrochemical current densities (i_e) shown in Figure 5.1, were compared to the elemental current densities obtained from AESEC measurements. The results obtained during the polarization of alloys (A) BC-1, (B) C-22, and (C) G-35, are shown in Figure 5.2. To allow for the direct comparison of j_e with elemental current densities, i_M, where M was Ni, Cr, or Mo, a convolution procedure was carried out. This convolution procedure corrects i_e for the distribution of residence times through the flow cell and is detailed in a previous publication [16]. The comparison of the convoluted electrochemical current, i_e^*, with the sum of all elemental current densities, i_Σ, provided information on the faradaic yield of the anodic reactions. In measurements presented here, species released from the alloy and detected by ICP-AES were assumed to have dissolved as Ni(II), Cr(III), and Mo(IV). Oxidation states were assigned based on both *ex situ* surface analyses, presented later in this study, and thermodynamic data [31]. For reference, the original (untreated)

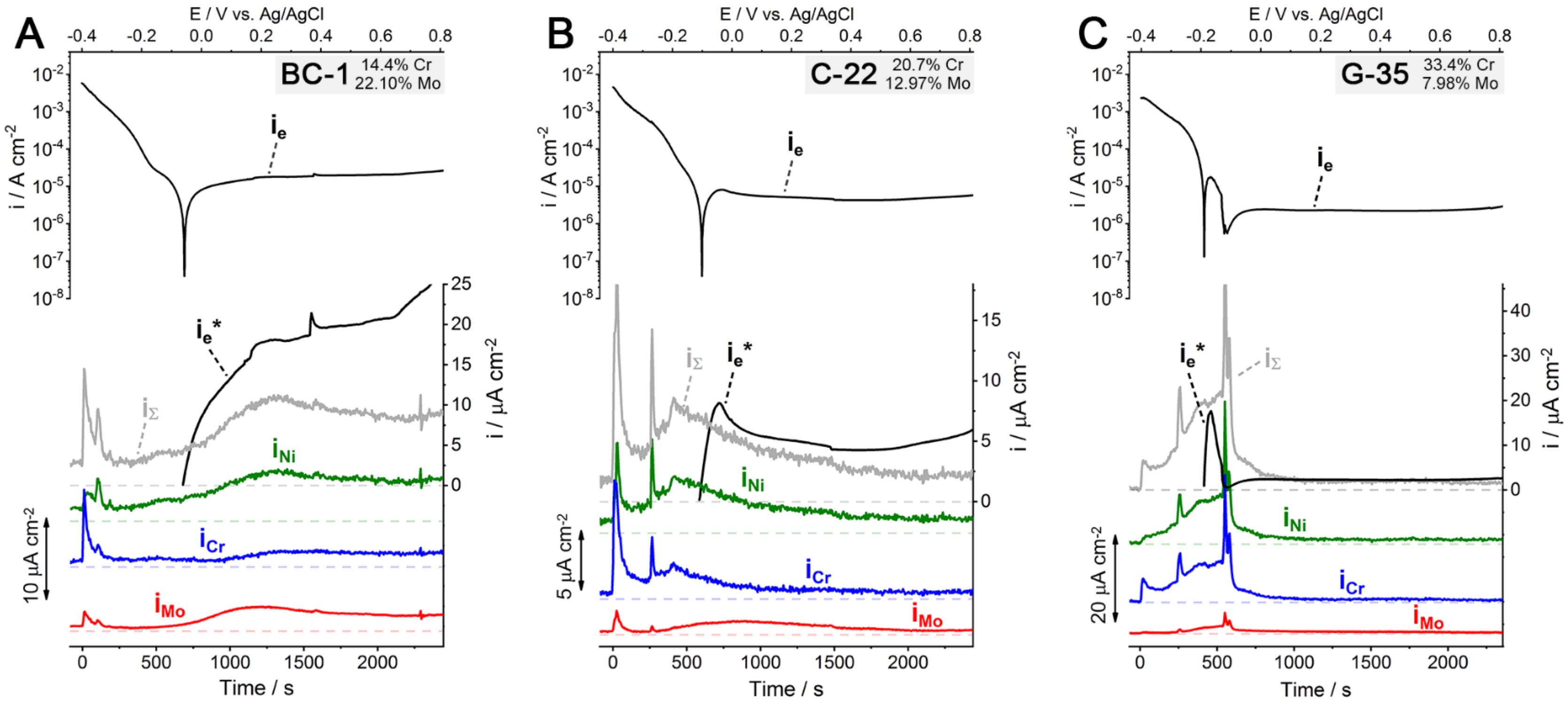

Figure 5.2 - Comparison of the convoluted electrochemical current density (i_e^*) with the instantaneous elemental (i_M) and sum current densities (i_Σ) for dynamic polarization experiments conducted in naturally aerated 1 M HCl at 75°C. Both the untreated (i_e) and the convoluted (i_e^*) electrochemical current densities are included for reference. The locations of $i = 0$ for i_Σ (and i_e^*), i_{Ni}, i_{Cr}, and i_{Mo} are indicated by the dashed lines. Values of i_M were treated with a moving boxcar average (n=5) in order to reduce noise resulting from relatively low dissolution rates. Alloy compositions (wt.%) shown here were taken from Table 5.2.

electrochemical current densities (i_e), plotted on log(i)-E axes, have been included at the top of Figure 5.2(A-C) while the values of i_e^*, i_Σ, i_{Ni}, i_{Cr}, and i_{Mo}, are shown below, as a function of time.

For alloy BC-1, immediately following the application of –0.4 V (or t = 0), increases in i_{Ni}, i_{Cr}, and i_{Mo} were observed which quickly stabilized at low values within the cathodic region, Figure 5.2(A). At applied potentials < $E_{i=0}$, i_Σ stabilized at ~5 µA cm^{-2}. As the applied potential was increased to values > $E_{i=0}$, i_Σ initially remained low, confirming the absence of an active region, before increasing to a maximum value of ~10 µA cm^{-2}, which then persisted throughout the passive region. Comparing i_e^* with i_Σ confirmed that a portion of the current measured by the potentiostat could not be accounted for by dissolution. In this case, differences between i_e^* and i_Σ are the result of oxidation reactions unrelated to dissolution; *i.e.*, the formation of oxidized surface species not detected by ICP-AES. This discrepancy, $i_\Sigma < i_e^*$, which persisted through the passive region, can be attributed to film growth [32]. The difference between i_e^* and i_Σ increased with increasing applied potential throughout the passive region suggesting that film growth was enhanced at higher potential, although obviously the effect of applied potential and exposure time cannot be entirely separated in potential sweep experiments.

Comparing the measurements made on alloy BC-1, Figure 5.2(A), to those made on alloys C-22 and G-35, Figures 5.2(B) and (C), revealed several similarities. Like on BC-1, the application of –0.4 V (t = 0) on alloys C-22 and G-35 resulted in momentary increases in i_{Ni}, i_{Cr} and i_{Mo}. Consistent with the role of Mo in suppressing active dissolution, the maximum value of i_Σ was lower for alloy C-22 (12.97 wt.% Mo) than for alloy G-35 (7.98 wt.% Mo). For alloy G-35, values of i_Σ exceeded values of i_e^* during active dissolution, suggesting that some metal dissolution was coupled directly to cathodic reactions in this potential range, and therefore did not generate measurable net electrochemical current. At higher applied potentials, where film formation occurred, values of i_Σ were smaller than values of i_e^* for both alloys, as also observed for alloy BC-1. This indicated an anodic contribution to film growth. Based on the difference between i_Σ and i_e^*, film growth appeared highest for BC-1, followed by C-22, and lastly G-35. Nonetheless, the difference between i_Σ and i_e^* increased as the applied potential increased, although not as obviously for G-35.

The identity of the specific elements accumulating on the surface as oxides may be obtained by considering normalized dissolution rate information as a function of applied potential, Figure 5.3. In this way, the potential regions of increased, decreased, and congruent dissolution were identified based on the bulk alloy composition. In the representation shown in Figure 5.3, a positive value ($(X_M/X_{Ni})\nu_{Ni} - \nu_M > 0$) indicated that the dissolution rate of element M (either Cr or Mo) was less than expected based on its bulk composition in the alloy, indicating its accumulation at the surface. On the other hand, a negative value ($(X_M/X_{Ni})\nu_{Ni} - \nu_M < 0$) indicated that the dissolution rate of element M

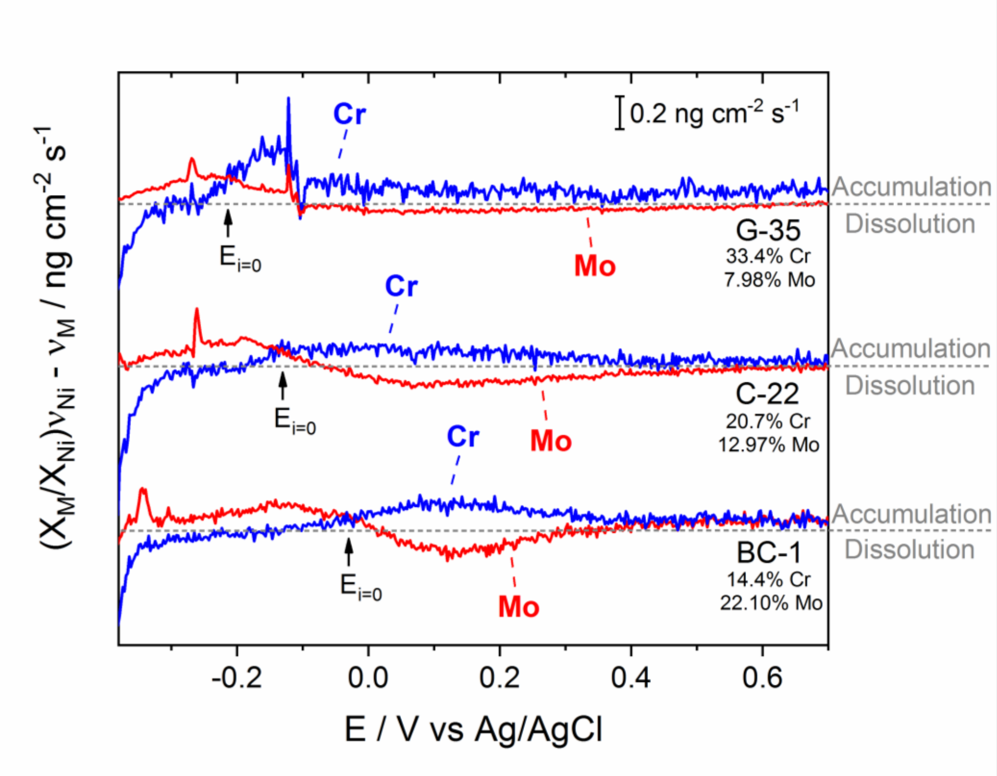

Figure 5.3 - Trends in Cr and Mo accumulation and excess dissolution during dynamic polarization experiments, Figure 5.1. Values of ν_{Ni} were normalized against the element M, either Cr or Mo. For each alloy, values of congruent dissolution (y = 0) are indicated by the dotted line. Alloy compositions (wt.%) shown here were taken from Table 5.2.

exceeded the value expected based on the alloy bulk composition; *i.e.*, M was selectively removed from the surface. The separations between depletion (or excess dissolution) and accumulation are indicated along the right ordinate-axis, Figure 5.3.

For all alloys, a transition between two distinct dissolution behaviours was found near the $E_{i=0}$. Below $E_{i=0}$, Cr was found to be the dominant cation released, while Mo species accumulated to some extent. However, at applied potentials higher than $E_{i=0}$, this trend was found to reverse, suggesting that a portion of the metal cations from the previously accumulated Mo species became the dominant species released and Cr species accumulated at the surface. While the data presented in Figure 5.3 cannot quantify the amount of Mo species remaining in the surface film, *ex situ* surface analyses, discussed below with potentiostatic data, found that oxidized Mo species were present in relatively large quantities (12-32 at.%) for films formed at high applied potential. This is discussed in greater detail below. As the applied potential increased through the region where film formation occurred, *i.e.*, at applied potentials higher than $E_{i=0}$, this opposing effect between accumulation of Cr species and dissolution of Mo species disappeared for BC-1 and C-22, indicating the formation of a film with a stable composition. This occurred at a lower potential for alloy BC-1 (22.10 wt.% Mo) than for alloy C-22 (12.97 wt.% Mo) - approximately 0.4 and 0.65 V, respectively. For the low Mo alloy G-35 (7.98 wt.% Mo), the accumulation of Cr species and dissolution of Mo species was maintained over the full potential range.

Although AESEC data collected during potentiodynamic polarization experiments highlighted changes in dissolution behaviour as a function of applied potential, the data were somewhat difficult to interpret. This was especially true in the context of film breakdown and passivation behaviour, where both the applied potential and the time play an important role [33]. To further investigate the transition between the active and passive states, potentiostatic measurements were employed.

5.3.2 Potentiostatic polarization behaviour

A potentiostatic approach was adopted, in which negative and positive applied potentials were used to force surface activation and passivation, respectively. Between the applied potentials, relaxation at open circuit was monitored. During both the applied potential and open circuit potential measurement period, dissolution behaviour was monitored with the premise being that the elemental dissolution rates are inversely proportional to the barrier properties of the film. Dissolution behaviour will be discussed in greater detail below. For all alloys, the potential measurements made during cyclic activation-passivation experiments are presented in Figure 5.4, where cathodic activation and electrochemically-assisted passivation processes are indicated by the red- and blue-shaded regions, respectively. Furthermore, locations during the polarization cycle considered for

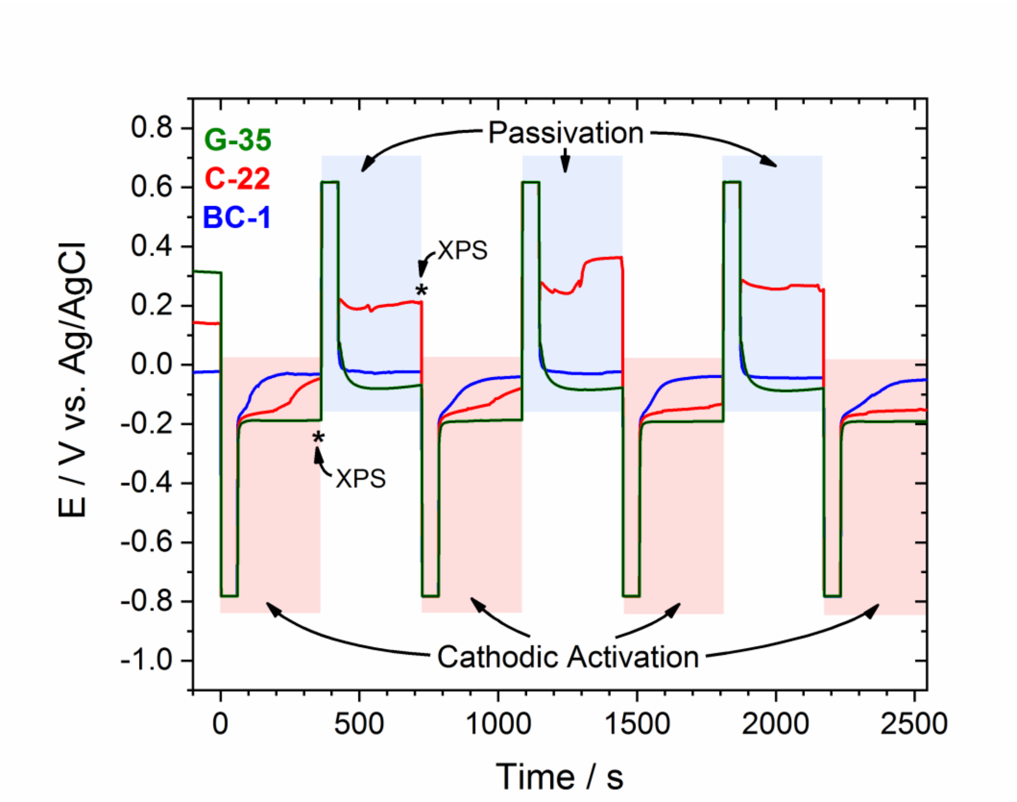

Figure 5.4 - Measured potentials during potentiostatic experiments. Red-shaded areas indicate the surface activation process involving both cathodic activation (60 s at –0.8 V vs Ag/AgCl) and spontaneous passivation (300 s at open-circuit). Blue-shaded areas indicate the electrochemically-assisted passivation process involving the application of 0.6 V vs. Ag/AgCl for 60 s, followed by a 300 s OCP measurement. Surface analysis by XPS was conducted at the indicated times (*).

subsequent surface analysis are indicated (*) in Figure 5.4 and will be further discussed below.

Cathodic activation was initiated by applying a potential of –0.8 V, a polarization at which high cathodic current densities were observed, typically on the order of –10 mA cm^{-2}. During this period, H_2 evolution occurred at a high rate, experimentally observed as bubbles exiting the flow cell. Similar activation procedures have been employed previously [21, 29, 34]. The resulting surface activation was confirmed by increases in dissolution rate observed using ICP-AES. While the mechanism of this activation is not completely understood, it may be explained by either the removal or the degradation of the film by the introduction of defect sites in the oxide, by the partial reduction of the Cr(III) film to the more soluble Cr(II) species, and/or by the physical removal of oxide scale due to the rapid formation of gas bubbles at the surface. Previous studies have shown that applications of large negative potentials increase the number of defects in the oxide film [35, 36], thermodynamic calculations suggest the reduction of Cr(III) to Cr(II) at the applied potential used for cathodic activation [21, 31, 37], and lastly, the possibility of releasing oxide scale from the surface cannot be omitted. The results presented here only demonstrate partial dissolution of excess Cr and Mo from the film and subsequent activation of the surface and do not allow for simple distinction between these mechanisms. Following surface activation and a period of open-circuit relaxation, electrochemically-assisted passivation occurred by the application of 0.6 V; this value was selected from the range of potentials where film formation was found to occur (see Figure 5.1). Experimentally, cathodic activation and electrochemically-assisted passivation processes were cycled to investigate the effect of repeated surface activation.

5.3.2.1 Surface activation

Potentials measured during the activation periods are indicated as red-shaded regions in Figure 5.4. Before the first cathodic activation, *i.e.*, t < 0 s, OCP values were related to the Cr-content of each alloy. Alloy G-35 (33.4 wt.% Cr) had the highest measured OCP, followed by C-22 (20.7 wt.% Cr), and lastly BC-1 (14.4 wt.% Cr). This was consistent with the influence of Cr-content on oxide films formed in relatively non-aggressive environments, in this case, an air formed (or native) oxide [38]. After being activated, *i.e.*, after the polarization at –0.8 V, this trend was found to reverse. Once activated, the alloy's ability to re-establish an oxidized surface condition, as indicated by an increase in the OCP, was related to its Mo-content. In our previous work, we demonstrated that Mo-content was important to the stability of the oxide film, as well as in stifling active dissolution behaviour in acidic solutions [39, 40]. It was shown that Mo accumulated on the surface under transpassive conditions was released to solution upon a return to passive conditions [18]. Above, we showed a similar accumulation/release mechanism applied for the transition from active to passive conditions, Figure 5.3. Other studies have also highlighted the ability of alloyed Mo to improve corrosion resistance in acidic solutions [6, 41]. In the data presented here, alloys BC-1 (22.10 wt.% Mo) and C-22 (12.97 wt.% Mo) demonstrate increases in OCP after being activated, while the OCP of alloy G-35 (7.98 wt.% Mo) stabilized at relatively low values. For alloy BC-1, OCP values rapidly increased and stabilized at approximately –0.03 V, comparable to values measured before activation, *i.e.*, t < 0 s. For alloy C-22, OCP values increased more slowly and stabilized at –0.05 V after the first activation, approximately 0.2 V below the OCP measured at t < 0 s. In the case of alloy G-35, OCP values stabilized quickly and did not increase with time. Instead, OCP values measured for alloy G-35 stabilized at –0.18 V, approximately 0.5 V below values measured at t < 0 s. While the behaviour of OCP remained consistent for repeated activation cycles, shown in Figure 5.4, alloys BC-1 and C-22 both demonstrated a weakened ability to recover with repeated active-passive cycles. In the case of alloy BC-1, achieving a steady-state condition during consecutive activation cycles required increasing amounts of time. In the case of alloy C-22, OCP values measured after activation periods were found to stabilize at lower values as the number of cycles increased.

The normalized dissolution rates, ν'_M, measured during the first cathodic activation process and the subsequent open circuit period are presented in Figure 5.5. Since similar dissolution patterns were observed during repeated activation processes, only the first activation period will be discussed. However, the dissolution behaviour obtained for the full potentiostatic experiment (Figure 5.4) has been included in the supporting information (Appendix A). Before the first cathodic activation, *i.e.*, t < 0 s, the dissolved cation concentrations were below the limits of detection by ICP-AES, consistent with the presence of a protective oxide film. However, during the polarization at –0.8 V, a surge of metal dissolution was observed, confirming activation of the surface. During this activation process, labelled in Figure 5.5, the values of both ν'_{Cr}, and ν'_{Mo} were found to be greater than that of ν_{Ni}, suggesting the excess dissolution of Cr and Mo from the electrode surface. For all alloys, Cr was found to be the dominant metal cation released from the surface, with smaller amounts of Mo also being released. This is consistent with the measured composition of oxides formed on Cr/Mo-containing alloys [32, 42, 43] and suggests the surface is activated by the partial removal of the oxide film during polarization at –0.8 V.

Upon release to open-circuit, again labelled in Figure 5.5, alloys showed dissolution behaviour consistent with the spontaneous passivation of the surface. Both Cr and Mo species were found to accumulate at the surface (*i.e.*, ν'_{Mo}, $\nu'_{\mathrm{Cr}} < \nu_{\mathrm{Ni}}$): however, the accumulation of Mo species dominated this process. This was consistent with observations made during dynamic-polarization experiments, where Mo species were found to be the dominant species accumulated at potentials below the apparent $E_{i=0}$ (see Figure 5.3). Unsurprisingly, the ability of the surface to spontaneously passivate could be related to the Mo content of the alloy. Shown in Figure 5.5(A), alloy BC-1 (22.10 wt.% Mo) showed an immediate accumulation of Mo (and Cr) species, which quickly trended toward congruent dissolution (*i.e.*, $\nu'_{\mathrm{Mo}} = \nu'_{\mathrm{Cr}} = \nu_{\mathrm{Ni}}$) at a low overall dissolution rate. Comparison of the dissolution rates observed for the native oxide (*i.e.*, $t < 0$ s) with those of the re-established passive oxide (*i.e.*, $t > 250$ s), suggest the excellent ability of this alloy to recover from the surface activation process. This was consistent with the discussion of OCP values following activation, Figure 5.4, which suggested that alloy BC-1 quickly returned to a state similar to that of the native oxide (*i.e.* $t < 0$ s). Values of OCP were approximately –0.02 V, regardless of whether the surface had been activated by cathodic polarization, electrochemically passivated (discussed below), or had a native oxide. The ability of alloy BC-1 to resist damage to the oxide film has been previously attributed to its high Mo content [40, 44].

As shown in the discussion of OCP, following the activation of alloy C-22, OCP values increased toward a plateau, Figure 5.4, suggesting the re-establishment of an oxide layer. This was, however, significantly slower than the behaviour found for alloy BC-1, again

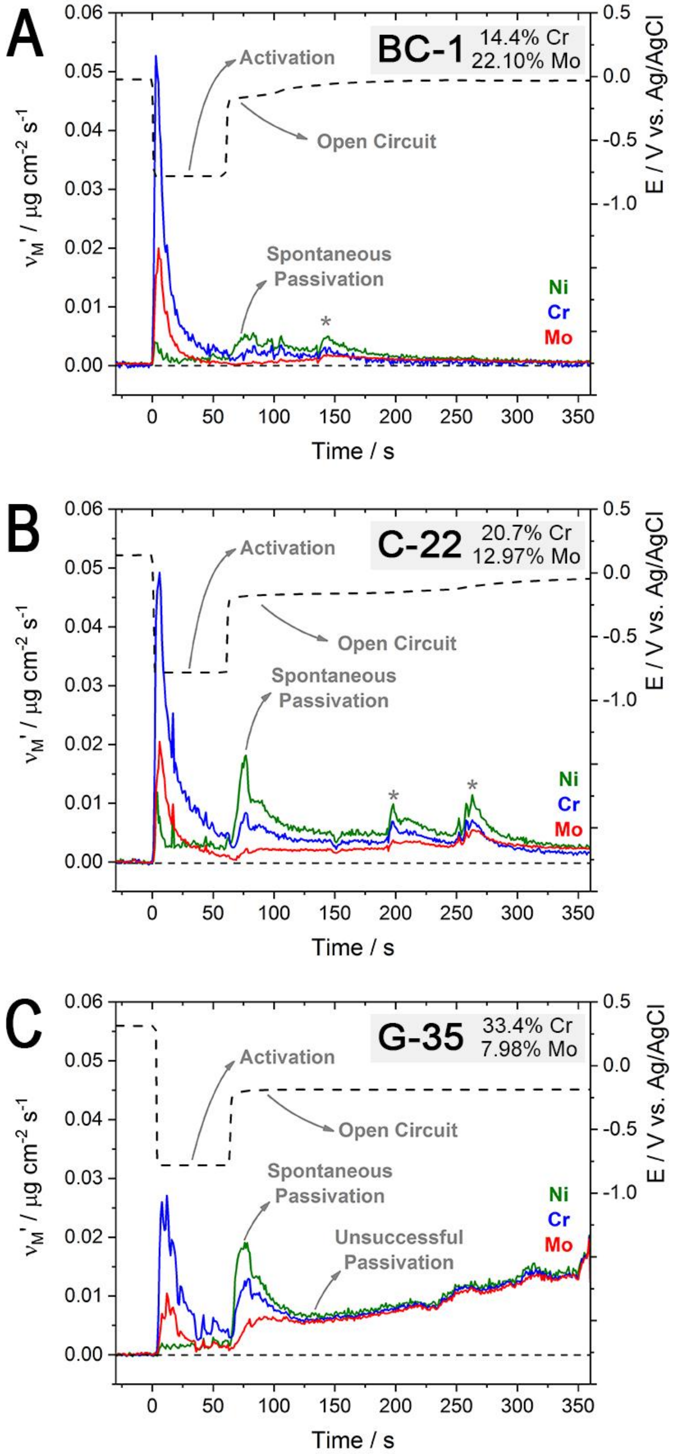

Figure 5.5 - Normalized dissolution rates obtained during the first surface activation (–0.8 V vs. Ag/AgCl) and subsequent open circuit potential measurement for alloy (A) BC-1, (B) C-22, and (C) G-35. All dissolution rates are normalized to the Ni-content in the alloy, Equation 5.3. For clarity, dissolution transients observed during the spontaneous passivation process are indicated (*). The Cr and Mo contents (wt.%) shown here were taken from Table 5.2.

suggested by the OCP. The dissolution behaviour shown in Figure 5.5(B), confirmed these observations, showing that alloy C-22 required a longer time than alloy BC-1 to spontaneously passivate and restore low dissolution rates following surface activation. Following the release to open-circuit, accumulation of both Cr and Mo species occurred, as observed for alloy BC-1. Elemental dissolution rates trended toward congruent behaviour and stabilized at low total dissolution rates, confirming the successful passivation of alloy C-22.

During the spontaneous passivation, momentary increases in elemental dissolution rates were occasionally observed for both alloy BC-1 and alloy C-22, indicated by (*) in Figures 5.5(A) and (B), although they were more frequent and severe for the lower-Mo-containing alloy C-22. These dissolution transients are the result of film breakdown events during the early stages of passivation. Corresponding features were not observed during OCP measurements, when negative-going potential transients would be typical. When dissolution rates were converted into values of i_{M} and i_{Σ}, transients were found to correspond to current increases of between 9 and 31 µA cm^{-2}. An example of the converted currents can be found in the supporting information (Appendix B). According to previously reported polarization resistance (R_P) values, these current transients are commonly accompanied by potential transients ≤ 3 mV [30]. During repeated activation processes, momentary increases in dissolution rates were consistently observed during the spontaneous passivation of alloy C-22 and, to a lesser extent for alloy BC-1. It is worth mentioning that with each dissolution transient, the separation between ν'_{Mo} (and ν'_{Cr}) and ν_{Ni} increased, suggesting an increased accumulation of Mo species following an ‘event’ which then slowly approached congruent behaviour. When another event occurred, the separation (or accumulation) again increased, before approaching congruent behaviour. This behaviour is consistent with the role of alloyed Mo in the repair of localized breakdown events, which has been shown to occur by the deposition of Mo-rich species at sites of damage [37, 45].

As shown in Figure 5.5(C), the dissolution behaviour observed after the surface activation of alloy G-35 differed from that of BC-1 and C-22. While initially accumulation of Mo and

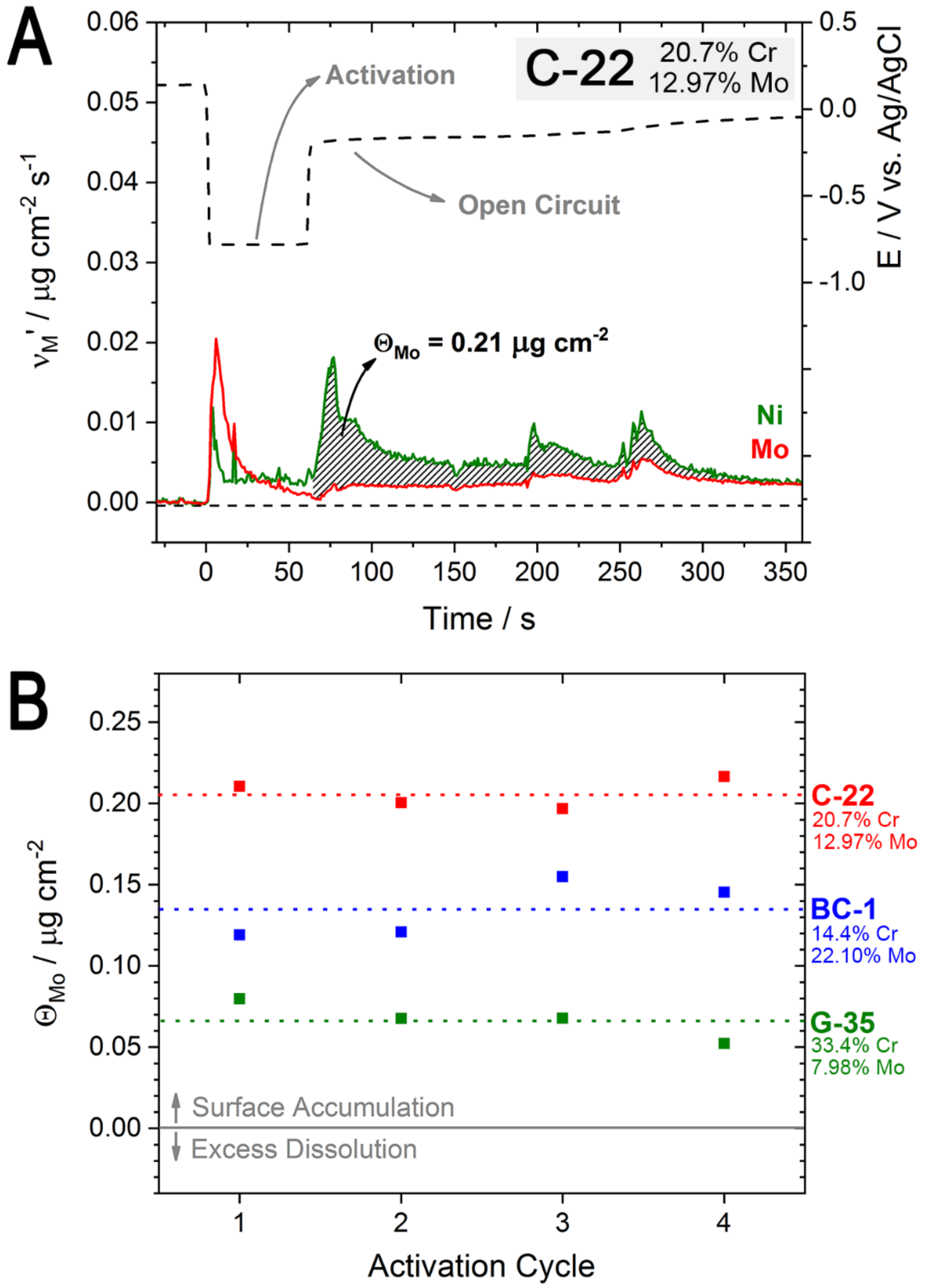

Figure 5.6 - Quantification of Mo accumulation (Θ_{Mo}) during spontaneous passivation. (A) Graphical representation of the area considered as accumulation of Mo species during the first activation process on alloy C-22. (B) Values of Θ_{Mo} for repeated activation processes for all alloys. Dotted lines indicate calculated averages. The Cr and Mo contents (wt.%) shown here were taken from Table 5.2.

Cr species was observed following the release to open circuit, after approximately 50 s the elemental dissolution became congruent and rates increased with time. Together the occurrence of congruent dissolution and the continuous increase in dissolution rates, may indicate unsuccessful passivation of alloy G-35. This is consistent with expectations for G-series alloys, which are not noted for their corrosion resistance to HCl solution as a result of their relatively low Mo contents, typically between 5 and 8 wt.% [46, 47]. While alloy G-35 does contain a considerable amount of Mo, 7.98 wt.%, these differences in spontaneous passivation behaviour suggest some critical concentration of (or ratio between) alloyed Cr and Mo must exist to promote film stability in acidic Cl^--containing environments.

The extent of Mo species accumulation (Θ_{Mo}) was quantified during the spontaneous passivation processes using Equation 5.4. A graphical representation of the area corresponding to accumulation of Mo species for alloy C-22 is highlighted in Figure 5.6(A) as an example. The Θ_{Mo} values for all alloys obtained over repeated activation processes are shown in Figure 5.6(B). Although the accumulation of Mo species would be expected to scale with an alloy's Mo content, the experimentally determined values of Θ_{Mo} show that accumulation increased according to: G-35 (7.98 wt.% Mo) < BC-1 (22.10 wt.% Mo) < C-22 (12.97 wt.% Mo). Furthermore, comparing values obtained over repeated activation cycles, alloy C-22 was found to consistently show the highest Θ_{Mo} value.

An explanation for this behaviour is based on the observations of the dissolution transients during the spontaneous passivation of alloy C-22 (Figure 5.5(B)). There are two mechanisms by which Mo increases corrosion resistance that are largely agreed upon: however, their details remain an area of ongoing research [11]. First, Mo content is beneficial in establishing a stable oxide film, especially in acidic chloride media [6]. Here, during the spontaneous passivation process observed for alloys BC-1 and C-22, accumulation of Mo species was found to be dominant, as dissolution rates stabilized at low values. Second, Mo content is vital in the repair of localized breakdown events [48]. While BC-1 was able to quickly form a stable oxide film, and exhibited only small breakdown events, alloy C-22 displayed much larger breakdown events. During these events, the increased separation between ν'_{Mo} and ν_{Ni} indicated increased accumulation of

Mo species following each event. Alloyed Mo is well known to promote the deposition of polymeric molybdate species at the breakdown site to stifle or block further dissolution [37, 45]. If events are both frequent and severe, as for alloy C-22, one would expect the accumulation of Mo species at the surface to be greater than that at the surface of an alloy like BC-1 that experiences only minor breakdown events and more rapidly establishes a stable passivating oxide.

5.3.2.2 Electrochemically-assisted passivation

Although the ability of the oxide film present on each alloy to recover from surface activation was of primary interest, the electrochemically-assisted passivation processes are also worth mentioning. Seen in the blue-shaded regions in Figure 5.4, after the application of 0.6 V, OCP values were found to increase relative to the values measured after activation. This increase was most significant for alloy C-22, followed by G-35, and lastly BC-1. The normalized dissolution behaviour recorded during this process was similar for all alloys, Figure 5.7. During the polarization at 0.6 V, all alloys showed the selective dissolution of Mo (*i.e.,* $\nu'_{\mathrm{Mo}} > \nu_{\mathrm{Ni}}$) and the accumulation of Cr species ($\nu'_{\mathrm{Cr}} < \nu_{\mathrm{Ni}}$). While passive oxide films formed on Cr/Mo-containing alloys are known to accumulate both Cr and Mo species, the selective removal of Mo species observed here was believed to be the consequence of the previous surface activation and spontaneous passivation process. As discussed above, during spontaneous passivation all alloys were found to accumulate Mo species at their surfaces. Additionally, this was consistent with dynamic experiments (Figure 5.3) which highlighted the excess dissolution of Mo and accumulation of Cr species at applied potentials higher than the apparent value of $E_{i=0}$. Previously, we demonstrated the dynamic nature of Mo species, which concentrate at the surface in the event of film breakdown and are partially released during the re-formation of Cr oxides [18].

While the dissolution behaviour of all alloys suggested the re-formation of a Cr-rich surface film, differences in the electrochemically-assisted passivation behaviour were observed. In the case of alloys BC-1 and C-22, dissolution rates were found to quickly approach the limits of detection once the electrode potential was released to open-circuit. In contrast, alloy G-35 showed a significantly slower decrease in dissolution rates than the other alloys,

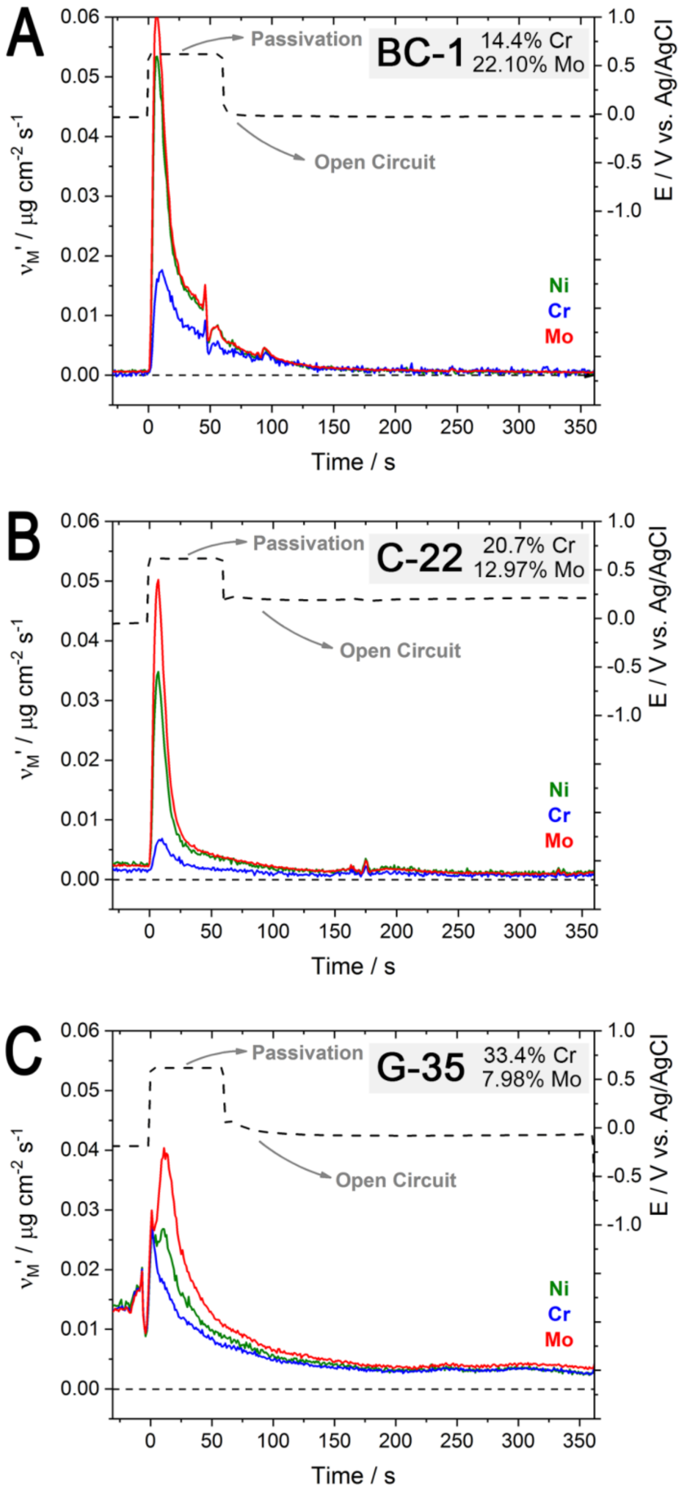

Figure 5.7 - Normalized dissolution rates obtained during the first electrochemically-assisted passivation process (0.6 V vs. Ag/AgCl) and subsequent open circuit potential measurement for alloy (A) BC-1, (B) C-22, and (C) G-35. All dissolution rates are normalized to the Ni-content in the alloy, Equation 5.3. The Cr and Mo contents (wt.%) shown here were taken from Table 5.2.

despite having the highest Cr content (33.4 wt.% Cr), and established a steady-state congruent dissolution rate rather than re-establishing passivity. These differences suggest that a critical film composition is important in controlling the barrier layer properties in HCl solutions.

5.3.3 Surface analysis

Surface compositions were determined after both surface activation (including spontaneous passivation) and electrochemically-assisted passivation using XPS. The experimental locations considered for surface analyses are indicated by (*) in Figure 5.4. Since similar dissolution patterns were observed for repeated activation/passivation processes, the surface compositions were analyzed only following the first activation/passivation processes. Survey spectra obtained for the three alloys in both

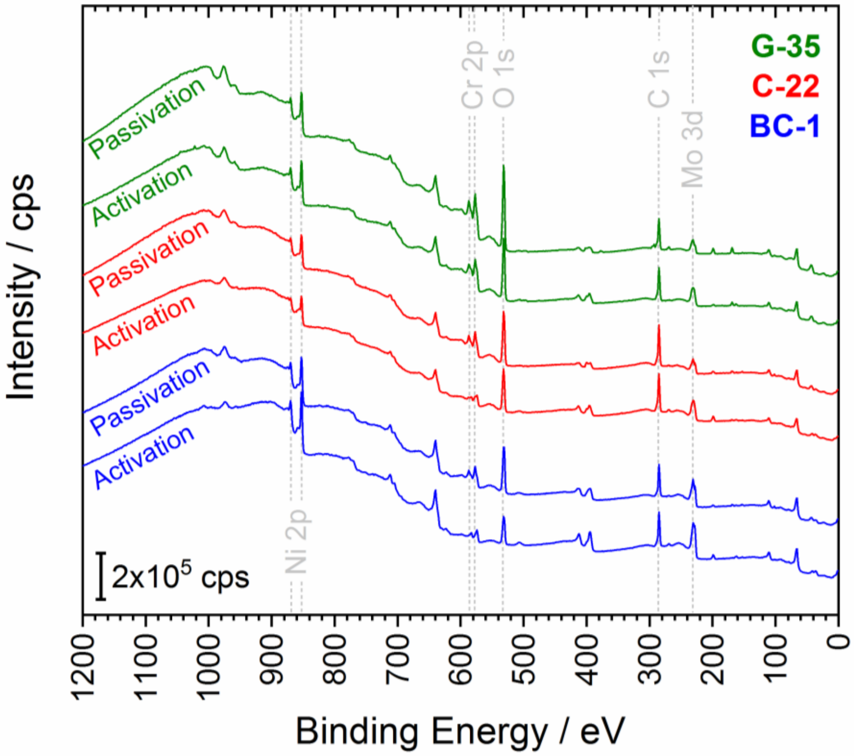

Figure 5.8 - Comparison of survey spectra collected for alloys G-35, C-22, and BC-1 following activation and passivation processes. Experimental locations used to prepare samples for surface analysis are shown in Figure 5.4. Quantification of the Ni $2p_{3/2}$, Cr 2p, Mo 3d, and O 1s peaks is given in Table 5.4.

conditions are compared in Figure 5.8. Subtle differences in the intensities of the Ni 2p, Cr 2p, and Mo 3d signals between the activated and passivated surface conditions were found. For all alloys, the intensity of the Mo 3d signal was higher following activation than it was for the passive surface condition. In contrast, the Cr 2p signal was higher following passivation than it was for the active surface condition. These changes, quantified using the Ni $2p_{3/2}$, Cr 2p, and Mo 3d signals, are summarized in Table 5.4.

Since the oxidized alloy surface species were of primary interest here, the O 1s signal was not considered in the surface compositions listed in Table 5.4. Oxide films formed on various Cr-containing alloys during exposure to a variety of conditions are known to be on the order of a few nm thick [15, 42, 49, 50]. Since the XPS has an effective analysis depth of 5-10 nm [51], which is thicker than the oxide film, the photoelectron signals for Ni, Cr, and Mo obtained from survey spectra are expected to originate from both metallic and oxidized components. Information on oxide compositions was extracted by deconvolution of chemical state information present in high-resolution spectra.

Table 5.4 - Surface composition (at.%) of G-35, C-22, and BC-1 after surface activation (including spontaneous passivation) and electrochemically-assisted passivation processes, considering the Ni $2p_{3/2}$, Cr 2p, and Mo 3d signals.

Alloy	**Condition**	**Ni $2p_{3/2}$**	**Cr 2p**	**Mo 3d**
G-35	Activation	36.8	46.3	16.9
	Passivation	33.8	56.2	10.0
C-22	Activation	45.7	24.2	30.1
	Passivation	38.1	46.1	15.8
BC-1	Activation	52.5	14.8	32.7
	Passivation	42.4	32.3	25.3

High-resolution spectra obtained for the Ni $2p_{3/2}$, Cr $2p_{3/2}$, and Mo 3d photoelectron peaks, as well as the deconvoluted chemical states, for specimens analyzed after both activation and passivation are presented in Figure 5.9. In all cases, the Ni $2p_{3/2}$ signal was dominated by metallic Ni (86.4 to 100 at.%), as shown in Figures 5.9(A), (D), and (G). The contributions from NiO and $Ni(OH)_2$ were found not to exceed a total of 13.6 at.%.

The high-resolution Cr $2p_{3/2}$ spectra recorded on alloys BC-1 (Figure 5.9(B)), C-22 (Figure 5.9(E)), and G-35 (Figure 5.9(H)), indicate mixtures of Cr_2O_3, $Cr(OH)_3$, and metallic Cr. This was true for both the activated and passivated surfaces. Following surface activation (and spontaneous passivation), the contribution from oxidized Cr species was relatively low compared to that of the metallic species, especially for the low-Cr alloy BC-1. The concentration of oxidized Cr species after activation was found to increase with increasing Cr content of the alloy, with BC-1 (14.4 wt.% Cr) < C-22 (20.7 wt.% Cr) < G-35 (33.4 wt.% Cr). The contributions from oxidized Cr species were higher following the electrochemically-assisted passivation process than those measured on alloys after surface activation (and spontaneous passivation).

Deconvolution of high-resolution Mo 3d spectra collected on the three alloys, Figure 5.9(C) BC-1, (F) C-22, and (I) G-35, after both activation and electrochemically-assisted passivation processes, revealed a complex mixture of metallic and oxidized Mo species (Mo(IV), Mo(V), and Mo(VI)). In some analyses, a small amount of S contamination was also observed. The S 2s signal, which overlapped with the Mo 3d signal, was subtracted using the chemical state information provided by analysis of the S 2p peak. The relative amount of oxidized Mo species was found to decrease on the electrochemically passivated surfaces compared to those which had been activated (and spontaneously passivated). This was consistent with AESEC results which demonstrated the tendency of Mo species to accumulate during spontaneous passivation and be removed during the electrochemically-assisted passivation process. The spectra in Figure 5.9 indicate a clear preference for Mo(IV) surface species after spontaneous passivation, while Mo(VI) species dominated after electrochemically-assisted passivation. Thermodynamics supports the formation of higher valence state Mo species such as MoO_3 or MoO_4^{2-} [31], with the latter being known to undergo complex polymerization reactions at low pH [37, 45, 52].

While deconvoluted high-resolution spectra provide information on the ratios of oxides to metal as well as the distribution of various oxidized species, they do not provide a true representation of what is on the surface. A more representative analysis of surface composition can be obtained by coupling the information provided by the survey spectra

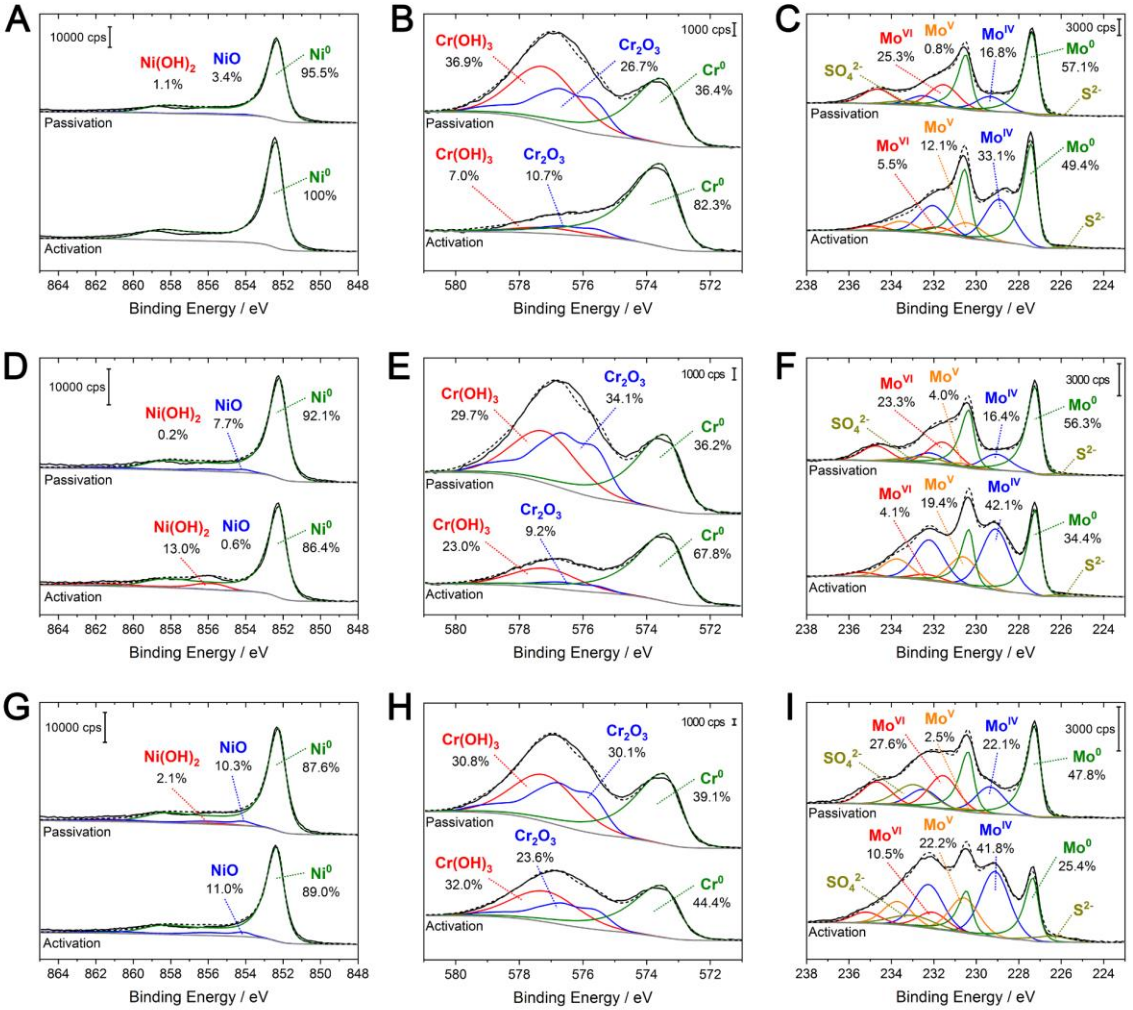

Figure 5.9 - High resolution Ni 2p$_{3/2}$, Cr 2p$_{3/2}$, and Mo 3d spectra collected on alloys (A-C) BC-1, (D-F) C-22, and (G-I) G-35. Surface analysis was conducted after activation (bottom) and passivation (top) steps, as discussed for potentiostatic polarization data. Experimental data (solid black) are presented along with the resultant fits (dotted black curves) and individual components considered in the deconvolution (solid curves in various colours).

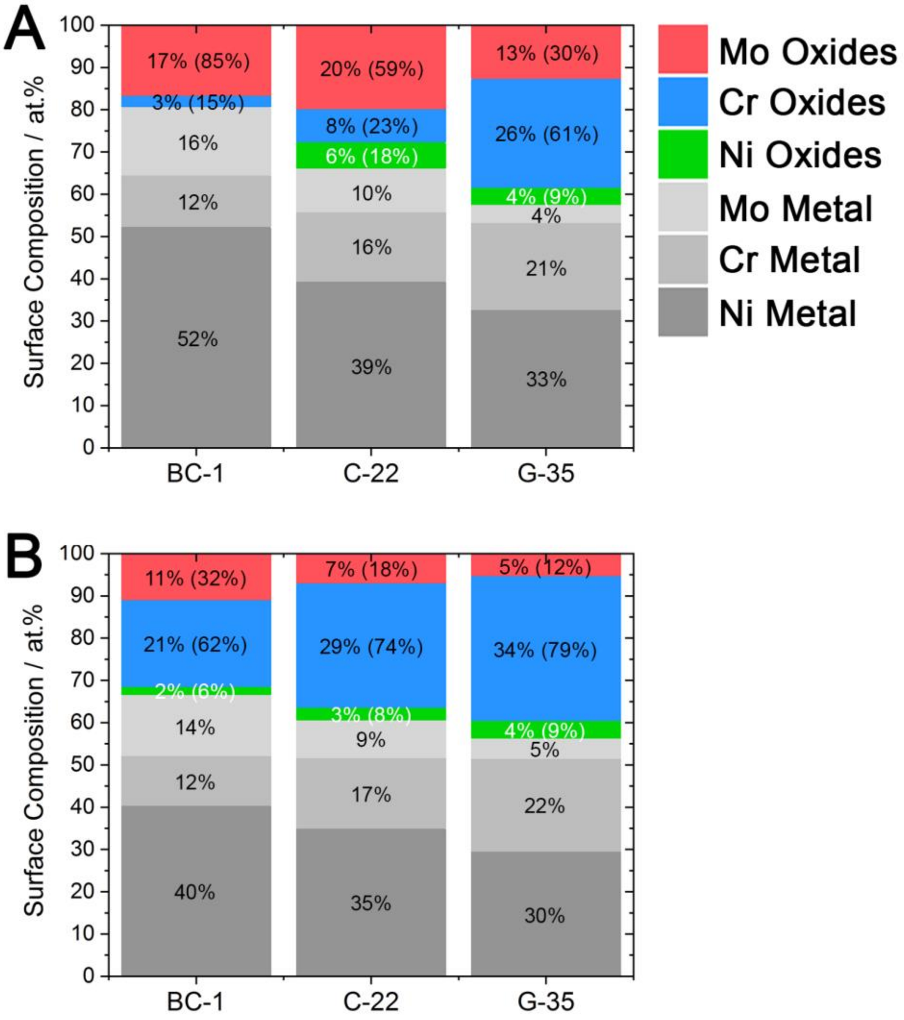

Figure 5.10 - Surface compositions of BC-1, C-22, and G-35 after (A) surface activation and (B) electrochemically-assisted passivation processes. Experimental locations used to prepare samples for surface analysis are shown in Figure 5.4. For the oxidized components, the relative oxide composition is also indicated in parentheses.

(*i.e.*, the average surface composition) and the deconvoluted high-resolution spectra (*i.e.*, the relative speciation concentrations). Shown in Figure 5.10, are the relative surface compositions expressed in terms of the metallic (Ni, Cr, and Mo) and oxidized contributions ($Ni(OH)_2$, NiO, Cr_2O_3, $Cr(OH)_3$, Mo(IV), Mo(V), and Mo(VI)).

After surface activation and spontaneous passivation, Figure 5.10(A), the amount of oxidized Mo surface species increased in the order G-35 < BC-1 < C-22, consistent with the trends observed by AESEC, as expressed by the values of Θ_{Mo}, Figure 5.6(B). Both the AESEC and XPS data indicate that alloy C-22 exhibits the largest amount of Mo-rich surface species following surface activation and spontaneous passivation. For surfaces analyzed after electrochemically-assisted passivation, Figure 5.10(B), all alloys demonstrated a decrease in oxidized Mo content and an increase in oxidized Cr content relative to their activated counterparts. This change was consistent with observations made by AESEC, which showed a tendency of Mo species to accumulate during spontaneous passivation (*i.e.*, after activation) and subsequently be released alongside the accumulation of Cr-rich surface species during electrochemically-assisted passivation.

5.4 Conclusions

Using the *operando* measurements afforded by atomic emission spectroelectrochemistry (AESEC), the dissolution behaviour of Hastelloy BC-1, C-22, and G-35, was studied during the surface activation, spontaneous passivation, and electrochemically-assisted passivation in 1 M HCl (75°C). Following surface activation, the accumulation of Mo species was found to dominate the spontaneous passivation behaviour, however, the accumulation of Cr species was also an important factor. After surface activation, high Mo content alloys, BC-1 (22.10 wt.% Mo) and C-22 (12.97 wt.% Mo), were found to rapidly recover, however, alloy C-22 required a slightly longer time and exhibited transient behaviour consistent with film breakdown. After processes of surface activation and spontaneous passivation, the accumulation of Mo species was found to be higher for alloy C-22 than for alloy BC-1, despite its lower Mo concentration. This was attributed to Mo deposition that occurred during the transient breakdown behaviour observed for alloy C-22 and not alloy BC-1. In the case of alloy G-35 (7.98 wt.% Mo), while an attempt to spontaneously passivate the activated surface was apparent, elemental dissolution rates rapidly increased, with congruent behaviour suggesting active dissolution. During electrochemically-assisted passivation processes, previously accumulated Mo species were found to be partially removed while accumulation of Cr species dominated the film formation process. The concept of Mo species accumulation and subsequent dissolution is consistent with previous studies conducted on film breakdown/repair. Data acquired by AESEC were also compared to the results of *ex situ* XPS surface analysis. Both relative surface composition and oxidation state information were discussed, with connections made to the AESEC data. Most notably, the observation suggesting the large accumulation of Mo species on the moderate Mo content alloy (C-22) was consistent between both AESEC and XPS measurements. These findings suggest the dual role of alloy Mo in stabilizing and repairing the oxide film.

5.5 References

[1] J.R. Davis, Nickel, cobalt, and their alloys, ASM international, 2000.

[2] N. Priyantha, P. Jayaweera, D.D. Macdonald, A. Sun, An electrochemical impedance study of alloy 22 in NaCl brine at elevated temperature. i. corrosion behavior, *Journal of Electroanalytical Chemistry*, 572 (2004) 409-419.

[3] X. Wu, S. Voyshnis, A. Seyeux, Y. Chumlyakov, P. Marcus, ToF-SIMS study of oxide films thermally grown on nickel-base alloys, *Corrosion Science*, 141 (2018) 175-181.

[4] A.C. Lloyd, J.J. Noël, S. McIntyre, D.W. Shoesmith, Cr, Mo and W alloying additions in Ni and their effect on passivity, *Electrochimica Acta*, 49 (2004) 3015-3027.

[5] N.S. Zadorozne, C.M. Giordano, M.A. Rodriguez, R.M. Carranza, R.B. Rebak, Crevice corrosion kinetics of nickel alloys bearing chromium and molybdenum, *Electrochimica Acta*, 76 (2012) 94-101.

[6] A. Mishra, D.W. Shoesmith, P. Manning, Materials selection for use in concentrated hydrochloric acid, *Corrosion*, 73 (2017) 68-76.

[7] J.W. Oldfield, W.H. Sutton, Crevice corrosion of stainless steels i. a mathematical model, *British Corrosion Journal*, 13 (1978) 13-22.

[8] J.W. Oldfield, W.H. Sutton, Crevice corrosion of stainless steels ii. experimental studies, *British Corrosion Journal*, 13 (1978) 104-111.

[9] P. Marcus, Corrosion mechanisms in theory and practice, CRC press, 2011.

[10] K. Gusieva, L.K. Cwalina, W.H. Blades, G. Ramalingam, J.H. Perepezko, P. Reinke, J.R. Scully, Repassivation behavior of individual grain facets on dilute Ni−Cr and Ni−Cr−Mo alloys in acidified chloride solution, *Journal of Physical Chemistry C*, 122 (2018) 19499-19513.

[11] K. Lutton Cwalina, C.R. Demarest, A.Y. Gerard, J.R. Scully, Revisiting the effects of molybdenum and tungsten alloying on corrosion behavior of nickel-chromium alloys in aqueous corrosion, *Current Opinions in Solid State & Materials Science*, 23 (2019).

[12] A.J. Samin, C.D. Taylor, First-principles investigation of surface properties and adsorption of oxygen on Ni-22Cr and the role of molybdenum, *Corrosion Science*, 134 (2018) 103-111.

[13] X.-x. Yu, A. Gulec, C.M. Andolina, E.J. Zeitchick, K. Gusieva, J.C. Yang, J.R. Scully, J.H. Perepezko, L.D. Marks, In situ observations of early stage oxidation of Ni-Cr and Ni-Cr-Mo alloys, *Corrosion*, 74 (2018) 939-946.

[14] V. Maurice, H. Peng, L.H. Klein, A. Seyeux, S. Zanna, P. Marcus, Effects of molybdenum on the composition and nanoscale morphology of passivated austenitic stainless steel surfaces, *Faraday Discussions*, 180 (2015) 151-170.

[15] K. Lutton, K. Gusieva, N. Ott, N. Birbilis, J.R. Scully, Understanding multi-element alloy passivation in acidic solutions using operando methods, *Electrochemistry Communications*, 80 (2017) 44-47.

[16] K. Ogle, S. Weber, Anodic Dissolution of 304 Stainless steel using atomic emission spectroelectrochemistry, *Journal of The Electrochemical Society*, 147 (2000) 1770.

[17] K. Ogle, J. Baeyens, J. Swiatowska, P. Volovitch, Atomic emission spectroelectrochemistry applied to dealloying phenomena: I. The formation and dissolution of residual copper films on stainless steel, *Electrochimica Acta*, 54 (2009) 5163-5170.

[18] J.D. Henderson, X. Li, D.W. Shoesmith, J.J. Noël, K. Ogle, Molybdenum surface enrichment and release during transpassive dissolution of Ni-based alloys, *Corrosion Science*, 147 (2019) 32-40.

[19] V. Shkirskiy, P. Maciel, J. Deconinck, K. Ogle, On the time resolution of the atomic emission spectroelectrochemistry method, *Journal of The Electrochemical Society*, 163 (2016) C37-C44.

[20] K. Ogle, Atomic emission spectroelectrochemistry: real-time rate measurements of dissolution, corrosion, and passivation, *Corrosion*, 75 (2019) 1398-1419.

[21] X. Li, K. Ogle, The passivation of Ni-Cr-Mo alloys: time resolved enrichment and dissolution of Cr and Mo during passive-active cycles, *Journal of The Electrochemical Society*, 166 (2019) C3179-C3185.

[22] V. Shkirskiy, P. Keil, H. Hintze-Bruening, F. Leroux, P. Volovitch, K. Ogle, Observation of l-cysteine enhanced zinc dissolution during cathodic polarization and its consequences for corrosion rate measurements, *Electrochimica Acta*, 184 (2015) 203-213.

[23] M.C. Biesinger, B.P. Payne, A.P. Grosvenor, L.W.M. Lau, A.R. Gerson, R.S.C. Smart, Resolving surface chemical states in XPS analysis of first row transition metals, oxides and hydroxides: Cr, Mn, Fe, Co and Ni, *Applied Surface Science*, 257 (2011) 2717-2730.

[24] M.C. Biesinger, B.P. Payne, L.W.M. Lau, A. Gerson, R.S.C. Smart, X-ray photoelectron spectroscopic chemical state quantification of mixed nickel metal, oxide and hydroxide systems, *Surface and Interface Analysis*, 41 (2009) 324-332.

[25] M.C. Biesinger, C. Brown, J.R. Mycroft, R.D. Davidson, N.S. McIntyre, X-ray photoelectron spectroscopy studies of chromium compounds, *Surface and Interface Analysis*, 36 (2004) 1550-1563.

[26] P.A. Spevack, N.S. McIntyre, Thermal reduction of molybdenum trioxide, *The Journal of Physical Chemistry*, 96 (1992) 9029-9035.

[27] N.S. Zadorozne, C.M. Giordano, R.B. Rebak, A.E. Ares, R.M. Carranza, Anodic behavior of alloy 22 in bicarbonate media effect of alloying, *Procedia Materials Science*, 8 (2015) 510-518.

[28] D.D. Macdonald, A. Sun, N. Priyantha, P. Jayaweera, An electrochemical impedance study of alloy-22 in NaCl brine at elevated temperature: ii. reaction mechanism analysis, *Journal of Electroanalytical Chemistry*, 572 (2004) 421-431.

[29] B. Laurent, N. Gruet, B. Gwinner, F. Miserque, K. Rousseau, K. Ogle, Dissolution and passivation of a silicon-rich austenitic stainless steel during active-passive cycles in sulfuric and nitric acid, *Journal of The Electrochemical Society*, 164 (2017) C892-C900.

[30] J.D. Henderson, B. Almusned, M. Momeni, S. Anderson, V. Dehnavi, D. Zagidulin, D.W. Shoesmith, J.J. Noel, Investigating the influence of Cr and Mo additions to commercial Ni-based alloys exposed to neutral and acidic chloride solutions, *Journal of the Electrochemical Society*, 167 (2020) 131512.

[31] M. Pourbaix, Atlas of electrochemical equilibria in aqueous solutions, National Association of Corrosion Engineers, Houston, TX, 2nd English edn, (1974) 384-392.

[32] X. Zhang, D. Zagidulin, D.W. Shoesmith, Characterization of film properties on the Ni Cr Mo alloy C-2000, *Electrochimica Acta*, 89 (2013) 814-822.

[33] J. Velázquez, J. Van Der Weide, E. Hernández, H.H. Hernández, Statistical modelling of pitting corrosion: extrapolation of the maximum pit depth-growth, *International Journal of Electrochemical Science*, 9 (2014) 4129-4143.

[34] X. Li, J. Han, P. Lu, J.E. Saal, G.B. Olson, G.S. Frankel, J.R. Scully, K. Ogle, Dissolution and passivation of a Ni-Cr-Fe-Ru-Mo-W high entropy alloy by elementally resolved electrochemistry, *Journal of The Electrochemical Society*, 167 (2020) 061505.

[35] P. Jakupi, D. Zagidulin, J.J. Noël, D.W. Shoesmith, The impedance properties of the oxide film on the Ni–Cr–Mo alloy-22 in neutral concentrated sodium chloride solution, *Electrochimica Acta*, 56 (2011) 6251-6259.

[36] X. Zhang, Z. Qin, D. Zagidulin, J.J. Noël, D.W. Shoesmith, Effect of oxide film properties on the kinetics of O_2 reduction on alloy C-22, *Journal of The Electrochemical Society*, 164 (2017) C911-C917.

[37] X. Shan, J.H. Payer, Characterization of the corrosion products of crevice corroded alloy 22, *Journal of The Electrochemical Society*, 156 (2009) C313-C321.

[38] A.C. Lloyd, J.J. Noël, N.S. McIntyre, D.W. Shoesmith, The open-circuit ennoblement of alloy C-22 and other Ni-Cr-Mo alloys, *Journal of Metals*, 57 (2005) 31-35.

[39] B. Kobe, M. Badley, J.D. Henderson, S. Anderson, M.C. Biesinger, D. Shoesmith, Application of quantitative X-ray photoelectron spectroscopy (XPS) imaging: investigation of Ni-Cr-Mo alloys exposed to crevice corrosion solution, *Surface and Interface Analysis*, 49 (2017) 1345-1350.

[40] J.D. Henderson, N. Ebrahimi, V. Dehnavi, M. Guo, D.W. Shoesmith, J.J. Noël, The role of internal cathodic support during the crevice corrosion of Ni-Cr-Mo alloys, *Electrochimica Acta*, 283 (2018) 1600-1608.

[41] M.B. Rockel, The effect of molybdenum on the corrosion behaviour of iron-chromium alloys, *Corrosion*, 29 (1973) 393-396.

[42] J.D. Henderson, A. Seyeux, S. Zanna, M.C. Biesinger, D.W. Shoesmith, J.J. Noël, P. Marcus, Investigating the transport mechanisms governing the oxidation of Hastelloy BC-1 by in situ ToF-SIMS, *Corrosion Science*, 159 (2019) 108138.

[43] L. Wang, A. Seyeux, P. Marcus, Thermal stability of the passive film formed on 316L stainless steel surface studied by ToF-SIMS, *Corrosion Science*, (2019) 108395.

[44] N. Ebrahimi, J.J. Noël, M.A. Rodriguez, D.W. Shoesmith, The self-sustaining propagation of crevice corrosion on the hybrid BC1 Ni–Cr–Mo alloy in hot saline solutions, *Corrosion Science*, 105 (2016) 58-67.

[45] P. Jakupi, F. Wang, J.J. Noël, D.W. Shoesmith, Corrosion product analysis on crevice corroded Alloy-22 specimens, *Corrosion Science*, 53 (2011) 1670-1679.

[46] R.W. Revie, Uhlig's corrosion handbook, John Wiley & Sons, 2011.

[47] U. Heubner, Nickel alloys, CRC Press, 2000.

[48] R. Newman, The dissolution and passivation kinetics of stainless alloys containing molybdenum (part i), *Corrosion Science*, 25 (1985) 331-339.

[49] E. Gardin, S. Zanna, A. Seyeux, A. Allion-Maurer, P. Marcus, Comparative study of the surface oxide films on lean duplex and corresponding single phase stainless steels by XPS and ToF-SIMS, *Corrosion Science*, 143 (2018) 403-413.

[50] T. Hanawa, S. Hiromoto, K. Asami, Characterization of the surface oxide film of a Co–Cr–Mo alloy after being located in quasi-biological environments using XPS, *Applied Surface Science*, 183 (2001) 68-75.

[51] P. Van der Heide, X-ray photoelectron spectroscopy: an introduction to principles and practices, John Wiley & Sons, 2011.

[52] R.S. Lillard, M.P. Jurinski, J.R. Scully, Crevice corrosion of alloy 625 in chlorinated ASTM artificial ocean water, *Corrosion Science*, 50 (1994) 251-265.

Chapter 6

6 The role of internal cathodic support during the crevice corrosion of Ni-Cr-Mo alloys

(Henderson (*et al.*), *Electrochim. Acta*, **2018**, 283, 1600-1608.)

Abstract:

Coupling of metal oxidation in crevice corrosion to both O_2 reduction on surfaces external to the crevice and H^+ reduction occurring within the crevice, was studied using a galvanostatic crevice corrosion technique in conjunction with weight loss analyses. Results suggest internal H^+ reduction is a significant contributor to the crevice corrosion of the studied alloys in 5 M NaCl at 120 °C. Repeat experiments suggest damage can be as much as doubled by H^+ reduction. This process, however, can be minimized by alloying additions of Mo, which permit the deposition of Mo-rich corrosion products within an active crevice. Due to difficulties experienced during corrosion product removal, the results presented herein are anticipated to be underestimates of the actual extent of this process. Consequently, damage predictions based on the availability of O_2 and other oxidants in the service environment may significantly underestimate the actual extent of corrosion on Ni-Cr-Mo alloys.

6.1 Introduction

Ni-based alloys are industrially important due to their robust corrosion resistant properties. Typically containing measurable amounts of Cr and Mo, these alloys have found applications in a range of industries, including petrochemical, nuclear, and chemical processing. Understanding and predicting their corrosion performance, and designing new, optimized alloys, requires a fuller understanding of the role of alloying elements and the nature of the corrosion processes.

Alloying additions of Cr are understood to induce strongly passive behaviour, due to the growth of a Cr(III)-rich oxide layer, a feature similar to what is seen in stainless steels [1]. However, alloying elements are much more soluble in the face-centred cubic (FCC) crystal structure of Ni-alloys than they are in Fe-based alloys, which allows for the accommodation of greater amounts of alloying additions in Ni-based alloys, while avoiding the formation of possibly deleterious secondary phases.

Mo is typically added to increase the stability of the oxide film and resistance to localized corrosion processes [1, 2]. Mo is also understood to suppress active dissolution under conditions where Cr becomes soluble, including acidic and highly oxidizing environments [3]. However, the content of alloying elements must be adjusted carefully because they affect not only corrosion properties but also materials cost, mechanical performance, weldability, etc. Many attempts to suggest an optimal alloy composition have been made; however, such a composition has not yet been achieved.

According to critical crevice solution (CCS) theory, the initiation of active crevice corrosion involves the development of a deaerated, acidic solution within the occluded geometry [4, 5]. Typically, crevice corrosion on Ni-based alloys is thought to be supported by O_2 reduction external to the occluded region. However, in the case of Ti-alloys, crevice corrosion has been shown to involve the coupling of metal dissolution to both O_2 reduction on external surfaces and H^+ reduction within the acidified crevice, as depicted in Figure 6.1 [6]. The presence of this coupling has been shown to intensify damage by 400% or more on these alloys [6, 7, 8].

Recently, electrochemical evidence has suggested that cathodic support for crevice corrosion of Ni alloys can also involve both O_2 reduction outside the crevice and H^+ reduction in its interior, resulting in intensified damage on Ni-based alloys [9]. This was inferred from observations that more than the expected quantity of damage was incurred by coupons that were made to undergo crevice corrosion under the application of constant anodic current. Although initially presented as a possibility, this inference was later supported by findings that revealed that once initiated, crevice corrosion on Ni-Cr-Mo alloys can support itself through an internal cathodic reaction [10]. It is no surprise that this feature has been overlooked in the literature since many studies have focused on techniques such as potentiodynamic-galvanostatic-potentiodynamic (PD-GS-PD) tests. Although these techniques are effective in ranking the relative corrosion resistance of alloys in terms of breakdown/repassivation potentials, they provide no mechanistic information. The work presented herein was undertaken to more fully document this previously unexplored feature.

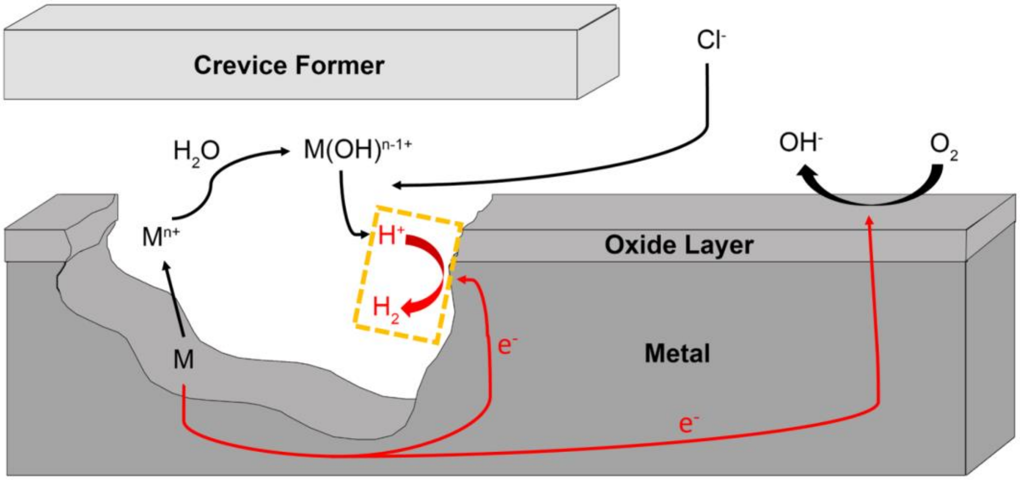

Figure 6.1 - Schematic representation of the critical crevice chemistry that develops within an active crevice [6].

In this paper the presence of the previously overlooked internal cathodic reaction on Ni-based alloys is examined using a galvanostatic technique in conjunction with weight loss analyses. Repeat experiments suggest that propagation damage can be as much as doubled by the internal H^+ reduction reaction. Through the analysis of a series of commercial alloys with differing amounts of the same alloying elements, we are trying to understand how alloy composition affects this process. The Ni-based alloys Hastelloy G-30, G-35, C-22, and BC-1, were selected for this study, based mainly on their varying Mo-content, since Mo-rich corrosion products have been extensively studied and are believed to stifle active corrosion [11, 12]. Herein, we evaluate the prevalence of the H^+ reduction reaction occurring during the crevice corrosion of Ni-based alloys in relation to the resulting damage morphology and the extent and type of corrosion product deposition.

6.2 Experimental

6.2.1 Material preparation

Alloy samples, provided by Haynes International (Kokomo, IN, USA), were received as mill-annealed sheets with a thickness of 3.18 mm (1/8"). Crevice coupons were formed from 15 mm wide strips cut from the plate stock. The compositions, as reported by Haynes International, are listed in Table 6.1.

Table 6.1 - Nominal compositions in weight (wt.) % of studied alloys as reported by Haynes International. 'Bal.' indicates alloying element which constitutes the balance. 'M' indicates an alloying or impurity element's maximum weight percentage.

Alloy	**Ni**	**Cr**	**Mo**	**Fe**	**W**	**Cu**	**Nb**	**Co**	**Mn**	**V**	**Al**	**Si**	**C**
G-35	Bal.	33.2	8.1	2^M	0.6	0.3^M	--	1^M	0.5^M	--	0.4^M	0.6^M	0.05^M
G-30	Bal.	30	5.5	15	2.5	2	0.8	5	1.5	--	--	0.8^M	0.03^M
C-22	Bal.	22	13	3	3	0.5^M	--	2.5^M	0.5^M	0.35^M	--	0.08^M	0.01^M
BC-1	Bal.	15	22	2^M	--	--	--	--	0.25	--	0.5^M	0.08^M	0.01^M

Prior to electrochemical measurements, all coupons were ground using wet silicon carbide (SiC) paper, sequentially from P600 to P1200 grit, carefully sonicated in a 1:1 mixture of EtOH and deionized (DI) water (18.2 MΩ cm) for 2 minutes, rinsed with DI water, and then dried in a stream of ultra-high purity Ar gas. Polished crevice coupons were then stored in a vacuum desiccator for a 24-hour period prior to use, to help assure an accurate gravimetric measurement.

Samples being prepared for electron backscatter diffraction were subjected to further polishing (1 μm diamond suspension) and a final etching step to expose grain boundaries. Different etching procedures were used for the various alloys due to differences in their corrosion resistance. Hastelloy G-30 and G-35 were etched by manual swabbing with a mixture (3:2:2) of HCl, CH_3COOH, and HNO_3. Hastelloy C-22 and BC-1 were electrochemically etched in an oxalic acid ($C_2H_2O_4$) solution (10 wt.%) by the application of a 0.2 A cm^{-2} for 15 s.

Solutions of 5 M NaCl were prepared using reagent grade NaCl (Caledon Laboratory Chemicals, Georgetown, ON) and DI water. Solutions were saturated with air by vigorous physical agitation immediately preceding each experiment.

6.2.2 Electrochemical setup

Crevice corrosion experiments were performed in a Hastelloy pressure vessel (Parr Instrument Co., Model 4621), outfitted as an electrochemical cell with four pressure-tight electrode feedthroughs. A brief description of this setup is given here, while additional information can be found in Chapter 2. All potential measurements were made using a homemade saturated Ag/AgCl (0.197 V vs SHE) reference electrode (RE). Prior to each experiment, the RE potential was measured against a 'master' saturated calomel electrode used only for the purpose of calibration. The WE was assembled using a single-crevice approach which has been extensively detailed elsewhere [13-15]. This design forms a single crevice between the V-shaped WE and a PTFE crevice former, which are held securely by a Udel® block. Udel® bushings were used to prevent electrical contact between the WE and the rods and bolts used to secure the crevice assembly. This arrangement ensures the formation of a single electrically connected crevice.

Once assembled, the vessel was pressurized (~414 kPa) with ultra-high purity nitrogen gas (Praxair, Mississauga, ON) and tested for leaks. The vessel was then placed in a heating mantle and the temperature was elevated to 120 ± 2 °C and maintained there for the duration of the experiment. After the experimental temperature was established, crevice corrosion was initiated using galvanostatic polarization. The total applied charge (Q_A) was controlled by applying a constant current through the WE and manipulating the duration of an experiment. At applied currents of 100, 75, 50, and 25 µA, the corresponding experimental times were 1, 1.33, 2, and 4 x 10^6 s, respectively, in order to maintain a consistent Q_A of 100 C. Each experiment was monitored by measuring the potential response using a Solartron model 1284 potentiostat (Solartron Analytical, Hampshire, UK).

6.2.3 Surface analysis

Following electrochemical experiments, routine surface analysis was conducted using Hitachi S-4500 field emission and Hitachi SU3500 variable pressure scanning electron microscopes (SEM). Unless otherwise stated, corrosion products were removed prior to surface analysis, through a cleaning process involving both sonication and manual swabbing with cotton-tipped applicator sticks. Energy-dispersive X-ray spectroscopy (EDS) was conducted on a Hitachi SU3500 variable pressure SEM in combination with an Oxford Aztec X-Max50 X-ray analyzer. Aztec software allowed for both point analyses as well as the acquisition of EDS maps.

Electron backscatter diffraction (EBSD) was conducted on a Hitachi SU6600 field emission gun (FEG) SEM. The FEG-SEM was outfitted with an HKL Nordly EBSD detector to collect Kikuchi patterns. Data analysis was carried out using the HKL Channel 5 software suite (Oxford Instruments). All crystal orientation information was indexed according to the FCC crystal structure.

Surface profilometry was conducted on a KLA Tencor P-10 surface profiler (Milpitas, CA, USA) and used to determine the maximum depth of penetration and overall damage morphology within a corroded crevice. The instrument was outfitted with a stylus containing a tungsten point, fixed with a diamond tip (radius ~2 μm). The stylus was scanned over the surface at 50 μm s^{-1}.

6.3 Results and discussion

6.3.1 Galvanostatic crevice corrosion

Detailed in Figure 6.2 is the typical potential response of an artificial crevice while under galvanostatic control. Following the application of constant current, the potential increases rapidly due to oxide growth. The potential increase eventually reaches an approximately steady state in which the rates of film growth and destruction are approximately equal. It is in this region where passive oxide film breakdown attempts occur, resulting in negative-going potential transients. Typically, a large number of these transients are observed as the passive film breaks and the potential drops but then readily returns to the steady-state potential, *i.e.*, the surface repassivates. However, over time, as the CCS chemistry develops as a result of chemical reactions during these metastable events within the occluded region, the likelihood that a given breakdown event will successfully initiate crevice corrosion increases. The success of any individual breakdown event in initiating crevice corrosion

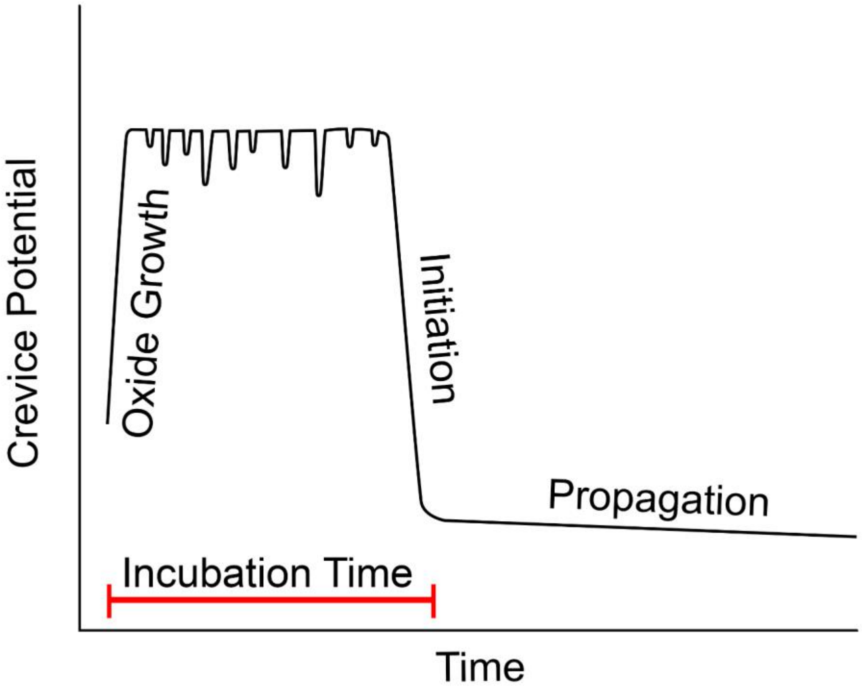

Figure 6.2 - Graphical representation of typical potential behaviour for a crevice electrode under galvanostatic control.

depends on the accumulation of incremental chemical changes resulting from prior initiation attempts. The total time required for a successful breakdown event is often referred to as the incubation time. Since features such as the incubation time rely heavily on the dynamic chemistry evolving within the crevice, only general observations are made. The overall behaviour has been discussed in previous publications which have utilized galvanostatic polarization to control the crevice corrosion of Ni-Cr-Mo alloys [9, 10, 13].

6.3.2 Potential behaviour of C-22

The typical response of alloy C-22 follows the behaviour described in Figure 6.2, and is illustrated in Figure 6.3 at applied currents of 100, 75, 50, and 25 μA. Initially, oxide growth occurs at approximately the same rate in each case, and is independent of the applied current. The maximum potential reached was however typically found to be higher with higher applied currents. A possible explanation for this is related to the nature of the

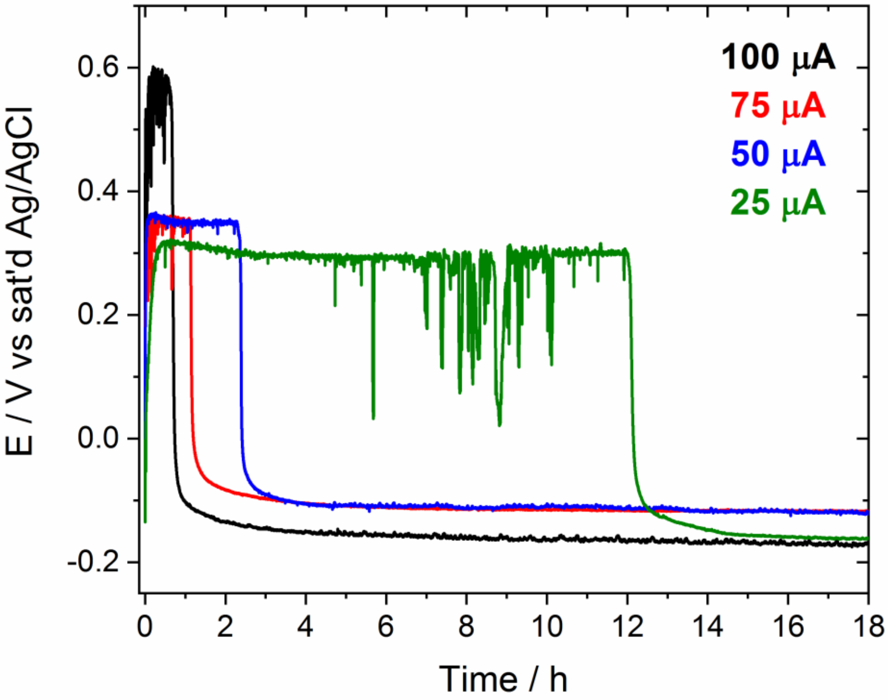

Figure 6.3 - Potential-time response of C-22 crevice electrode while under galvanostatic control (100, 75, 50, and 25 μA).

film formed under varied applied currents. Jakupi *et al.* demonstrated that oxides grown at high applied potentials (>300 mV vs sat'd Ag/AgCl) were typically thick and defect-rich [13]. Although not explicitly demonstrated here, it is expected that higher applied currents result in similar thick, defect-rich films. The ensuing increase in film resistance forces the measured potential to higher values in order to maintain the applied current. Once the potential plateau is achieved, negative-going potential transients are observed. No connection was made between the frequency and severity of these events and the applied current. These events are believed to be random, and the success of any individual event relies on the crevice chemistry developed as a consequence of prior events as described earlier. What is apparent is that the average time required for a successful breakdown event to occur, *i.e.*, the incubation time, increases as the applied current decreases. We believe this to be a result of the decreased rate at which the CCS is developed.

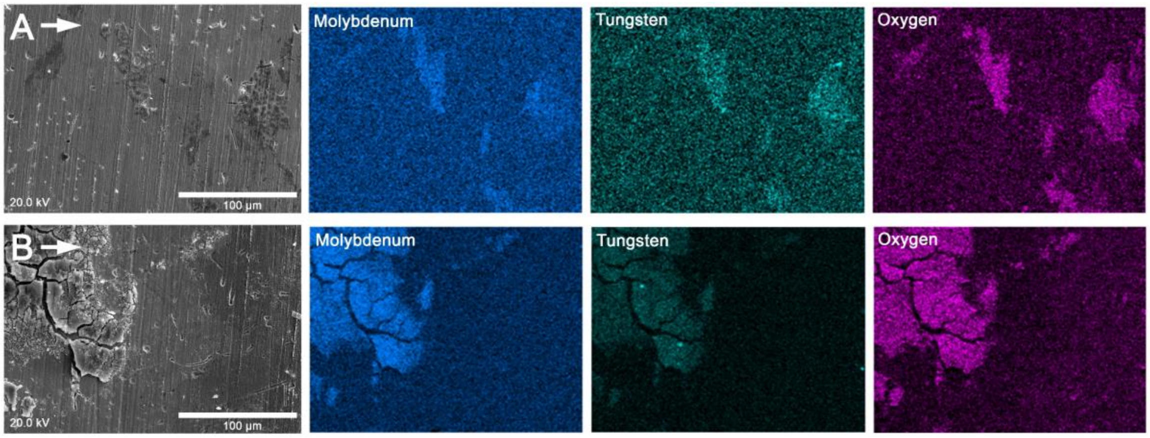

Figure 6.4 - Secondary electron micrographs and element distribution maps of crevice site following (A) several initiation attempts and (B) successful initiation. Both coupons were corroded galvanostatically at 75 µA.

Once crevice corrosion is initiated, the propagation potential appears to be independent of the applied current. However, interpretation of crevice behaviour by monitoring changes in the propagation potential is complicated by the large ohmic drop within the active crevice. Once crevice corrosion is initiated, the high solution resistance within the crevice, coupled with the flow of current, results in a potential drop, which means the measured potential is valid only outside the crevice mouth, and not in the crevice interior. Therefore, we have not attempted to understand the behaviour of the propagation potential.

In order to relate features of the measured potential to any corresponding physical damage, we conducted a study in which we withdrew the applied current following characteristic potential behaviour. Of particular interest during this study were the negative-going potential transients occurring during the time of the potential plateau. Knowledge of the early stages of damage allows for more accurate interpretation of fully corroded coupons, which will be discussed later. In total two potential responses were analyzed: that occurring immediately following initiation (Figure 6.4(A)), and that observed after a small amount of propagation had occurred (Figure 6.4(B)).

As shown in Figure 6.4(A), immediately following initiation the total amount of damage is minimal, with polishing lines remaining clearly visible. Areas of localized attack are present and appear primarily along grain boundaries. A thin covering of Mo-, W-, and O-rich corrosion products was found surrounding areas of damage. A large amount of these products was detached during the disassembly of the crevice, and it is generally believed that these products deposit to cover areas of damage in acidified crevices [16]. Crevice coupons from experiments that were terminated after a short period of propagation had a similar damage signature; however, damage was intensified, suggesting a natural progression, shown in Figure 6.4(B). The progression appears to involve predominantly corrosion along grain boundaries. Furthermore, these coupons were again covered by Mo-, W-, and O-rich corrosion products. However, the corrosion product deposits were thicker, as illustrated by the increased EDX signal intensity relative to the background. The deposition of these products has been said to stifle active dissolution, causing active sites to relocate within the crevice [14]. From these experiments we concluded that damage begins at local sites, predominantly along grain boundaries, and progresses as corrosion products begin to deposit.

6.3.3 Potential behaviour of different alloys

A direct comparison of the potential response observed for BC-1, C-22, G-35, and G-30, under the application of 100 μA is outlined in Figure 6.5. Upon the application of constant current both BC-1 and C-22 exhibit a rapid increase in potential as a result of oxide growth, as previously discussed. The rate at which the potential increases is dependent on the Cr content of the alloy reflecting the rate of film growth. As a consequence, the potential response of C-22 (22 wt.% Cr) increases more rapidly and to a higher final potential than for BC-1 (13 wt.% Cr). Furthermore, the frequency and amplitude of breakdown events appears to have a dependence on Mo content. In comparison, BC-1 (22 wt.% Mo) displays less frequent potential transients with smaller excursions than C-22 (13 wt.% Mo). This is the result of the greater ability of BC-1 to repassivate film breakdown events resulting from increased Mo content. These observations have similarities to those previously discussed in studies employing the galvanostatic crevice corrosion technique on different Ni-Cr-Mo alloys [9].

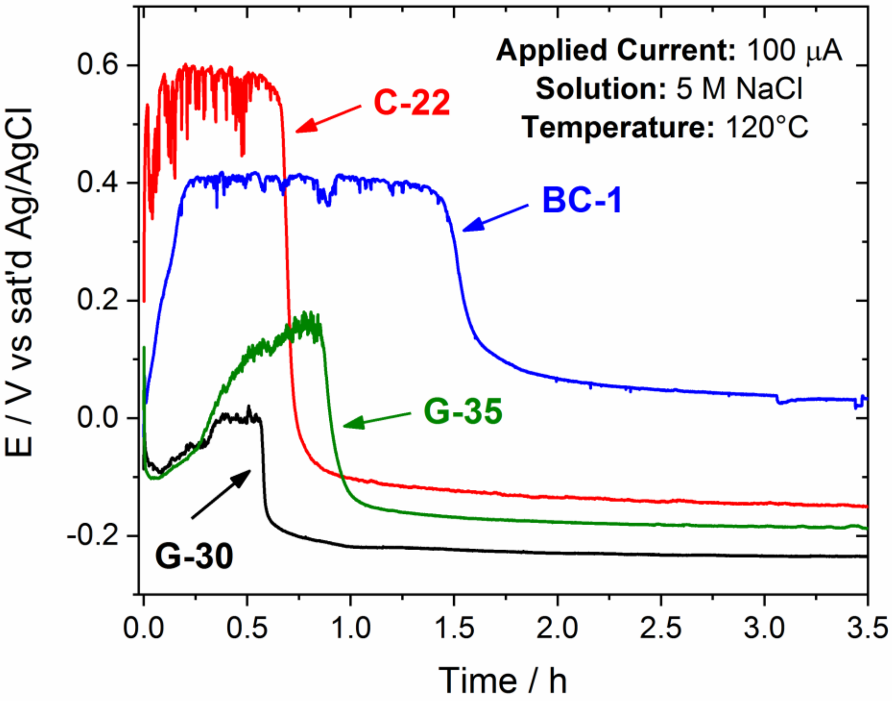

Figure 6.5 - Comparison of the potential-time response of BC-1, C-22, G-35, and G-30, while under galvanostatic control of 100 μA.

The potential behaviour seen for alloy G-35 and G-30 was found to deviate from the previously described behaviour. Although an initial increase in potential is observed, it is short lived and precedes a period of instability followed by successful breakdown. The maximum potential reached is much lower than the threshold potential once thought to be a requirement for the initiation of galvanostatically controlled crevice corrosion of Ni-Cr-Mo alloys [10]. These results, together with a series of additional experiments (*e.g.*, Chapters 3 and 5), suggest differences in oxide film stability in solutions anticipated during the development of crevice corrosion. This could be a result of Mo content insufficient to stabilize the oxide film as acidity develops [2, 3]. The cause of this deviation will be the focus of a future publication. Herein, the focus will be on the presence and extent of an internal cathodic reaction as well as the effect of composition on these processes.

In all cases, following a successful initiation event, the propagation potential was found to be relatively stable, aside from only minor fluctuations. Such fluctuations suggest localized breakdown events within the active crevice. Since the final damage morphology displays a single corroded region, it is likely that these potential fluctuations are the result of breakdown events along the periphery of the active crevice. Notably, the propagation potentials were found to decrease as the Mo content of the alloy decreases. This is consistent with previous observations made on different Ni-Cr-Mo alloys [9].

In consideration of each of the propagation potentials, H^+ reduction within the crevice, serving as the additional cathodic reaction, is considered thermodynamically possible. For instance, if the pH inside the active crevice is assumed to be 0, the potential for H^+ reduction at 120 °C is calculated to be 0.035 V (vs sat'd Ag/AgCl) (assuming 1×10^{-6} atm H_2). Since each of the propagation potentials is consistently less than 0.035 V (vs sat'd Ag/AgCl), the H^+ reduction reaction can be considered thermodynamically possible within an active crevice. In addition, the effects of IR drop at locations deep within the creviced region are not accounted for, but would only strengthen the thermodynamic argument. Lastly, the crevice pH used to calculate the reduction potential is conservative, given literature reports that the pH would be < 0 [12, 16, 17].

6.3.4 Internal cathodic support

Following the completion of each experiment, crevice coupons were thoroughly cleaned to remove corrosion products formed in damaged areas. With the purpose of obtaining measurable weight loss, each experiment was conducted until a total applied charge (Q_A) of 100 C was reached. The large weight loss which resulted allowed for the accurate calculation of a charge equivalent to the weight loss (Q_W). This was calculated according to Faraday's law, Equation 6.1, where W is the weight loss, F is Faraday's constant, n_{avg} is the weighted average oxidation number of metal cations created, and m_{avg} is the weighted average molar mass, calculated based on the alloy composition.

$$Q_W = WF\left(\frac{n_{avg}}{m_{avg}}\right) \tag{6.1}$$

$$\left(\frac{n_{avg}}{m_{avg}}\right) = \sum_{i=1}\left(\frac{X_i n_i}{m_i}\right) \tag{6.2}$$

The calculation used for the effective oxidation number:molar mass ratio is outlined in Equation 6.2, were X_i is the mass fraction, n_i is the number of electrons transferred during oxidation, and m_i is the molar mass of the respective alloying element. For simplicity, only major alloying elements (Ni, Cr, Mo, W, and Fe) were considered in these calculations and congruent metal dissolution was assumed. Values of X_i were calculated from the nominal compositions reported by Haynes International (Table 6.1). The values used for n_i were discerned using thermodynamic values for all elements except Mo and W. Based on thermodynamic data, Ni, Cr, and Fe were anticipated to oxidize to form Ni(II), Cr(III), and Fe(II) species in the CCS. The same set of E-pH diagrams indicates the oxidation of Mo and W to Mo(IV) and W(IV) species [16, 18]; however, literature reports suggest that the corrosion products formed within an active crevice environment contain mainly Mo(VI) and W(VI) species [13,14]. Furthermore, the calculated effective oxidation number:molar mass ratio (n/M) is similar to that of other literature reports [19].

In order to determine the extent of internal cathodic support, the total sustained damage (Q_W) was compared to that measured electrochemically (Q_A). The value of Q_A accounts only for the damage sustained by coupling of corrosion to the external reduction of O_2 on the counter electrode. In contrast, the value of Q_W corresponds to the total amount of damage resulting from corrosion coupled to all possible cathodic reactions. Therefore, the difference between the two values indicates the amount of damage arising from coupling to cathodic reactions occurring within the crevice, *i.e.*, H^+ reduction in the crevice interior. Since negative-going potential transients, observed during the early stages of polarization on all alloys, correspond to localized corrosion events within the crevice, the total Q_A (100 C) was considered rather than only the charge passed after initiation. The extent of internal cathodic support for corrosion of alloy C-22 at a series of applied currents, reported as a percentage of the total amount of corrosion damage (*i.e.*, $(Q_W - Q_A)/Q_W \times 100\%$) is illustrated in Figure 6.6. Through this methodology, the presence of an internal cathodic support process is apparent. From these results, it is clear that corrosion rate calculations that consider O_2 as the only oxidant underestimate the extent of corrosion damage.

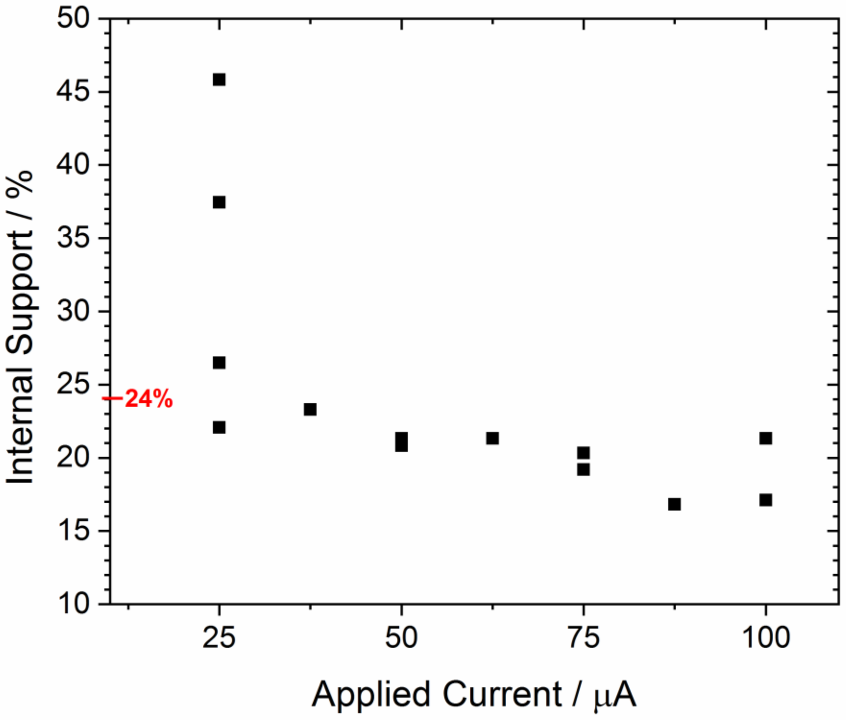

Figure 6.6 - Internal support (%) as a function of applied current on C-22. Indicated along the left axis is the average considering all measurements.

At the lowest examined current, 25 µA, the contribution of internal cathodic support was significant, but the actual extent of it is irreproducible. The values range, from 22.1 to 45.8%, likely a result of the evolution of damage morphology occurring within the active crevice. Based on post-corrosion analyses, it is apparent that the tendency under the application of small currents is to drive deeper penetration within the crevice. We believe that these deep areas have an increased ability to support the development and/or maintenance of the CCS. Conversely, at higher applied currents, the tendency of damage to spread laterally across an alloy surface is less effective at supporting the developing CCS. The propensity of damage to spread laterally at higher applied current has been discussed elsewhere [14]. The hypothesis that damage morphology plays a role in establishing an internal cathodic reaction will be explored further at the end of this paper.

With the realization that an internal cathodic reaction is indeed significant during the crevice corrosion of C-22 the question remains how the composition of the alloy affects this process. The ability of Mo-rich corrosion products to stifle active dissolution has been investigated in the context of different forms of localized corrosion. In a study focused on artificial pits, Newman showed the tendency of Mo to locate at defect sites, inhibiting dissolution at locations which would otherwise corrode [20, 21]. Shan *et al.* demonstrated the tendency of dissolved Mo and W to precipitate within an active crevice, while other dissolved alloying elements tend to deposit outside the active region [16]. Jakupi *et al.* later characterized the Mo-rich corrosion products found within an active crevice as polymeric Mo(VI) species using Raman spectroscopy [22]. In the present work, we attempt to characterize the effect of Mo(VI) deposition on internal cathodic support of crevice corrosion by studying the behaviour of Ni alloys G-30, G-35, C-22, and BC-1 polarized galvanostatically at a single applied current.

The degree of internal cathodic support determined from $(\mathrm{Q_W} - \mathrm{Q_A})/\mathrm{Q_W} \times 100\%$ analyses of BC-1, C-22, G-35, and G-30 crevice coupons corroded at an applied current of 100 μA are shown in Figure 6.7. In this representation, the internal cathodic support is compared to the Mo + W content of the alloy. The two are considered in sum because W behaves much like Mo; *i.e.*, W-rich corrosion products deposit and stifle dissolution [16, 23]. This treatment assumes that the magnitude of the effect is the same per unit mass for both Mo and W, however some literature reports claim that Mo is twice as effective as W in protecting an alloy on a per-weight basis [3, 24, 25]. Whether or not the relative amounts of internal cathodic support in Figure 6.7 are compared to the Mo, Mo + 0.5 W, or Mo + W content of each alloy, the conclusions are the same.

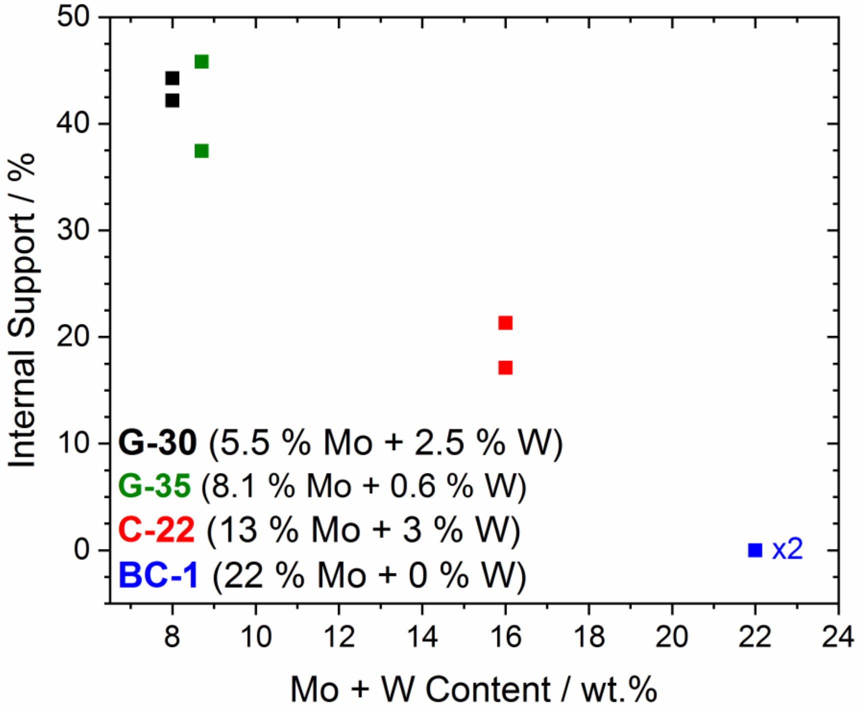

Figure 6.7 - Internal support (%) as a function of Mo + W content. Coupons corroded galvanostatically at 100 μA.

The Mo + W content is inversely proportional to the magnitude of the internal support process. As the Mo + W content increases, the extent to which the internal H^+ reduction reaction is able to intensify damage decreases. For alloy G-30, containing only 5.5 wt.% Mo and 2.5 wt.% W, the internal cathodic reaction has been shown to intensify damage as much as an additional 76.1%. Likewise, for alloy G-35 (8.1 wt.% Mo and 0.6 wt.% W) the internal cathodic reaction was found to intensity damage by as much as an additional 72.1%. Alloy C-22, which contains 13 wt.% Mo and 3 wt.% W, has an average 23.8% increase in the expected damage based on the applied charge, while BC-1 (22 wt.% Mo) exhibits a weight loss measurement suggesting negligible internal support (approximately zero).

It should be explicitly mentioned that the weight loss method used to quantify the internal support is a rather crude process that relies on removal of the corrosion product, which is difficult, due to the irregular surface morphology and locations of deep penetration. Consequently, the weight loss values used to calculate Q_W represent an underestimate of the actual extent of corrosion damage, and therefore so are the levels of internal cathodic support determined by comparison of Q_A and Q_W. Nonetheless, the data presented highlight the importance of considering such a process, and the extent to which alloy composition may promote or suppress it.

To support this analysis, an identical experiment (100 C of charge applied at 100 μA) was performed on an alloy G-30 coupon with no crevice. In this case, the potential remained in the transpassive range (~0.82 V (vs sat'd Ag/AgCl)) throughout the entire polarization period, and no negative-going transients were observed. The measured weight loss corresponded to 65.0 C of charge equivalent (compared with 179.2 C for the electrode with the crevice). With no crevice, the weight loss is less than expected, rather than more. The "missing" 35 C charge equivalent to weight loss in this experiment likely corresponds to the mass of residual oxide that could not be stripped from the metal surface after the polarization experiment, consistent with the contention that the Q_W values represent an underestimate of the actual extent of corrosion damage.

6.3.5 Damage progression

The removal of corrosion product from coupons initially used to quantify internal cathodic support also benefitted post-corrosion analyses by exposing the otherwise hidden variations in crevice corrosion damage. Each of the examined alloys illustrates differences in damage morphology, while sharing subtle features, such as those discussed during the study of initiation (Figure 6.8). The corrosion damage (Figure 6.8(A-D)) achieved maximum penetration depth in proximity to the crevice mouth. This is a feature commonly observed during the crevice corrosion of Ni-Cr-Mo alloys, and in a practical sense represents and arises from the re-tracing of the active-passive polarization curve within the crevice as a consequence of the local ohmic drop within the occluded geometry [26, 27].

In general, the maximum depth of penetration was greatest for alloy G-35 and G-30. In contrast, alloy BC-1 consistently revealed the lowest maximum depth of penetration. For the damage sites represented in Figure 6.8(A-D) the maximum depth of penetration was found to be approximately 310, 295, 265, and 76 μm on alloys G-30, G-35, C-22, and BC-1, respectively.

Information regarding how damage develops within the active crevice was uncovered by comparing the SEM images shown in Figure 6.8(E-H). Alloy BC-1 (Figure 6.8(E)), shows features which resemble the damage observed during initiation studies (recall Figure 6.4). This implies that for this alloy, following initiation, the readily deposited corrosion products impede damage progression and instead force dissolution to relocate along the periphery of the damage site. As a result, the damage morphology fails to develop beyond the features observed during early propagation. This is consistent with the observation that BC-1 typically shows shallow corrosion penetration in comparison to C-22, G-35, and G-30. Alloy C-22 (Figure 6.8(F)), which is anticipated to deposit corrosion products less readily, due to the decreased Mo content, shows similar features along the periphery of the crevice, yet has what appears to be a more advanced level of damage in the center of the crevice. This suggests that C-22 requires a longer time to deposit corrosion products sufficient to force the applied current elsewhere (*i.e.*, to the periphery). Lastly, alloys G-35 and G-30, Figures 6.8(G) and (H), respectively, which are anticipated to have the poorest ability to deposit corrosion products, shows almost no lateral progression of damage. Instead the periphery of the damaged region shows some localized attack along grain boundaries, and displays features of preferential etching. This suggests a global instability of the oxide film exposed to the developing CCS, consistent with observations made during the discussion of the potential response for G-35 and G-30 under galvanostatic conditions. As one traverses from the periphery toward the area of greatest depth, there is an immediate drop off in topography (shown in both Figure 6.8 (C/D) and (G/H)) which suggests the failure of Mo-rich products to deposit on the surface. This is consistent with literature reports which have shown that an increased rate of molybdate deposition forces damage to spread laterally across the surface [14]. The ineffective deposition process occurring on G-35 and G-30 allows active metal dissolution to continue relatively uninhibited, and therefore damage penetrates deep into the bulk material.

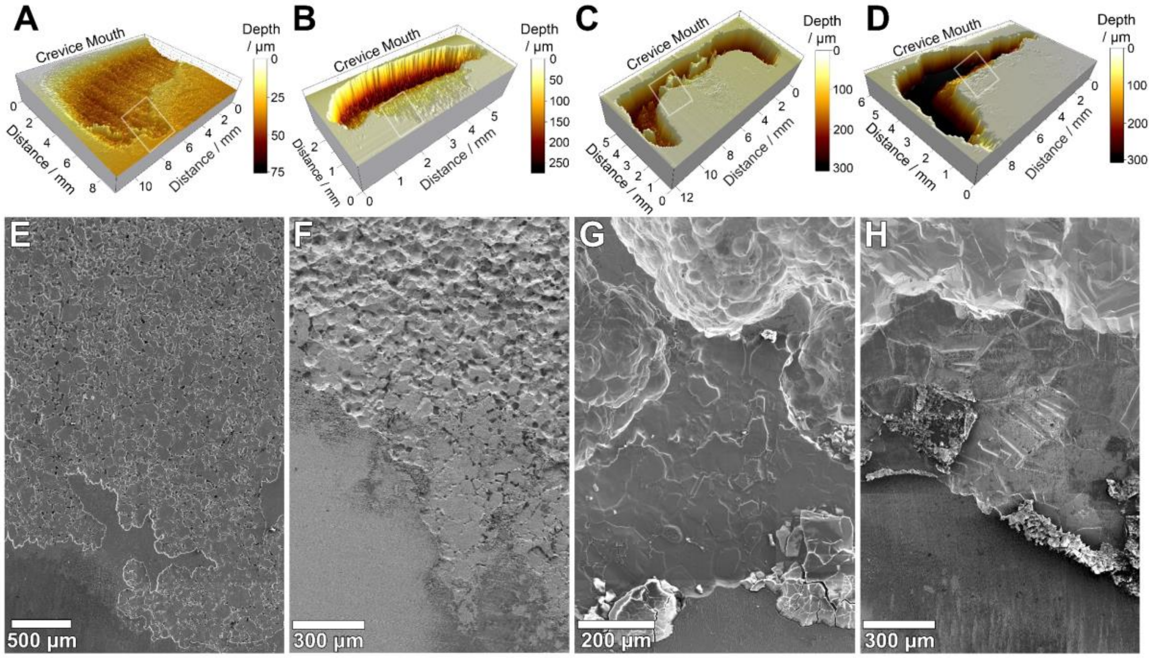

Figure 6.8 - Three-dimensional reconstruction from surface profilometry (A-D) and secondary electron micrographs (E-H) of crevice damage on BC-1, C-22, G-35, and G-30, respectively. Approximate location of each micrograph is indicated on their respective surface profile. All coupons were corroded galvanostatically at 100 µA for a total applied charge of 100 C.

Conclusions may be drawn between changes in crevice geometry and the intensity of the internal H^+ reduction reaction. Greater crevice corrosion penetration depths, whether the result of low Mo (and W) content or low applied current (discussed above), coincide with a higher degree of internal cathodic support. Based on our observations, internal cathodic support of crevice corrosion is less important on alloys containing high amounts of Mo (and W). It appears that these alloys develop a crevice geometry that is less suitable for the development of the CCS, and that the deposition of Mo- and W-rich corrosion products limits the surface area available for the H^+ reduction reaction within the crevice. At low applied currents, damage is limited to a small area and penetrates deep into the alloy surface, and conversely, when high currents are applied, the corrosion reaction and the consequent damage are forced to spread laterally across the surface. This suggests that a key factor in the crevice corrosion process may be the maintenance of a minimum local current density at active sites. This suggests that under natural (vs galvanostatically-driven) corrosion conditions, crevice corrosion damage will tend to penetrate deeply in limited areas, rather than spreading laterally across the surface. Therefore, the susceptibility of an alloy to enhancement of crevice corrosion by coupling to the internal cathodic reaction seems to be determined by the content of Mo + W, which hinder internal H^+ reduction by blocking the potentially cathodic surface with corrosion products and by limiting the establishment of a crevice geometry conducive to development of the CCS.

The hypothesis of corrosion product deposition governing the damage morphology and internal cathodic support is reinforced by the fact that the metallographic features of each alloy are similar; hence, there are no obvious microstructural features that could contribute to the differences in damage morphology between alloys. Previously published work has demonstrated that the corrosion susceptibility of the grain boundaries within a Ni-Cr-Mo alloy depends to some degree on their coincidence site lattice (CSL) classification (Σ value) [28,29]. Of particular interest are the $\Sigma3$ and the $\Sigma(>29)$ boundaries, the latter being termed random boundaries (R). These boundaries are considered low- and high-energy, respectively. The random boundaries have been shown to be more susceptible to attack than the lower energy boundaries [10,28,30].

We used EBSD to quantify the abundance on the three alloys of grain boundaries of each CSL Σ value. The results are presented in Figure 6.9. We found no significant difference in grain boundary make-up between the alloys; each alloy contains approximately 70% $\Sigma3$ boundaries. This is explained by the face-centred-cubic lattice and the similar heat treatment imposed on the alloys during fabrication. Given that each alloy possesses approximately the same abundance of random grain boundaries, which are particularly susceptible to corrosion, one might expect the damage to follow similar progression for each alloy, however, the results shown in Figure 6.8 demonstrate otherwise. Therefore, the differences in damage morphology between alloys must be the result of differences in composition. Likewise, there is no apparent microstructural feature that would render one alloy more or less susceptible to the intergranular attack discussed above. Instead, it is likely that changes occurring within the occluded region (*i.e.*, deposition of corrosion products) control the evolution of damage morphology. On alloy BC-1, which has the highest Mo + W content, the damage never gets beyond the initial stages and instead is forced to spread laterally across the surface. Alloy C-22, which has a moderate Mo + W content, has areas surrounding the central damage site which resemble early stages of corrosion. However, in the central areas the damage is more developed and crevice corrosion begins to attack grain bodies indiscriminately. On alloys G-35 and G-30, which have the lowest Mo + W content, crevice corrosion damage penetrates deeply, possibly providing a more optimum environment to sustain the internal H^+ reduction reaction.

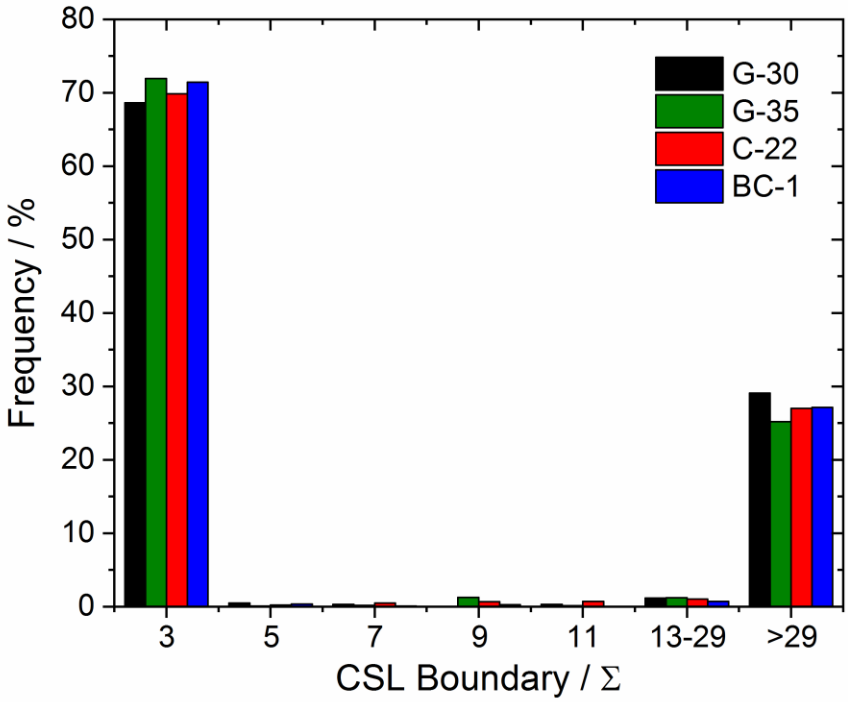

Figure 6.9 - Frequency of ordered grain boundaries according to coincidence site lattice notation for Hastelloy G-30, G-35, C-22, and BC-1. Random grain boundaries are defined as $\Sigma(> 29)$.

6.4 Conclusions

The presence of an internal cathodic support reaction, likely H^+ reduction, occurring during the crevice corrosion of Ni-based alloys has been implicitly demonstrated. For the investigated alloys, this process has been found to have the ability to intensify the anticipated crevice damage by as much as ∼79%. The intensity of H^+ reduction within the crevice is thought to be dependent on the evolving geometry of the host crevice and the blocking of cathodic sites by deposition of Mo- and W-rich corrosion products. Crevice damage that penetrates deeply supports the development of the CCS, and therefore the internal H^+ reduction reaction. As a result, low-Mo and W alloys, such as alloys G-35 and G-30, are particularly susceptible to this process. Consequently, we conclude that Mo- and W-rich corrosion products not only stifle active dissolution, but also limit the ability of H^+ reduction to intensify damage.

Furthermore, damage was also found to penetrate more deeply when the alloys were driven to corrode by small applied currents than when large currents were applied. This is particularly concerning for corrosion under natural conditions, where the applied current is zero.

Finally, our work demonstrates that corrosion damage predictions based solely on the availability of O_2 and other oxidants in the service environment will significantly underestimate the actual extent of corrosion on Ni-based alloys, an important concern that has not previously been demonstrated.

6.5 References

[1] K. Hashimoto, K. Asami, A. Kawashima, H. Habazaki, E. Akiyama, The role of corrosion-resistant alloying elements in passivity, *Corrosion Science*, 49 (2007) 42-52.

[2] V. Maurice, H. Peng, L.H. Klein, A. Seyeux, S. Zanna, P. Marcus, Effects of molybdenum on the composition and nanoscale morphology of passivated austenitic stainless steel surfaces, *Faraday Discussions*, 180 (2015) 151-170.

[3] A. Mishra, D.W. Shoesmith, P. Manning, Materials selection for use in concentrated hydrochloric acid, *Corrosion*, 73 (2017) 68-76.

[4] J.W. Oldfield, W.H. Sutton, Crevice corrosion of stainless steels ii. experimental studies, *British Corrosion Journal*, 13 (1978) 104-111.

[5] J.W. Oldfield, W.H. Sutton, Crevice corrosion of stainless steels i. a mathematical model, *British Corrosion Journal*, 13 (1978) 13-22.

[6] J.J. Noël, The electrochemistry of titanium corrosion, Ph.D. Thesis, Department of Chemistry, University of Manitoba, Winnipeg, Manitoba, 1999.

[7] X. He, J.J. Noël, D.W. Shoesmith, Temperature dependence of crevice corrosion initiation on titanium grade-2, *Journal of The Electrochemical Society*, 149 (2002) B440-B449.

[8] L. Yan, J.J. Noël, D.W. Shoesmith, Hydrogen absorption into Grade-2 titanium during crevice corrosion, *Electrochimica Acta*, 56 (2011) 1810-1822.

[9] N. Ebrahimi, P. Jakupi, J.J. Noël, D.W. Shoesmith, The role of alloying elements on the crevice corrosion behavior of Ni-Cr-Mo alloys, *Corrosion*, 71 (2015) 1441-1451.

[10] N. Ebrahimi, J.J. Noël, M.A. Rodriguez, D.W. Shoesmith, The self-sustaining propagation of crevice corrosion on the hybrid BC1 Ni–Cr–Mo alloy in hot saline solutions, *Corrosion Science*, 105 (2016) 58-67.

[11] P. Marcus, On some fundamental factors in the effect of alloying elements on passivation of alloys, *Corrosion Science*, 36 (1994) 2155-2158.

[12] N.S. Zadorozne, C.M. Giordano, M.A. Rodriguez, R.M. Carranza, R.B. Rebak, Crevice corrosion kinetics of nickel alloys bearing chromium and molybdenum, *Electrochimica Acta*, 76 (2012) 94-101.

[13] P. Jakupi, J.J. Noël, D.W. Shoesmith, Crevice corrosion initiation and propagation on alloy-22 under galvanically-coupled and galvanostatic conditions, *Corrosion Science*, 53 (2011) 3122-3130.

[14] P. Jakupi, J.J. Noël, D.W. Shoesmith, The evolution of crevice corrosion damage on the Ni–Cr–Mo–W alloy-22 determined by confocal laser scanning microscopy, *Corrosion Science*, 54 (2012) 260-269.

[15] P. Jakupi, D. Zagidulin, J.J. Noël, D.W. Shoesmith, Crevice corrosion of Ni-Cr-Mo alloys, *ECS Transactions*, 3 (2007) 259-271.

[16] X. Shan, J.H. Payer, Characterization of the corrosion products of crevice corroded alloy 22, *Journal of The Electrochemical Society*, 156 (2009) C313-C321.

[17] M. Nishimoto, J. Ogawa, I. Muto, Y. Sugawara, N. Hara, Simultaneous visualization of pH and Cl^- distributions inside the crevice of stainless steel, *Corrosion Science*, 106 (2016) 298-302.

[18] R.S. Lillard, M.P. Jurinski, J.R. Scully, Crevice corrosion of alloy 625 in chlorinated ASTM artificial ocean water, *Corrosion Science*, 50 (1994) 251-265.

[19] J.R. Hayes, J.J. Gray, A.W. Szmodis, C.A. Orme, Influence of chromium and molybdenum on the corrosion of nickel-based alloys, *Corrosion Science*, 62 (2006) 491-500.

[20] R. Newman, The dissolution and passivation kinetics of stainless alloys containing molybdenum (part ii), *Corrosion Science*, 25 (1985) 341-350.

[21] R. Newman, The dissolution and passivation kinetics of stainless alloys containing molybdenum (part i), *Corrosion Science*, 25 (1985) 331-339.

[22] P. Jakupi, F. Wang, J.J. Noël, D.W. Shoesmith, Corrosion product analysis on crevice corroded alloy-22 specimens, *Corrosion Science*, 53 (2011) 1670-1679.

[23] M. Miyagusuku, R.M. Carranza, R.B. Rebak, Inhibition mechanism of phosphate ions on chloride-induced crevice corrosion of alloy 22, *Corrosion*, 71 (2015) 574-584.

[24] E.C. Hornus, C.M. Giordano, M.A. Rodriguez, R.M. Carranza, R.B. Rebak, Effect of temperature on the crevice corrosion of nickel alloys containing chromium and molybdenum, *Journal of The Electrochemical Society*, 162 (2015) C105-C113.

[25] E.C. Hornus, M.A. Rodriguez, R.M. Carranza, C.M. Giordano, R.B. Rebak, Effect of environmental variables on crevice corrosion susceptibility of Ni-Cr-Mo alloys for nuclear repositories, *Procedia Materials Science*, 8 (2015) 11-20.

[26] G.F. Kennell, R.W. Evitts, Crevice corrosion cathodic reactions and crevice scaling laws, *Electrochimica Acta*, 54 (2009) 4696-4703.

[27] G.F. Kennell, R.W. Evitts, K.L. Heppner, A critical crevice solution and IR drop crevice corrosion model, *Corrosion Science*, 50 (2008) 1716-1725.

[28] P. Jakupi, J.J. Noël, D.W. Shoesmith, Intergranular corrosion resistance of sigma-3 grain boundaries in alloy 22, *Electrochemical and Solid-State Letters*, 13 (2010) C1-C3.

[29] N. Ebrahimi, P. Jakupi, A. Korinek, I. Barker, D.E. Moser, D.W. Shoesmith, Sigma and random grain boundaries and their effect on the corrosion of the Ni-Cr-Mo alloy 22, *Journal of The Electrochemical Society*, 163 (2016) C232-C239.

[30] J.J. Gray, B.S. El Dasher, C.A. Orme, Competitive effects of metal dissolution and passivation modulated by surface structure: an AFM and EBSD study of the corrosion of alloy 22, *Surface Science*, 600 (2006) 2488-2494.

Chapter 7

7 Investigating the corrosion behaviour of corrosion resistant alloys in solutions containing dilute fluoride ions

Abstract:

The ability of fluoride ions, in trace concentrations, to promote film instability and transpassive dissolution was shown for several corrosion resistant alloys. While the addition of fluoride ion was found to decrease the transpassive dissolution potential by approximately 0.1 V, the decrease was particularly pronounced in mildly acidic media (pH 5). Results suggest that the decreased potential range of stability for the heavily-relied-upon Cr(III)-rich oxide film is a concern in the presence of oxidizing impurities which may push the corrosion potentials toward the transpassive region. The decreased potential range of passive film stability was observed using both dynamic and static polarization experiments and supported by solution and surface analyses.

7.1 Introduction

The role of halide anions, particularly chloride (Cl^-), in corrosion processes has been extensively discussed in the literature [1-4]. However, information regarding corrosion induced by the presence of fluoride ions (F^-) is much less abundant, especially for corrosion in conditions other than concentrated hydrofluoric acid (HF). Research on corrosion resistant alloys exposed to concentrated HF is required by industries such as the petrochemical industry, which employs high concentrations of HF in alkylation units. These units, which are usually built of carbon steel, operate under extremely acidic conditions [5]. Failure of these structures becomes possible when the HF concentration drops, or the temperature is increased, resulting in increased corrosion rates [5]. To minimize damage, acid concentrations are kept high in HF alkylation units.

Recent research has focused on determining optimal Ni-based alloy compositions to improve corrosion resistance and mechanical properties in concentrated HF solutions. Li *et al.* demonstrated the importance of the formation of a Mo-rich surface layer on corrosion resistance of Ni alloys in 5.2 M HF [6]. Although the ability to form a Mo-rich surface layer improved the corrosion resistance, further improvements could be realized with Cu additions. With alloying additions of 2 wt.% Cu, the Mo oxide film previously observed was replaced by a segregated Cu-rich surface layer [7], yielding an increase in corrosion resistance relative to alloys containing no Cu. Among the commercially available Ni-alloys, Hastelloy C2000 has been of particular interest in this regard, due to its Cu content [8]. Unfortunately, the information reported in these studies is not immediately applicable to environments containing low F^- concentrations and/or pH values near-neutral, *e.g.*, pH 5 to 9.

Research involving the corrosion behaviour of corrosion resistant alloys in low or trace concentrations of F^- is sparse, with the most relevant studies conducted on dental materials and materials used in proton exchange membrane fuel cell (PEMFC) applications [9-13]. However, the materials used in dental applications are commonly Ti-based, due to their biocompatibility; therefore, these studies, although instructive, are not useful for large-scale material applications where the use of Ti-based alloys is not appropriate.

Accordingly, the petrochemical industry lacks data regarding the corrosion behaviour of corrosion resistant alloys exposed to trace F^- environments; however, there are several industrial processes which may introduce low or trace concentrations of F^- during refinery processing. Commonly employed cleaning solvents, acidizing procedures used to increase the productivity of reservoirs [14], and the reprocessing of F^--containing refinery streams, can act as sources of F^- contamination throughout refinery operations. Therefore, determining the extent of interaction between F^- and the materials found within the refinery is essential to ensure safe operation.

As described, most previous work has focused on concentrated F^- environments, and little is known on the corrosion of corrosion resistant alloys in dilute F^- solutions (concentrations up to 5000 ppm) and at increased temperatures (80-120°C) and pH values close to neutral.

Thus, the motivation for this project was the development of an understanding of the effects of F^- on a variety of commercially available alloys that could be appropriate in such an environment. In addition, experiments were conducted in the presence of Cl^-, a common co-contaminant in refinery environments [14]. Electrochemical investigations in the form of open-circuit and polarization experiments were conducted in relevant environments. Complementary surface and solution analyses were performed following potentiostatic polarization experiments to understand changes in film composition and structure as a function of the applied potential and the solution environment.

7.2 Experimental

7.2.1 Material preparation

Both Ni- and Fe-based alloys were received as mill-annealed sheets. Ni-alloys were provided by Haynes International (Kokomo, IN, USA), while Fe-based alloys were purchased from McMaster-Carr (Elmhurst, IL, USA). The nominal compositions, reported in Table 7.1, are in accordance with ASTM B462 and A240.

Coupons were cut and machined to the desired size from the mill-annealed sheets. Prior to electrochemical measurements, coupons were ground with a series of wet SiC papers (P600-P1200) to remove any damage incurred during the machining process and to create a reproducible surface. Coupons intended for subsequent surface analysis were further ground until a final step using P4000 SiC paper to minimized surface topography. Prepared coupons were then sonicated in a 1:1 mixture of deionized (DI) water (18.2 $M\Omega\ cm^{-2}$) and EtOH for 30 seconds, rinsed in DI water, and then dried in a stream of argon (Ar) gas. In all cases, the coupons were prepared immediately before each experiment.

Solutions were prepared using reagent grade Na_2SO_4 (Fisher Scientific), KF (VWR International), NaCl (Caledon Laboratory Chemicals), and DI water (Thermo Scientific Barnstead™ Nanopure™). The pH of each solution was adjusted using solutions of H_2SO_4 (Caledon Laboratory Chemicals) and NaOH (Fisher Scientific). To ensure adequate solution conductivity during all experiments, a supporting electrolyte (0.1 M Na_2SO_4) was employed, with the specified concentrations of F^- and Cl^- added to this solution.

Table 7.1 - Nominal compositions (wt.%) of studied alloys. M indicates an alloying element's maximum concentration, while, Bal. indicates the element making up the balance due to fluctuations in composition. * indicates that concentration also contains tantalum.

Alloy	**Ni**	**Cr**	**Mo**	**Fe**	**W**	**Cu**	**Nb***	**Co**	**Mn**	**Ti**	**Al**	**V**	**N**	**Si**	**C**
SS316L	14^{M}	18^{M}	3^{M}	Bal.	--	--	--	--	2	--	--	--	0.10	0.75	0.03
SS2205	6.5^{M}	23^{M}	3.5^{M}	Bal.	--	--	--	--	2^{M}	--	--	--	0.2^{M}	1^{M}	0.03^{M}
C2000	Bal.	23	16	3^{M}	--	1.6	--	2^{M}	0.5^{M}	--	0.5^{M}	--	--	0.08^{M}	0.01^{M}
C22	Bal.	22	13	3	3	0.5^{M}	--	2.5^{M}	0.5^{M}	--	--	0.35^{M}	--	0.08^{M}	0.015^{M}
C276	Bal.	16	16	5	4	0.5^{M}	--	2.5^{M}	1^{M}	--	--	0.35^{M}	--	0.08^{M}	0.01^{M}
625	Bal.	21	9	5^{M}	--	0.5^{M}	3.7	1^{M}	0.5^{M}	0.4^{M}	0.4^{M}	--	--	0.5^{M}	0.1^{M}

7.2.2 Electrochemical measurements

Electrochemical experiments were conducted in a polytetrafluoroethylene (PTFE) electrochemical cell, fabricated in-house, as shown in Figure 7.1(A). Two lids were constructed for use with the cell, depending on experimental needs. The first lid was designed with three inlets for electrode connections, as depicted in Figure 7.1(B). A second lid was designed with eight inlets for electrode connections, making the simultaneous measurement of up to six working electrodes (WE) possible, as depicted in Figure 7.1(C). A saturated Ag/AgCl electrode (0.197 V vs. SHE) and a platinum coil were employed as the reference (RE) and counter electrodes (CE), respectively. Both lids had inlet and outlet fittings used for solution sparging. All connections were wrapped in PTFE tape to ensure a secure, airtight fit. Once assembled, the cell was secured in a custom-machined clamp to ensure no movement of fittings during heating or Ar sparging. Temperature control was achieved using a custom-built heating reservoir adapted for use with an external isothermal water circulator. The fully assembled electrochemical cell, clamp, and heating reservoir are illustrated in Figure 7.1(A). Once assembled, the electrochemical cell was secured in the heating reservoir, and an initial 30-min heating/purging period was observed. During this time, the temperature of the heating reservoir was increased to the desired set-point and the experimental solution was sparged vigorously with Ar gas. After this initial period, the rate of Ar-sparging was lowered and the experiment was carried out.

Corrosion behaviour was studied at both open-circuit (*i.e.*, the corrosion potential (E_{CORR}) was monitored as a function of time) and during dynamic and static polarization experiments. In studies investigating behaviour at E_{CORR}, the electrochemical cell was outfitted with one coupon of each of the six alloys, serving as working electrodes. Measurements began 24 h after the cell and electrodes were installed into the heating reservoir. Measurements, taken at 24 h intervals, included E_{CORR} and linear polarization resistance (LPR) measurements. Behaviour was studied for a total of 360 h (15 days). LPR measurements were carried out by polarizing each WE ± 15 mV (vs. ECORR) at a scan rate of 10 mV min^{-1}. Polarization resistance (R_P) values were then extracted from the slope of the current density response (Δi) to potential changes (ΔE). Between measurements, the RE was removed from the cell to avoid long-term drift.

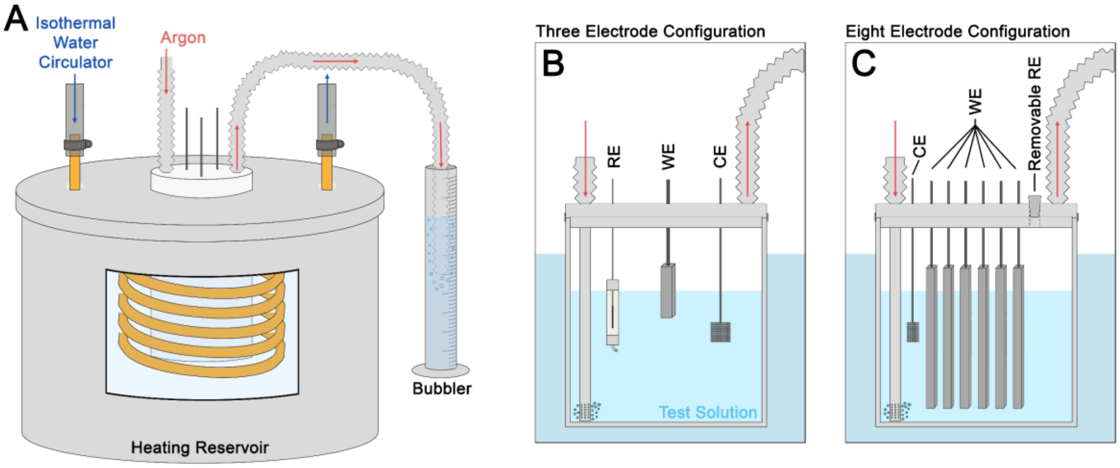

Figure 7.1 - Schematic illustration of the (A) full assembled PTFE electrochemical cell placed within the heating reservoir, with a cut-away showing the placement of cell and heat-exchanger coils. Insets show a cross section of the electrochemical cell in the (B) three electrode and (C) eight electrode configurations.

All dynamic and static polarizations began with a 90-min E_{CORR} measurement followed by a 30-min potentiostatic hold (–0.500 V vs Ag/AgCl) as a cathodic pre-treatment to ensure a reproducible surface between repeat experiments. Upon completion of the cathodic treatment, either a dynamic or a static polarization experiment was carried out. In potentiodynamic experiments, the potential was scanned in the positive direction from the hold potential at a scan rate of 10 mV min^{-1} until the resultant current reached the chosen anodic limit (10 mA). In potentiostatic experiments, immediately following the potential hold, the electrode was polarized to the desired potential in a single step. Following the completion of all experiments, the temperature of the electrochemical cell was checked to make sure it had remained at the set temperature. Experimental coupons were stored in an Innovative Technology PureLab HE Ar-filled glovebox during the period between completion of the electrochemical experiment and commencement of the surface analysis. All electrochemical measurements were repeated a minimum of two times.

7.2.3 Surface analysis

X-ray photoelectron spectroscopy (XPS) analyses were carried out on the Kratos AXIS Nova and Kratos AXIS Supra spectrometers located at Surface Science Western (Western University). In all spectra, an Al Kα (1486.7 eV) monochromatic X-ray source was used. The Au $4f_{7/2}$ metallic binding energy (83.95 eV) was used as a reference point for calibration of the instrument work function. Both survey and high-resolution spectra were collected on all coupons. For Ni-based coupons the Ni 2p, Cr 2p, Mo 3d, Cu 2p, O 1s, S 2p, and C 1s were collected. For Fe-based coupons, the Fe 2p, Cr 2p, Mo 3d, O 1s, S 2p, and C 1s were collected. CasaXPS software (v.2.3.19) was used to process spectra. All spectra were charge-corrected by adjusting the C-C binding energy in the high-resolution C 1s spectrum (284.8 eV). Fitting parameters used in the deconvolution of high-resolution spectra were taken from the work of Biesinger *et al.* (Ni [15, 16], Cr [16, 17], and Fe [16]) and Spevack *et al.* (Mo [18]).

7.2.4 Solution analysis

Solution samples collected at the completion of potentiostatic polarization experiments were analyzed using inductively coupled plasma mass spectrometry (ICP-MS) at the Biotron Research Facility (Western University). Samples were diluted, filtered (0.45 µm), and then analyzed using an Agilent 7700x ICP-MS. The instrument was calibrated using aqueous standards in 2% HNO_3.

7.3 Results and discussion

7.3.1 Behaviour at the corrosion potential

The behaviour under natural corrosion conditions was studied in the base electrolyte, 0.1 M Na_2SO_4, as well as in 0.1 M Na_2SO_4 + 5000 ppm F^- + 1000 ppm Cl^-. In both solutions, values of E_{CORR} and R_P were measured at 1 d intervals for a total of 15 d. Considering the behaviour of all six alloys in both solutions, only minor differences were found. In both solutions, values of E_{CORR} were found to stabilize within the range of approximately −0.2 to −0.32 V and showed only minor fluctuations between measurements, Figure 7.2(A). Similarly, values of R_P were found to approach an apparent steady-state condition, Figure 7.2(B). All alloys exhibited excellent corrosion performance in both solutions, as suggested by the relative stability of E_{CORR} values and measured R_P values in the range of 10^6 – 10^7 Ω cm^2. A few general points are, however, worth mentioning.

Comparing the Ni- and Fe-based alloys studied here, the Ni-based alloys experience only slightly better corrosion resistance under natural corrosion conditions. As shown in Figure 7.2(B), this was true for both solutions examined here, *i.e.*, with or without F^-/Cl^-. Both stainless steel alloys, SS316L and SS2205, were found to exhibit R_P values lower than those measured on Ni-based alloys at the completion of the 15-d period. Amongst Ni-based alloys, C2000 was found to have the highest R_P values in both solutions. Nonetheless, all measurements made under natural corrosion conditions suggest the behaviour of these alloys was consistent with strong passivity, regardless of the solution composition [19].

While electrochemical studies showed that the alloys behaved comparably in both 0.1 M Na_2SO_4 and 0.1 M Na_2SO_4 + 5000 ppm F^- + 1000 ppm Cl^-, subtle differences in surface composition were identified by XPS. Table 7.2 summarizes the normalized surface compositions for coupons following the 15-d exposure experiment. For all alloys, a substantial decrease in Cr content was observed following exposure to the F^-/Cl^- containing solution, which was not the case for the same materials after exposure to only the 0.1 M Na_2SO_4 solution. These changes are facilitated by an interaction of Cr with one or both of these anions and will be discussed in greater detail below.

It is worth mentioning that, while SS2205 and SS316L contain alloyed Ni in the amounts of 6.5 and 14 wt.%, respectively, the quantification of Ni by XPS was made difficult by a series of peak overlaps. More specifically, the series of Auger signals (LMM) produced by Fe overwhelmed the relatively weak signal produced by the alloyed Ni (2p). Similarly, peak overlaps complicated quantification of Fe in the Ni-based alloys, even though they contain alloyed Fe ranging from 3 to 5 wt.%. In this case, the Auger signals (LMM) produced by Ni overwhelmed the photoelectron signal produced by alloyed Fe (2p). While not considered in the quantification, it is expected that Ni and Fe represent a small portion

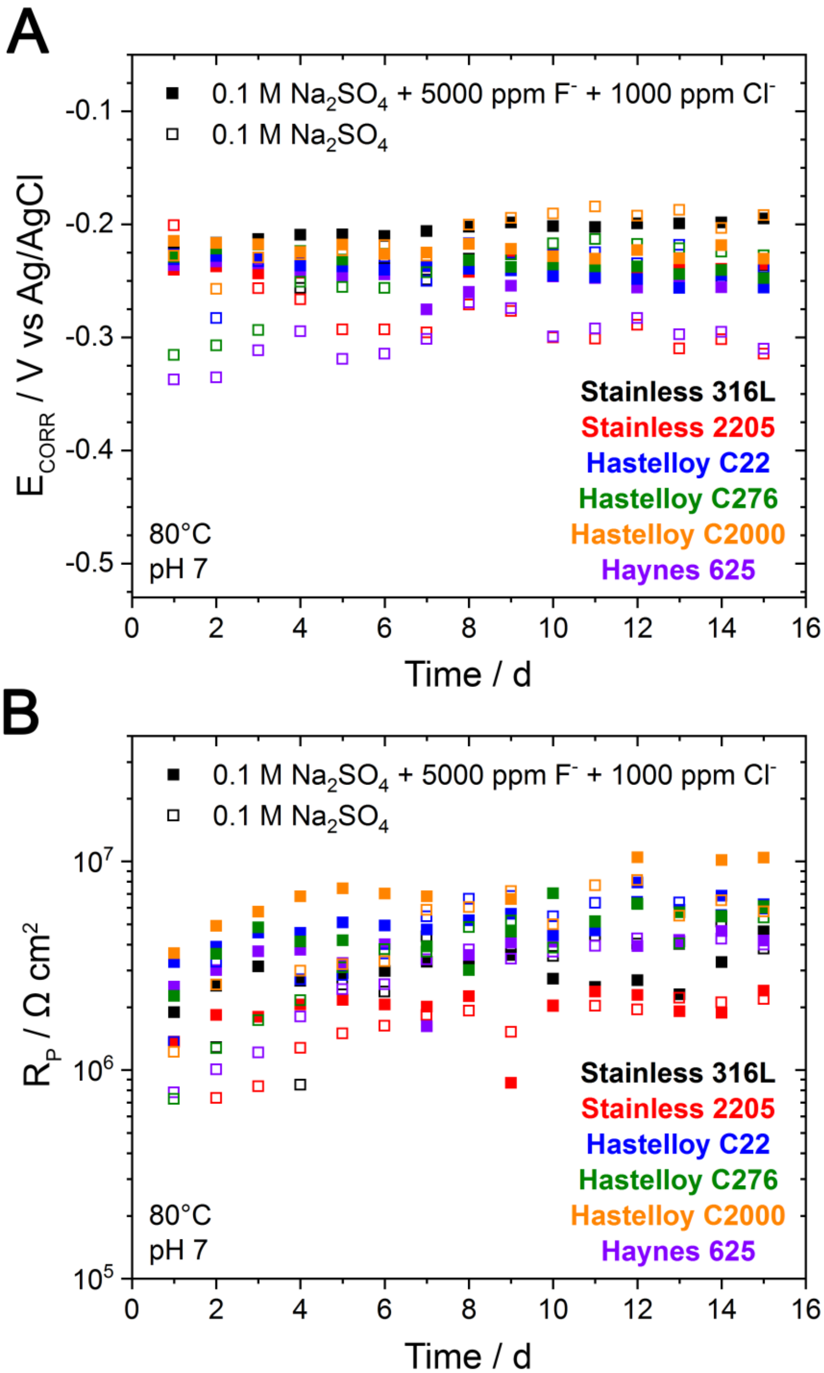

Figure 7.2 - Comparison of measured (A) E_{CORR} and (B) R_P values over a 15-day period in the absence of F^- or Cl^- (▫) and with the addition of 5000 ppm F^- and 1000 ppm Cl^- (▪).

of oxidized surface species on Fe- and Ni-based alloys, respectively [20, 21]. Also, the element Nb, despite making up 3.7 wt.% of Alloy 625, was not detected by XPS at the end of these exposure tests.

Table 7.2 - Normalized surface compositions (at.%), determined by XPS, of alloys after exposure to 0.1 M Na_2SO_4 or 0.1 M Na_2SO_4 + 5000 ppm F^- + 1000 ppm Cl^- (pH 7).

Alloy	Solution	Ni	Fe	Cr	Mo	Cu
SS2205	0.1 M Na_2SO_4	--	30.6	64.8	4.6	--
	0.1 M Na_2SO_4 + 5000 ppm F^- + 1000 ppm Cl^-	--	54.8	43.1	2.1	--
SS316L	0.1 M Na_2SO_4	--	44.9	53.0	2.1	--
	0.1 M Na_2SO_4 + 5000 ppm F^- + 1000 ppm Cl^-	--	73.5	25.1	1.3	--
C2000	0.1 M Na_2SO_4	35.8	--	50.7	9.0	4.5
	0.1 M Na_2SO_4 + 5000 ppm F^- + 1000 ppm Cl^-	72.0	--	22.6	3.2	2.2
625	0.1 M Na_2SO_4	24.3	--	68.5	7.2	--
	0.1 M Na_2SO_4 + 5000 ppm F^- + 1000 ppm Cl^-	71.3	--	25.5	3.2	--
C22	0.1 M Na_2SO_4	37.5	--	55.7	6.8	--
	0.1 M Na_2SO_4 + 5000 ppm F^- + 1000 ppm Cl^-	74.4	--	22.2	3.3	--
C276	0.1 M Na_2SO_4	26.5	--	65.1	8.4	--
	0.1 M Na_2SO_4 + 5000 ppm F^- + 1000 ppm Cl^-	79.2	--	17.7	3.1	--

7.3.2 Potentiodynamic polarization behaviour

Polarization curves recorded both in the base electrolyte and in solutions containing various F^- and Cl^- concentrations are shown in Figure 7.3(A-D). In all solutions, the current-potential relationship was consistent with the formation of a protective oxide film, in agreement with the observations made at E_{CORR} (discussed above). Current densities measured in the passive region were $\leq 10^{-6}$ A cm^{-2}, as is typical for Cr-containing alloys [21]. Formation of a passive film was observed in all solutions, regardless of the anion concentration. Passive films did not appear susceptible to localized breakdown, which would be indicated by momentary increases in current density. However, as applied potentials were increased, current densities were found to increase, indicating the onset of transpassive film breakdown. Here, the electrochemical conversion of Cr(III) into soluble Cr(VI) species, Equation 7.1, resulted in damage to the passive film. This process,

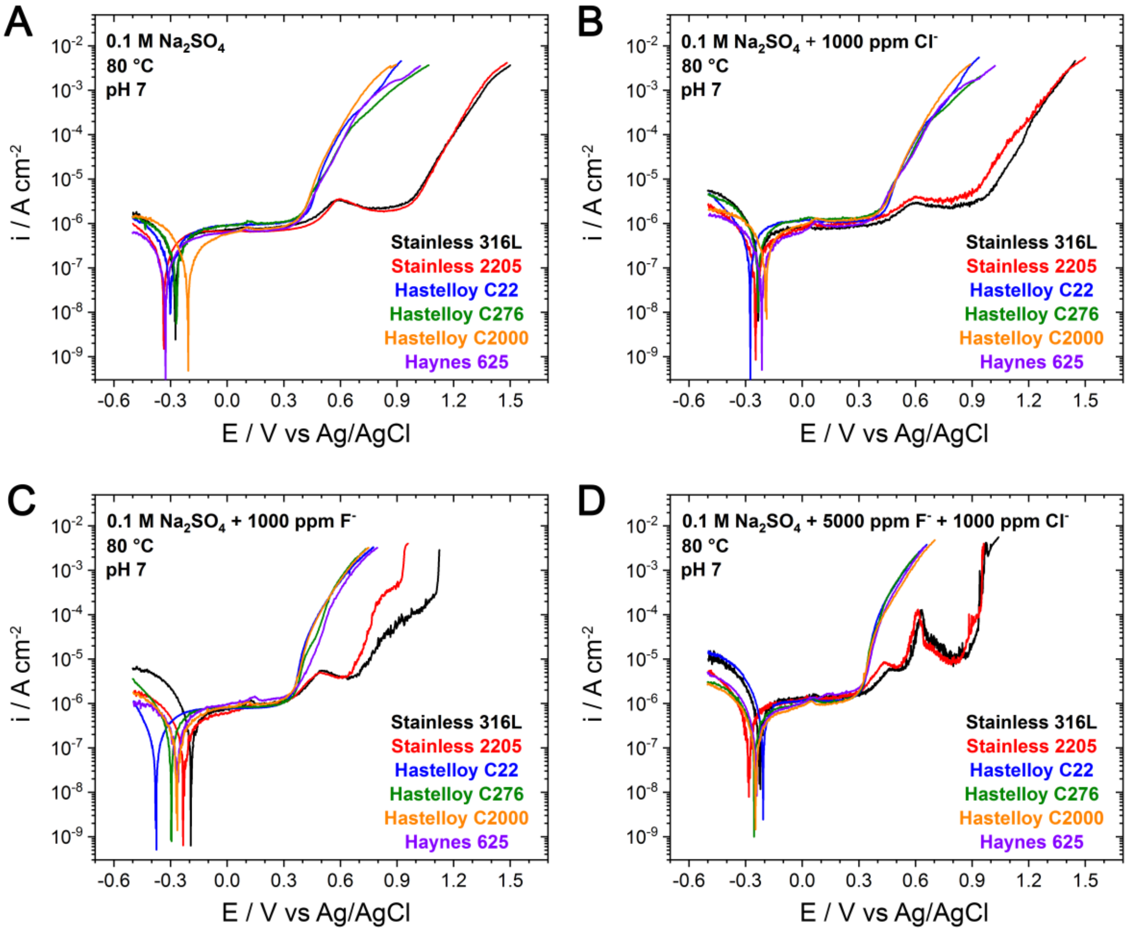

Figure 7.3 - Potentiodynamic polarization behaviour of alloys in 0.1 M Na_2SO_4 solution (A) in the absence of F^- or Cl^-, (B) with 1000 ppm Cl^-, (C) with 1000 ppm F^-, and (D) with 5000 ppm F^- + 1000 ppm Cl^-.

commonly referred to as transpassive dissolution, has been extensively studied on Ni-, Fe-, and Co-based alloys [1, 21-24].

$$\mathrm{CrO_4}^{2-} + 8\,\mathrm{H}^+ + 3\,\mathrm{e}^- \rightleftharpoons \mathrm{Cr}^{3+} + 4\,\mathrm{H_2O} \qquad (7.1)$$

Prior to the onset of transpassive dissolution, all alloys displayed a small feature within the passive region. This feature, which occurred at approximately 0.100 V, appeared as a slight increase in current density. However, in all cases the current density returned to the original passive current density, indicating the re-establishment of passivity. This feature has not been reported in the literature and the cause is currently unknown. Nevertheless, the significance of this behaviour, in relation to corrosion, appears to be minor.

As the applied potential increased beyond the onset of transpassivity, current densities rapidly increased on Ni-based alloys, due to continued metal dissolution following film breakdown. For Cr-containing alloys, the rates of dissolution following transpassive film breakdown have been shown to be increased by increases in Mo-content and suppressed by increases in Fe-content [25-27]. This is consistent with data presented here which show a higher rate of increase of the current density with potential for alloy C2000 (16 wt.% Mo) than for alloy 625 (9 wt.% Mo), Figure 7.3(A-C). This increase has been tentatively assigned to an ill-defined catalytic effect of Mo on transpassive dissolution [25-27]. Fe-based alloys were found to have a secondary passive region at applied potentials higher than the onset of electrochemical conversion of Cr(III) to Cr(VI). While current densities increased at the onset of the Cr(III) oxidation, a second current plateau was observed for the Fe-based alloys. This was the result of corrosion inhibition by Fe(III) oxides formed at the surface [19]. Within this secondary passive region, current densities were found to be 2-3 times higher than those recorded in the primary passive region. The secondary passive region was comparable on SS316L and SS2205, and persisted until ~ 0.900 V.

While comparing Figure 7.3(A) and (B) illustrates that the addition of 1000 ppm Cl^- resulted in no visible change to the polarization behaviour relative to the base electrolyte, the addition of F^- ions was found to modify the current-potential response. The current-potential responses of alloys exposed to 1000 ppm F^- and 5000 ppm F^- (with 1000 ppm Cl^-) are displayed in Figure 7.3(C) and (D), respectively. F^- ions mainly influenced the transpassive behaviour; a direct comparison of the transpassive behaviour recorded in the different experimental solutions is given in Figure 7.4 for (A) alloy C22 and (B) SS2205. As indicated by the markings along the lower ordinate axis, the introduction of F^- ion resulted in a decrease in the onset potential of Cr(III) oxidation. In comparison to solutions without F^-, the breakdown of the passive region was decreased by ~0.100 V in the presence of F^- ions.

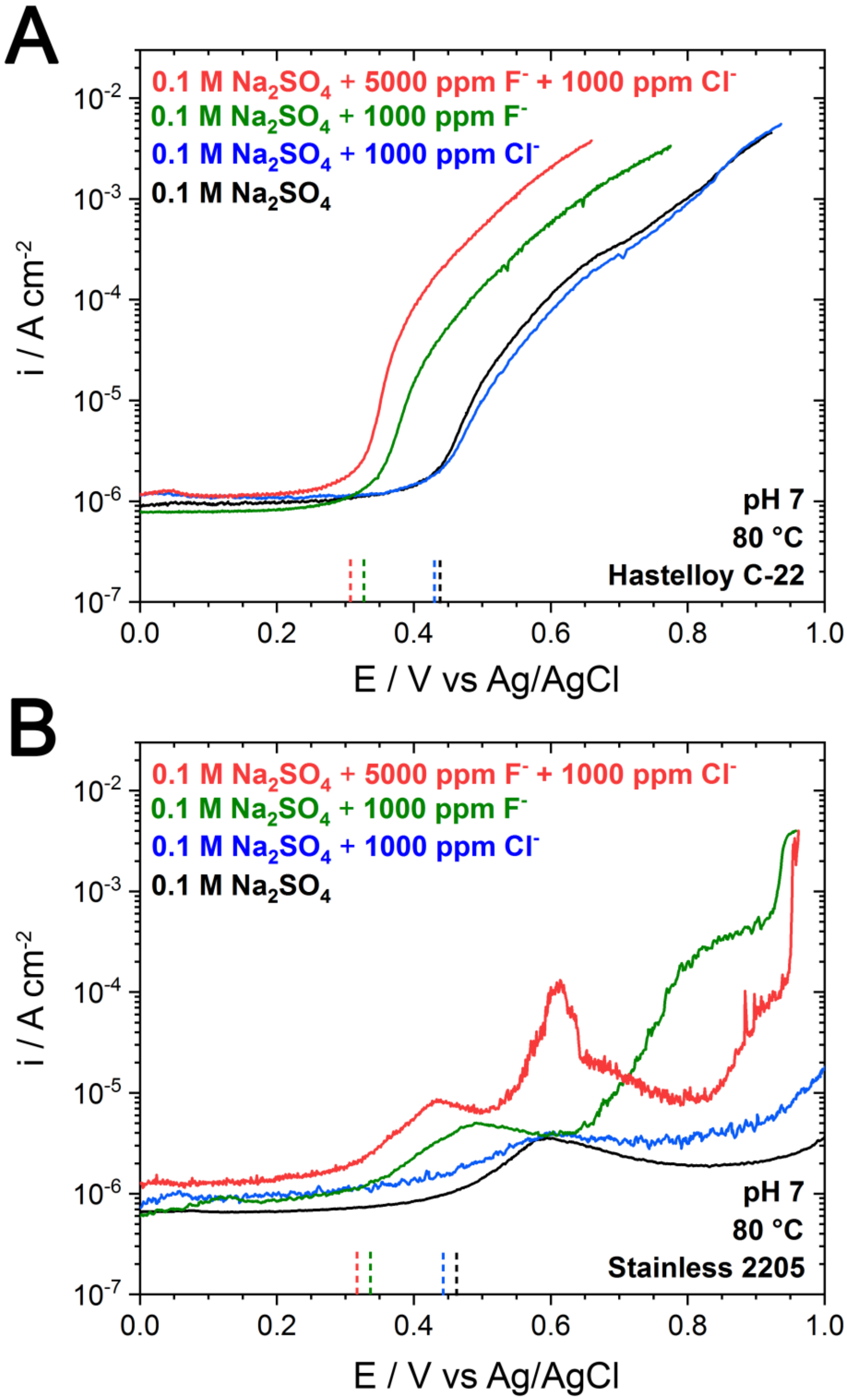

Figure 7.4 - Comparison of transpassive regions for (A) alloy C22 and (B) SS2205 exposed to the various solutions indicated in the legend. Extracted transpassive onset potentials are indicated by the markings along the lower ordinate axis.

Furthermore, considering the secondary passive region present on SS2205 and SS316L, Figure 7.3(C), the introduction of 1000 ppm F^- resulted in a loss of stability in the secondary passive region and an eventual breakdown at ~0.65 V. In solutions containing 5000 ppm F^- and 1000 ppm Cl^-, while the breakdown of the secondary passive layer was observed, a subsequent decrease in current density suggested that a film repair/deposition process occurred as the potential was increased further, as shown in both Figure 7.3(D) and Figure 7.4(B). While an attempt to repassivate the surface is apparent, fluctuations in current density observed beyond the breakdown potential (*i.e.*, for potentials > 0.6 V) indicates that this "reformed" film is only partially stable and, hence, susceptible to further breakdown. In general, the presence of F^- has been shown to lead to enhanced reactivity at Fe-based alloy surfaces through the formation of soluble Fe-F species [28-31].

A series of potentiodynamic experiments were also conducted at pH 5 and 9 for both the base electrolyte and the electrolyte containing 0.1 M Na_2SO_4 + 5000 ppm F^- + 1000 ppm Cl^-. In general, the polarization behaviour, including the primary and secondary passive regions, as well as changes in transpassivity, were similar to those found in pH 7 solutions (Figure 7.3) and are therefore not shown. In the pH range 5-9, all alloys maintained current densities less than 10^{-6} A cm^{-2} in the primary passive region, consistent with the presence of a Cr(III)-rich oxide layer [19]. Based on the solubility data for Cr species, a decrease in pH to values less than ~4 would be required to challenge this passivity [19, 32]. Wang *et al.* studied the behaviour of SS316 in H_2SO_4 (pH 1) with and without Cl^- and F^- [2]. Under their conditions, active behaviour was observed at low potentials, with an active-to-passive transition and, hence, the establishment of passivity occurring only as the potential was increased. Currents in the active region were found to be increased by F^- but not by Cl^-. In addition, Wang *et al.* did not observe a secondary passive region, which is not surprising at such low pH, where the solubility of Fe(III) species would be considerably higher than in the experiments presented here [32].

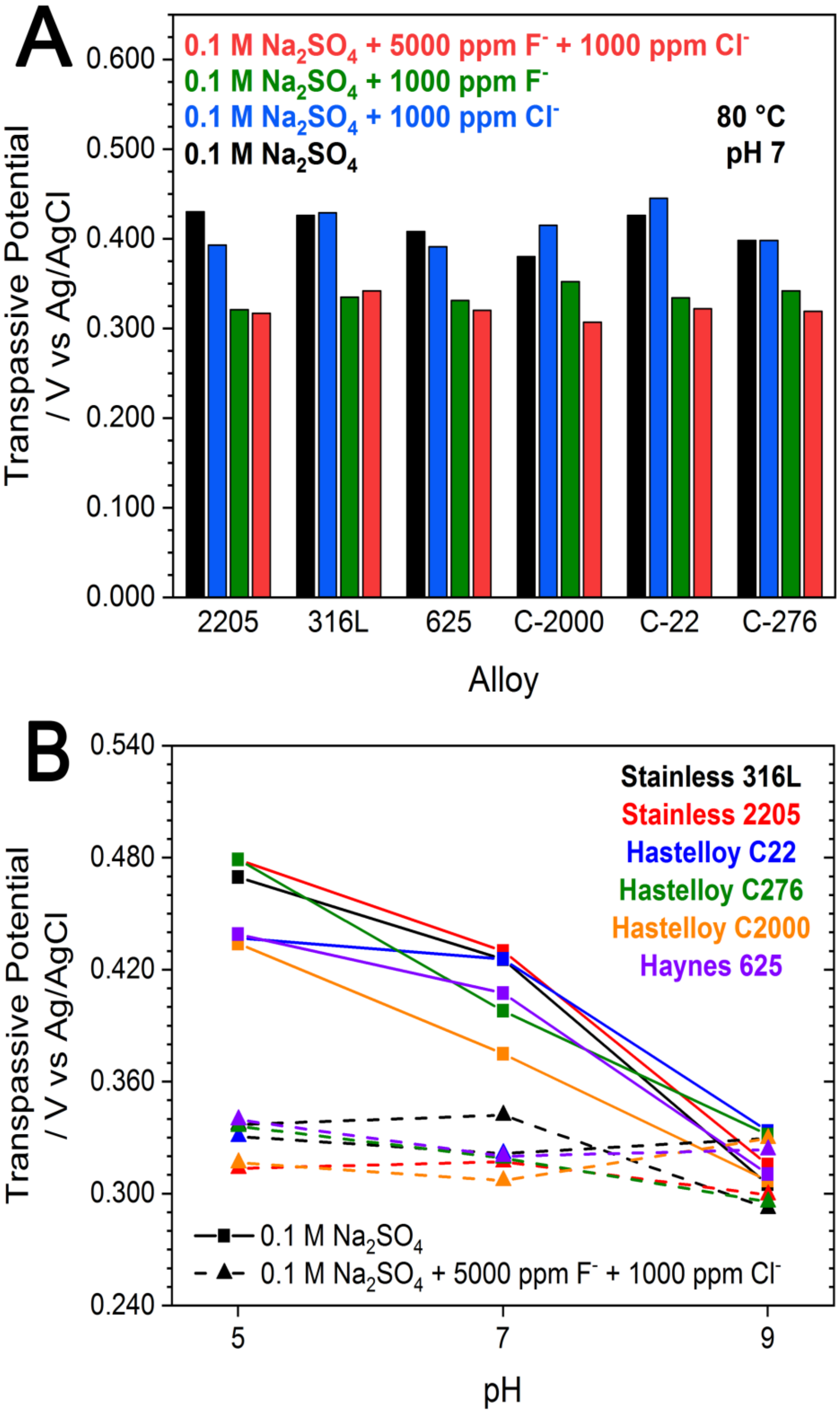

Figure 7.5 - Average (n = 2-4) transpassive potentials of alloys in different solutions at pH 7 (A), and (B) a comparison of the transpassive potentials of alloys in the 0.1 M Na_2SO_4 and 0.1 M Na_2SO_4 + 5000 ppm F^- + 1000 ppm Cl^- solutions as a function of pH.

Under the examined conditions, the most significant impact of F^- ions appears to be an early onset of transpassive dissolution. The average (n = 2-4) transpassive potentials found in the various solutions at pH 7, and the influence of changes in pH in the range 5-9 are depicted in Figure 7.5(A) and (B), respectively. At pH 7, in solutions containing F^- ion, shown as green and red in Figure 7.5(A), the alloys were found to undergo transpassive dissolution at lower applied potentials than in solutions without F^- ions. On average, the onset of transpassivity was found to decrease by ~0.1 V with the addition of F^-, which is believed to be the result of an interaction of F^- with the Cr(III)-rich film, resulting in the formation of CrF_3 species [2, 29, 33], Equation 7.2. These interactions have been shown to result in the conversion of the insoluble Cr_2O_3 film into the semi-soluble CrF_3 species, ultimately leading to the degradation of the protective passive film. Similar behaviour has been found on other metals including Fe, Ni, Ti, Al, and Sn [34-38].

$$\mathrm{Cr_2O_3} + 6\,\mathrm{H^+} + 6\,\mathrm{F^-} \rightleftharpoons 2\,\mathrm{CrF_3} + 3\,\mathrm{H_2O} \qquad (7.2)$$

A comparison of the average transpassive potentials exhibited by alloys immersed in the base electrolyte, 0.1 M Na_2SO_4, and the most ionically concentrated solution, 0.1 M Na_2SO_4 + 5000 ppm F^- + 1000 ppm Cl^-, at the three pH values investigated (5, 7, and 9) is shown in Figure 7.5(B). Overall, during immersion in the base electrolyte, alloys exhibited decreasing transpassive onset potentials as solutions became more alkaline. This was attributed to the pH dependence of the equilibrium potential for the redox conversion of Cr(III) to Cr(VI) [19], Equation 7.1. At pH 9, the presence of F^- exerted no influence on the transpassive potential, but its influence increased markedly as the pH was decreased. While the influence of F^- ions on the onset of transpassivity was apparent for pH 5 and 7, changes were less severe at pH 9. It is likely that the decreasing solubility of Cr(III) species across the range of pH values (5, 7, and 9) limits the formation of these Cr-F species [19].

7.3.3 Potentiostatic polarization behaviour

Potentiostatic polarization experiments were conducted on two alloys, SS2205 and C2000. These alloys were selected based on their extensive use in the petrochemical industry (SS2205) and for literature reports regarding the beneficial effects of Cu addition on the corrosion behaviour in F^--containing solutions (C2000). Changes in surface composition and dissolved metal concentrations were monitored at the conclusion of polarization measurements by XPS and ICP-MS, respectively.

Current densities recorded at applied potentials of −0.100, 0, 0.100, 0.200, and 0.300 V, in solution containing 5000 ppm F^- and 1000 ppm Cl^- (pH 5) are shown in Figure 7.6 and Figure 7.7 for C2000 and SS2205, respectively. For clarity, data are presented on both semi-log (A) and log-log (B) axes. At the lower applied potentials, *e.g.*, −0.100, 0, and 0.100 V, observations were similar for C2000 and SS2205. Plotting these data on log-log axes, Figure 7.6(B) and Figure 7.7(B), demonstrates that the current densities decreased with time in an approximately linear fashion for the entire 8-h period. These decreases in current density are consistent with the anodic formation of a passive oxide film. Unlike SS2205, at an applied potential of 0.100 V, C2000 achieved a steady-state condition for t > 2 h, indicating that the film growth process was accompanied by a dissolution process (steady-state is achieved once the rates of film growth and film dissolution become equal).

At higher potentials, *e.g.*, 0.200 and 0.300 V, both C2000 and SS2205 showed current densities decreasing with time; however, current densities were higher as the applied potential increased. Although current densities initially showed a decreasing trend, sudden increases in current densities were observed, indicating breakdown of the passive oxide formed at shorter times. Current densities were considerably lower, almost two orders of magnitude, on the Fe-based alloy (Figure 7.7) than on the Ni-based alloy (Figure 7.6). Considering the dynamic polarization behaviour, Figure 7.3, the protection provided by Fe(III) oxides is apparent; lower measured current densities on SS2205 are explained by the higher stability of Fe(III) oxide at higher potentials [19].

Current transients recorded on C2000 and SS2205 at 0.200 and 0.300 V in the base electrolyte solution were compared to those from solution containing F^-/Cl^- in Figure 7.8 and Figure 7.9, respectively. First, considering the transients recorded at the lower applied potential, 0.200 V, films grew for a minimum of 9000 and 2000 s on C2000 and SS2205, respectively. Beyond this period, we observed differences in the corrosion behaviour between alloys exposed to solutions containing F^-/Cl^- and those exposed to the base

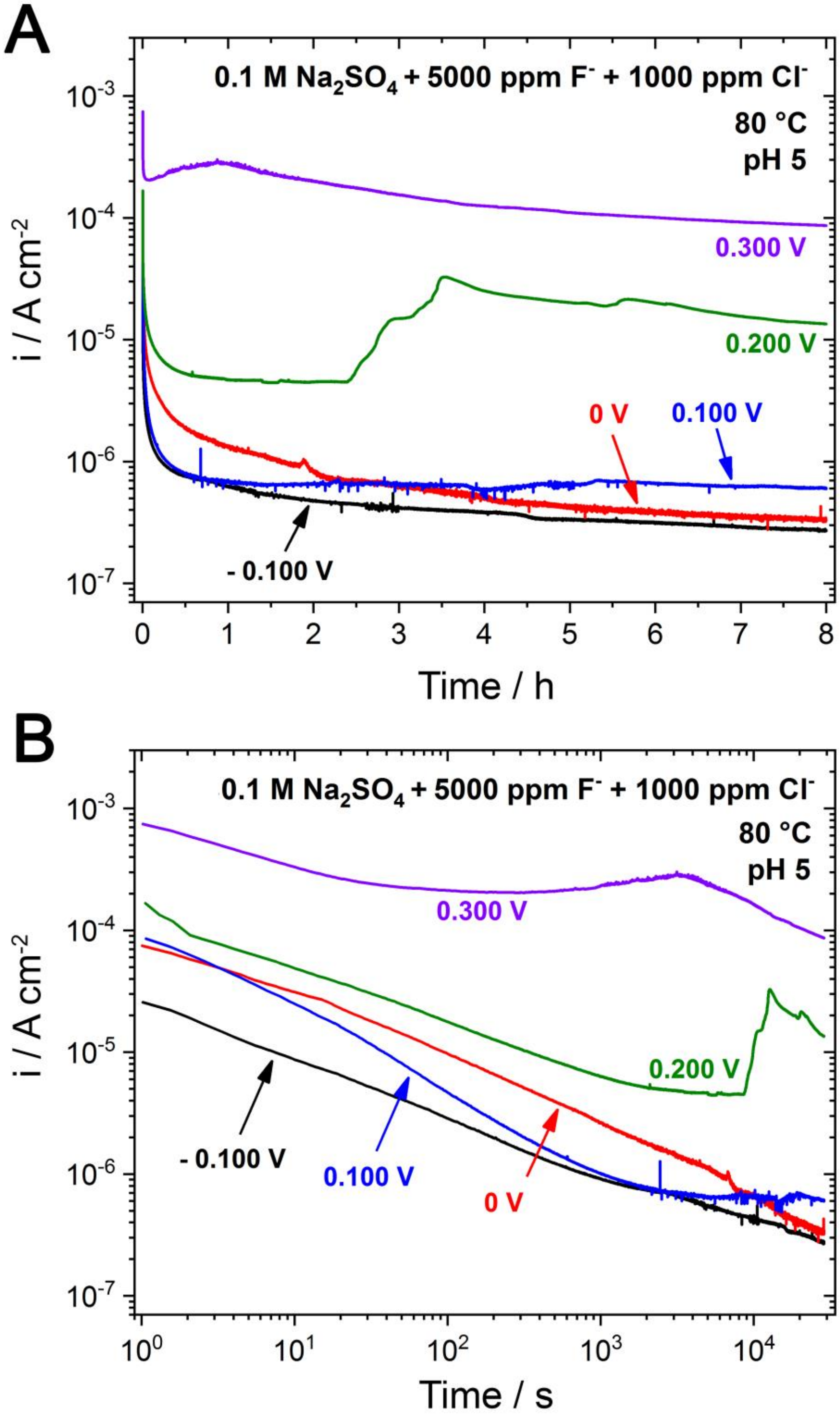

Figure 7.6 - Current-time response for C2000 electrodes polarized at −0.100, 0, 0.100, 0.200, and 0.300 V while immersed in 0.1 M Na_2SO_4 + 5000 ppm F^- + 1000 ppm Cl^- solution. The same data are presented as (A) log(i)-time and (B) log(i)-log(t) plots.

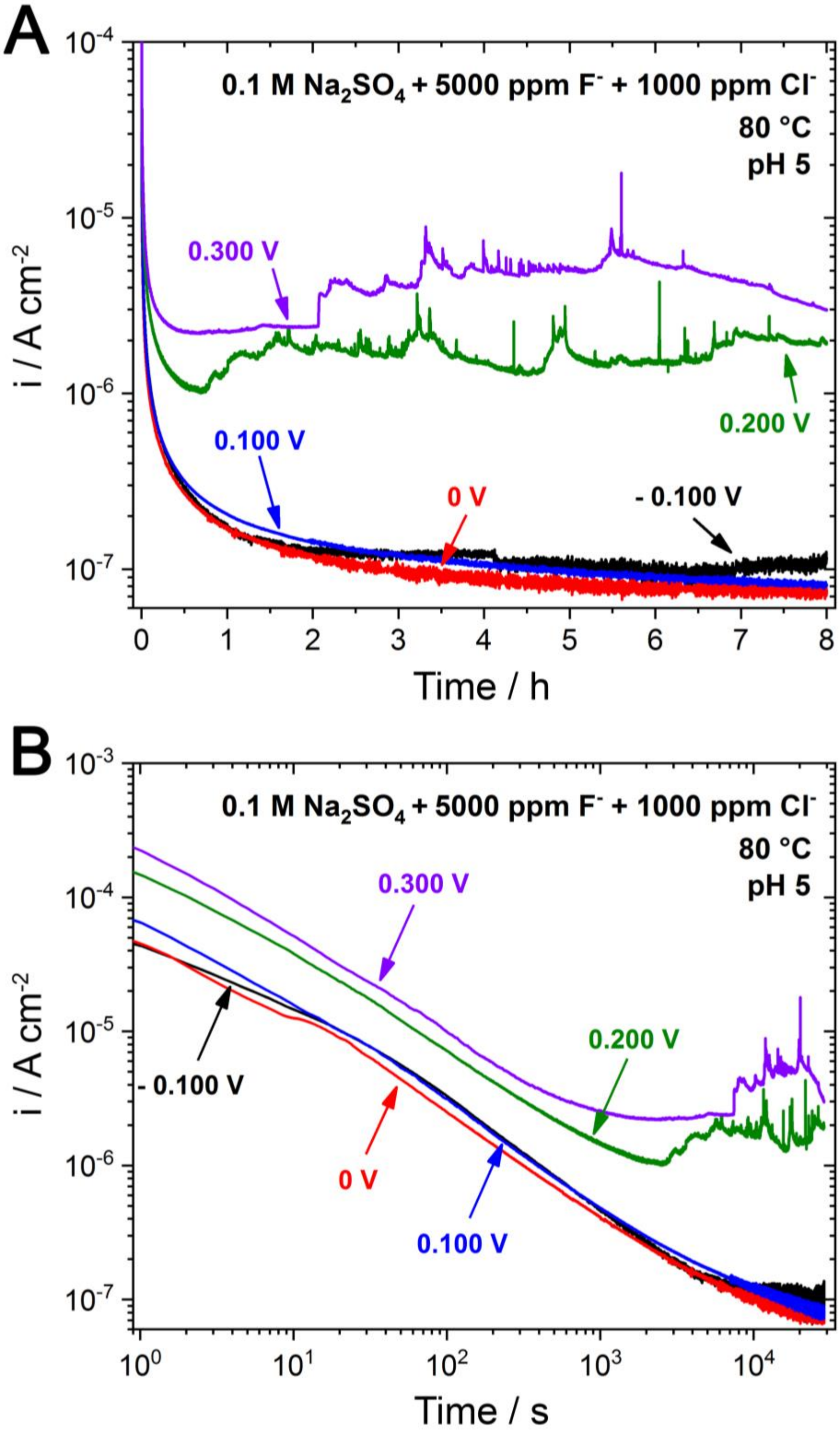

Figure 7.7 - Current-time response for SS2205 coupons polarized at −0.100, 0, 0.100, 0.200, and 0.300 V while immersed in 0.1 M Na_2SO_4 + 5000 ppm F^- + 1000 ppm Cl^- solution. The same data are presented as (A) log(i)-time and (B) log(i)-log(t) plots.

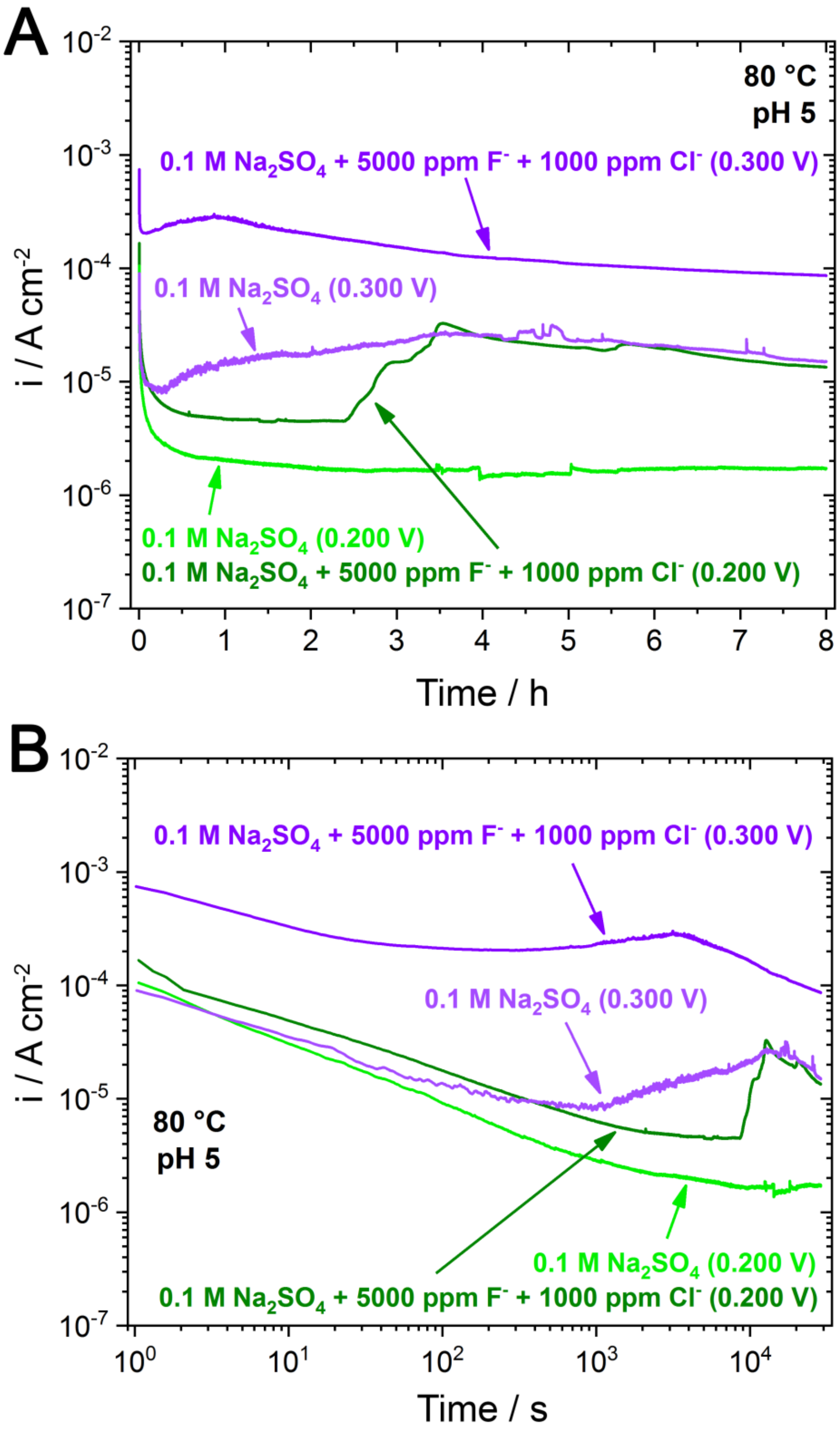

Figure 7.8 - The effect of F^- and Cl^- addition to the base electrolyte (0.1 M Na_2SO_4) is compared for applied potentials of 0.200 and 0.300 V for alloy C2000. Presented as (A) log(i)-time and (B) log(i)-log(t) plots.

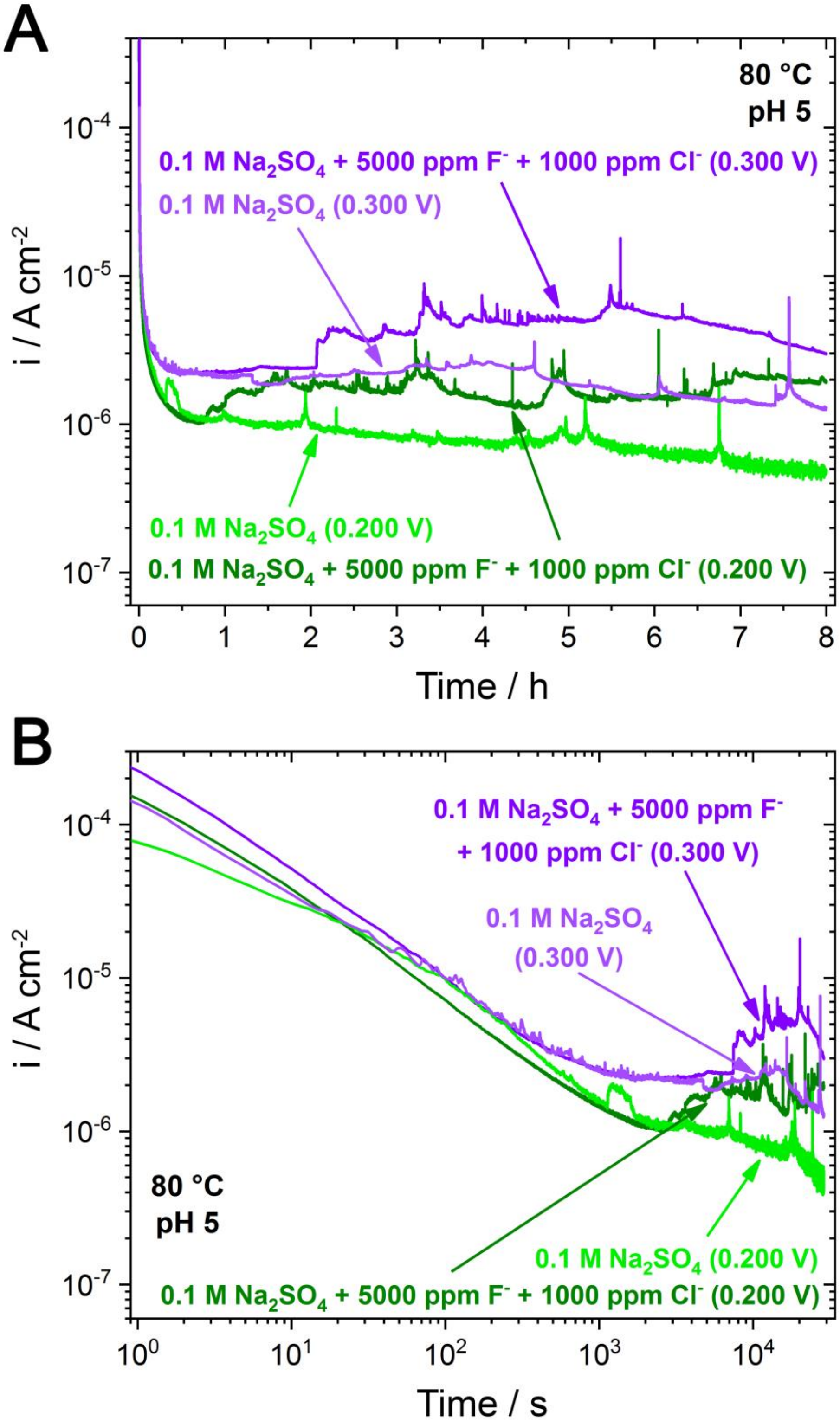

Figure 7.9 - The effect of F^- and Cl^- addition to the base electrolyte (0.1 M Na_2SO_4) is compared for applied potentials of 0.200 and 0.300 V for SS2205. Presented as (A) log(i)-time and (B) log(i)-log(t) plots.

electrolyte only. In the case of C2000, exposed to the base electrolyte, Figure 7.8, film growth continued until a steady-state was eventually attained. In the solution containing F^-/Cl^-, film growth continued until currents began to increase at $t > 9000$ s, suggesting film breakdown. In the case of SS2205, Figure 7.9, following the initial period of film growth, minor current transient became apparent in the base electrolyte. All transients returned to the background current values, suggesting repassivation. Despite these metastable events, film growth continued, as suggested by further decreases in current densities over time. In the F^-/Cl^- containing solution, breakdown behaviour was more frequent than the behaviour observed in the base electrolyte. In solutions containing F^-/Cl^-, an increase in background current density occurred at $t > 3000$ s, suggesting the presence of competing film formation and dissolution processes.

At the highest applied potential, 0.300 V, differences between the current transients recorded on materials exposed to the F^-/Cl^--containing solutions and those exposed to the base electrolyte were again apparent. While an initial film growth process was observed on C2000 in both solutions, current densities measured in the F^-/Cl^--containing solution were approximately one order of magnitude higher than those measured in the base electrolyte, Figure 7.8. Furthermore, in both solutions, the presence of current fluctuations suggests the general instability of the surface oxide, which is not unexpected, due to the onset of transpassive dissolution at higher applied potentials. In the case of SS2205, current densities measured during the film growth were similar in both the base electrolyte and in the solution containing F^-/Cl^-, Figure 7.9. At $t > 4000$ s, passive film breakdown behaviour became apparent in both the base electrolyte and the F^-/Cl^--containing solution, however, the current fluctuations were more pronounced when F^- was present.

Solution analysis, obtained by ICP-MS, confirmed metal ion release at the onset of film breakdown at an applied potential of 0.300 V, in solutions containing F^-/Cl^-. The concentrations of dissolved Ni and Fe, the alloy matrix elements for C2000 and SS2205, respectively, are shown as function of the applied potential in Figure 7.10. For both C2000 and SS2205, concentrations of dissolved Ni or Fe, respectively, remained below limits of detection (indicated as a dotted line) for applied potentials ≤ 0.200 V. The ability of Ni and Fe to remain below detection limits, despite the 8-h polarization, is evidence of the protective nature of the oxide films formed at these potentials. At an applied potential of 0.300 V, passivity gave way to transpassive behaviour, as confirmed by the sudden increase in Ni and Fe concentrations. This is especially true for C2000, where Ni suddenly became detectable at levels approximately 12 times the limit of detection, and SS2205, where Fe became detectable only at the applied potential of 0.300 V. Comparing the concentrations of dissolved metal ions from C2000 and SS2205, one can note that concentrations of dissolved Fe from SS2205 were significantly lower than the levels of Ni released from C2000. This agreed with the measurement of lower current densities on SS2205 than on C2000.

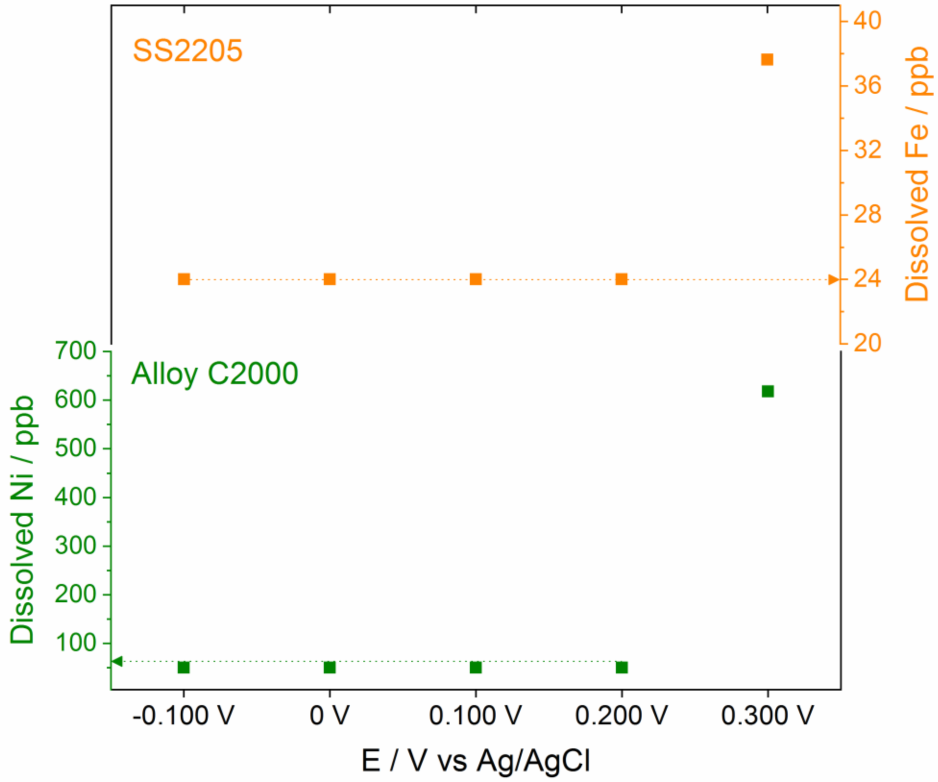

Figure 7.10 - Concentrations of dissolved alloy matrix elements, determined by ICP-MS, as a function of applied potential. Solution samples taken at the completion of potentiostatic polarization experiments on SS2205 and C2000 in 0.1 M Na_2SO_4 + 5000 ppm F^- + 1000 ppm Cl^- (pH 5 and 80°C). Values expressed in µg L^{-1} (ppb).

Alloy surface compositions following potentiostatic experiments in solutions containing 5000 ppm F^- and 1000 ppm Cl^- were investigated by XPS. Surface compositions obtained by the quantification of survey spectra are summarized in Table 7.3 and Table 7.4 for C2000 and SS2205, respectively. As expected, the surface composition was dominated by Cr on C2000 and by both Cr and Fe on S2205 within the passive region. At 0.300 V, *i.e.*, with the onset of transpassivity, the apparent concentrations of the individual metals decreased. This mainly reflects the thickening of the oxide film, such that XPS analysis, which determines a weighted average composition of the outermost several nanometres of the surface, detects less of the underlying metal and more oxygen, resulting in what seems like dilution of the metal concentration. To a lesser extent, the formation of higher oxidation states of Cr, Fe, and Mo at these potentials, and their subsequent hydrolysis, also contribute to this dilution effect.

Table 7.3 - Surface composition (at.%), determined by XPS, of C2000 coupons immersed in a solution containing 0.1 M Na_2SO_4 + 5000 ppm F^- + 1000 ppm Cl^- (pH 5 and 80°C) and polarized at the indicated potential for 8 h. The contribution of the C 1s signal has been factored out of the reported data.

	Ni	**Cr**	**Mo**	**O**	**F**
−0.100 V	2.9	14.4	3.7	77.9	1.1
0 V	3.7	15.3	4.3	75.2	1.5
0.100 V	5.4	15.3	3.9	72.4	3.1
0.200 V	3.0	15.8	4.1	74.7	2.5
0.300 V	1.3	11.5	0.3	84.9	2.0

Although both F^- and Cl^- were present in solution, only F was detected on the surface following potentiostatic polarization experiments. This suggests that F^- may be incorporated into the growing oxide, a feature that would explain the breakdown of the oxide at lower potentials when F^- is present. The incorporation of F into surface oxides has been observed in acidic F^--containing media [39]. Here, the tendency of F to remain in the surface appears to increase with increasing potentials. At high potentials, the small decrease in the concentration of F can be attributed to the sharp increase in O content achieved in this region.

Table 7.4 - Surface composition (at.%), determined by XPS, of SS2205 coupons immersed in a solution containing 0.1 M Na_2SO_4 + 5000 ppm F^- + 1000 ppm Cl^- (pH 5 and 80°C) and polarized at the indicated potential for 8 h. The contribution of the C 1s signal has been factored out of the reported data.

	Fe	**Cr**	**Mo**	**O**	**F**
−0.100 V	23.1	12.4	0.8	62.9	0.8
0 V	27.7	8.4	0.5	63.0	0.4
0.100 V	21.0	14.9	0.7	62.4	0.9
0.200 V	16.0	6.4	0.8	76.2	0.6
0.300 V	20.8	2.0	0.1	75.7	1.3

Two additional features are worth noting:

1. The absence of a signal for Cl indicates that it is not incorporated into the oxide, at least not in detectable concentrations. This is consistent with the results in Figure 7.2, which show that the addition of Cl^- to the base electrolyte (at pH 7) had little influence on the potentiodynamic polarization curve.
2. No signal was observed for Cu on alloy C2000, indicating that no segregation of Cu to the alloy/solution interface took place during anodic oxidation. Some studies in concentrated HF have shown Cu segregation to the interface [7], which could indicate that this process does not take place in the pH range 5-9.

Normalized surface compositions, incorporating chemical state information, are shown in Figure 7.11(A) & (B) for C2000 and SS2205, respectively. Here, the normalized surface composition obtained from survey spectra was combined with the chemical state information provided by deconvoluting high-resolution spectra. In the passive region (−0.100 V to 0.200 V), surfaces of both C2000 and SS2205 were dominated by oxidized Cr/Fe species, consistent with the presence of the barrier layer associated with

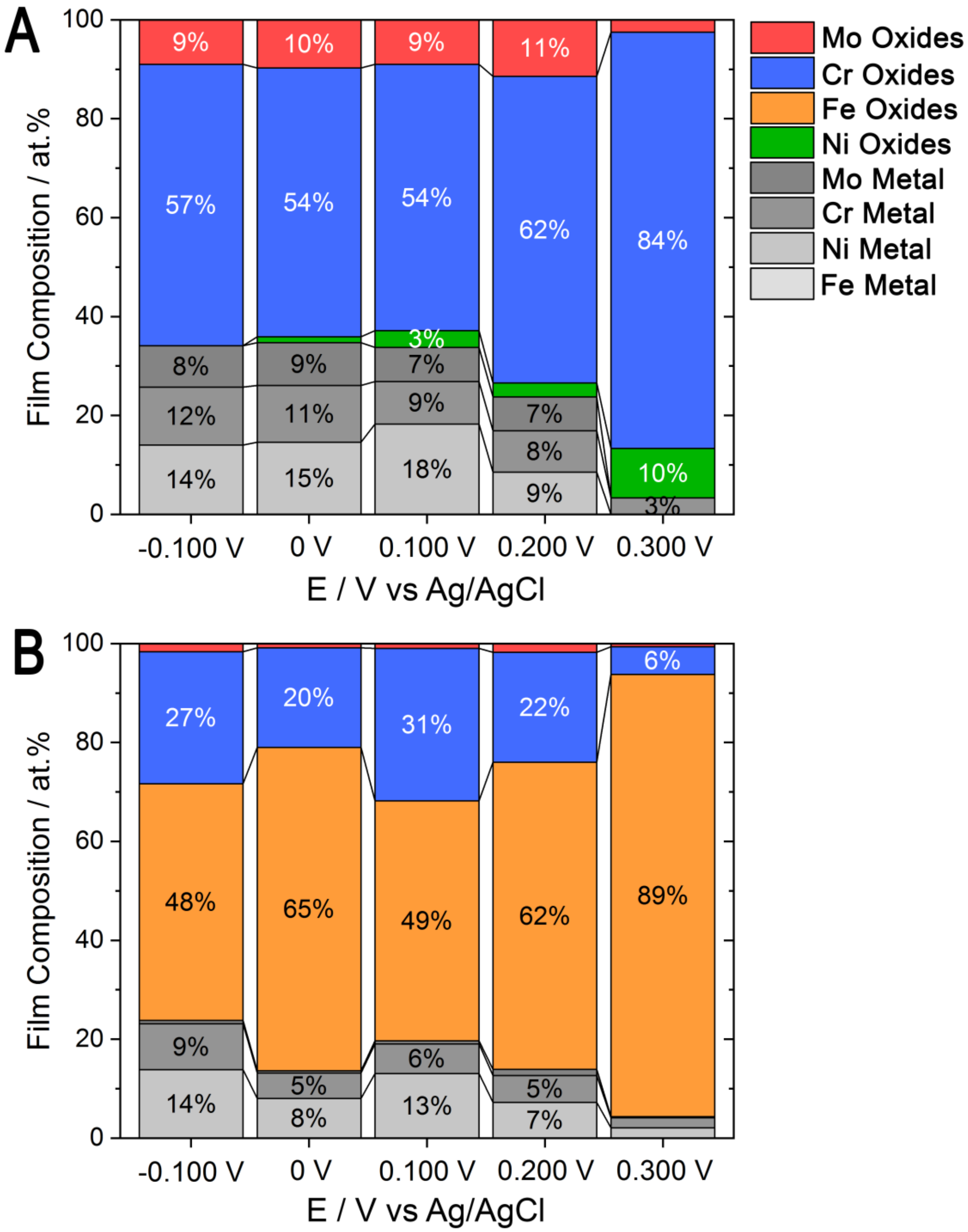

Figure 7.11 - Normalized surface composition (at.%), determined by XPS, of (A) C2000 and (B) SS2205 showing major alloying elements (Ni or Fe, Cr, Mo) and their compounds following potentiostatic polarization. Components contributing ≤ 2 at.% are not labelled.

passivity [4, 21]. For both alloys, signals representing metallic components demonstrate the passive oxide to be relatively thin within the passive region and to thicken once the potential was increased into the transpassive region (0.300 V). In a previous study of electrochemically grown films on C2000, Zhang *et al.* demonstrated the tendency for the oxide thickness to increase near the onset of transpassive dissolution [21]. Although not shown here, the $Ni(OH)_2$ content of the film on C2000, a signature for its tendency to dissolve, becomes noticeable for potentials between 0 and 0.100 V [21].

Following the polarization experiments, the electrode surfaces were examined by scanning electron microscopy to determine changes in surface morphology resulting from dissolution during the polarizations. In all cases, the degree of dissolution attack was too small to observe, as evidenced by the retention of grinding lines generated by surface preparation procedures.

7.4 Conclusions

The ability of fluoride ions to decrease the onset potential for transpassive breakdown on Cr-containing alloys, and to challenge the secondary passive window of Fe-based alloys, has been documented. Dynamic polarization experiments demonstrated that onset potentials for the transpassive region were decreased by approximately 0.100 V in the presence of fluoride ions. This was particularly apparent in slightly acidic solutions (pH 5) and becomes less severe at higher pH. Potentiostatic polarization experiments support observations regarding the ability of fluoride ions to promote transpassive dissolution.

Findings suggest that Fe-based alloys experience lower corrosion rates at the onset of transpassive dissolution compared to Ni-based alloys. This was attributed to the protectiveness and low solubility of oxidized Fe species within the surface film at potentials beyond the electrochemical conversion of Cr(III) to Cr(VI).

While values of E_{CORR} recorded under the conditions employed here are less than those required for transpassive film breakdown, the role of fluoride ions is expected to become important in the presence of oxidizing impurities commonly found in industrial processes.

7.5 References

[1] S. Pahlavan, S. Moazen, I. Taji, K. Saffar, M. Hamrah, M.H. Moayed, S. Mollazadeh Beidokhti, Pitting corrosion of martensitic stainless steel in halide bearing solutions, *Corrosion Science*, 112 (2016) 233-240.

[2] Z.B. Wang, H.X. Hu, Y.G. Zheng, Synergistic effects of fluoride and chloride on general corrosion behavior of AISI 316 stainless steel and pure titanium in H_2SO_4 solutions, *Corrosion Science*, 130 (2018) 203-217.

[3] H.S. Klapper, N.S. Zadorozne, R.B. Rebak, Localized corrosion characteristics of nickel alloys: a review, *Acta Metallurgica Sinica (English Letters)*, 30 (2017) 296-305.

[4] Z. Wang, A. Seyeux, S. Zanna, V. Maurice, P. Marcus, Chloride-induced alterations of the passive film on 316L stainless steel and blocking effect of pre-passivation, *Electrochimica Acta*, 329 (2020) 135159.

[5] Materials for storing and handling commercial grades of aqueous hydrofluoric acid and anhydrous hydrogen fluoride, in: NACE Technical Committee Report (5A171), NACE International, Houston, TX, 2007.

[6] Y. Li, X. Fan, N. Tang, H. Bian, Y. Hou, Y. Koizumi, A. Chiba, Effects of partially substituting cobalt for nickel on the corrosion resistance of a Ni–16Cr–15Mo alloy to aqueous hydrofluoric acid, *Corrosion Science*, 78 (2014) 101-110.

[7] Y. Li, X. Xu, Y. Hou, C. Zhang, F. Wang, K. Omura, Y. Koizumi, A. Chiba, Regulating the passive film of NiCoCrMo alloy in hydrofluoric acid solution by small addition of Cu, *Corrosion Science*, 98 (2015) 119-127.

[8] R.B. Rebak, J.R. Dillman, P. Crook, C.V.V. Shawber, Corrosion behaviour of nickel alloys in wet hydrofluoric acid, *Materials and Corrosion*, 52 (2001) 289-297.

[9] J.N. Saba, D.A. Siddiqui, L.C. Rodriguez, S. Sridhar, D.C. Rodrigues, Investigation of the corrosive effects of dental cements on titanium, *Journal of Bio- and Tribo-Corrosion*, 3 (2017) 1-7.

[10] J.C.M. Souza, S.L. Barbosa, E.A. Ariza, M. Henriques, W. Teughels, P. Ponthiaux, J.-P. Celis, L.A. Rocha, How do titanium and Ti6Al4V corrode in fluoridated medium as found in the oral cavity? An in vitro study, *Materials Science and Engineering C*, 47 (2015) 384-393.

[11] A.V. Rodrigues, N.T.C. Oliveira, M.L. dos Santos, A.C. Guastaldi, Electrochemical behavior and corrosion resistance of Ti–15Mo alloy in naturally-aerated solutions, containing chloride and fluoride ions, *Journal of Materials Science: Materials in Medicine*, 16 (2015) 1-9.

[12] A. Kocijan, K.D. Merl, M. Jenko, The corrosion behaviour of austenitic and duplex stainless steels in artificial saliva with the addition of fluoride, *Corrosion Science*, 53 (2011) 776-783.

[13] Y. Yang, L. Guo, H. Liu, Influence of fluoride ions on corrosion performance of 316L stainless steel as bipolar plate material in simulated PEMFC anode environments, *International Journal of Hydrogen Energy*, 37 (2012) 1875-1883.

[14] P. Rae, G. di Lullo, Matrix acid stimulation - A review of the State-Of-The-Art, Society of Petroleum Engineers, (2003).

[15] M.C. Biesinger, B.P. Payne, L.W.M. Lau, A. Gerson, R.C. Smart, X-ray photoelectron spectroscopic chemical state quantification of mixed nickel metal, oxide and hydroxide systems, *Surface and Interface Analysis*, 41 (2009) 324-332.

[16] M.C. Biesinger, B.P. Payne, A.P. Grosvenor, L.W.M. Lau, A.R. Gerson, R.C. Smart, Resolving surface chemical states in XPS analysis of first row transition metals, oxides and hydroxides: Cr, Mn, Fe, Co and Ni, *Applied Surface Science*, 257 (2011) 2717-2730.

[17] M.C. Biesinger, C. Brown, J.R. Mycroft, R.D. Davidson, N.S. McIntyre, X-ray photoelectron spectroscopy studies of chromium compounds, *Surface and Interface Analysis*, 36 (2004) 1550-1563.

[18] P.A. Spevack, N.S. McIntyre, Thermal reduction of MoO_3, *Journal of Physical Chemistry*, 96 (1992) 9029-9035.

[19] M. Pourbaix, Atlas of electrochemical equilibria in aqueous solutions, National Association of Corrosion Engineers, Houston, TX, 1974.

[20] X. Cheng, Z. Feng, C. Li, C. Dong, X. Li, Investigation of oxide film formation on 316L stainless steel in high-temperature aqueous environments, *Electrochimica Acta*, 56 (2011) 5860-5865.

[21] X. Zhang, D. Zagidulin, D.W. Shoesmith, Characterization of film properties on the Ni Cr Mo alloy C-2000, *Electrochimica Acta*, 89 (2013) 814-822.

[22] A.K. Mishra, D.W. Shoesmith, The activation/depassivation of nickel–chromium–molybdenum alloys: An oxyanion or a pH effect - part ii, *Electrochimica Acta*, 102 (2013) 328-335.

[23] A.W.E. Hodgson, S. Kurz, S. Virtanen, V. Fervel, C.O.A. Olsson, S. Mischler, Passive and transpassive behaviour of CoCrMo in simulated biological solutions, *Electrochimica Acta*, 49 (2004) 2167-2178.

[24] J.D. Henderson, X. Li, D.W. Shoesmith, J.J. Noël, K. Ogle, Molybdenum surface enrichment and release during transpassive dissolution of Ni-based alloys, *Corrosion Science*, 147 (2019) 32-40.

[25] M. Bojinov, G. Fabricius, T. Laitinen, T. Saario, Transpassivity mechanism of iron-chromium-molybdenum alloys studied by AC impedance, DC resistance and RRDE measurements, *Electrochimica Acta*, 44 (1999) 4331-4343.

[26] M. Bojinov, I. Betova, R. Raicheff, Influence of molybdenum on the transpassivity of a Fe + 12%Cr alloy in H_2SO_4 solutions, *Journal of Electroanalytical Chemistry*, 430 (1997) 169-178.

[27] I. Betova, M. Bojinov, P. Kinnunen, T. Laitinen, P. Pohjanne, T. Saario, M. Vilpas, Transpassive dissolution mechanism of Ni-based alloys in a simulated bleaching solution, *Journal of the Electrochemical Society*, 149 (2002) B499-B509.

[28] J.L. Galvez, J. Dufour, C. Negro, F. Lopez-Mateos, Determination of iron and chromium fluorides solubility for the treatment of wastes from stainless steel mills, *Chemical Engineering Journal*, 136 (2008) 116-125.

[29] P. Marcus, Corrosion mechanisms in theory and practice, 3rd ed., CRC Press, 2011.

[30] J. Hem, Chemical factors that influence the availability of iron and manganese in aqueous systems, GSA Bulletin, 83 (1972) 443-450.

[31] A. Macías, M.L. Escudero, The effect of fluoride on corrosion of reinforcing steel in alkaline solutions, *Corrosion Science*, 36 (1994) 2169-2180.

[32] C.F. Baes, R.E. Mesmer, The hydrolysis of cations, Wiley, 1976.

[33] A.V. Ingle, V.S. Raja, J. Rangarajan, P. Mishra, Corrosion resistant Al-Cr-Mo alloy coating on type 316L stainless steel bipolar plates for proton exchange membrane fuel cell applications, *Fuel Cells*, 19 (2019) 708-723.

[34] J.L. Trompette, The comparative breakdown of passivity of tin by fluorides and chlorides interpreted through the ‘law of matching affinities’ concept, *Corrosion Science*, 94 (2015) 288-293.

[35] S.M. Castro, M.J. Ponces, J.D. Lopes, M. Vasconcelos, M.C.F. Pollmann, Orthodontic wires and its corrosion - the specific case of stainless steel and beta-titanium, *Journal of Dental Sciences*, 10 (2015) 1-7.

[36] H.-H. Strehblow, B. Titze, B.P. Loechel, The breakdown of passivity of iron and nickel by fluoride, *Corrosion Science*, 19 (1979) 1047-1057.

[37] M. Mirjalili, M. Momeni, N. Ebrahimi, M.H. Moayed, Comparative study on corrosion behaviour of nitinol and stainless steel orthodontic wires in simulated saliva solution in presence of fluoride ions, *Materials Science and Engineering C*, 33 (2013) 2084-2093.

[38] B.J. Plankey, H.H. Patterson, C.S. Cronan, Kinetics of aluminum fluoride complexation in acidic waters, *Environmental Science & Technology*, 20 (1986) 160-165.

[39] M.C. Li, C.L. Zheng, H.C. Lin, C.N. Cao, Electrochemical corrosion behaviour of type 316 stainless steel in acid media containing fluoride ions, *British Corrosion Journal*, 36 (2001) 179-183.

Chapter 8

8 Conclusions and future work

8.1 Conclusions

This thesis has investigated various mechanistic features important during the corrosion of Ni-based alloys. The data provides new information necessary for an improved understanding of the corrosion behaviour and improved material selection criteria.

For commercially available Ni-based alloys, the influence of Cr and Mo additions was investigated during exposure to neutral and acidic chloride solutions at 75 °C. When the alloys were exposed to 3 M NaCl, the corrosion behaviour both at E_{CORR} and under an applied potential was consistent with passive behaviour. Increases in Cr content resulted in lower corrosion rates; however, only minor benefits were observed above 15 wt.% Cr. Resistance measurements made using both LPR and EIS techniques yielded values on the order of 10^6 Ω cm^2. The corrosion behaviour of alloys exposed to 1 M HCl + 2 M NaCl, at both E_{CORR} and during applied potential polarization, improved with increasing Mo content. Alloys containing higher Mo content were found to have lower corrosion rates, improved film stability, and enhanced repassivation behaviour. During corrosion at E_{CORR}, alloy BC-1 (22.1 wt.% Mo) was found to retain a partially protective oxide film, as suggested by R_P values, which remained approximately two orders of magnitude higher than for the low Mo containing alloys; C-22 (12.97 wt.% Mo), G-35 (7.98 wt.% Mo), and G-30 (4.97 wt.%). A low-frequency inductive feature in the impedance spectra suggested that active dissolution on alloys C-22, G-35, and G-30 involved coupled electrochemical reactions, *e.g.*, an adsorbed intermediate. In potentiodynamic experiments, active dissolution was found to be suppressed by increases in Mo content, consistent with the behaviour at E_{CORR}. Interestingly, alloys G-35 and G-30 displayed a region of net cathodic current at applied potentials greater than the active-to-passive transition. The removal of O_2, the anticipated oxidant, showed that Mo also played a key role in stabilizing the oxide film, with passive current densities (at 0 V vs SCE) scaling in the order BC-1 (22.1 wt.% Mo) < C-22 (12.97 wt.% Mo) < G-35 (7.98 wt.% Mo) < G-30 (4.97 wt.% Mo). Lastly, potentiostatic experiments indicated that films formed on low-Mo-containing alloys were more susceptible to frequent and severe localized breakdown.

Complementary information related to the fate of individual alloying elements during corrosion was obtained using the AESEC technique. When alloys were exposed to 1 M NaCl, real-time dissolution rates indicated that, in the presence of a passive film (*i.e.*, at applied potentials < 0.6 V vs Ag/AgCl) dissolution rates remained below the limits of detection. At more positive applied potentials, dissolution rates increased, due to the transpassive dissolution of the passive film. During transpassive dissolution, all alloys were found to accumulate Cr and Mo species at the surface, based on the comparison to the bulk alloy composition. During repassivation, caused by a decrease in the applied potential, the previously accumulated Mo species were released from the surface, suggesting a mechanism of only temporary protection during film breakdown. This dynamic behaviour of Mo deposition/release was attributed to changes in the local pH caused by the hydrolysis of dissolved metal cations. In support of this theory, this dynamic behaviour of Mo species was particularly pronounced for the high-Fe-containing alloys G-30 (15.9 wt.% Fe) and C-22 (3.79 wt.% Fe). Under transpassive conditions, the dissolution and hydrolysis of Fe(III) species are expected to lead to a more rapid local acidification compared to dissolution and hydrolysis of Ni(II) species. As a result, while Fe is added at the expense of Ni to reduce the overall cost of the alloy, it may positively impact corrosion performance under highly oxidizing conditions.

Using the AESEC technique, dissolution behaviour was also studied during surface activation, spontaneous repassivation, and electrochemically promoted passivation in 1 M HCl at 75°C. Following activation, spontaneous repassivation on open circuit was found to involve the accumulation of both Cr and Mo species on the alloy surface, with accumulation of the latter species the dominant influence. The ability to recover from surface activation improved with increases in the Mo content of the alloy. For high Mo containing alloys, BC-1 (22.10 wt.% Mo) and C-22 (12.97 wt.% Mo), repassivation was found to be rapid following damage to the oxide. However, alloy C-22 required slightly longer times while exhibiting metastable breakdown events. Since both repassivation and film breakdown involve the accumulation of Mo species, alloy C-22 was found to accumulate a greater amount of Mo species, despite the alloy's lower Mo content than alloy BC-1. For alloy G-35 (7.98 wt.% Mo), while attempts to repassivate the damaged oxide were apparent, increases in dissolution rate and the congruent dissolution ratio suggest the onset of active dissolution following surface activation. During electrochemically promoted passivation, the previously accumulated Mo species were found to be partially released to solution while the accumulation of Cr species dominated the film formation process. Results obtained using AESEC were also compared to the results of *ex situ* XPS analyses. Consistent with AESEC data, the accumulation of oxidized Cr species was greater for passivated surfaces than for repassivated surfaces, and this effect also increased according to the Cr content of the alloy. The accumulated Mo species were found to be mainly Mo(IV) and Mo(VI) on surfaces that were spontaneously repassivated and electrochemically passivated, respectively. After spontaneous repassivation the largest accumulation of Mo species was found for the moderate-Mo-containing alloy (C-22), consistent with AESEC data. This is consistent with information provided by AESEC measurements and suggests the importance of Mo in both stabilizing the oxide film and repairing damage occurring in the film.

The mechanism of crevice corrosion, specifically the role of internal cathodic reactions, was investigated by coupling galvanostatic crevice experiments to weight loss measurements. Data suggested an internal cathodic reaction, specifically the reduction of H^+, supports the crevice corrosion reaction on Ni-based alloys. For the investigated alloys, this internal cathodic reaction was shown to intensify the anticipated damage by as much as ~80%. The extent of this intensification appeared to be dependent on the evolving geometry of the crevice and the blocking of cathodic sites by the deposition of Mo- and W-rich corrosion products. The extent of damage penetration into the alloy within the crevice was proportional to the extent of H^+ production and hence to the extent of the internal H^+ reduction reaction. As a result, the low-Mo(W) alloys, G-30 and G-35, were particularly susceptible to internally supported crevice corrosion since Mo- and W-rich corrosion products not only stifle active dissolution but also limit the occurrence of H^+ reduction. It was also found that damage penetrated more deeply when the alloys were driven to corrode by small as opposed to large applied currents. This is particularly concerning for corrosion under natural conditions, where the applied current is zero. These findings suggest that an expectation that corrosion damage will be supported solely on the availability of O_2 and other oxidants outside the crevice would significantly underestimate the real extent of corrosion damage on Ni-based alloys.

The role of F^- ions in trace concentrations during the corrosion of both Ni- and Fe-based alloys was investigated at pH values 5 to 9 at 80°C. The passive film stability of all investigated alloys decreased in the presence of F^-, as indicated by the decrease of the onset potential for transpassive dissolution of the alloy. For Fe-based alloys, the stability of a secondary passive region, due to the formation of Fe oxides at high potentials, was also affected by the presence of F^- ions. In potentiodynamic experiments, the onset potential for transpassive dissolution was reduced by ~100 mV when F^- was present. This was particularly apparent in slightly acidic solutions (pH 5) and became less severe at higher pH. Constant potential experiments confirmed the ability of F^- ions to promote transpassive dissolution. Fe-based alloys were found to experience lower transpassive dissolution rates than Ni-based alloys. This was attributed to the protectiveness and low solubility of Fe(III) species formed within the surface film at transpassive potentials when the electrochemical conversion of Cr(III) to the more soluble Cr(VI) was possible.

8.2 Future work

Throughout this thesis, data have been presented which demonstrate the role of individual alloying elements during the corrosion of Ni-based alloys. Consistent in all data, Mo species were shown to have an important role in controlling breakdown and repassivation behaviour. While data obtained by traditional electrochemical techniques could not offer detailed information related to the fate of individual alloying elements, AESEC measurements allowed for monitoring of real-time elemental dissolution behaviour. This provided several unique observations which advance the current understanding of the role of alloying elements, in particular Mo. Under conditions of transpassive dissolution, the accumulation of Mo species was found to have a transient role in protecting the compromised Cr-rich film. During activation/repassivation of alloys in acidic solution, Mo species were found to dominate the reformation process, while Cr species played a less extreme role. Unfortunately, through all these investigations no information related to oxide film structure was obtained. Future work should employ techniques of high spatial and lateral resolution such as atom probe tomography (APT), transmission electron microscopy (TEM), and depth-profiling Auger electron spectroscopy. This will provide information regarding the role of alloying elements in relation to film structure and corrosion performance.

In the investigation of polarization behaviour in acidic solution, alloys G-30 and G-35 demonstrated an unexpected transition from net anodic to cathodic current in a range of applied potentials greater than the active-passive transition. While H^+ reduction was considered the dominant cathodic reaction in acidic solution, O_2 reduction was shown to occur throughout the passive region. As a result, the transition from net anodic to cathodic current at the onset of film formation was attributed to the rapid rate of O_2 reduction, which occurred at higher rates on the high-Cr, low-Mo alloys, G-30 and G-35. It was speculated that this behaviour could be related to the defect structure of the oxide film; however, it was not experimentally shown. Future investigations may explore why O_2 reduction kinetics are faster on high-Cr, low-Mo alloys than low-Cr, high-Mo alloys. While Mott-Schottky plots, constructed from impedance data, may be used to obtain information on the electronic properties of the oxide film, information obtained from potentiostatic polarization tests suggest that films formed under these conditions are susceptible to breakdown behaviour. As a result, the system cannot be considered stable during the relatively long times required to collect EIS spectra, a requirement for valid data. Instead, *ex situ* photoluminescence measurements may be explored to obtain information on the electronic properties of the oxide film.

In the investigation of polarization behaviour in solutions containing F^- and Cl^- ions, the presence of F^- ions was found to decrease passive film stability. Both dynamic and static polarization data collected in solutions containing 1000 ppm F^- exhibited a decreased window of potentials for which passive behaviour was observed. In contrast, data collected in solutions containing 1000 ppm Cl^- showed no such decrease in passive film stability. For Fe-based alloys, the upper potential limit of the passive region was generally larger than that of Ni-based alloys due to the formation of Fe(III) oxides. However, in the presence of 1000 ppm F^-, this extended region also exhibited a decreased stability. Interestingly, in the most concentrated solution studied, containing 5000 ppm F^- + 1000 ppm Cl^-, an attempt to recover the stability of this extended passive region was observed as well as the occurrence of metastable breakdown events. At present, it is unclear whether this is due to a synergistic effect of F^-/Cl^- or due to a change in behaviour as the F^- concentration increases. Future investigations should expand the range of concentrations investigated here, including solutions containing either F^- or Cl^- as well as combined F^-/Cl^- compositions. Additionally, future investigations may extend the range of solution pH investigated here while maintaining trace F^-/Cl^- ion concentrations, since there appears to be lack of available information in the literature.

Appendices

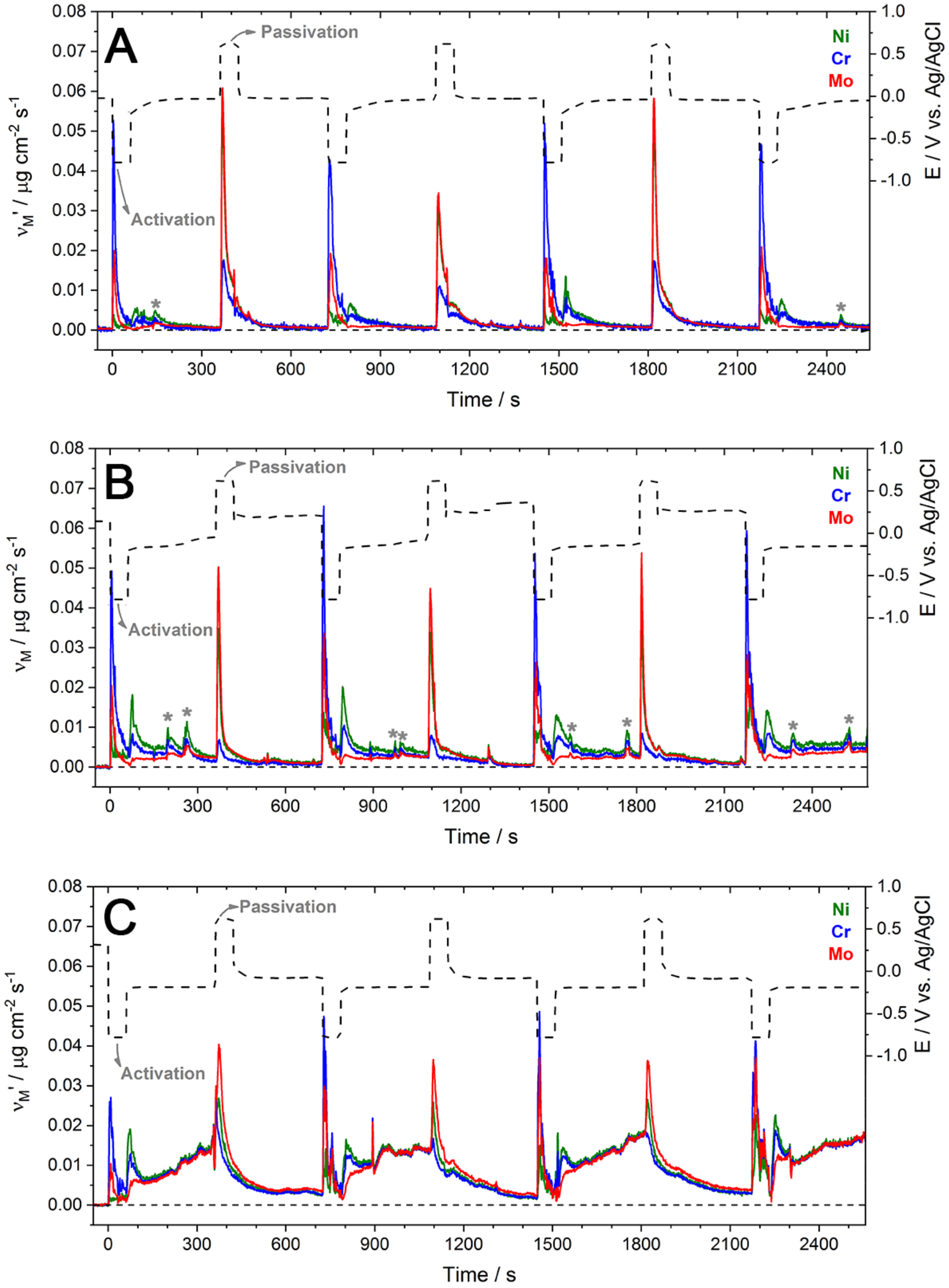

Appendix A - Normalized dissolution rates obtained during the repeated activation and electrochemically-assisted passivation processes for alloys (A) BC-1, (B) C-22, and (C) G-35. All dissolution rates are normalized to the Ni-content in the alloy, Equation 5.3.

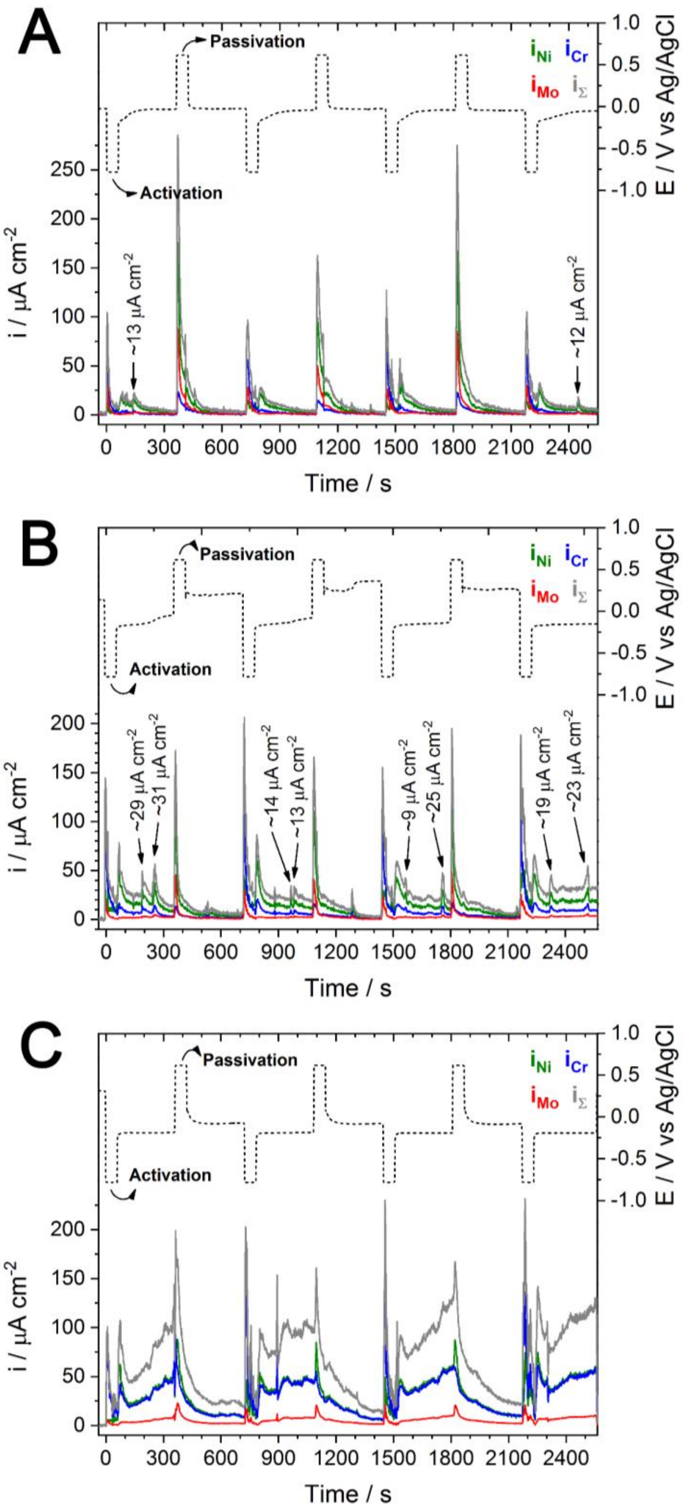

Appendix B - Instantaneous elemental (i_M) and sum current densities (i_Σ) for potentiostatic polarization experiments on alloys (A) BC-1, (B) C-22, and (C) G-35. Currents calculated for Ni(II), Cr(III), and Mo(IV). At maximum current increase corresponding to transients (or breakdowns) are indicated.

Curriculum vitae

JEFFREY DANIEL HENDERSON

EDUCATION

Doctor of Philosophy, Physical/Analytical Chemistry 2015-2021
The University of Western Ontario, London, ON, Canada

Bachelor of Science, Honors Specialization in Chemistry, with distinction 2011-2015
The University of Western Ontario, London, ON, Canada

WORK AND RELATED EXPERIENCES

Graduate Research Assistant 2015-2021
The University of Western Ontario, London, ON, Canada

President 2017-2020
Western University Electrochemical Society Student Chapter, London, ON

Student Representative – Individual Membership Committee 2018-2020
The Electrochemical Society, Pennington, NJ, USA

Visiting Researcher Summer 2018
École Nationale Supérieure de Chimie de Paris, Paris, France

Undergraduate Research Assistant Summer 2015
The University of Western Ontario, London, ON, Canada

Senior Undergraduate Thesis Student 2014-2015
The University of Western Ontario, London, ON, Canada

SCHOLARSHIPS AND AWARDS

Mitacs Elevate Fellowship – Postdoctoral	2021-2023
Alexander Graham Bell Canada Graduate Scholarship – Doctoral	2017-2020
Dennis B. Dutton Award for Student Leadership Excellence	2020
ECS Canada Section Student Award	2019
Oral Prize (1st) – NACE Southern Ontario Student Section Symposium	2019

Oral Prize (2nd) – Canadian Chemistry Conference and Exhibition	2019
Poster Prize (3rd) – NACE Corrosion Conference	2019
Top Downloaded Paper – Surface & Interface Analysis	2017-2018
N. Steward McIntyre Surface Science Award	2018
Herbert H. Uhlig Summer Fellowship	2018
ASPIRE Travel Bursary	2018
Michael Smith Foreign Study Supplement	2018
Ontario Graduate Scholarship (Declined)	2017-2018
Alexander Graham Bell Canada Graduate Scholarship – Masters	2016-2017
Queen Elizabeth II Graduate Scholarship in Sci. and Tech. (Declined)	2016-2017
Poster Prize (1st) – International Society of Electrochemistry Meeting	2017
Poster Prize (2nd) – NACE Southern Ontario Student Section Symposium	2017
Queen Elizabeth II Graduate Scholarship in Sci. and Tech.	2015-2016
NACE Graduate Student Book Award	2016
Poster Prize (3rd) – Canadian ECS Symposium	2016
Undergraduate Student Research Award	2015
Oral Prize (3rd) – Southern Ontario Undergraduate Student Chemistry Conference	2015
Garnet Alexander Woonton Scholarship	2014
James Hall Norton Memorial Award	2014
Ray Leroi Allen Scholarship	2014
James Hall Norton Memorial Award	2013
Laurene Paterson Estate Scholarship	2013
Ray Leroi Allen Scholarship	2013

PEER-REVIEWED PUBLICATIONS *(* indicates equal contribution)*:

1) Henderson, J.D.; Ramamurthy, S.; Filice, F.P.; Biesinger, M.C.; Shoesmith, D.W.; McGarvey, B.; Noël, J.J. Investigating the corrosion behaviour of corrosion resistance alloys in solutions containing dilute fluoride ions. **(Revisions Submitted)**

2) Henderson, J.D.*; Li, X.*; Filice, F.P.; Zagidulin, D.; Biesinger, M.; Kobe, B.; Shoesmith, D.W.; Ogle, K.; Noël, J.J. Investigating the role of Mo and Cr during the activation and passivation of Ni-based alloys in acidic chloride solution *J. Electrochem. Soc.* **Accepted** (DOI: 10.1149/1945-7111/abe47a)

3) Henderson, J.D.; Almusned B.; Momeni, M.; Dehnavi, V.; Zagidulin, D.; Shoesmith, D.W.; Noël, J.J. Investigating the influence of Cr and Mo additions to commercial Ni-based alloys exposed to neutral and acidic chloride solutions. *J. Electrochem. Soc.* **2020**, 167, 131512.

4) Li, X.*; Henderson, J.D.*; Filice, F.P.; Zagidulin, D.; Biesinger, M.C.; Sun, F.; Qian, B.; Shoesmith, D.W.; Noël, J.J.; Ogle, K. The contribution of Cr and Mo to the passivation of Ni22Cr and Ni22Cr10Mo alloys in sulfuric acid. *Corros. Sci.* **2020**, 176, 109015**.**

5) Dehanvi, V.; Henderson, J.D.; Dharmendra, C.; Amirkhiz, B.S.; Shoesmith, D.W.; Noël, J.J.; Mohammadi, M. Corrosion Behaviour of Electron Beam Melting Ti6Al4V: Effects of Microstructural Variation. *J. Electrochem. Soc.* **2020**, 167, 131505.

6) Henderson, J.D.; Seyeux, A.; Zanna, S.; Biesinger, M.C.; Shoesmith, D.W.; Noël, J.J.; Marcus, P. Investigating the transport mechanism during the oxidation of Hastelloy BC-1 by in situ ToF-SIMS. *Corros. Sci.* **2019**, 159, p. 108138.

7) Henderson, J.D.*; Li, X.*; Shoesmith, D.W.; Noël, J.J.; Ogle, K. The surface enrichment and release of molybdenum during the transpassive dissolution of Ni-based alloys. *Corros. Sci.* **2019**, 147, p. 32-40.

8) Filice, F.P.*; Henderson, J.D.*; Li, M.S.M; Ding, Z. Correlating Live Cell Viability with Membrane Permeability Disruption Induced by Trivalent Chromium. *ACS Omega.* **2019**, 4 (1), p. 2142-2151.

9) Henderson, J.D.; Ebrahimi, N.; Dehnavi, V.; Shoesmith, D.W.; Noël, J.J. The Role of Internal Cathodic Support during the Crevice Corrosion of Ni-Cr-Mo Alloys. *Electrochim. Acta.* **2018**, 283, p. 1600-1608.

10) Kobe, B.; Badley, M.; Henderson, J.D.; Anderson, S.; Biesinger, M.; Shoesmith, D. Application of quantitative X-ray photoelectron spectroscopy (XPS) imaging: investigation of Ni-Cr-Mo alloys exposed to crevice corrosion solution. *Surf. Interface Anal.* **2017**, 49, p. 1345-1350.

11) Henderson, J.D.*; Filice, F.*; Li, M.S.M.; Ding, Z. Tracking Live Cell Response to Hexavalent Chromium Toxicity by Scanning Electrochemical Microscopy. *ChemElectroChem*. **2017**, 4, p. 856-863.

12) Li, M.S.M.; Filice, F.; Henderson, J.D.; Ding, Z. Probing Cd^{2+}-Stressed Live Cell Membrane Permeability with Various Redox Mediators in Scanning Electrochemical Microscopy. *J. Phys. Chem. C.* **2016**, 120 (11), p. 6094-6103.

13) Filice, F.; Li, M.S.M.; Henderson, J.D.; Ding, Z. Mapping Cd^{2+}-induced membrane permeability changes of single live cells by means of scanning electrochemical microscopy. *Anal. Chim. Acta.* **2016**, 908, p. 86-94.

14) Henderson, J.D.; Filice, F.; Li, M.S.M.; Ding, Z. Tracking Live Cell Response to Cadmium (II) Concentrations by Scanning Electrochemical Microscopy. *J. Inorg. Biochem.* **2016**, 158, p. 92-98.

15) Filice, F.; Li, M.S.M.; Henderson, J.D.; Ding, Z. Three-Dimensional Electrochemical Functionality of an Interdigitated Array Electrode by Scanning Electrochemical Microscopy. *J. Phys. Chem. C.* **2015**, 119, p. 21473-21482.

CONFERENCE PRESENTATIONS *(* indicates presenting author)*:

ORAL PRESENTATIONS

1) Li, X.; Henderson, J.D.; Shoesmith, D.W.; Noël, J.J; Ogle, K.* "Elucidating the Role of Mo during the Passivation of Ni-Cr-Mo Alloys: Real Time Analysis of Elemental Dissolution and Surface Enrichment." Pacific Rim Meeting on Electrochemical and Solid-State Science (PRiME 2020), **October 4th - 9th, 2020**. *(Invited Lecture)*

2) Henderson, J.D.* "Atomic Emission Spectroelectrochemistry (AESEC) in the Investigation of the Behaviour of Alloying Elements." Canadian Electrochemical Society (ECS) Symposium, Kingston, Ontario, **December 19th, 2019.** *(Award Lecture)*

3) Filice, F.P.*; Henderson, J.D.; Shoesmith, D.W.; Noël, J.J. "Modelling the Crevice Corrosion of G-30 Ni-Cr-Mo Alloy by Moving Boundary Finite Element Method Simulations." 3rd Annual University of Western Ontario ECS Student Chapter Graduate Student Research Symposium, London, Ontario, **December 9th, 2019.**

4) Henderson, J.D.; Ebrahimi, N.; Li, X.; Ogle, K.; Noël, J.J.* "The complementarity of Cr and Mo reinforcing oxide protectiveness on Ni-Cr-Mo Alloys." 236th Electrochemical Society (ECS) Meeting, Atlanta, GA, USA, **October 13th - 17th, 2019.** *(Invited Lecture)*

5) Henderson, J.D.; Seyeux, A.; Zanna, S.; Biesinger, M.; Shoesmith, D.; Marcus, P.; Noël, J.* "Investigating the transport mechanisms governing the oxidation of Hastelloy BC-1 by in situ ToF-SIMS." Materials Science & Technology 2018, Portland, OR, USA, **September 29th - October 3rd, 2019**.

6) Li, X.*; Henderson, J.D.; Shoesmith, D.W.; Noël, J.J.; Ogle, K. "Surface enrichment of Mo during transpassive dissolution of Ni-alloys." EUROCORR 2019 - European Federation of Corrosion Conference, Seville, Spain, **September 9th - 13th, 2019**.

7) Henderson, J.D.*; Li, X.; Shoesmith, D.W.; Noël, J.J.; Ogle, K. “Molybdenum surface enrichment and release during transpassive dissolution of Ni-based alloys.” NACE - Northern Area Eastern Conference, Ottawa, ON, Canada, **October 20th - 23rd, 2019**.

8) Henderson, J.D.*; Li, X.; Shoesmith, D.W.; Noël, J.J.; Ogle, K. “Molybdenum surface enrichment and release during transpassive dissolution of Ni-based alloys.” 9th Annual NACE Southern Ontario Student Section Symposium, London, ON, Canada, **July 25th - 26th, 2019**. *(1st place award)*

9) Henderson, J.D.*; Li, X.; Shoesmith, D.W.; Noël, J.J.; Ogle, K. “Molybdenum surface enrichment and release during transpassive dissolution of Ni-based alloys.” 102nd Canadian Chemistry Conference and Exhibition (CCCE), Quebec City, QC, Canada, **June 3rd - 7th, 2019**. *(2nd place award)*

10) Henderson, J.D.*; Li, X.; Shoesmith, D.W.; Noël, J.J.; Ogle, K. “Investigating the role of alloying elements on the corrosion properties of Ni-based alloys.” ASPIRE Award Lecture, Western University, London, Ontario, **February 25th, 2019**.

11) Henderson, J.D.; Ebrahimi, N.; Dehnavi, V.; Li, X.; Ogle, K.; Shoesmith, D.W.; Noël, J.J.* “Atomic emission spectroelectrochemistry (AESEC) investigation of alloying element behaviour in Ni-Cr-Mo alloy composition.” Fall Meeting of the Electrochemical Society Canadian Section Canadienne, Montreal, QC, **November 10th, 2018.** *(Invited lecture)*

12) Henderson, J.D.; Ebrahimi, N.; Dehnavi, V.; Li, X.; Ogle, K.; Shoesmith, D.W.; Noël, J.J.* “The roles of alloy composition, (external) oxygen reduction and (internal) proton reduction in the crevice corrosion of Ni-Cr-Mo alloys.” Materials Science & Technology 2018, Columbus, OH, USA, **October 14th - 18th, 2018**. *(Keynote Lecture)*

13) Henderson, J.D.*; Ramamurthy, S..; Noël, J.J.; Shoesmith, D.W.; McGarvey, B. “Corrosion Behaviour of Typical Engineering Materials Used in Refinery Processes in Solutions Containing Dilute Fluoride Ions.” Sarnia Technology Applications & Research, Imperial Oil, Sarnia, Ontario, **July 26th, 2017**.

14) Henderson, J.D.*; Ebrahimi, N.; Anderson, S.; Shoesmith, D.W.; Noël, J.J. “The Role of Internal Cathodic Support during the Crevice Corrosion of Ni-Cr-Mo Alloys.” 7th Annual NACE Southern Ontario Student Section Symposium, Hamilton, ON, **July 19th - 20th, 2017**.

15) Binns, W.J.*; Henderson, J.D.; Zagidulin, D.; Shoesmith, D.W. “The Effects of Mg Content on the Cathodic Kinetics of Al_6(Fe, Mn) Particles in Al Brazing Sheets Alloys” Gordon Research Seminar (Aqueous Corrosion), New London, New Hampshire, **July 9th - 15th, 2016**.

16) Henderson, J.D.*; Filice, F.P.; Li, M.S.M.; Ding, Z. “Tracking Live Cell Response to Heavy Metal Toxicity by Scanning Electrochemical Microscopy.” Southern Ontario Undergraduate Student Chemistry Conference. Mississauga, Ontario, **March 21st, 2015**. *(3rd place award)*

POSTER PRESENTATIONS

17) Henderson, J.D.*; Li, X.; Filice, F.P.; Biesinger, M.C.; Shoesmith, D.W.; Noël, J.J.; Ogle, K. "The use of atomic emission spectroelectrochemistry (AESEC) to study the behavior of nickel alloys under industrially-relevant conditions." NACE – Corrosion 2020, Houston, TX, USA, **March 15th - 19th, 2020**.

18) Henderson, J.D.*; Li, X.; Shoesmith, D.W.; Noël, J.J.; Ogle, K. "Molybdenum surface enrichment and release during transpassive dissolution of Ni-based alloys." NACE - Northern Area Eastern Conference, Ottawa, ON, Canada, **October 20th - 23rd, 2019**.

19) Henderson, J.D.*; Li, X.; Shoesmith, D.W.; Noël, J.J.; Ogle, K. "Molybdenum surface enrichment and release during transpassive dissolution of Ni-based alloys." 9th Annual NACE Southern Ontario Student Section Symposium, London, ON, Canada, **July 25th - 26th, 2019**.

20) Henderson, J.D.*; Li, X.; Shoesmith, D.W.; Noël, J.J.; Ogle, K. "Molybdenum surface enrichment and release during transpassive dissolution of Ni-based alloys." 2nd annual ECS Guelph Young Researchers Symposium, Guelph, ON, Canada, **June 21st, 2019**.

21) Henderson, J.D.*; Li, X.; Shoesmith, D.W.; Noël, J.J.; Ogle, K. "Molybdenum surface enrichment and release during transpassive dissolution of Ni-based alloys." 102nd Canadian Chemistry Conference and Exhibition (CCCE), Quebec City, QC, Canada, **June 3rd - 7th, 2019.**

22) Henderson, J.D.*; Li, X.; Shoesmith, D.W.; Noël, J.J.; Ogle, K. "Molybdenum surface enrichment and release during transpassive dissolution of Ni-based alloys." Centre for Advanced Materials and Biomaterials Research Day. London, Ontario, **April 17th, 2019**.

23) Henderson, J.D.*; Li, X.; Shoesmith, D.W.; Noël, J.J.; Ogle, K. "Molybdenum surface enrichment and release during transpassive dissolution of Ni-based alloys." NACE – Corrosion 2019, Nashville, TN, USA, **March 24th - 28th, 2019**. (3rd place award)

24) Badley, M.*; Henderson, J.D.; Almusned, B.; Shoesmith, D.W.; Noël, J.J. "Analysis of Ni-Cr-Mo superalloys using X-ray Photoelectron Spectroscopy imaging." Gordon Research Seminar & Conference (Aqueous Corrosion), New London, New Hampshire, **July 9th - 15th, 2018**.

25) Henderson, J.D.*; Ebrahimi, N.; Anderson, S.; Shoesmith, D.W.; Noël, J.J. "The Role of Internal Cathodic Support during the Crevice Corrosion of Ni-Cr-Mo Alloys." 68th International Society of Electrochemistry (ISE) Meeting, Providence, RI, USA, **August 27th - September 1st, 2017**. *(1st place award)*

26) Henderson, J.D.*; Ebrahimi, N.; Anderson, S.; Shoesmith, D.W.; Noël, J.J. "The Role of Internal Cathodic Support during the Crevice Corrosion of Ni-Cr-Mo Alloys." 6th Annual NACE Southern Ontario Student Section Symposium, Hamilton, ON, **July 19th - 20th, 2017**. *(2nd place award)*

27) Henderson, J.D.*; Ebrahimi, N.; Anderson, S.; Shoesmith, D.W.; Noël, J.J. "The Role of Internal Cathodic Support during the Crevice Corrosion of Ni-Cr-Mo Alloys." CSC

- 100th Canadian Chemistry Conference and Exhibition, Toronto, ON, **May 28th - June 1st, 2017**.

28) Kobe, K.*; Badley, M.; Henderson, J.D.; Anderson, S.; Biesinger, M.C.; Shoesmith, D. "Investigation of oxide films on Ni-Cr-Mo alloys using quantitative XPS imaging." Surface Canada, Montreal, Ontario, **May 9th - 12th, 2017**.

29) Henderson, J.D.*; Ebrahimi, N.; Anderson, S.; Shoesmith, D.W.; Noël, J.J. "The Role of Internal Cathodic Support during the Crevice Corrosion of Ni-Cr-Mo Alloys." NACE - Corrosion 2017, New Orleans, LA, USA, **March 26th - 30th, 2017**.

30) Henderson, J.D.*; Ebrahimi, N.; Anderson, S.; Shoesmith, D.W.; Noël, J.J. "The Role of Internal Cathodic Support during the Crevice Corrosion of Ni-Cr-Mo Alloys." Fallona Family Interdisciplinary Research Showcase, London, Ontario, **January 16th, 2017.**

31) Henderson, J.D.*; Ebrahimi, N.; Anderson, S.; Shoesmith, D.W.; Noël, J.J. "The Role of Internal Cathodic Support during the Crevice Corrosion of Ni-Cr-Mo Alloys." Canadian Electrochemical Society (ECS) Symposium, Oshawa, Ontario, **November 12th, 2016**. (3rd place award)

32) Henderson, J.D.*; Ebrahimi, N.; Anderson, S.; Shoesmith, D.W.; Noël, J.J. "The Role of Internal Cathodic Support during the Crevice Corrosion of Ni-Cr-Mo Alloys." NACE - Northern Area Eastern Conference, Toronto, Ontario, **October 31st - November 2nd, 2016**.

33) Henderson, J.D.*; Ebrahimi, N.; Anderson, S.; Shoesmith, D.W.; Noël, J.J. "The Role of Internal Cathodic Support during the Crevice Corrosion of Ni-Cr-Mo Alloys." Gordon Research Seminar & Conference (Aqueous Corrosion), New London, New Hampshire, **July 9th - 15th, 2016**.

34) Binns, W.J.*; Henderson, J.D.; Zagidulin, D.; Shoesmith, D.W. "The Effects of Mg Content on the Cathodic Kinetics of Al_6(Fe,Mn) Particles in Al Brazing Sheets Alloys" Gordon Research Seminar & Conference (Aqueous Corrosion), New London, New Hampshire, **July 9th - 15th, 2016**.

35) Li, M.S.M.*; Filice, F.P.; Henderson J.D.; Ding, Z. "Induction of Membrane Permeability of T24 Cells through Cd^{2+} Stimulation using Scanning Electrochemical Microscopy." Gordon Research Conference (Cell Biology of Metals), Mount Snow, Vermont, **July 26th - 31st, 2015**.

36) Filice, F.P.*; Li, M.S.M.; Henderson, J.D.; Ding, Z. "Mapping of Single Live Cell Membrane Permeability when Exposed to Toxic Cd^{2+} by Means of Scanning Electrochemical Microscopy." Gordon Research Conference (Cell Biology of Metals), Mount Snow, Vermont, **July 26th - 31st, 2015**.

37) Li, M.S.M.*; Filice, F.P.; Henderson J.D.; Ding, Z. "A SECM Study on the Effects of Cadmium on Membrane Permeability in Human Bladder Cancer Cells." Centre for Advanced Materials and Biomaterials Research Day. London, Ontario, **April 27th, 2015**.